CORNELL UNIVERSITY
Center for Radiophysics and Space Research

ITHACA, N. Y.

CRSR 849

OBSERVATIONS OF FAR-INFRARED MOLECULAR EMISSION LINES FROM THE ORION MOLECULAR CLOUD

Paul Joseph Viscuso, Ph.D.

August 1986

OBSERVATIONS OF FAR-INFRARED MOLECULAR EMISSION LINES FROM THE ORION MOLECULAR CLOUD

A Thesis
Presented to the Faculty of the Graduate School
of Cornell University
in Partial Fulfillment of the Requirements for the Degree of
Doctor of Philosophy

by
Paul Joseph Viscuso
August 1986

Mark Hamit

Observations of Far-Infrared Molecular Emission Lines From the Orion Molecular Cloud

Paul J. Viscuso, Ph.D.
Cornell University 1986

The Orion Nebula has been the subject of intensive study for over one hundred years. Far-infrared (FIR) molecular line observations of CO in the shock region surrounding the infrared source IRc2 have suggested that the molecular hydrogen density in the shocked and post-shock gas is roughly $3 \times 10^6\,\mathrm{cm}^{-3}$. The temperature of this gas is on the order of 750–2000 K. IRc2, like other nearby infrared sources within the Nebula, is thought to be a site of recent star formation. This object is apparently at the center of a massive bipolar molecular outflow of gas, which is producing a shock front where it meets the ambient molecular cloud surrounding IRc2. Study of such regions is important for the understanding of the chemical and physical processes that are involved in the formation of stars from molecular clouds.

Recently, several far-infrared transitions among the low-lying levels of OH have been observed toward IRc2. OH is thought to be abundant, and it plays an important role in the chemical evolution of the shock and post-shock regions. The OH emission serves as a sensitive probe of the temperature and density for the shock-processed gas.

A rigorous treatment of the radiative transfer of these measured transitions is performed using the escape probability formalism. From this analysis, we determine the temperature of the OH-emitting region to be on the order of 40 K. This suggests that the gas is part of the post-shock gas that has cooled sufficiently, most likely by way of radiative cooling by CO. Such cooling from shock temperatures of several thousand degrees can be accomplished in 100 years. A molecular hydrogen density of $3 \times 10^7\,\mathrm{cm}^{-3}$ and an OH column density of $1.0 \times 10^{17}\,\mathrm{cm}^{-2}$ is found. The beam filling factor is determined to be 36%.

To better understand the role of OH in the Nebula, more observations will have to be made at higher spectral and spatial resolution. A continuously tunable grating Fabry-Perot spectrometer has been built to achieve spectral resolution of $15\,\mathrm{km\ s^{-1}}$. Instruments such as these will help in determining the dynamics of the OH gas from line profiles. Higher spatial resolution must await the next generation of infrared telescopes.

Biographical Sketch

The author was born on [redacted] in [redacted], the second and final child of Paul Viscuso and Lucille [redacted] Viscuso. Lancaster was to be his home for the next 23 years. At the age of 10, he decided that it was time to master the accordion. After 19 years, he's still trying. His interest in astronomy began at the ripe age of 12 after he set up his new telescope in the backyard and looked at Jupiter and the Galilean moons. He hasn't been the same since.

At the age of 16, the author began a part-time job at Lancaster Newspapers as a mailer. After graduating from Franklin and Marshall College in 1979 with an A.B. in Physics and Philosophy, the author promptly quit his job as a mailer and looked for more appropriate work. He found it and enjoyed seven months employment in an Italian bakery. Thus began a life-long love of baking. Deciding that waking up every morning at 4 o'clock was not to his liking, he quit the bakery and became a graduate student in infrared astronomy at Cornell, where he would see that unholy hour come and go past him more times than he cares to remember.

In the fall of 1981, he found out what contra-dancing really was, and started playing the dance music on his accordion. In 1984, he met Betsy Gamble and Eric Pallant, and the three formed a dance band. The world hasn't been the same since. Playing for dances has led him to towns such as Brattleboro, Vermont and Brooklyn, New York.

During his six year tour of duty as a graduate student, he travelled to exotic places such as Mountain View, California and Panama City, Panama to observe celestial objects. He also learned how to shave off a beard (namely his own) on a C-141 at 41000 feet in less than 10 minutes with a Swiss Army knife and a razor. He will be leaving Cornell and the field of infrared astronomy this fall to study millimeter and sub-millimeter astronomy as a post-doctoral fellow at the University of Massachusetts in Amherst.

to my parents and grandparents,
that their labors and sacrifices
shall always be remembered

Acknowledgments

The work that this thesis represents could not have been accomplished by a single individual, but only by a team of people working toward a common goal. I heartily acknowledge those people here. Of the final version of my committee, I am first and foremost indebted to Professor Martin Harwit. As my thesis advisor, Martin has played a major role in my development. His insights into astrophysical problems have proven invaluable, and it has been a pleasure to work with him. The decency and respect with which he has treated his students and colleagues alike stand as a testament to his value as a friend and advisor.

I also wish to thank the other members of my committee, Professors Peter Gierasch, Ed Salpeter, and James Cordes. Peter played a more active role than most other minor members, having been a former advisor. He introduced me to the microphysics of clouds; a project from which much was learned, and is appreciated more with time. Ed's physical insight into everything has been a constant source of inspiration. My only regret is that there are not 'ten-to-the-god-knows-how-many' Salpeters around. Jim was the first person to introduce me to radio astronomy, and I hope that his example will serve me well as I take up residence at the Five College Radio Astronomy Observatory at the University of Massachusetts this fall.

For moral support in the early years at Cornell, I stand indebted to Professors Jim Cordes, Ira Wasserman, Steven Beckwith, and James Houck. Of my teachers at Franklin & Marshall College who have continued to teach me not only physics, but a lot about myself and life, I am proud to list here Dr. John Howell and Dr. Alan Bruns. They have helped to keep me on the straight and narrow, and have been instrumental in making me realize what I really want from life.

Much advice, support, and help on this research project discussed within have come from a host of people. Dr. Gordon Stacey was my colleague in arms, until he received his Ph.D. last year and moved to Berkeley. Gordon has been a major source of help and inspiration, and I hope that we will continue to support each other in the years ahead. I gratefully acknowledge Noel Kurtz, who was our resident mechanical engineer; Scott Smyers, who was our resident computer programmer and

electronics builder; and Chuck Fuller, our research support specialist for the last 3 years. I also thank Dr. David Chernoff for much advice on the interpretation of the OH data. I am glad that you beat me in completing your thesis.

It is my pleasure to acknowledge the advice and help of George Gull. George resoldered our dewars two weeks before a flight series – on several occasions. To our machinist, Dave Overbaugh, goes my thanks for many jobs well done. Keep up the excellence. Jim Houck has been a source of clever ideas that have helped us in instrumentation development. Thanks also to Tom Herbst and Paul Graf for helpful hints about Fabry-Perot systems. For her patience and dedication to the art of aluminum mesh-deposition onto wedged quartz, the Hinge's first-born spectrum goes to Nellie Whetten.

It is also fitting at this time to acknowledge the ground crews of the NASA Lear Jet and Kuiper Airborne Observatory for their dedicated service over the years. Very special thanks go to the pilots, especially George Tucker and Pat Morris, for services rendered above and beyond the call of duty. *Un' brindisi* to the vintners of Napa, Sonoma, and Alexander valleys!

I wish to give recognition to Drs. Edwin F. Erickson and Michael Haas, as well as Phil Duffy, at NASA-Ames Research Center. Their help in securing the 84 μm observations was invaluable.

Moral support is always necessary, especially when one undergoes the rigors of graduate school. To the old guard that has gone before me, I gratefully will remember the many several-hour discussions about life that I had with Rida Farouki and Terry Gaetz. To the rest of the old men's club, I tip my hat to Guy Miller, Steve Schneider, Mark Shure, and 'Colonel' Steve Lee.

To the contemporary guard, I gratefully acknowledge Sean Colgan and Louise Barsy Colgan. Sean has been a good friend and a constant source of help, and I owe him several months work that he saved me by providing a copy of his radiative transfer code. Best of luck to both of you in California. To the CRSR hockey team, Damon Simonelli, John Wang, Tom Herbst, and Mike Skrutskie, special thanks are yours. Thanks also go to Mike for introducing me to infrared observing at HBO. The two-liter coke bottles made the grueling all-night runs worthwhile. Thanks go

to Edvige Corbelli, for bringing a bit of the old country to me. Buona fortuna in Italia! To the master of abuse, Chris Magri, best of luck to you and Sylvie.

I have been lucky enough to have had some sort of social life outside of the group and the department. Here I acknowledge the non-graduate students, or as they are better known, the real people.

For all of the pleasures that playing music has brought to me, I am most indebted to Betsy Gamble, Eric Pallant, and Rich Sobel. Their excellence has inspired me, and my craziness has inspired them. I hope to never lose touch with them and with the music we have shared so often.

For emotional support throughout the years, I am grateful to several special people. To Jan Seiden, best of luck with your graduate work at Hopkins. Your friendship will be a lasting treasure. For helping me smile through the darkest days, I am indebted to Leslie Osborne. May you find happiness wherever you are. To my best friend, Maren Cooke, go my most sincere and warmest thanks and appreciation. And to Betsy Gamble, you are a rare and special person. May our friendship continue to grow in the years ahead. Without all of you, the past two years would have been very difficult. Amherst is not that far away.

It is a privilege to acknowledge here a special friend. She brought to this department a smiling face and a rare ability of excellence in the classroom. Her work in galactic astronomy is done with the greatest of care, and her knowledge and command of the subject is extraordinary. For all of her support, past, present, and future, I give especial thanks to Professor Martha Haynes.

I shall remain indebted to Martin Harwit, Jim Houck, Martha Haynes, and Peter Gierasch for having so much faith in me and writing letters of recommendation, as well as for doing a bit of lobbying in Amherst. Martha, the check will be in the mail shortly.

Sylvia Corbin deserves much earned gratitude. As our secretary, she has always taken care of the business and manuscript end of things, and keeps the groups running. I'll never figure out how she always knows what to do or whom to contact. Thanks for making all of those travel arrangements. The department probably can't afford to pay you what you are really worth. I will miss you when I

leave. Thanks also to Barbara Boettcher, for her excellent drawings of the figures in this thesis and in the published papers.

To a bunch of crazy people that are near and dear to my heart and have become a second family to me; love and gratitude go to Gerda, Stanley, Santha, Lori, and especially Carla Cooke. Best of luck with the baby, Santha. Amherst is even closer.

I acknowledge the friends that I've left behind in Lancaster, especially those in the old mailroom crew: Jere Kendig, my 'brother'; Ed Birchall, the volleyball and Cheshire expert; Jim Miller and family crew members, best of luck on First Street; Tom Hippel, nightside pressroom foreman, you are a good friend; and Larry 'Albie' Albright, who redefined the word 'courage' for me. The times together are permanently etched upon my memory.

For all of those who have touched my life, or whose lives I have touched, each encounter has helped me be what I am today. Unless you have liability insurance, it may be best not to acknowledge your influence.

For the taxpayers of the world, your unintentional contributions to research have helped advance the peaceful sciences and their role in the world. Let us hope that the humanitarian scientific ethos lives on.

To Dr. Luigi Domenico Francesco Vertucci, it's been a distinct pleasure to have spent these last 4 or 5 years together. I hope you enjoy the comforts of the Shady Lane Rest Home and Insane Asylum after your stay at Cornell is over.

Lastly, and certainly not least, I acknowledge my family members. For my grandparents, Domenico and Elisabetta Viscuso and Francesco and Philomena de Pancrazio, who sought a new life in a new land; your decades of hard work and sacrifices have inspired me onward. To Lucille and Paul Viscuso, my mom and dad, you taught me well. I hope that I never give you reason to lose faith in me. I'll never lose faith in you. And for my sister Betty and her children, thanks for the support and the opportunity to be called 'Uncle'. Best of luck to you and your new life.

Table of Contents

List of Tables

List of Figures

Nel mezzo del cammin di nostra vita
mi ritrovai per una selva oscura
che la diritta via era smarrita.
Ahi quanto a dir qual era è cosa dura
esta selva selvaggia e aspra e forte
che nel pensier rinova la paura!

DANTE ALIGHIERI, *Inferno*

Midway in the journey of our life
I found myself in a dark wood,
for the straight way was lost.
Ah, how hard it is to tell what that
wood was, wild, rugged, harsh;
the very thought of it renews the fear!

DANTE ALIGHIERI, *Inferno*

I. Introduction

The infrared part of the electromagnetic spectrum spans three orders of magnitude in wavelength, from 1 to 1000 microns (μm). We may roughly divide this range into three regimes: near-infrared (1–10 μm), mid-infrared (10–100 μm), and far-infrared (100–1000 μm). The portion of the far-infrared (FIR) from 300 to 1000 μm is also known as the sub-millimeter regime. Heterodyne techniques are usually employed in sub-millimeter work, whereas incoherent instruments such as grating spectrometers, interferometers, and Fabry-Perot spectrometers are the mainstay for observing the rest of the infrared spectrum. In chapter II, we discuss the instrumentation used to collect most of the data presented in this thesis. The optical hardware includes our grating spectrometer and lamellar-grating interferometer. In chapter III, we introduce our novel, continuously tunable, hinged grating Fabry-Perot spectrometer.

Continuum emission in the infrared is observed from a large variety of astronomical sources, including H II regions, molecular clouds, planets, comets, circumstellar shells, extended stellar atmospheres, galaxies, and quasars. This emission tells us much about these objects, including such physical parameters as temperature and density. Dust particle sizes can also be inferred from such observations. Infrared continuum emission studies have also been used to determine the hydrogen to helium ratios for in the atmospheres of Jupiter and Saturn.

Atomic and molecular line emission in the infrared has been observed from most of these objects as well. Ionized and neutral atomic transitions, for example, can tell us much about the H II regions surrounding hot O and B stars and white dwarfs associated with planetary nebulae (Shure 1985). Hyperfine atomic transitions of ionized carbon and ionized and neutral oxygen are among the principal coolants in the interstellar medium (Stacey 1985). Infrared observations of molecular transitions from the gaseous planets such as Jupiter and Saturn have led to a better understanding of the gas dynamics of these systems (see, for example,

Haas et al. 1985; Tokunaga et al. 1980).

The visual extinction caused by intervening clouds of dust along the line of sight is not a problem in most of the infrared spectrum. We are able to *see* star formation regions embedded in dust clouds using infrared measurements while the nascent stars remain optically hidden from view behind their cloak of dust and gas.

The earth's atmosphere is opaque over most of the far-infrared spectrum, owing to absorption by water vapor and other trace constituents such as CO_2 and O_3. This makes it necessary to make all of the FIR observations at high-altitude. The National Aeronautics and Space Administration (NASA) provides two airborne observatories for the purposes of infrared and sub-millimeter astronomical research. The Lear Jet contains a 12 inch, f/6.5 telescope while the Kuiper Airborne Observatory (KAO) houses a 91 cm, f/17 telescope. The observations that are discussed in this thesis were obtained with the KAO, using our grating spectrometer in conjunction with the interferometer to obtain an instrumental resolution, $\lambda/\Delta\lambda$, of up to 4000. Stressed gallium-doped germanium detectors cooled to 2 K give us sensitivity in the spectral range 100–195 μm.

One of the most intensely studied star formation regions is the Orion Nebula and its associated molecular cloud, OMC-1. Being only 500 parsecs distant, it is also one of the closest of such regions. The nebula is thought to be quite young, perhaps several tens of thousands of years old, and there are indications that star formation is still happening deep within. One of the young stellar objects that has been found is an infrared source known as IRc2. This object seems to be at the center of a massive bipolar outflow which is pushing into the surrounding ambient molecular cloud, giving rise to shock structures on the order of 10^{17} cm in size with temperatures in the range 750 to 2000 K (Erickson et al. 1982; Watson 1982). The temperatures and densities were derived from molecular hydrogen and CO observations (Beckwith et al. 1978; this work, chapter V; and references therein). The molecular hydrogen density in the shocked and post-shock gas is roughly $3\text{–}10 \times 10^6\,\mathrm{cm}^{-3}$.

At these temperatures and densities, the CO is collisionally excited by the H_2, especially the higher J rotational levels. The optically thin transitions in the FIR part of the spectrum are not very sensitive to densities above $10^5\,\mathrm{cm}^{-3}$ and

temperatures above their excitation temperatures. These transitions are thus good yardsticks by which we may measure the amount of CO present in the shocked gas. We report in chapter V the first astronomical detection of the $J = 15 \rightarrow 14$ rotational transition of CO at 173.631 μm toward OMC-1. The 173 μm line flux is consistent with other CO rotational line fluxes measured and reported previously by Stacey et al. (1982), Stacey et al. (1983), and Watson (1982). The data support the view that the CO-emitting region is contained within the post-shock gas of molecular hydrogen density $\sim 3 \times 10^6\,\mathrm{cm}^{-3}$ and kinetic temperature of $\sim 750\,\mathrm{K}$. The mass of hydrogen that is associated with this region is between 1.0 and 1.5 $\mathrm{M}_\odot$.

Another important molecular constituent of the gas, according to chemical equilibrium models, is OH. It is possible to determine the physical parameters of the OH-emitting region by using the same line of analysis that was used for the CO. We need to collect a data base of as many rotational transitions as is possible, and then try to determine the temperature and density of the emitting region using conventional radiative transfer theory. To this end, we have made observations of the $^2\Pi_{3/2}\ J = \frac{7}{2} \rightarrow \frac{5}{2}$ rotational transitions of OH at 84.42 and 84.60 μm and of the $^2\Pi_{1/2}\ J = \frac{3}{2} \rightarrow \frac{1}{2}$ rotational transitions at 163.12 and 163.40 μm. Coupling these data with the $^2\Pi_{3/2}\ J = \frac{5}{2} \rightarrow \frac{3}{2}$ (119.23 and 119.44 μm) data of Watson et al. (1985), we are able to construct a model of the OH-emitting region in which the above data are consistent. This model, discussed in chapter V, makes use of the new experimental H_2–OH collisional cross-sections of Andresen, Häusler, and Lülf (1984) and Schinke and Andresen (1984), which are significantly different from earlier values calculated by Dewangan and Flower (1981, 1983).

Since we have measured rotational transitions that involve the 5 lowest rotational energy levels, the data are not very temperature sensitive for temperatures above about 100 K. We cannot, therefore, determine the temperature of the OH-emitting region. If the temperature is 100 K, then we are talking about the post-shock gas which will form a column roughly 10^{17} cm deep (Genzel 1985). However, if the temperature is near 1000 K, then we are looking at the gas near to or within the shock-front. Since we expect an enhancement of about a factor of 40 of the OH within a thin sheet about 10^{14} cm deep (Draine and Roberge 1982), then for

high-temperatures, this thin region of enhanced OH should dominate in the line emission.

The molecular hydrogen density that we derived from the OH data is quite insensitive to temperature. Whether the OH is coming from the shock front or from the post-shock gas, the density of H_2 in the emitting region is $\approx 1.0 \times 10^7\,cm^{-3}$. This compares favorably with the somewhat lower estimate from the CO data (Watson 1982). New and more accurate H_2–CO collision rates have been calculated by Schinke et al. (1985), and suggest that the older rates overestimated the large ΔJ cross-sections. We expect that the newer rates will require a slightly higher density.

The model used in chapter V makes use of somewhat simplified and idealized assumptions concerning the treatment of radiative transfer. In order to make better use of the data, we have constructed a numerical radiative transfer code based upon the escape probability formalism first introduced by Sobolev (1957). In chapter VI, we discuss the results of this code. We find that the three sets of infrared data (84, 119, and 163 μm) can be fitted by a one-component model. For high temperatures (T>50 K), the observed 163 μm flux is always too bright, usually by an order of magnitude. This rules out the shock front or hot post-shock gas as the source of the OH radiation. We find that the temperature of the gas must be about 40 K to produce the observed line ratios. The H_2 density is about $4 \times 10^7\,cm^{-3}$ and the OH column density is on the order of $10^{17}\,cm^{-2}$. This fits in with the present thinking of Melnick (1985) concerning OH in OMC-1.

The failure of the simple model used in chapter V to predict these low temperatures is a result of several factors. One reason for the incongruent conclusions of the two methods of analysis is that not all of the radiative processes were taken into account, and these processes are significant. For example, not every OH molecule that is excited into the $^2\Pi_{1/2}$ ladder will decay and emit a 163 μm photon. There are other routes of decay back down to the ground state. Another source of error was the inability to reliably estimate the level populations in the simplified model. A third effect is that the simple model assumes that photons may be trapped and reradiated throughout the cloud, whereas we know that the radiative processes must be local phenomena owing to the velocity gradient that exists in OMC-1.

Whereas the simple method of analysis presented in Chapter V is useful in the interpretation and understanding of the physics, it is good only as a first-order analysis of the data. For OMC-1, it is necessary to perform more exact numerical radiative transfer calculations. These calculations allow us to better determine the physical parameters of the OH-emitting region.

Better spectral and spatial resolution would greatly enhance our ability to understand the OH data. We have developed a unique Fabry-Perot spectrometer which will allow us to have spectral resolutions as small as $15\,\mathrm{km\,s^{-1}}$. Whereas this resolution is not unique to FP systems in and of themselves, the novel aspect of this instrument is that a grating is placed between the two highly reflecting plates. With this arrangement and proper placement of the two plates and the grating, it is possible to continuously tune the instrument over the range of $138\text{–}170\,\mu\mathrm{m}$. This tuning is achieved by a simple rotation of the grating. The plates never move, thus making the system a very sturdy and stable one that is well suited to space missions. This hinged grating Fabry-Perot is discussed in chapter III.

Finally, in chapter VII, we list what needs to be done for future work in order to resolve the OH issue. Also discussed are plans for redoing the CO calculations of McKee et al. (1982) and Watson (1982) using more accurate collisional cross-sections with H_2 computed by Schinke et al. (1985). It is expected that these new models may result in an upward revision of the temperature of the CO-emitting region, owing to the smaller collision rates for large ΔJ. Future plans for using the new Fabry-Perot spectrometer are also discussed.

II. Instrumentation

2.1 Introduction

The detection of FIR radiation is essential to the study of a wide variety of celestial objects. The central engines powering quasars could release much energy in the FIR. Abundances of neutral and ionized atomic species and physical conditions of the Galactic center can be deduced from FIR observations. This can also be done for active galactic nuclei and starburst galaxies such as M82 and NGC 1068 (Crawford et al. 1985). For example, recent infrared observations of Ne II emission from the central 2 parsecs of the Galaxy revealed evidence for a massive black hole in the center (Serabyn and Lacy 1985). Fine-structure lines from highly ionized species can determine temperatures and densities in the ionized regions of planetary nebulae and H II regions (Shure 1985; Herter, Helfer, and Pipher 1983). Temperature profiles of planetary atmospheres can be deduced from FIR continuum measurements. Emission data of molecular and atomic transitions in the FIR can tell us about the physical conditions in the shock regions associated with mass outflow from nascent stars. Circumstellar dust shells can best be studied in the infrared. Galaxies that were formed in the early universe will also have much of their energy output redshifted into the infrared part of the spectrum. Virtually the whole gamut of objects that are known to exist can be seriously studied in the far-infrared.

Although broad-band photometry, such as that done by the infrared astronomical satellite (IRAS), is important in these studies, it is necessary to have high spectral resolution in order to gain a deeper understanding of the physical conditions within these regions. For example, the O I $^3P_1 \rightarrow {}^3P_2$ fine structure transition at 63.17 μm is one of the major coolants in the interstellar medium (ISM). With broadband photometry, it is impossible to deduce the contribution of this line to the astrophysics of the ISM. However, with high spectral resolution instruments, this

line can be separated from the continuum. The instruments which can provide us with this kind of resolution are grating spectrometers; Michelson, lamellar-grating, and Fabry-Perot interferometers; and heterodyne receivers.

The energy of a FIR photon is ~0.01 eV, two orders of magnitude below the average energy involved in chemical reactions. For this reason, no photographic emulsions are available that can detect FIR photons. The most efficient method of detecting these photons is the use of extrinsic photoconductive material such as gallium-doped germanium (Ge:Ga). More will be said about detectors later.

2.2 Why Airborne Astronomy?

2.2.1 Atmospheric Transmission

The detection of FIR radiation is hampered by the water vapor in the atmosphere. Carbon dioxide, CO_2, and ozone, O_3, play a somewhat lesser role in the absorption of FIR photons, as well. In figure 2.1, we see the transmission of the atmosphere for wavelengths between 120 and 170 μm at 4 different altitudes (Traub and Stier 1976). At an altitude equivalent to that of the top of Mauna Kea in Hawaii (4 km), we see that the transmission is ~0% for nearly the entire range of wavelengths. This makes ground-based work in the FIR virtually impossible.

As we move up into the atmosphere, the transmission begins to greatly improve. For unmanned balloon packages at 28 km, there are rather narrow atmospheric features, but most of the spectrum is relatively free from absorption. For manned observations, the highest altitude available for reasonably sized instruments is that reachable by aircraft. It is important to also be above the troposphere, the section of the atmosphere closest to the earth's surface. It is in the troposphere where convection occurs and, hence, weather. Due to the convection, the water vapor content at the higher altitudes in the troposphere can still be quite high. The tropopause, the top of the troposphere, is usually at an altitude between 33000 and 41000 feet. An altitude of 14 km provides us with many clear windows in the FIR. Pressure-broadened water vapor absorption features, however, do still provide a significant amount of blockage of FIR photons from astronomical sources.

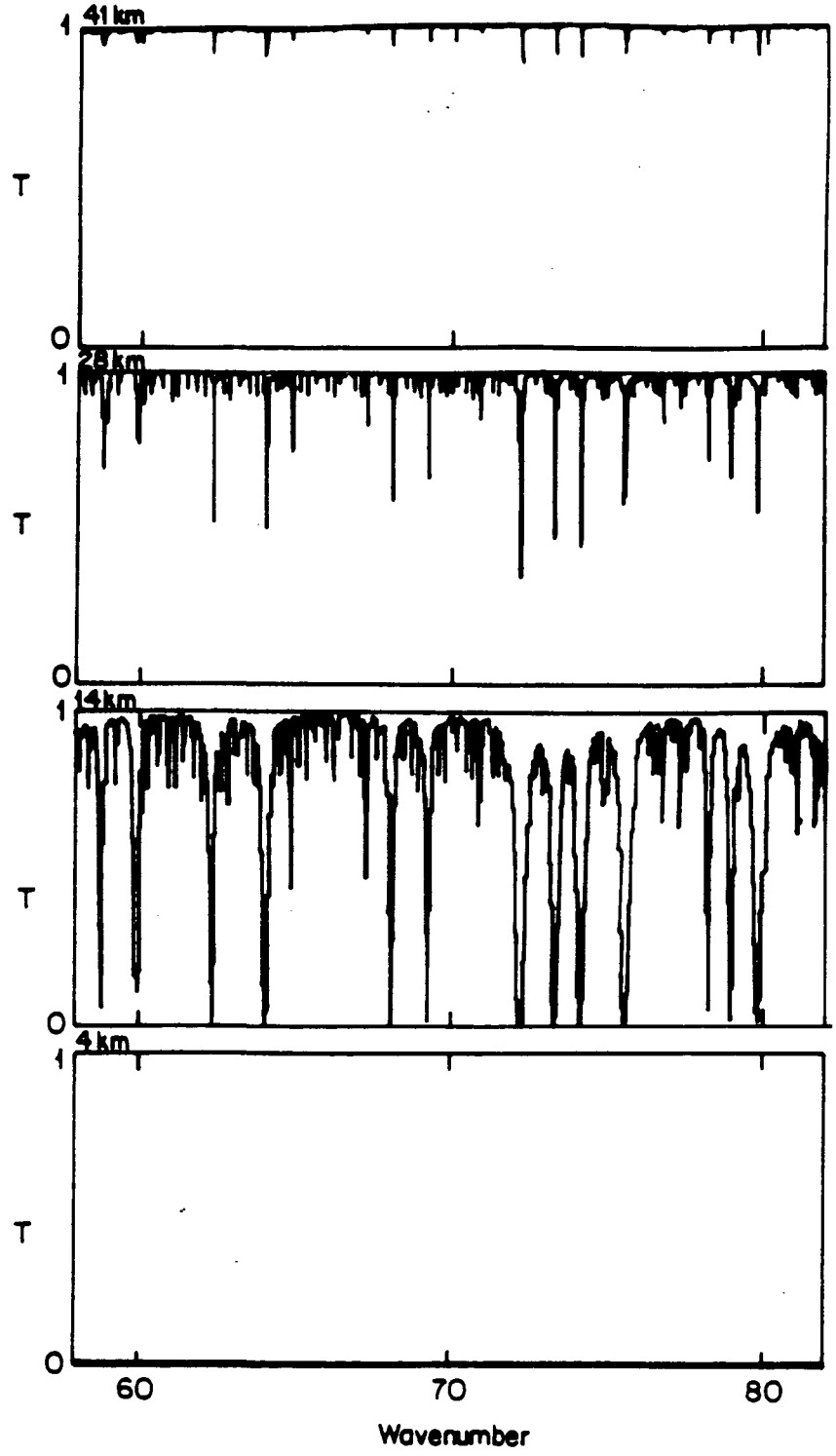

FIGURE 2.1 Atmospheric transmission profiles for four altitudes: 41 km, 28 km, 14 km, and 4 km. From Traub and Stier (1976).

The advantages of airborne packages over balloon-borne telescopes are better pointing and target-tracking accuracy and the control that the observer actually has over the observations. One of the disadvantages is that at the lower altitudes of airplanes such as the Kuiper Airborne Observatory (KAO), one is still bothered by telluric features and, at times, also by clouds.

2.2.2 Airplane Environment

Since we must make use of an observing platform that can penetrate the stratosphere, we use the KAO. The KAO is a Lockheed L300 configured as a prototype version C-141A Starlifter jet transport that is operated by NASA/Ames Research Center from Moffett Field Naval Air Station in California. Sitting in a cavity in the port side of the forward section of the plane is a 0.91 m Cassegrain telescope. The optics constitute an f/17 system.

The KAO is large enough to comfortably accomodate a retinue of observers and staff onboard. Six or seven observers can be on a flight (as opposed to only two on NASA's Lear Jet; Stacey 1985). Five flight personnel are also on board to operate the telescope and associated support systems. They include the following. The mission director coordinates interaction of the KAO staff, the investigator team, and the flight crew. He also assures optimum support of research activities. The telescope operator activates and controls telescope stabilization while the systems monitor is responsible for the proper operation of the oscillating secondary mirror and the telescope cavity. The Airborne Data Acquisition and Management System (ADAMS) is run by the ADAMS operator. The tracking operator acquires the astronomical objects of interest in the closed-circuit video system which allows us to guide on the object or suitable nearby guide stars. Since the telescope has a limited range of motion in azimuth ($\pm 2^\circ$), it is necessary for the plane to fly in a specified direction in order to observe a certain object at a specific time. For this reason, a flight plan which lays out the routes that must be taken in order to observe the objects of interest must be worked out and filed at least one day before flight. The flights generally begin and end at Moffett Field and last up to 7.5 hours, of which 6.5 hours can be dedicated to observing. Optimizing the flight plans involves

rearranging the observing sequence of sources, choosing the latitude and longitude where the observations can start (within reasonable distance of Moffett, that is), and choosing the time of takeoff which gives best results. Other considerations to take into account in the optimization of the flight plan are several restricted military warning areas over which flying could be hazardous that need to be avoided as well as the added bonus that the winds that the aircraft will encounter are generally not very well known one or more days before takeoff. These could alter the flight plan significantly if they are drastically different from the assumed winds. All of these factors add up to making the optimization of a flight plan a highly evolved art. NASA provides the users with several navigators for just this purpose.

2.2.3 The Telescope

The telescope that is onboard the KAO consists of a primary paraboloid of diameter 36 inches (91.5 cm). The effective focal length is 610 inches yielding a focal ratio of f/17. The diffraction limit at 150 μm is roughly 6.2 mm. At a scale of $14''$/mm at the focal plane, a 4×4 mm aperture corresponds to a $\approx 1' \times 1'$ beam size.

The telescope is supported in the airplane by an air bearing. This spherical bearing allows the telescope to float with a minimum amount of friction and influence from any airplane rotations. The system is gyro-stabilized to allow accurate tracking of celestial objects. Most investigator packages use the Nasmyth instrument cavity. Once the investigator's instruments are attached to the Nasmyth cavity, the telescope must be balanced to insure the proper operation of the gyros.

Since the telescope is in contact with the ambient air at altitude, this will cool down the telescope. It has been found that an image shift of up to $2'$ will result from this cooling. In order to minimize the shift during flight, it is possible to pre-cool the telescope before flight to a temperature of -30°C. In reality, the pre-cool may get the temperature of the primary mirror down to 0°C. The efficiency of the pre-cool is dependent on ambient temperature and relative humidity.

2.2.4 The Chopper

At an altitude of 14 km and a wavelength of 150 μm, the emissivity of the atmosphere is 0.13 (Traub and Stier 1976). The ambient temperature is -50°C, or 223 K. With an instrumental resolution of 200 ($\lambda/\Delta\lambda$), this corresponds to an incident flux of 2.8×10^{-8} W cm^{-2} str^{-1}. This is at least a factor of 5 stronger than any flux we may hope to receive from the most luminous astronomical sources. Not only do we see the atmosphere, but the telescope is also a source of FIR photons. All of these background sources will dominate the signal.

It is desirable to subtract out this background, and this can best be done by a method called 'chopping'. Chopping consists of switching the beam from on-source to off-source and then to on-source again. This is usually done at a frequency of 25–35 Hz since the fluctuations in the background can occur on relatively short time-scales. Chopping is accomplished by having the secondary mirror of the telescope wobble. In chopping, the on-source beam will have the ordinary background contribution plus that of the source. The off-source beam will only have the background. By subtracting the two, we find the source contribution. For the KAO, the chopper throw can be as large as 15′, although for amplitudes of this size, the chopper efficiency (ratio of cycle time in the beams to the cycle time between beams) decreases. For most sources a throw of 4–6′ is sufficient.

2.2.5 Tracking and Guiding

Once the object to be studied is acquired in the field of view of the telescope, it must be tracked. This is done using the KAO tracker camera and tracking computer. The pointing accuracy of the camera is about ±5″. Since most FIR sources are not in themselves optical sources, it is necessary to use a guiding system which enables one to guide on a nearby star while the telescope boresight is looking at the FIR source. We have used Professor James R. Houck's offset-guider coupled to the KAO tracking system in order to track objects that we have studied. The mean guiding error is about 5″. The relative positions of the appropriate guide stars to the sources are calculated before flight.

2.2.6 Data Acquisition

The data acquisition software that is run on our IMSAI computer was developed by Charles Fuller at Cornell University. The software package will run a motor drive box which controls the spectrometer grating and the interferometer movable mirror position. The program also will record and average the signal strengths. The drive box was constructed by Scott Smyers in Ithaca. Scott also wrote the fast-fourier transform package that is used to generate spectra from the interferometer data.

Figure 2.2 shows a schematic layout of our system as it is interfaced with the KAO. The instrumentation is attached to the telescope and controlled by the data acquisition software. The telescope position is controlled by the tracking computer. The IMSAI acknowledges when the tracking computer has lost track of the guide star and, if this occurs, will stop taking data until the tracking computer has reacquired the guide star. The IMSAI is also interfaced with the ADAMS computer. From ADAMS, it acquires such housekeeping data as the object name, rotation angle, boresight water vapor readings (in microns of precipitable H_2O), universal time, etc.

The chopped signal from the detectors is demodulated by Ithaco lock-in amplifiers. These amplifiers use the telescope secondary driver as a frequency reference. The output of the Ithacos is an analog voltage signal between -10 and $+10$ volts. This signal is then routed to an analog-to-digital converter board in the IMSAI computer. The data acquisition program will sample this input to determine the signal strength. The data are sent to ADAMS to be stored on tape. It is also written to floppy disks for post-flight reduction on the IMSAI.

2.3 Detectors

2.3.1 Overview

There are several different types of detectors that may be used for infrared astronomy. Bratt (1977) gives a detailed account of the physics of infrared detectors. A short summary follows here. These may be separated into two classes:

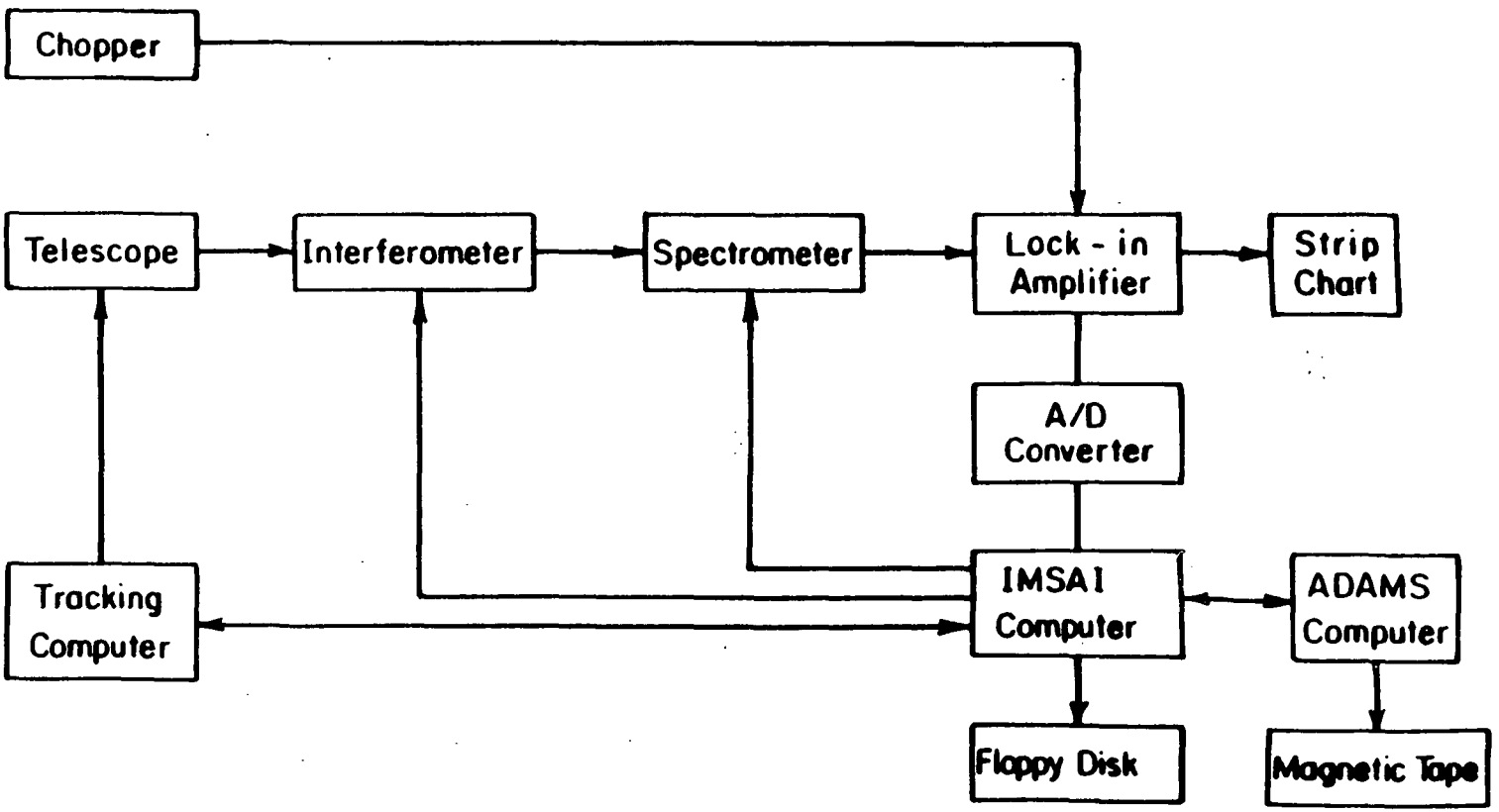

FIGURE 2.2 KAO-IMSAI-Interferometer interface. After Melnick (1981).

thermal and quantum detectors. Quantum detectors may be further divided into intrinsic and extrinsic detectors. Another division of quantum detectors is into photoconductive and photovoltaic detectors.

Thermal detectors, or bolometers, have been widely used in IR astronomy. Bolometers absorb the incident radiation which heats up the crystal. This increase in temperature will change a characteristic of the detector, such as its resistance. The most popular bolometer is the low-temperature germanium bolometer (Low 1961). The germanium bolometer is sensitive to radiation from 1 μm to 1 mm. For a more detailed discussion of thermal detectors, see Gillett, Dereniak, and Joyce (1977) and references therein.

In quantum detectors, also known as photon detectors, the incident photons interact to produce free charges in the semiconductor crystal. There are two modes of operation: the photoconductive and the photovoltaic mode. In the photovoltaic mode, the freed carriers are separated by the intrinsic electric field that is generated by a diode junction. One can then measure a change in one of the diode characteristics, which could be a current change at zero bias voltage or a voltage change at zero current. An example of photovoltaic detectors is the indium-antimonide (InSb) detector used for $\lambda < 5.5\,\mu$m.

For photoconductors, two types of electronic excitation are utilized: i) intrinsic excitation and ii) extrinsic excitation. For intrinsic photoconductors, the transition occurs in the pure semi-conductor material between the valence band and the conduction band. This transition can only occur if the photon has an energy greater than the band gap energy, Eg. The temperature of the detector must also be below the band gap energy. Examples of intrinsic photoconductors and their band gap energies (in microns) are Si (1.2 μm), Ge (1.8 μm), InSb (5.6 μm), and $Hg_{1-x}Cd_xTe$ (8–15 μm) (Lena 1978).

Most of the observations that are reported in this work have been made using extrinsic Ge:Ga. Extrinsic photoconductors consist of semiconductor material in which impurities are implanted during the crystal growth. Germanium or silicon usually serves as the matrix into which either group IIIa elements (B, Al, Ga, In, or Tl) or group Va elements (P, As, Sb, or Bi) are implanted. In the crystal lattice,

one of the dopant atoms will replace one of the matrix atoms.

2.3.2 Ge:Ga Detectors

Let us consider our Ge:Ga detectors. Since Ge has 4 valence electrons, it will form covalent bonds with 4 neighboring Ge atoms by sharing an electron. At an impurity site, the Ga has only 3 valence electrons. (The Ga is called an acceptor impurity since it can accept an electron. Group Va elements have 5 valence electrons and are called donors.) With only 3 valence electrons, there is one electron missing that would complete the bonding arrangement. In effect, a hole is created which is loosely bound to the impurity site.

The existence of impurities actually introduces discrete levels just above the valence band. When a photon is absorbed by the detector, an electron is excited from the valence band into one of these impurity acceptor levels. Alternatively, a hole is excited into the valence band. When an electric field is applied across the detector, the hole can now move until it recombines at another impurity site. The number of passes that the hole makes through the detector before it recombines is known as the photoconductive gain, G_p.

The fraction of incident photons which actually excite the charge carriers in the detector is known as the quantum efficiency, η. It is desirable to have a high quantum efficiency; viz., $\eta \approx 1$. This requires having a high dopant level; however, if the dopant level is too high, then the energy levels due to each impurity atom will begin to overlap. This phenomenon is known as impurity banding. With too many impurity sites, the photoconductive gain will decrease since the mean free path for the charge carriers will be small and the resulting responsivity will also be small. Therefore, the doping must be kept at a low level. Since the quantum efficiency, and hence the cross-section for absorption of a FIR photon, will be relatively small with the low doping levels, it is advantageous to have a larger detector crystal. With typical doping levels, the mean free path of an impurity site ionizing photon is roughly 5 mm. This means that detectors should be on the order of 5 mm in size. Unfortunately, detectors are rather susceptible to cosmic rays (Houck and Briotta 1982). The bigger the detector, the larger the cross-section for absorption of cosmic

rays. For this reason, detector dimensions are kept small.

The dimensions of our Ge:Ga detectors are $1 \times 1 \times 3$ mm. Since these sizes do not provide for adequate opacity to FIR photons, it is necessary to place the detectors in integrating cavities. These cavities allow the incoming photons to be trapped and pass through the detector until most have been absorbed by the detector.

The acceptor impurity energy levels for Ge:Ga are about 10^{-2} eV above the valence band with doping levels of $\sim 2 \times 10^{14}\,\mathrm{cm}^{-3}$. This corresponds to a cutoff wavelength of about $120\,\mu$m. Price (1961) and Hall (1962) have reported that uniaxially stressing the detector along the [100] crystallographic axis splits the four-fold degeneracy into two doubly degenerate bands, one with slightly higher energy and one with slightly lower energy. The splitting is proportional to the applied stress, and a stress of 6.6×10^7 kgf m^{-2} will result in a gap between the valence band and the acceptor levels of 6 meV (Haller, Hueschen, and Richards 1979; Kazanskii, Richards, and Haller 1977). This results in a photoconductive response out to wavelengths of $\approx 205\,\mu$m. We have achieved sensitivity out to roughly $195\,\mu$m with our detectors. It should be noted that for low signal levels, Ge:Ga used as a photoconductor is 2 or 3 orders of magnitude more sensitive at these wavelengths than bolometers.

Our detector material was ordered from Eagle-Picher in the form of 2.75″ diameter wafers. These wafers were cut 3mm thick along the [100] axis. The germanium was doped with 2.1×10^{-14} atoms cm^{-3} of gallium. The residual impurity level was less than $10^{13}\,\mathrm{cm}^{-3}$. Haller, Hueschen, and Richards (1979) describe the process of making ohmic contacts. Boron ions are implanted into the two faces of the wafer, first at a surface density of 10^{14} ions cm^{-2} at an energy of 25 keV, and then at a dosage of 2×10^{14} ions cm^{-2} at 50 keV. Next, the wafers are annealed in an argon atmosphere at 200 °C in order to remove implantation damage. This process also activates the boron. The faces are then wetted with 500 Å of palladium upon which is deposited a $1\,\mu$m layer of gold for electrical contact.

Since a stress needs to be applied to the detector, the detector must be mounted in a housing. We also need an integrating cavity, so the housing will also

serve this purpose. The detector housings are made of hard brass. This material has the hardness that is needed in order to minimize the cold flow that would be associated with aluminum housings (Watson 1982) and also has a high coefficient of thermal expansion. Most of the stress that a detector experiences is due to the differential thermal contraction between the housing and the detector upon being cooled down to liquid helium temperatures (4.2 K). Hence, the housing must be made of a material that will undergo a substantial contraction during cooldown. Stacey (1985) discusses in detail the manufacture and design of housings and detectors. Other descriptions of stressed detector construction can be found in Watson (1982) and in Haller, Hueschen, and Richards (1979).

The first astronomical detection made with stressed gallium-doped germanium detectors was in 1980 (Russell et al. 1980). This observation was of the 157 μm C II line in Orion. This line is one of the dominant coolants in the ISM.

2.3.3 Detector Performance

The total number of photons absorbed per unit time interval can be written as

$$N_\nu = \frac{I_\nu \, \Omega \, A \, \tau_\nu \, \eta_\nu \, \delta\nu}{h\,\nu} \ \mathrm{s}^{-1} \ , \tag{2.1}$$

where I_ν is the specific intensity in erg $\mathrm{s}^{-1}\,\mathrm{cm}^{-2}\,\mathrm{str}^{-1}\,\mathrm{Hz}^{-1}$, Ω is the solid angle of radiation incident upon the detector, A is the collecting area upon which the radiation is incident, τ_ν is the transmission of the optics, η_ν is the quantum efficiency, and $\delta\nu$ is the bandpass. In a diffraction limited system, the product $A\Omega$ is equal to $4.7\lambda^2$. If we use the system resolution, R, in place of the bandpass, then we can rewrite (2.1) to be

$$N_\nu = \frac{4.7 \, I_\nu \, \lambda^2 \, \tau_\nu \, \eta_\nu}{h\,R} \ \mathrm{s}^{-1} \ . \tag{2.2}$$

For the present, let us consider only the background radiation incident upon the detectors. In this case, at an altitude of 14 km, the detector will be looking at radiation coming from the earth's atmosphere, which behaves like a grey body with temperature T_ν and emissivity ϵ_ν. With an emissivity of 0.13 at 150 μm (Traub and Stier 1976) and a temperature of about 220 K, the number of photons absorbed

by the detector is given as

$$N_\nu \sim 2 \times 10^{11}\, R^{-1} \text{ photons s}^{-1} , \tag{2.3}$$

where we have assumed an instrument transmission of roughly 30% and a quantum efficiency of 0.15 (Stacey 1985). The fluctuation in the number of detected photons from the background radiation is given as

$$\Delta N_\nu = [2\, N_\nu\, B(1 + \eta_\nu\, \bar{n}_\nu)]^{\frac{1}{2}} , \tag{2.4}$$

where B is the electrical bandwidth and $\bar{n}_\nu$ is the photon occupancy which is simply $(e^{h\nu/kT} - 1)^{-1}$ (Boyd 1982). The first term on the right side of (2.4) is known as 'shot noise' and is due to the uncorrelated arrival rate of photons. The second term known as 'excess noise', and is due to the correlated bunching of photons. This excess noise is important when $h\nu < kT$. Using (2.2) in (2.4), we find that

$$\Delta N_\nu \approx 3 \times 10^6 [\frac{\tau_\nu\, \eta_\nu}{R}(1 + 1.8\eta_\nu)]^{\frac{1}{2}} . \tag{2.5}$$

It is clear that in order to decrease the photon fluctuations which contributes to the noise of the system, we can either decrease the throughput, decrease the quantum efficiency, or increase the resolution. Decreasing the throughput will have the effect of also decreasing the signal strength. Since the signal strength is proportional to τ_ν and the noise is proportional to the square root of τ_ν, the signal-to-noise ratio would be proportional to $\tau_\nu^{1/2}$. Decreasing the throughput will therefore degrade the overall performance of the system. The same argument may be used for the quantum efficiency. It is only by increasing R that we can improve the system. This assumes that photon noise dominates all other sources of noise.

Other sources of noise include phonon-generated noise in the detector, background radiation from warm filters and other optical parts in the light path, and electronic noise from the rest of the circuit. Phonon noise can be minimized by having high-purity detector material and by also cooling the detector down to 2 K or less. With cold optics and filters, the background emission will be limited to that

caused by the atmosphere. With careful wiring and design, the electronic noise can also be minimized. In theory, one should be able to achieve background limited photon noise.

During actual observations, we have found that the background fluctuations are on the order of 5 or 10 times larger than those due to photon noise. These fluctuations are probably caused by a combination of changes in the air mass, changes in the sky temperature and emissivity, and turbulence inside or outside the telescope cavity. It is still the case that higher resolution will lower the background noise. For more discussions on background-limited detections in the FIR, see Boyd (1982); Gillett, Dereniak, and Joyce (1977); and Keyes and Quist (1970).

2.4 Dewars

Since it is advantageous to have the optics and the detectors at temperatures close to or below that of liquid helium (4 K), we place the spectrometer, filters, and detectors within a helium-cooled dewar. The dewar consists of a 3.5 liter stainless steel cryogen can which has a thick copper block, or work surface, at one end to which are affixed the detector housings and the spectrometer. The copper acts as a good conductor and provides for adequate cooling of the detectors through their brass housings. The thickness of the copper provides for mechanical as well as thermal stability.

Surrounding the cryogen can are about 16 layers of aluminized mylar (super-insulation). The insulation reflects most of the radiation coming from warmer parts of the dewar and helps to keep the helium from boiling at an unacceptable rate. The average hold time for 3.5 liters of liquid helium is roughly 22 hours.

Surrounding the cryogen can and the spectrometer is a cylindrical shell of stainless steel that is wrapped with another 30 layers of super-insulation. This is then all placed inside an outer can which is evacuated. The cylindrical shell provides a radiation shield from the room temperature radiation emitted by the outer can. Evacuating the dewar minimizes the heat path from the cryogen to the outside world.

Inside the dewar is placed activated charcoal wrapped in aluminum foil with

holes punctured in it. This serves as the *getter*, which absorbs the heavier molecules left in the vacuum jacket of the dewar and which are not cryogenically frozen out at liquid nitrogen temperatures (77 K). The outer can must be connected to the helium can in some fashion. At the spectrometer end, the connection is via a double-triangular fiberglass system to the outer can. The fiberglass offers low heat conductivity as well as provides for several points of stabilization. On the cryogen can end, the connection to the outside world is made via a thin-walled neck. This neck is made of 0.010 " stainless steel and welded onto the top of the can. In years past, it was attached with a silver-solder joint. However, these joints began to fail regularly several weeks before a flight series and we have since gone to using heli-arc welds. Most likely, with the silver-solder joints, not all of the flux was cleaned out of the joint and it slowly corroded. The weakened joints would then not be able to handle the thermal shock sustained upon cooldown. The welds are stronger and do not require the use of flux.

The cooldown process can take anywhere from 12 to 24 hours. Once the dewar is assembled, the vacuum jacket needs to be evacuated. Gases will adsorb onto the superinsulation, making it necessary to pump on the jacket for up to 10 hours. New cement or paint may also outgas for several hours as well. Once the pressure in the jacket is down to 30 millitorr or less, the cryogen can is filled with liquid nitrogen. The nitrogen will cryo-pump out most of the rest of the gas in the vacuum jacket. The nitrogen also provides a cheap and effective way to cool down the spectrometer and cryogen can as far as possible before using liquid helium. Helium prices are about thirty times higher than those for nitrogen. Once thermal equilibrium is reached in about 2 hours, we then pump on the nitrogen in the dewar. By lowering the ambient pressure over the liquid nitrogen to about 100 torr, we can cool the nitrogen down to roughly 55 K. At this point, the nitrogen is frozen solid. To effectively decrease the temperature of the spectrometer, it is necessary to have the dewar holding nitrogen for at least 6 hours.

After this time, the solid nitrogen can be partially melted by the addition of liquid nitrogen. This is then dumped and liquid helium is introduced into the cryogen can after one makes sure that all of the nitrogen is out of the can. Otherwise,

the nitrogen can form a sheet of ice between the helium and the work surface and lower the thermal conductivity enough to adversely affect the performance of the detector. It takes the fill and evaporation of about 15 to 20 liters of helium before thermal equilibrium is reached. Since Ge:Ga requires temperatures on the order of 2 K or less, we need to lower the pressure over the helium in order to lower the helium temperature, as was done with the nitrogen. The hold time of the cryogen can when we pump on the helium is 14 to 16 hours.

2.5 Filters

Stressed gallium-doped germanium detector material is sensitive to radiation of $\lambda < 200\,\mu$m. This includes photons in the mid- and near-infrared regimes, as well as in the visible part of the spectrum. The grating spectrometer is capable of passing a relatively narrow bandwidth ($\lambda/\Delta\lambda \approx 210$). However, if the grating is efficiently diffracting radiation of wavelength λ, then it will also efficiently diffract radiation of wavelength $\lambda/2, \lambda/3$, and so on. It is desirable to filter out the unwanted radiation that can be diffracted. This is done by using several different types of filters.

The first optical material that the incident radiation encounters is a window on the side of the dewar. The window material is composed of 0.25mm thick polyethylene, which is transparent to radiation from about 16 μm well into the millimetric regime. Polyethylene serves as a rugged window material that is non-permeable (except slightly to helium gas) and non-soluble in water, hence preserving the vacuum inside the dewar. The polyethylene window is at room temperature.

The next filter that the incident beam encounters is a diamond dust scattering filter which is placed in the aperture of the spectrometer. This filter is composed of a monolayer of diamond dust that is pressed into melted polyethylene. The diamond dust is 8–16 μm in size and is purchased from the Dunnington Comp., Chester Springs, PA. The resulting filter is 0.15 mm thick and 0.5″ in diameter. The dust scatters visible and near infrared radiation out of the beam, and works best when it is far away from the detector and in a slow (high focal ratio) beam. See Watson (1982) for more details on diamond dust scattering filters and their construction.

The radiation that goes on unimpeded by the diamond dust scattering filter will pass through a 1mm thick BaF_2 crystal. The BaF_2 has a very high reflectivity for wavelengths between 18 and 58 μm (Armstrong and Low 1973). This band corresponds to the ionic vibration band within the crystal. Alkali crystal filters that display this phenomenon are known as reststrahlen (residual rays) filters.

The index of refraction for the alkali crystals is $\sim$ 2.4. With such a high index, the reflection losses at the interfaces are $\sim$ 30%. In order to minimize these losses, the filters are coated with a thin layer of polyethylene ($n_i \approx 1.5$). This allows roughly 81% of the incident radiation to pass through. The BaF_2 filters transmit $\sim$ 90% of the radiation at 157 μm.

Another problem of these filters is the Fabry-Perot action that results if the faces are parallel. This is not a particularly welcome attribute to the system, since this action will allow only narrow bands through. This can be avoided by hand polishing the faces of the crystals. If the faces are wedged or non-planar, which is the usual result from hand polishing, then the Fabry-Perot action will be minimized.

The last filter through which the radiation passes before it goes to the detector is another reststrahlen filter of AgCl that is about 0.5 mm thick. The band stop for this filter is from 42–100 μm and it transmits ~80% at 157 μm. All of the filters are cooled down to liquid helium temperature in order to minimize the amount of background radiation introduced into the beam. It has also been observed by Hadni et al. (1965) that the cut-on and cut-off wavelengths for a reststrahlen filter are much sharper at 4 K than at room temperature. This effect is due to the change in phonon population for $kT \ll h\nu$.

Other reststrahlen filters and their stop bands are listed in Table 2.1. For the Fabry-Perot spectrometer, a film of polyethylene impregnated with carbon is used in place of the diamond dust scattering filter. This 'black poly' transmits $\approx$ 70% at 153 μm. The cut-on wavelength for the black poly depends on the density and size of the carbon particles. For the material that we have used, this cut-on is around 50 μm. An additional reststrahlen filter of CsBr is used in order to cut out radiation shortward of 140 μm. CsBr has a stop band between 87 and 125 μm at 4 K.

Table 2.1 Infrared Filter Properties at 4 K

Sample	Thickness (in mm)	T_{max}	Stopband(μm)
Sapphire	1	0.59	7–18, 20–23
Crystal quartz	0.86	0.78	20–27
LiF	2	0.65	13–34
CaF_2	1	0.68	13–38
SrF_2	1	0.71	20–45
BaF_2	1.5	0.65	18–58
KCl	2.4	0.8	37–72
NaBr	1.2	0.88	42–78
KBr	1	0.53	52–85
AgCl	1	0.60	42–100
KI	2.2	0.88	60–100
CsBr	1	0.68	87–125
CsI	1	0.65	115–155
TlCl	1.5	0.70	52–190
KRS-5	1.3	0.82	83–300

Properties of infrared filters at 4 K. Included is the thickness of the sample, the maximum transmission, and the stop band, that range of wavelengths for which the reflectivity is close to unity. Data from Armstrong and Low (1973).

Fixed Fabry-Perot etalons can be used as filtering devices. In the FIR, it is possible to also use metal meshes. These meshes will transmit or reflect radiation with a wavelength on the order of and longer than the spacing on the mesh, depending on whether the grid pattern is inductive or capacitive. For more information on filters, their construction and properties, see, for example, Stacey (1985), Watson (1982), Armstrong and Low (1973), and Kimmitt (1970).

2.6 Electronics

The charged carriers that are excited by the absorbed photons in the detector will add to the bias current that is already flowing through the detector. This change in current is measured by using a transimpedance amplifier (TIA). Figure 2.3 shows a schematic of the circuit. The circuit is composed of a source follower which feeds into an operational amplifier (op amp). The feedback loop goes to a load resistor which is connected to the detector. The source follower is a 2N6484 junction field-effect transistor (JFET). One gate is connected to ground. The source belonging to that gate is then connected to the positive feedback pin of an LM308 op amp. The other source is connected to the negative feedback pin. The op amp will act to keep the voltage at the negative feedback pin the same as the voltage at the positive feedback pin. It does this by controlling the voltage output, V_{out}. Since the JFET is matched, the other gate that is connected to the detector and load resistor is at a virtual ground. What this means is that the current flowing through the load resistor is equal in magnitude but opposite in direction to the current flowing through the detector. This can be written as

$$\frac{V_{\text{bias}}}{R_{\text{d}}} = \frac{V_{\text{out}}}{R_{\text{load}}} \,. \tag{2.6}$$

We see that if V_{bias} is 0, then V_{out} should also be 0. However, the two channels on the JFET may not be perfectly matched and phonon and Johnson noise will create a dark current flowing through the detector. In order to accomodate for this, a variable resistance to ground is placed between the two feedback pins of the op amp. By adjusting the variable resistor, we may zero out the dark current.

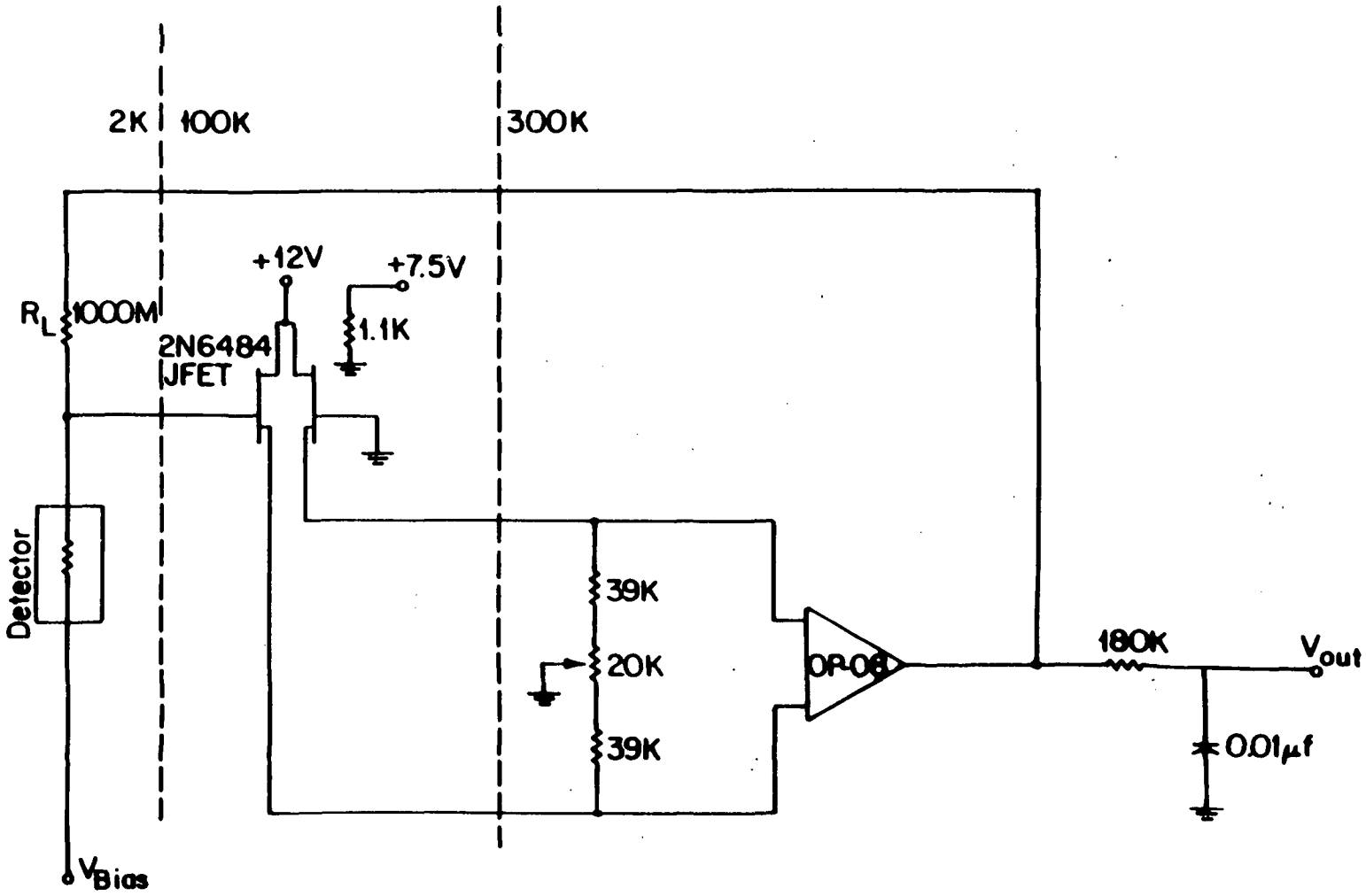

FIGURE 2.3 Schematic of transimpedance amplifier circuit used for FIR detectors.

When FIR radiation is absorbed by the detector, an additional current due to the photo-excited charged carriers drifting in the bias potential is produced. In order to maintain the virtual ground, an equal but opposite change in current must be induced in the load resistor. This is done by varying V_{out}. This change in V_{out} can then be measured. Since the amount of radiation falling onto the detector varies periodically with the chopper, the measured change in V_{out} is accomplished with a de-modulation circuit. We use an Ithaco lock-in analyzer in order to find the amplitude of the sinusoidal change in V_{out}.

Sources of electronic noise in the system include the detector, the load resistor, the source follower, and the rest of the electronic circuit. Before 1983, G118AL MOSFETs were used as source followers. The MOSFETs worked well at liquid helium temperatures and so could be placed as close as possible to the detector and load resistor. This is important since the resistances of both are on the order of 10^9 to $10^{10}\,\Omega$. With impedances this high, shunt capacitive effects become important and pickup and microphonics will become a problem if wires are too long. Hence, the G118AL transistors were used since they could be placed on the work surface next to the detector. Unfortunately, the electronic noise from the MOSFETs dominated the other sources of noise. JFETs, on the other hand, are electrically much quieter. The only problem with silicon JFETs is that they do not operate below temperatures of roughly 60 K. Since we need the FET to be close to the detector/load resistor, it must be somehow isolated from the work surface and heated. The optimum operating temperature is between 100 and 150 K (Lengeler 1974), where the transductance is a maximum.

The method used to isolate and heat the JFET is a relatively straightforward and simple one inspired by George Gull. In the spectrometer, there are two detectors and hence, the need for two source followers. A FET is mounted with rubber cement at the end of an 'L' section made of thin-walled 1/4″ fiberglass rods. The fiberglass is mounted to the work surface as close to the detectors as possible while keeping the FET outside of the spectrometer. This is necessary due to the requirement that the FETs be heated and the copious infrared radiation produced by these relatively warm objects could dominate the background radiation field and hence the system

noise. The heating is accomplished by using a 1.1 kΩ Allen-Bradley carbon resistor. A copper wire is wound around the body of the resistor and then soldered to the two drains on the FET. The wire and resistor are enshrouded in a blanket of rubber cement to insure good thermal contact. A current of 4 to 5 milliamperes is sufficient to keep the FETs at operating temperature.

The fiberglass posts are notched in order to keep the heat conductivity low between the work surface and the JFET. The wires from the JFETs are wound tightly around the fiberglass posts and tacked down with rubber cement in order to minimize the microphonics and to provide a long thermal path between the JFETs and the cold work surface.

The rest of the circuitry which is outside the dewar contributes negligible amounts of noise to the system. I have incorporated an electronic voltage source for the bias voltage. Before 1983, the bias voltage was supplied by batteries which were capable of delivering a very stable and electrically quiet potential. The electronic bias voltage source made from off-the-shelf components has been found to also be quite stable. It is buffered by an RC circuit with a time constant of 10 seconds. This insures against high frequency oscillations that may be induced by vibrations in the aircraft structure during operation. The measured noise of the bias source is about 15×10^{-9} V $\mathrm{Hz}^{-1/2}$ at a frequency of 35 Hz. This is comparable to that measured for the batteries. The 60 Hz pickup is minimal in the circuit. One significant advantage of the electronic bias source is that it is maintenance free. One need not worry about forgetting to check the batteries. The noise contributed by the rest of the circuit is on the same order as that of the bias source.

The load resistor will contribute to the measured noise of the system. The noise due to the resistor is known as Johnson noise, and its source is the random thermal motions of the electrons in the conducting material (Nyquist 1928). It is given by the formula

$$v = (4kTR\Delta f)^{\frac{1}{2}} \text{ volt } \mathrm{Hz}^{-\frac{1}{2}} , \tag{2.7}$$

where k is Boltzmann's constant, T is the absolute temperature, R is the resistance, and Δf is the electrical bandwidth. For a load resistor with $R = 3 \times 10^9\,\Omega$ at $T = 2\,\mathrm{K}$, the Johnson noise will be roughly $6\times10^{-7}\,\mathrm{volt\,Hz}^{-1/2}$. This is a factor of

40 times the noise from the TIA circuitry.

The detector will contribute several types of electrical noise. The resistance of the detectors at 2 K is on the order of 1000 MΩ. Johnson noise from the detector will therefore be on the order of 6×10^{-7} volt $Hz^{-1/2}$. Ohmic contact noise due to the interface between the semiconductor material and the gold contacts on the faces of the crystal can be significant. Advances in the manufacturing of the detectors has led to significant reduction in the contact noise. Impurities in the detector material will also contribute to the noise. Impurities within the material we have used are less than 10^{-13} cm^{-3}. Haller has achieved impurity densities one to two orders of magnitude less than this in recent years (Stacey 1986, private communication). At a bias potential of zero volts, we have been able to measure Johnson noise.

The wires that carry small currents to high resistance components are susceptible to microphonic pickup. This is a shunt capacitance problem for which the most simple solution is to tie or glue down the wires to the work surface so that they are not going to move. We use a combination of Kimwipe tissue and rubber cement to glue the wires down in an orderly fashion on the work surface. The wires that connect the work surface to the outside world are run alongside the cryogen can and then wrapped around the neck on tissue before being soldered to the connector pins. These wires are also glued down to the surfaces they touch. Microphonics has not been much of a problem. Most microphonics are high frequency, which are filtered out with a low-pass filter that has a 3dB point at 88 Hz. Coaxial cables are used to shield the wires that run from the dewar to the pre-amp box. This distance should be as short as possible to avoid any unnecessary pickup.

It was mentioned earlier that cosmic rays can be absorbed by the detectors. The absorption of that much energy will momentarily saturate the detector and cause a spike in the output voltage. This spike will have a very small rise time due to the nature of the event. Houck and Briotta (1982) designed a circuit that would look for a large differential rise in voltage and activate a sample-and-hold circuit for a period of time that one may adjust. This circuit has been built and employed in our pre-amp box. We have used an LF198 sample-hold device in place of the LM-2 found in the original design due to its superior characteristics. We have chosen a

gain of 75 for the output voltage. The in-flight noise has been reduced about 10% due to the use of this circuit.

2.7 The Spectrometer

2.7.1 Grating Theory

For spectroscopic work in the far-infrared, we have used a combination of a grating spectrometer and a lamellar-grating interferometer. The spectrometer has a bandpass of roughly 0.7 μm, yielding an instrumental resolution of ≈ 210.

Monochromators use gratings in order to disperse the incoming radiation by diffraction. If one considers a planar reflection grating, one essentially has a multi-mirrored surface. For FIR work, the separation of the rulings on the grating is usually on the order of the size of a wavelength, so each ruling acts as the source of one ray of light. Consider collimated radiation incident upon the grating. If we follow the light to each individual facet, and then follow it as it is diffracted, then we see that there will be a phase shift between adjacent rulings. In order for the diffracted light to still be in phase when it is collected, this phase shift must be an integral number of wavelengths. This constraint leads to the grating equation:

$$m\lambda = g[\sin\alpha + \sin\beta] \; . \tag{2.8}$$

Here, m is the diffraction order, λ is the wavelength of interest, g is the spacing between rulings, and α and β are the incident and diffraction angle relative to the grating normal, respectively. One sees that in 0^{th} order, the angle of diffraction is just the reflection angle ($\alpha = -\beta$). This is true regardless of wavelength. Hence, in 0^{th} order, all of the incident light will be diffracted in this direction. That is to say, there is no spectral dispersion in 0^{th} order. The amount of radiation that is allowed to go into the higher orders is small, making the grating most efficient where it does not disperse.

It is possible, however, to increase the efficiency of one of the orders by simply blazing the grating. A blazed grating, instead of consisting of alternate reflecting and non-reflecting lines, is composed of a series of steps. The angle of the

step relative to the plane of the grating is the blaze angle. A blazed grating will still diffract radiation in the same manner as an ordinary grating, but for certain wavelengths, most of the power will be directed to an order other than 0. This means that the grating will be highly efficient in a non-zero order where the desired dispersion is obtained.

The grating is only efficient in passing the radiation with electric field vectors perpendicular (s-plane) to the grating grooves (Loewen 1977). This causes a 50% loss of signal that can be measured by the detector. The grating efficiency for the s-polarization depends on the blaze angle. Calculations and experiment have shown that the efficiency is ~95% for $0.9 < \lambda/g < 1.8$ if the blaze angle is above 22° (Loewen 1977). For smaller blaze angles, the efficiency is not constant in this range, but peaks for $\lambda/g \sim 0.6$ and then decreases for longer wavelengths. Our grating has been blazed at 26° 45′ for 150 μm radiation. The grating was ruled and blazed by Bausch & Lomb Co., Rochester NY.

2.7.2 Spectrometer Design

The spectrometer is based on a Littrow-mode design that was developed by J. R. Houck and Dennis Ward (Houck and Ward 1979). A schematic is shown in figure 2.4. The original spectrometer operated at f/6.5, matching the Lear Jet telescope beam. Melnick (1981) improved the original design and converted it to f/17 optics. An f/17 beam of light enters the collimator from the telescope. The beam passes through the entrance aperture at A and encounters optical and near infrared filters at B. The FIR radiation continues onward, hitting a 45° mirror at C, and then impinges upon the secondary mirror at D. From here, the convex secondary will diverge the beam to a size about 3 inches in diameter at the primary mirror, E. This is important since the spectral resolution will depend on the number of rulings illuminated, and therefore on the beam size when it hits the grating.

At the primary, the beam is collimated and sent onto the grating to be dispersed. In Littrow mode, the angle of incidence and the angle of diffraction are the same (or nearly so). The diffracted light will then retrace the incident light's path. When the light reaches the secondary for the last part of its trip through the

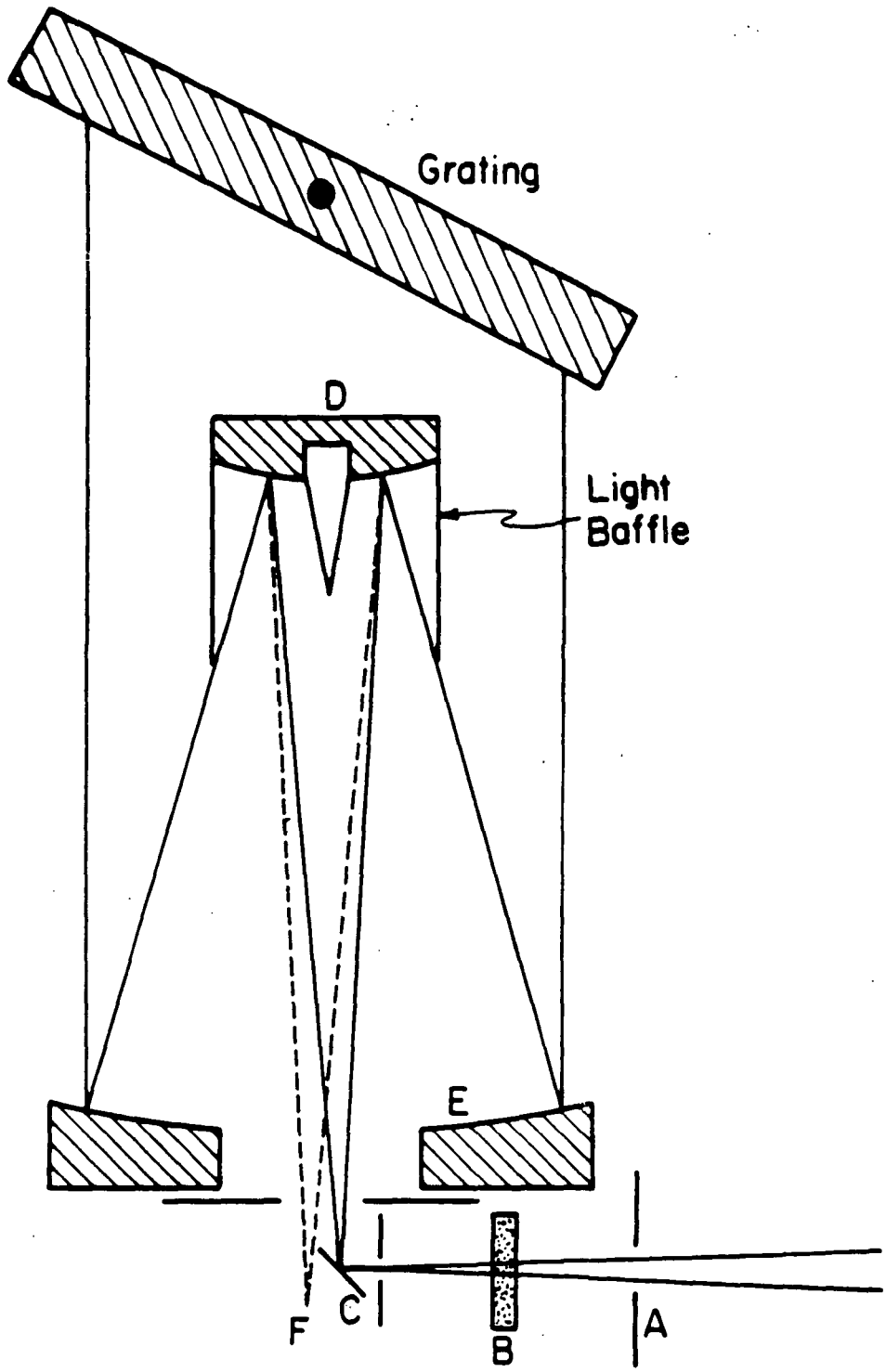

FIGURE 2.4 Schematic drawing of the FIR spectrometer used on the KAO.

system, it will fall upon two small diagonal mirrors at F which send the dispersed radiation into two detector integrating cavities. The detectors are separated by about 4 mm, which corresponds to a spectral separation of $\sim 0.8\mu$m.

The grating is controlled by a gear system that is connected to a stepping motor via a fiberglass rod. The rod is made of fiberglass in order to insure a minimum heat load on the cryogenically cooled spectrometer and work surface. The amount of torsional backlash that the rod experiences is equivalent to almost a tenth of a revolution. We compensate for this when the grating is being driven to a certain position. The vacuum inside the dewar is maintained by placing an o-ring around the fiberglass shaft where it exits the outer can of the dewar.

The spectrometer is constructed entirely of stress-relieved aluminum. This allows for uniform contraction while cooling to liquid helium temperatures. The spectrometer is bolted to the work surface, which is the copper bottom of the cryogen can. A thin film of N grease (Apiezon Products Ltd., London) is sandwiched between the work surface and the spectrometer flanges in order to provide better thermal contact.

2.7.3 Optics and Limitations

The primary and secondary glass mirrors that were used in the f/17 system were replaced in the fall of 1983 with aluminum mirrors in order to acquire better stability and ease of operation of the system. Since the spectrometer is bolted to the work surface and cooled down, the whole instrument undergoes thermal contraction. If the mirrors are made of glass, then the difference between the thermal contraction of glass and aluminum will shift the focus of the instrument several centimeters. Because the entrance windows to the detectors' light cones are 4×4 mm, or the size of the diffraction lobe, it is important that the focus be at these apertures. This is difficult to assure if the focus shifts during cooldown procedures.

If the whole system is constructed of the same material, then the spectrometer will undergo uniform thermal contraction during cooldown and the focus of the optical system will remain unchanged. That way, one may align the instrument at room temperature and accurately place the focus where it should be.

The convex secondary mirror is 3.43 cm in diameter with a radius of curvature of 5.258 cm. The concave primary mirror is 8.33 cm in diameter with a radius of curvature of 27.06 cm. These figures were arrived at after careful consideration of baffling and light loss due to the Cassegrain system. Because of the Cassegrain design, the central portion of the beam is blocked so that undispersed light from the secondary will not fall onto the detectors. For this system, the amount of light loss we have due to blockage of the central portion of the beam is 33%. About 90% of the stray radiation which comes into the optical path should be blocked. We have normally measured stray radiation through the system to be approximately 3% of the maximum signal.

The aluminum mirrors are overcoated with a thin layer of SiO to protect them from oxidation. The interior walls of the spectrometer are painted with Nextel-Black Velvet paint manufactured by 3M. The FIR absorption of this paint is about 80% (Melnick 1981). Care is taken to cover up any openings with silvered tape so that stray light may be kept at a minimum.

Operation of the spectrometer in Littrow mode has the advantage of a compact design which can easily fit into a 6 inch diameter housing and also accomodate two detectors. If the spectrometer were operated in an off-axis mode whereby the dispersed light did not retrace the path of the incident beam, then it would not be necessary to cut out the central 33% of the beam. An off-axis system, however, does not easily accomodate multiple stressed detectors *and* fit into a small package.

2.8 Spectrometer Operation

2.8.1 Calibration

Once the dewar is assembled and cooled down, the system must be calibrated. The dewar is placed upon a stand that is known as the Mock Lear. The test stand can deliver a range of beams, from f/6.5 (simulating the Lear Jet telescope) to f/17 (for the KAO optical system) and slower.

In order to detect FIR radiation, we need to chop. This is accomplished in the lab by using an aluminum chopping wheel which allows us to look alternately at

reflected 300 K radiation and then at glass spheres that are cooled to liquid nitrogen temperature (77 K). The glass is opaque at FIR wavelengths and therefore acts as a blackbody source. The amount of radiation falling into the dewar from a blackbody of temperature T is given by

$$F_\lambda = \frac{2h\,c^2}{\lambda^4}\,\frac{1}{e^{hc/\lambda kT}}\,\Omega\,A\,R^{-1}\,, \qquad (2.9)$$

where A is the aperture area, Ω is the solid angle of the beam as seen by the aperture, and R is the instrumental resolution. For the Mock Lear setup, we have

$$F_\lambda = 5.2\times10^{-8}\left(\frac{1}{e^{0.48/\lambda_{100}}-1}-\frac{1}{e^{1.87/\lambda_{100}}-1}\right)\frac{1}{R\,\lambda_{100}^4}\ \text{Watt}\,, \qquad (2.10),$$

where λ_{100} is the wavelength in units of 100 μm. At 153 μm, the flux reaching the dewar is $2.3\times10^{-8}\,R^{-1}$ W. The dewar assembly sits 17 inches from the chopper, in a cradle in which it may be twisted and tilted to align it with the beam. Once the dewar has been peaked up in this fashion, the electronics may be tested.

If the bias voltage across the detector is zero, then there is no electric field to move the excited charge carriers. As the bias voltage is slowly increased, the charges will begin to move further, but will still move slow enough for most of them to recombine. As the voltage is increased still further, the response of the detector will level off and stay constant until near the breakdown bias voltage. We find that the point of leveling off for our detectors is at a bias voltage near 160 mV.

The gain of the system, G, is defined as the differential change in V_{out} with respect to V_{bias}. From (2.6), we see that this is simply the ratio of the resistivity of the load resistor to that of the detector. We find that as the bias voltage increases, this ratio also increases, which suggests that either there is ohmic heating of the detector or that the resistance of the detector is decreasing due to the better mobility of the charged carriers (and impurities) at higher voltages. Knowing the specific heat of Ge, the temperature change due to ohmic heating is expected to be less than 10^{-4} K. It is therefore most likely that the increased gain is due to the increased conductivity of the detector material.

It should be remembered that the measured signal is proportional to the response of the detector and to the gain. Since the gain increases while the response is constant for increasing bias, the signal will also increase with increasing bias. The most important measure is the signal-to-noise ratio, S/N. For bias voltages below a certain value, the signal increases faster than the noise. Above this value, the S/N decreases. We have found that for the Ge:Ga detectors, the optimum bias value is around 0.22–0.24 volts. Noises are typically on the order of 5μV for a 1 Hz bandwidth.

Now that everything has been optimized, the grating is rotated via a stepper motor. Use of a gear on a 10-turn potentiometer in the external drive train provides us with a solid reference point from which the grating may be accurately and repeatedly driven to any desired position. Figure 2.5 shows a typical calibration spectrum. The absorption features are mainly due to water vapor in the optical path. The central wavelength of these features are well known, and hence knowing the position of the stepping motor gives us a calibration of the grating in wavelength vs. step position. It should be noted that the absorption feature at 152 μm is due to the AgCl filter that is used, and not to any telluric features (Stacey 1985). Close, but distinguishable features in the spectrum assure us that the instrumental resolution of the spectrometer is around 210.

Many of the water vapor features are pressure broadened and saturated. Because of this, it is sometimes difficult to exactly determine the position of the center of the absorption line due to asymmetries in the wings and probable overlapping of lines. It is therefore desirable to have an evacuated chamber in which to calibrate the system. To this end, Charles Fuller designed and built an evacuated box which provides us with a chopped source, the choice of f/6.5 or f/17 optics, and several apertures at the source. The source is also movable in x and y coordinates, which allows us to do an aperture map of the spectrometer. The movement of the source is controlled by stepper motors and can be done under the direction of the IMSAI in one tenth the time that it used to take to do manually. The chamber can be evacuated to ~500 mTorr, which corresponds to roughly 1/1500 atmosphere. Figure 2.6 shows the spectrum obtained using this chamber. For comparison, Figure 2.7 is a

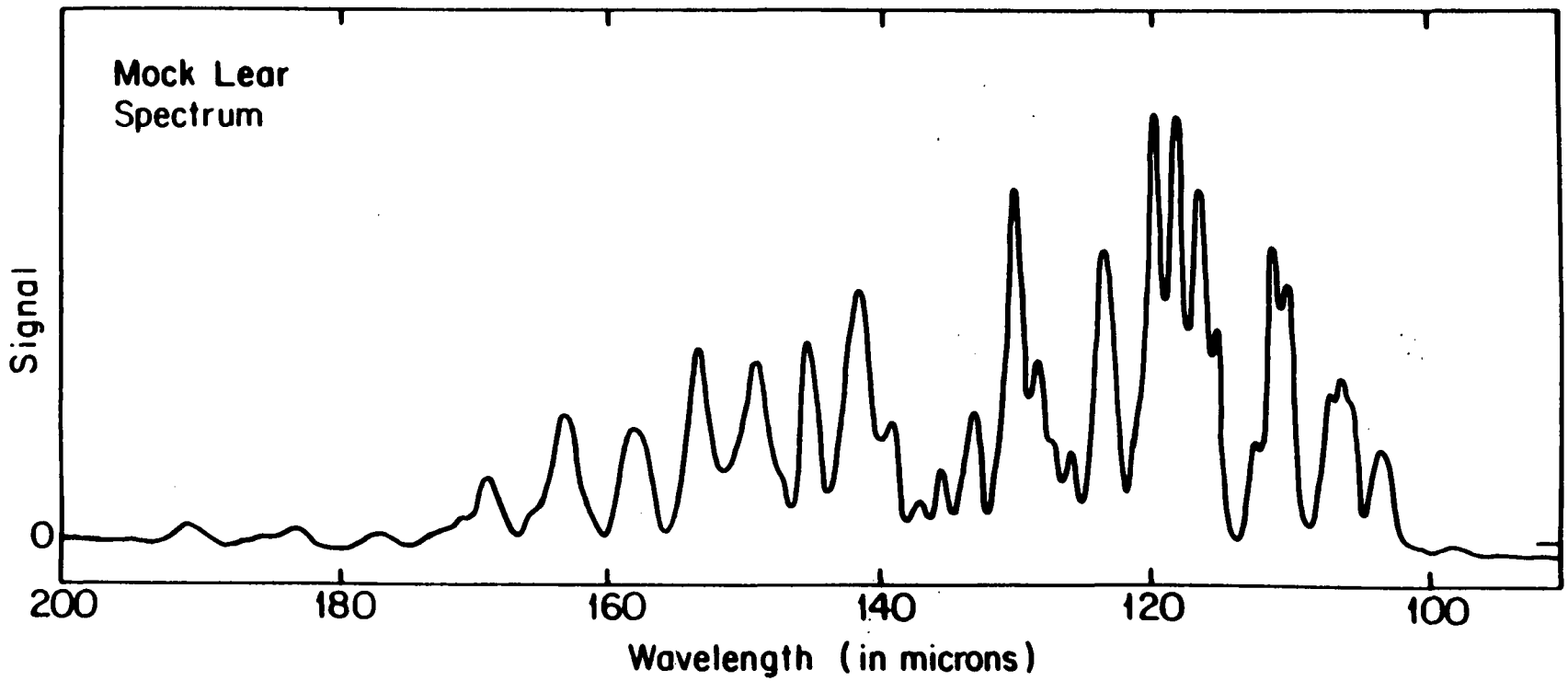

FIGURE 2.5 Laboratory calibration spectrum on the Mock Lear using the FIR spectrometer. The radiation passes through roughly 20 inches of air at atmospheric pressure and room temperature.

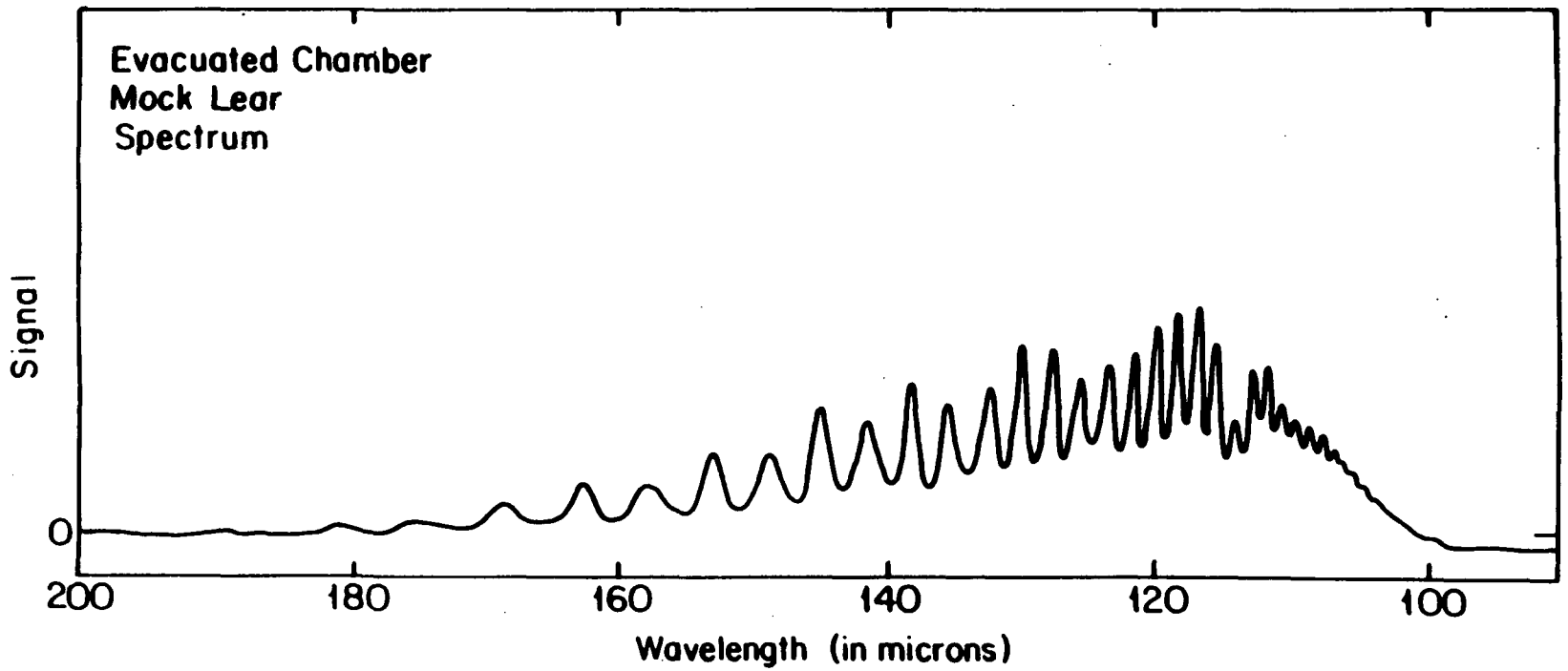

FIGURE 2.6 Same as Figure 2.5, except the air pressure in the optical path is roughly 10^{-3} atmosphere.

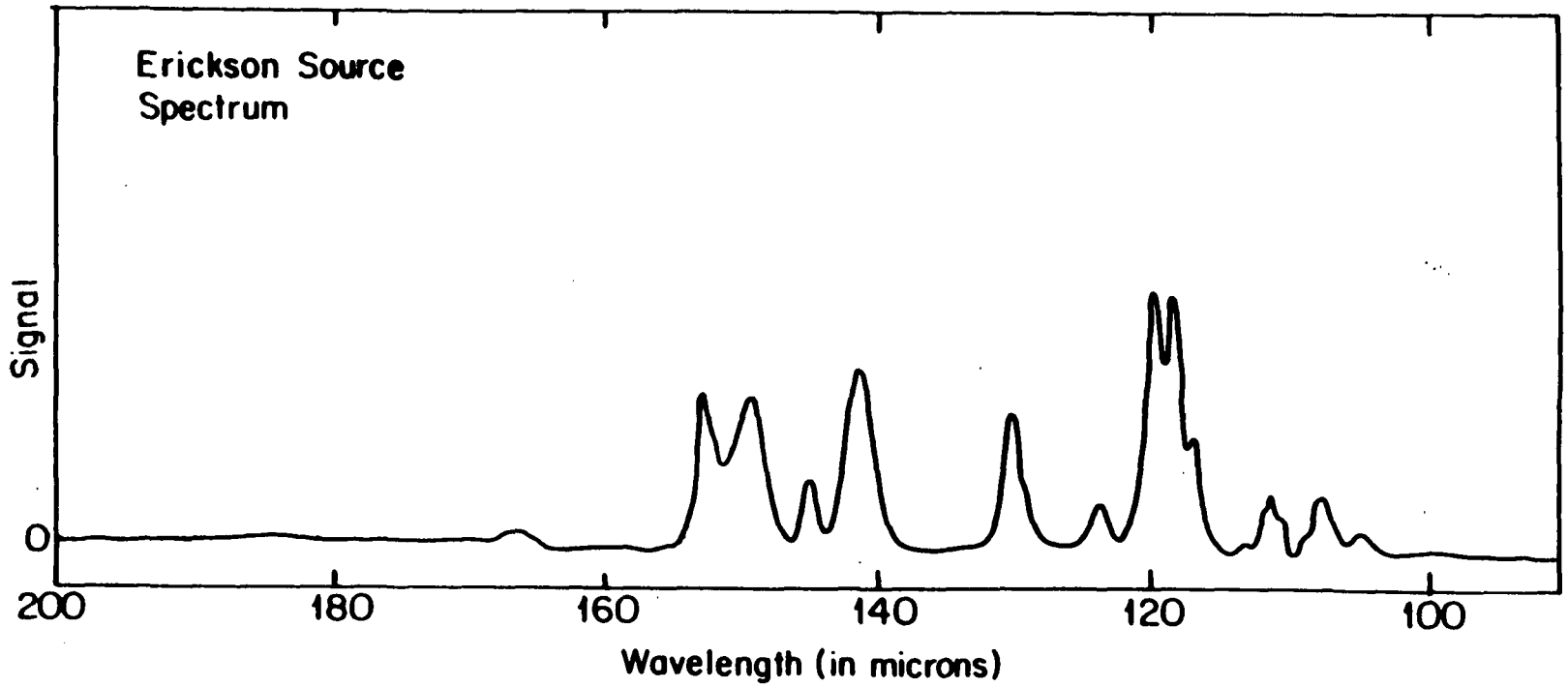

FIGURE 2.7 Same as Figure 2.5, except the optical path through air is increased from 20 inches to about 3.5 meters.

spectrum that was taken using a collimated source constructed by Dr. E. Erickson of NASA/Ames Research Center and mounted on the KAO secondary. The path traveled by the radiation through air is about 3 or 4 meters. One sees how fast the increasing water vapor content suppresses the FIR transmission.

It is necessary to calibrate the spectrometer after every cooldown for several reasons. Mechanical couplings are not placed in the same position, and it is therefore necessary to account for this. The first diagonal mirror in the spectrometer which the radiation encounters has also proved to be of a temperamental lot, shifting from cooldown to cooldown. If it does move, then the path of the radiation will change in the spectrometer and, hence, the angles of incidence and diffraction. It is therefore possible that, at a certain grating position, the measured wavelength can vary by almost a micron for different cooldowns. For these reasons, it is extremely important to calibrate. We have never noticed any shift of the calibration while the dewar was cold for extended periods of time, and so the spectrometer is highly stable while kept cold. The signal levels that we measure on different cooldowns may vary, but usually by not more than 10%. Diurnal and seasonal changes in humidity may contribute to these variations.

2.8.2 Spectrometer NEP

A measure of how well the system is performing overall is the noise equivalent power, or NEP. The NEP is defined as the amount of radiation which must be incident upon the system in order to provide a S/N ratio of 1 in one second for a bandwidth of 1 Hz. The NEP can be calculated quite simply by noting the amount of radiation incident upon the system at a particular wavelength and for a particular beam, and the S/N ratio that is measured at that wavelength. If λ is 153 μm and the resolution is 210, then we have 1.1×10^{-10} W falling onto an f/17 system. With a S/N ratio of 2300 for a 1 Hz bandwidth, this corresponds to an NEP of 5×10^{14} W Hz$^{-1/2}$.

2.9 The Interferometer

2.9.1 Goals and Inspirations

Moderate resolution spectroscopy possible with the grating spectrometer has made significant contributions to our understanding of the Galaxy and star formation regions within. There are, however, some disadvantages to moderate resolution ($R \sim 200 - 500$) instruments. For the moment, consider detecting an emission line at 140 μm. Let us look at the Orion Nebula in the direction of the BN-KL region. Furthermore, let the resolution of the instrument be 210, the line width be 30 km s^{-1}, and the line flux be 1.0×10^{-17} W cm^{-2}.

The continuum radiation from the dust grains in the nebula acts as a 70 K grey body with an emissivity of $20/\lambda$, λ being in microns (Werner et al. 1976). With an instrumental resolution of 210, the flux from the continuum is 5.3×10^{-16} W cm^{-2}. In order to see the line, we need to be able to measure the signal levels to within one part in 250 for a S/N ratio of 5 in the line. This is not always easy to do, especially when one has shifting amounts of water vapor in the boresight.

If we could suppress the continuum, the line strength won't change, but the line to continuum ratio (LCR) will improve. At a resolution of 1000, the LCR is now 0.1. At a resolution of 4000, this value goes up to about 0.4. The line width, being one part in 10^4, will still be situated well within the instrument profile and, therefore, will not be suppressed. With a LCR of 0.4, we need to measure a 40% change in the continuum level, as opposed to looking for a 2% change for a resolution of 200. Clearly, the chance of seeing the line is much better at higher resolution.

In low continuum sources, the line-to-continuum ratio is not much of a problem. However, another problem that exists for all sources is the fact that several lines may be close together. In particular, if we consider the CO $J = 16 \rightarrow 15$ rotational transition, and the OH $^2\Pi_{1/2}$ $J = 3/2^+ \rightarrow 1/2^-$ and $J = 3/2^- \rightarrow 1/2^+$ transitions, then we find that these lines occur at 162.812, 163.124, and 163.397 μm, respectively (Brown et al. 1982; Todd et al. 1976). Moderate resolution instruments cannot resolve these lines, and so if they are detected, confusion precludes one from determining which molecular line has been seen, as well as the flux levels of each

line. Only when the instrumental resolution is greater than 1200 can we resolve these lines.

Another reason why high-resolution instruments are desirable is that if the line profile can be resolved, then much information can be obtained concerning the kinematics of the gas. Profile information can, for example, provide data on turbulent line widths or thermal line widths of sources, and can even allow us to distinguish several sources that may be in the line of sight.

2.9.2 Design

It was with these considerations in mind that the FIR interferometer was designed and built by the Harwit group at Cornell (Harwit et al. 1981). In figure 2.8, a schematic of the interferometer is presented. Light from the telescope enters an aperture in the interferometer wall. The converging beam will hit a dichroic-coated glass which reflects the infrared and transmits the optical radiation. The optical radiation then goes to an offset guider which enables us to guide on a star as far away as $15'$ from the source. The guider was designed and constructed by J. R. Houck and his group at Cornell, and is kindly lent to us for our flights.

From the dichroic, the FIR radiation beam converges to a focus at the 4 mm size aperture at mirror A. The beam then diverges upon reflection and heads toward mirror B. A and B are flat front-silvered mirrors. The radiation then goes to mirror C, where it is collimated into a parallel beam which is reflected up to D. By this time, the image is about an inch in size. The radiation is then directed toward mirrors E and F, where it is split between the two. Mirror F can move relative to mirror E. After this, the beam is recombined, being reflected back to mirror D and then to mirror G, which takes the collimated beam and converts it back to an f/17 system while sending the light to the spectrometer. The system acts as a lamellar grating instrument, with mirrors E and F serving as the lamellae.

Stacey (1985) describes the original interferometer. There were some design changes that were implemented in 1984 January. Mirrors E and F were replaced with corner reflectors. Originally, E and F were side by side, and the beam directed

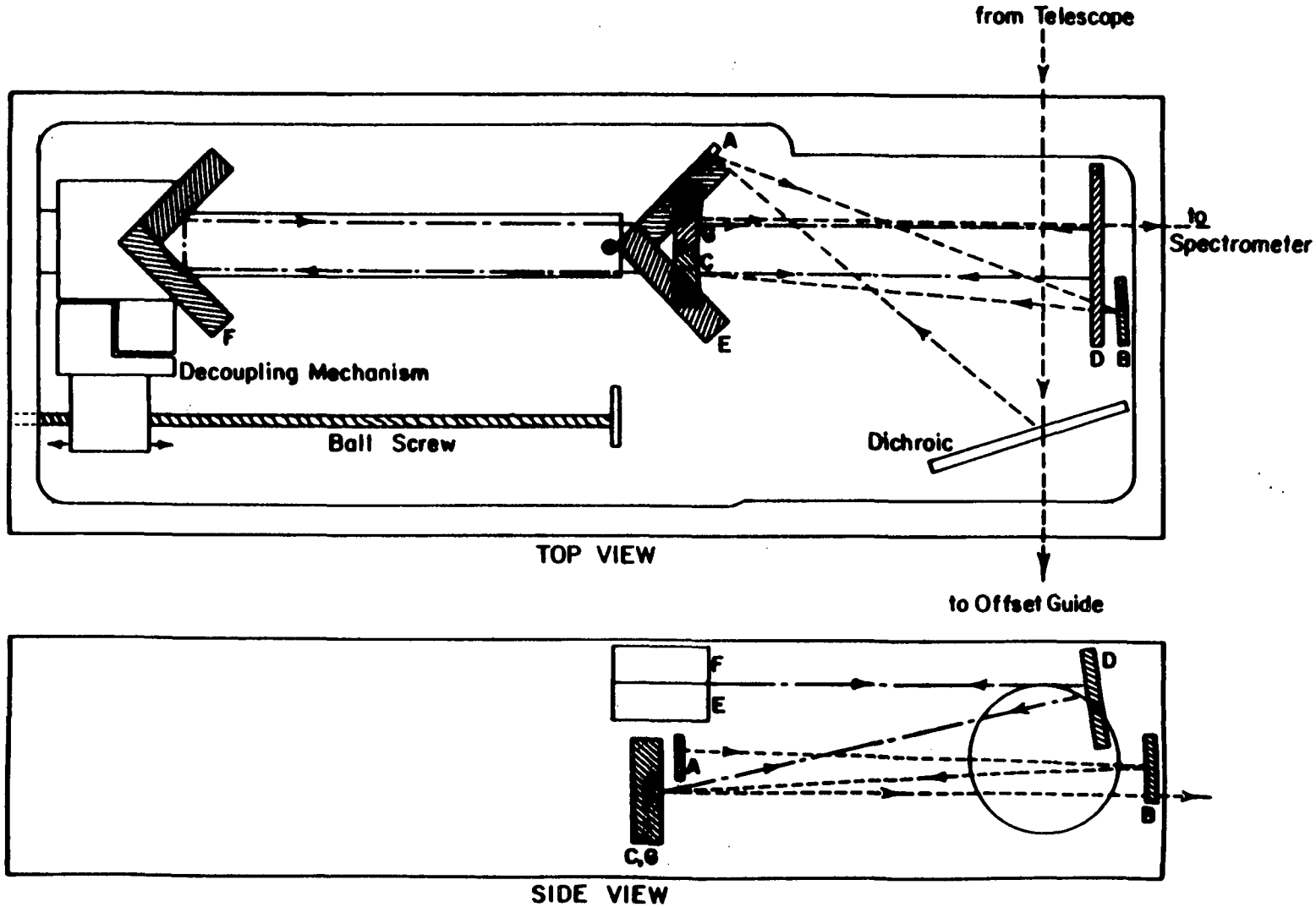

FIGURE 2.8 Schematic drawing of the FIR lamellar-grating interferometer. Mirror F is movable, and is capable of travelling up to 16 cm, yielding an optical path difference of 32 cm.

onto these mirrors was incident at an angle. This caused walkoff problems and limited the travel of the movable mirror to 2 inches. With the addition of the corner reflectors, this problem is now eliminated. The reflectors are optically polished solid aluminum, overcoated with SiO to prevent tarnishing.

Another improvement that was made to the interferometer was the increase in the length of travel for corner mirror F. As we will see, the resolution of the instrument depends on the optical phase delay between the two mirrors. The greater the phase delay, the higher the instrumental resolution will be. Originally, the distance travelled was 5 cm, but with the addition of a longer drive, that distance is now 16 cm. The drive stage consists of a stepper motor which turns a ball screw. The ball screw is coupled to the mirror mount through a mechanism which decouples any motions due to the ball screw that are not in a forward or backward direction. This insures that no wobbles due to a warped ball screw are translated to the movable mirror. The mirror mount, in turn, moves on a straight bar of stainless steel. Most of the design work was done by Noel Kurtz.

The stepper motor is geared to the ball screw so that one step of the motor corresponds to a 1.6 μm movement of mirror F. The ball screw is guaranteed accurate to 1 part in 10000 along the length of travel, and we have found this to be so. The actual step size seems to be more like 1.6001 μm from measurements of several CO rotational lines in M42, well within the tolerances and uncertainties of the measurements. No detectable wobbling of the image from the movable mirror is observed throughout the entire length of travel.

In order for this system to work, half of the beam must be imaged onto mirror E and the other half on mirror F. If the gap between the two mirrors is wide, then one will begin to lose signal and interference. We have found that most of the interference is due to the central part of the beam and it is therefore necessary that the mirrors be placed as close together as possible without touching. We have managed to place the mirrors $\sim 0.004''$ apart, or the thickness of a piece of paper.

The interferometer is constructed out of aluminum, while the ball screw is stainless steel. The stepper motor is a source of heat, and it can raise the temperature of the ball screw by 5 or 10 degrees Celsius. Since the ball screw is supported

by ball bearings at both ends, it is not in good thermal contact with the rest of the interferometer, only with the stepper motor through the gear train. The large thermal mass and effective cooling area of the interferometer prevents it from heating up very much, but the ball screw has little thermal inertia and poor thermal contact with the rest of the instrument. Hence, the ball screw will heat and expand. In so doing, it effectively has a temperature only about 5 degrees Celcius higher than the interferometer. The ball screw is not allowed to physically move back and forth for obvious reasons and is thus prevented from doing so at the stepper motor end. Hence, when the screw expands, it results in moving corner reflector F toward the dewar by about 16 μm. Thermal equilibrium is achieved after the stepper motor has been on for an hour or so. Until then, however, the position of the movable mirror is changing. The resultant change in the step size due to the expansion of the screw is only 1 part in 10000.

2.9.3 Theory

The radiation from the telescope first encounters the interferometer and then is passed to the grating spectrometer before ultimately hitting the detector. Let us, for the moment, assume that $S(\lambda)$ is the spectral profile of the radiation coming from the telescope. The grating spectrometer instrument profile is given by $\Psi(\lambda)$.

For radiation of wavenumber ν, incident on the corner reflectors, we have half of the beam falling on one reflector and half on the other. For an optical path difference between the corner reflectors, x, the value of the electric field vector upon recombination of the two beams is

$$E(x) = \frac{E_0}{2} + \frac{E_0}{2} e^{-i2\pi\nu x} , \tag{2.11}$$

where E_0 is the amplitude of the electric field for the entire beam. The intensity of the radiation is simply EE^*, or

$$I(x) = \frac{I_0}{2}[1 + \cos(2\pi\nu x)] , \tag{2.12}$$

where I_0 is E_0^2. What the detector will see is this intensity convolved with the in-

strument profile and the spectral profile. If $\phi(x)$ is the intensity hitting the detector, then it follows that

$$\phi(x) = \frac{I_0}{2} \int_0^\infty d\nu\, \Psi(\nu)\, S(\nu)\, [1 + \cos(2\pi\nu x)] \ . \tag{2.13}$$

The first term on the right hand side is a constant d.c. value we call $A_0/2$. A_0 is the average of $\phi(x)$ over all x. The second term is the one which contains all of the information about the incident radiation. Since the argument in the integral is symmetric, the integral may be rewritten as

$$\phi(x) = \frac{A_0}{2} + \frac{I_0}{4} \int_{-\infty}^\infty d\nu\, \Psi(\nu)\, S(\nu)\, e^{-i2\pi\nu x} \ . \tag{2.14}$$

If we let $\Phi(x) = \phi(x) - A_0/2$ and $\Gamma(\nu) = I_0\, S(\nu)\, \Psi(\nu)$, then (2.14) may be rewritten as

$$\Phi(x) = \frac{1}{4} \int_{-\infty}^\infty d\nu\, \Gamma(\nu)\, e^{-i2\pi\nu x} \ . \tag{2.15}$$

We recognize the integral to be the Fourier integral of $\Gamma(\nu)$, or in other words, the signal at the detector is 1/4 the Fourier integral of $\Gamma(\nu)$. Conversely, we can write

$$\Gamma(\nu) = 4\, \overline{\Phi}(\nu) \ , \tag{2.16}$$

where $\overline{\Phi}(\nu)$ is the Fourier transform of $\Phi(x)$.

If we know the instrumental profile, $\Psi(\nu)$, then by calculating $\Gamma(\nu)$ from $\Phi(x)$, we can determine the spectral profile, $S(\nu)$. This profile is actually a convolution of the atmospheric transmission profile and the source profile. Usually, the transmission profile is relatively flat over the spectral range of interest, since that range is small. Therefore, we can assume that $S(\nu)$ is proportional to the source profile.

In practice, it is impossible to perform Fourier integrals since that implies taking data over an infinite and continuous range of optical path differences. We can sample the spectrum by moving the mirror in bursts of $\Delta/2$ (for an optical path difference of Δ), and do this for 2n points centered around zero path difference. The

resulting interferogram will consist of a discrete series of data points, $\Phi(x_r)$. We can represent this function as a Fourier series,

$$\tilde{\Phi}(x) = A_0 + 2\sum_{m=1}^{n-1}\{A_m \cos(2\pi m\nu_0 x) + B_m \sin(2\pi m\nu_0 x)\} + A_n \cos(2\pi n\nu_0 x)\ . \quad (2.17)$$

Here, $x = r\Delta$, $n \leq r \leq n-1$, and ν_0 is the fundamental wavenumber equal to the inverse of the total optical path difference between the first and the last mirror positions, i.e., $\nu_0 = 1/2n\Delta$. It should be emphasized that $\tilde{\Phi}(x)$ is only an estimate of $\Phi(x)$.

By using the orthogonality properties of the cosine and sine functions, we can easily determine the coefficients:

$$A_m = \frac{1}{N}\sum_{r=-n}^{n-1}\Phi(x_r)\cos\left(\frac{2\pi mr}{2n}\right)\ , \quad (2.18)$$

$$B_m = \frac{1}{N}\sum_{r=-n}^{n-1}\Phi(x_r)\sin\left(\frac{2\pi mr}{2n}\right)\ , \quad (2.19)$$

for $m = 0, 1, \ldots, n$. One consequence of a finite Fourier series is that the spectrum covers a finite range. We see that the range of wavenumbers covered is $\nu = 0, \nu_0, 2\nu_0, \ldots, n\nu_0$. This range, which is equal to $1/2\Delta$, is the free spectral range, or FSR. Owing to the periodic nature of the sine and cosine functions, a mirror image of the spectrum will exist for $1/2\Delta \leq \nu \leq 1/\Delta$. This is also the case for the order on the other side. The spectrum will then alternate mirror images of itself in wavenumber space.

It is necessary to alias the orders so that we are only observing radiation coming from one order. That is to say, the radiation falling onto the detector cannot have a bandwidth $\delta\nu > 1/2\Delta$. If $\delta\nu$ is larger than the FSR, then the radiation which falls outside of the FSR will be folded back onto the spectrum. Aliasing is accomplished by using the grating spectrometer. For more information on Fourier series, integrals, and spectroscopy, see Gaskill (1978), Bell (1972), and Jenkins and Watts (1968).

One thought that is usually neglected is the fact that the radiation incident upon the two lamallae is not necessarily in phase with itself. If this is the case, how does this affect the interference patterns? Consider a beam of radiation that contains a random phase distribution. If half of the radiation is incident upon each of the lamellae, then each corner reflector should be illuminated by a subset of the photons with random phase distributions. Let us further assume that there are 2N wave packets in the beam, each packet having a phase ϕj. Let the optical path phase difference between the mirrors for radiation of wavenumber ν be ϵ. Then we find that the total electric field upon recombination is

$$E_{\mathrm{tot}} \propto \sum_{\mathrm{j}=1}^{\mathrm{N}} \mathrm{e}^{-\mathrm{i}\phi_{\mathrm{j}}} + \sum_{\mathrm{j}=1}^{\mathrm{N}} \mathrm{e}^{-\mathrm{i}(\phi_{\mathrm{j}}+\epsilon)} \,. \tag{2.20}$$

To find the intensity, we find EE^*. We find that

$$I \propto \sum_{\mathrm{j}=1}^{\mathrm{N}} \sum_{\mathrm{k}=1}^{\mathrm{N}} \left\{ 2\,\mathrm{e}^{-\mathrm{i}(\phi_{\mathrm{j}}-\phi_{\mathrm{k}})} + \mathrm{e}^{-\mathrm{i}(\phi_{\mathrm{j}}-\phi_{\mathrm{k}}-\epsilon)} + \mathrm{e}^{-\mathrm{i}(\phi_{\mathrm{j}}-\phi_{\mathrm{k}}+\epsilon)} \right\} . \tag{2.21}$$

Owing to the randomness of the individual phases, they are not correlated with each other and so the only non-zero terms that we find are for j = k. This reduces (2.21) to

$$I \propto 2(1+\cos\epsilon) \,. \tag{2.22}$$

Throwing in the appropriate constants of proportionality, we find that this is equivalent to (2.12), which was the result for a single wave-packet.

2.9.4 Determining Burst Sizes

The bandpass of the grating spectrometer is $\approx 0.7\,\mu$m FWHM. If we wish to effectively alias the orders we obtain from the interferometric action, we need to consider two things. First, the grating bandpass should be centered within the order. If λ is the wavelength corresponding to the peak of the grating bandpass, then it follows that

$$\frac{1}{\lambda} = \left(\mathrm{m}+\frac{1}{2}\right)\frac{1}{2\Delta} \,, \tag{2.23}$$

where m is the spectral order. Secondly, the grating bandpass should fit within the FSR.

If we choose λ and m, then by (2.23), we know the optical burst size, Δ. The mirror will move only half that amount, or

$$\Delta_{\text{mirror}} = \frac{\lambda(\text{m} + \frac{1}{2})}{4} . \tag{2.24}$$

Knowing the mirror burst and the distance travelled per step of the stepping motor, we can determine the number of steps to drive the stepper motor.

It is apparent that the FSR is determined solely by Δ. For a fixed Δ, the resolution, then, is determined by the number of data points that are taken. If a 32 point interferogram is taken, then the instrumental resolution will be the FSR divided by 16. With a 64 point interferogram, the resolution will be finer by a factor of 2 and so on. Hence, it is the total distance travelled that determines the resolution. By proper choice of Δ and m for a particular wavelength λ, as well as the number of data points, one can properly alias the spectral order and realize high resolution.

The actual operation of the interferometer is accomplished by taking one-sided interferograms and then reflecting them about zero-path. In order to do this effectively, zero-path must be known and maintained. Once the instrument is allowed to come to thermal equilibrium, the drift of zero-path throughout a flight may be no more than 6 μm, which corresponds to errors of $\sim$3% in the determination of the spectrum. Reflection of the spectra can be done since we may assume that mirror images would be obtained if we did sample on both side of zero. Reflecting saves half of the integration time.

2.9.5 The Fellgett Advantage

It would seem to be much more straightforward, in the quest for high spectral resolution, to simply build a bigger grating instrument. This has been done by Erickson et al. (1985). Aside from the difficulties of making a large grating (at 150 μm, the grating must be at least 50 cm long for a resolution of 5000) and an effi-

cient cryogen can to keep it and the detectors cold, there is a distinct disadvantage if the system noise is primarily electronic and not background limited.

Consider two systems, one a grating and the other an interferometer. Allow both to look at a spectral region of width $\Delta\nu$ in increments of $\delta\nu$. Let the total integration time be T. Then, for the grating, M steps must be taken, where M $= \Delta\nu/\delta\nu$. The total integration time per band $\delta\nu$ is simply T/M. If the noise is independent of signal strength, then the noise of each spectral band is given as

$$n_\nu \propto (T/M)^{\frac{1}{2}} . \tag{2.25}$$

For the interferometer, 2M data points must be taken in order to obtain comparable resolution. However, since each band is encoded in each point of the interferogram, the effective integration time per $\delta\nu$ is T. The noise per band is then proportional to $T^{1/2}$. The S/N ratios for gratings and interferometers may be written as

$$\frac{(S/N)_{Int}}{(S/N)_{Grat}} = \left(\frac{M}{8}\right)^{\frac{1}{2}} . \tag{2.26}$$

This is known as the Fellgett advantage. The factor of 8 comes into play because of the fact that the signal is modulated by a cosine with an amplitude equal to 1/2. The root mean square value for this term is simply $1/\sqrt{8}$.

If, on the other hand, the noise is proportional to the signal strength, the Fellgett advantage is lost. That can be seen by the following argument. For a background limited system, let $I(\delta\nu)$ be the intensity of radiation in the band $\delta\nu$. Then, other things being the same as above, for the grating, the noise should be proportional to the square root of the integration time per point and the band intensity, or

$$(S/N)_{Grat} \propto [(T/M)I(\delta\nu)]^{\frac{1}{2}} . \tag{2.27}$$

For the interferometer, the signal in a band is proportional to $TI(\delta\nu)$, assuming that $I(\delta\nu)$ is constant over the spectral range. At any one mirror position, all of the bands will contribute to the noise. In performing a Fourier transform, the noise will stay about the same, and be proportional to $TMI(\delta\nu)$. Hence, the signal to noise ratio for the interferometer is also proportional to $[(T/M)I(\delta\nu)]^{\frac{1}{2}}$. That is to say

that the Fellgett advantage is lost once the photon statistics dominate the source of noise. For more information on the Fellgett advantage, see Harwit and Sloane (1979), Bell (1972), and Carli (1972).

2.10 Operation and Performance

2.10.1 The Setup

In section 2.9.4, we discussed the choosing of the proper burst size and resolution for an interferogram. One of the constraints is that we properly alias the spectral orders. This is done using our grating spectrometer, which has a spectral bandpass of roughly 0.7 μm FWHM. We have found that a FSR of 2 μm or more allows us to properly alias with little or no folding over of the grating profile.

For flight operations, the interferometer is mounted onto the backplate of the telescope at the Nasmyth port. The mounting ring is fitted with o-rings on both sides, as are the top and bottom lids of the interferometer, to allow a good seal. This is important since the telescope cavity is at ambient pressure during flight at 41000 feet altitude while the plane's interior is kept at a pressure equivalent to an altitude of 8000 feet. If the seal was not tight, then moisture laden air from the plane interior would be travelling through the optical path, creating an additional source of noise.

The interferometer is also electrically isolated from the telescope by a thick ring of polyethylene and plastic sheaths and washers for the mounting bolts. The telescope focus is adjusted so that the focus of its f/17 beam is at the 4 mm aperture at mirror A in the interferometer. The dewar is then attached to the interferometer, as is the offset guider.

A typical observing program dictates that several emission lines of interest be observed during any one flight. In order to properly do this, the grating is calibrated relative to its stepper motor so that it may be positioned for the wavelengths of interest. The burst sizes for the interferometer are calculated for each wavelength, usually for several resolutions and free spectral ranges. Zero-path must also be found for the interferometer.

A data acquisition program written by Charles Fuller for the IMSAI computer is used to take the data and drive the stepper motors. Once the FIR source is obtained and centered in one of the chopped beams, the data are taken by setting up the grating and then integrating for 5 seconds or more at each mirror position of the interferometer. Once one interferogram is acquired, the data are written to floppy disk and also sent over to the ADAMS computer onboard. The interferometer is stepped backwards for the next run. This saves time in driving the mirror all the way back to zero path (upwards of 90 seconds for the full travel) and beginning again. The IMSAI is dedicated during this time to the data acquisition.

With data in hand on the ADAMS system, the Fourier transforms can be performed at an operator's terminal linked to the ADAMS computer. The program performs a fast Fourier transform (FFT) and was written by Scott Smyers with some modifications later added by various members of our group. The FFT routine is an algorithm that can be applied to an interferogram with 2^n points, and takes only a fraction of the computational ability that a normal discrete Fourier transform would take. The algorithm is an adaptation of that published by Cooley and Tukey (1965).

Rapid data reduction permits flexibility to change observing plans during flight. The FFT program uses the raw data, and so gives us a relatively good idea of what we are actually seeing. Post-flight data reduction includes searching the individual integrations for glitches due to cosmic rays or radio frequency interference and redoing the Fourier-transforms again. Various lag windows may be used at this point to effect an apodization. These are discussed in Stacey (1985).

2.10.2 Fringe Visibility and the Spectrometer

According to theory, the signal level for a monochromatic beam should fall to zero at the places of maximum destructive interference. In practice, the signal level doesn't. There are several reasons for this. The first and most obvious one is that the beam is not monochromatic. The grating resolution of 210 limits the amount of total destructive interference that one can have for a certain optical path difference, Δ. However, this limit still provides a maximum-to-minimum ratio, or

fringe visibility Q, of ~ 1000, and can be shown to be equal to

$$Q = 3\left(\frac{2R}{\pi(\mathrm{m}+\frac{1}{2})}\right)^3 , \tag{2.28}$$

where R is the grating resolution and m is the spectral order for the interferogram.

Misalignment of the interferometer could allow one of the corner reflectors to have more than half of the radiation falling on it and the other, of course, to have less. This would provide an imbalance which would act to lower the modulation. If β is the fraction of the radiation falling onto one of the mirrors, then Q is

$$Q = \frac{1}{1-4\beta+4\beta^2} . \tag{2.29}$$

At $\beta = 0.5$, Q is infinite. At $\beta = 0.6$, $Q = 25$. For 66% of the radiation falling onto one mirror, we have $Q = 10$.

In the above instrument configuration, we have found $Q \sim 4$ at best. It is possible to measure the radiation coming from each mirror, and this suggests that this is not the limiting factor. We have seen above that the resolution is also not to blame for such a low Q. Another factor which we have not considered is the spectrometer itself. If we remember, the central 33% of the beam is blocked due to the Littrow-mode operation. It is most likely that up to one-half of the interference is contained within this part that is discarded. While using the hinge Fabry-Perot spectrometer (outlined in chapter III), we have found Q on the order of 12. This instrument is an off-axis system and, therefore, has no central obstruction of the beam. For this reason, we believe that the efficiency of the interferometer is limited mainly by the grating spectrometer. Considering (2.12), we can see that a low Q implies a smaller modulation. This, in turn, implies that the Fourier transform will give results that are smaller by some efficiency factor. It is easy to show that the efficiency of the interferogram is $1 - Q^{-1}$. For a Q of 4, the efficiency is 75%. For a Q of 12, that number climbs to 92%. The efficiency is a slowly varying function of Q once Q is of order 4 or more.

III. The Hinged Grating Fabry-Perot FIR Spectrometer

3.1 Introduction

In Fourier transform systems (FTS), the resolution is dependent upon the total distance of travel of a mirror. At 150 μm, a resolution of 5000 requires a total travel of 38 cm. In order to resolve fine detail in molecular line emission, it is often necessary to have resolutions of 25000 or more. For a FTS, this means that the mirror must be driven a total of at least 1.88 meters. Constructing such an instrument with such a long travel length is difficult at best. Not only must one obtain a driving mechanism which is accurate to several microns over the total distance, but one also needs a guide that is straight over this distance for the movable mirror. To guard against flexure, the instrument would have to be severely massive. Our present interferometer has a weight of roughly 30 pounds, which would imply that a FTS with a resolution of 25000 would have a weight of over 150 pounds. An instrument of this size and bulk could not possibly fit on either the KAO or the Lear Jet. These factors alone would also lead to pointing and tracking problems for balloon-borne systems, and would preclude the use in space-borne infrared packages.

Gratings offer different problems that also prohibit using them for high resolution in the FIR. Again, if we desire resolutions of 25000 at 150 μm for a grating with 10 rulings per mm, we will need a grating that is at least 2.5 m in size. It is desirable to have the grating cooled along with the other optics and filters in order to minimize the background radiation. Building and cooling a spectrometer with a grating of this size is not an easy or practical proposition.

Obviously, if the optical path can be folded many times, we can have a high resolution system which fits in a small space. Fabry-Perot spectrometers (FPS) are just such a system. It is possible to easily obtain resolutions of 25000 in the FIR

with a Fabry-Perot that is no more than 10 cm in size.

Since a Fabry-Perot is operated much like a grating instrument, there is no multiplexing, or Fellgett, advantage. However, for the FIR, detector sensitivity is at present photon noise limited and we know that in this situation, the Fellgett advantage is lost by a Fourier transform system, such as an interferometer. Therefore, a FTS cannot offer an advantage in the signal-to-noise ratio over a FPS.

For these reasons, we have been inspired to design and construct a Fabry-Perot spectrometer system. This system, as will be shown in this chapter, is based upon placing a grating within the FP system itself. The etalon plates are fixed in position, and it is through a rotation of the grating that the FP is tuned. Because of this rotating action, the instrument is known as 'The Hinge'.

We shall first examine ordinary FPS systems in order to understand their characteristics, and then shall present the analysis, both qualitative and quantitative, of the Hinge system. The last part of this chapter will deal with laboratory results that demonstrate the workability of this unique Fabry-Perot instrument.

3.2 Fabry-Perot Spectrometers

3.2.1 Theory

FPS systems have been employed for many years, mainly in the optical and near infrared spectral regimes. For an overview of these FPS applications, see Roesler (1974) and Vaughan (1967). Basic FP theory is straightforward. We will for the most part adopt the nomenclature of Roesler (1974). Figure 3.1 demonstrates the Fabry-Perot action. Light from a collimated beam enters the Fabry-Perot etalon from the left. The etalon consists of two semi-transparent, optically flat windows that are parallel to each other and separated by a distance σ. After the light enters the cavity, it begins to bounce back and forth between the two plates. With each bounce, some of the radiation is passed through one plate and the rest is reflected to the other plate. Collecting optics on the right side of the etalon will focus the rays at the detector.

Let r and t be the reflection and transmission coefficients for the electric field

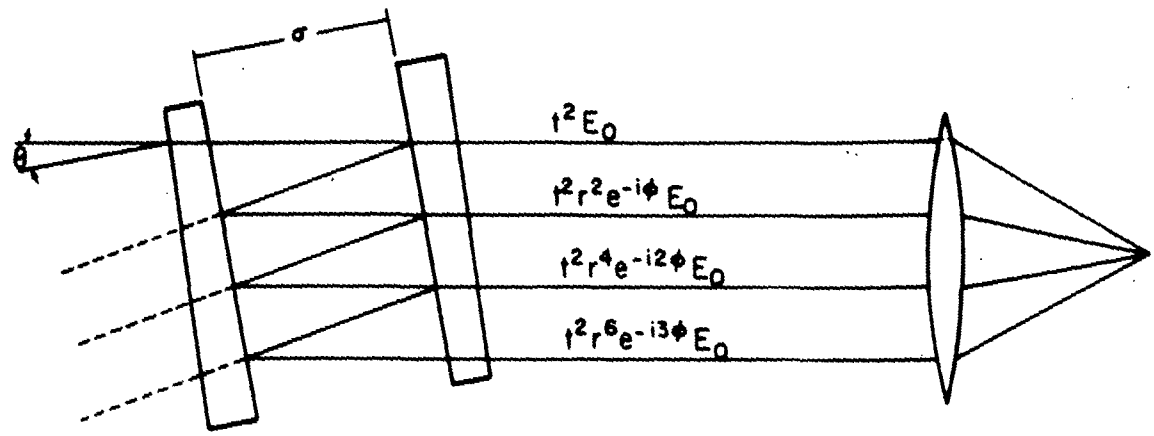

FIGURE 3.1 Schematic diagram of a Fabry-Perot system. Collimated light enters from the left at an angle of incidence, θ, and proceeds to bounce back and forth within the etalon. The radiation that passes through the system is collected by the focusing element at right and recombined. Each pass through the system introduces a phase delay with an attenuation of amplitude. Constructive and destructive interference lead to the familiar FP transmission profile.

vector with wavenumber ν. If E_0 is the amplitude of the initial electric field vector, then tE_0 will pass to the inside of the cavity. Upon encounter with the right-hand plate, some of the light will be passed ($t^2\,E_0$) and the rest (rtE_0) will be reflected. Of this reflected light, a fraction rt of it will pass through to the collecting optics. This light will be phase shifted from the initial beam by ϕ, where

$$\phi = 4\pi\,\sigma\,\nu\sec\theta\ . \tag{3.1}$$

The variables refer to those marked in figure 3.1 and we are assuming that the index of refraction is unity. As we follow the individual reflections and transmissions, we see that each subsequent transmission through the etalon is multiplied by a factor of $r^2\,e^{-i\phi}$. Summing over all of the transmissions gives us a total electric field of

$$E_{tot} = E_0 \sum_{n=0}^{\infty} t^2\,r^{2n}\,e^{-in\phi}\ . \tag{3.2}$$

Noticing that the sum is simply a geometric progression and solving for the intensity, we find that

$$I(\phi) = I_0\,\frac{T^2}{1 - 2\,R\,\cos\phi + R^2}\ , \tag{3.3}$$

where T is the transmission and R is the reflectance of one plate. I_0 is equal to $E_0E_0^*$. Algebraic manipulation will turn (3.3) into the well known Airy equation,

$$I(\phi) = I_0\,\frac{T^2}{(1-R)^2}\left[1 + \frac{4R}{(1-R)^2}\,\sin^2(\frac{\phi}{2})\right]^{-1}\ . \tag{3.4}$$

If there is no absorption ($R + T = 1$), then (3.4) reduces to

$$I(\phi) = I_0\left[1 + \frac{4R}{(1-R)^2}\,\sin^2(\frac{\phi}{2})\right]^{-1}\ . \tag{3.5}$$

It is easy to calculate the reflected intensity from the etalon,

$$I_{refl}(\phi) = I_0\,\frac{4R\,\sin^2(\frac{\phi}{2})}{(1-R)^2 + 4R\,\sin(\frac{\phi}{2})}\ . \tag{3.6}$$

Equations (3.5) and (3.6) show that energy is conserved in the process if there are no absorption losses.

When the sine term is zero, the transmitted intensity is 100% of the incident intensity. This occurs whenever

$$2\sigma\nu\sec\theta = \mathrm{m};\ \mathrm{m} = 0, 1, 2, \ldots\ . \tag{3.7}$$

The transmitted radiation consists of a series of fairly narrow peaks that are uniformly spaced in wavenumber (see figure 3.2). The spacing is called the free spectral range and is denoted by Q. From (3.1) and (3.7), we see that

$$Q = \frac{\cos\theta}{2\sigma}\ \mathrm{cm}^{-1}\ . \tag{3.8}$$

The instrumental resolution is not Q, but is the FWHM of one of the transmission peaks. One can easily derive that this $\delta\nu$ is given by

$$\delta\nu = \frac{2Q}{\pi}\sin^{-1}\left(\frac{1-R}{2\sqrt{R}}\right)\ . \tag{3.9}$$

For $R \gtrsim 0.8$, (3.9) is approximated as

$$\delta\nu = \frac{Q}{\pi}\frac{1-R}{\sqrt{R}}\ . \tag{3.10}$$

The reflective finesse is the ratio of the free spectral range to the FWHM and is given by

$$N_{\mathrm{R}} = \frac{\pi\sqrt{R}}{1-R}\ , \tag{3.11}$$

from which we find the theoretical resolution to be

$$R_{\mathrm{t}} = \frac{N_{\mathrm{R}}\nu}{Q} = \mathrm{m}N_{\mathrm{R}}\ , \tag{3.12}$$

where m is the order number given by (3.7). The contrast, C, is the ratio of the maximum transmission to the minimum transmission, and is given by

$$C = \left(\frac{1+R}{1-R}\right)^2\ . \tag{3.13}$$

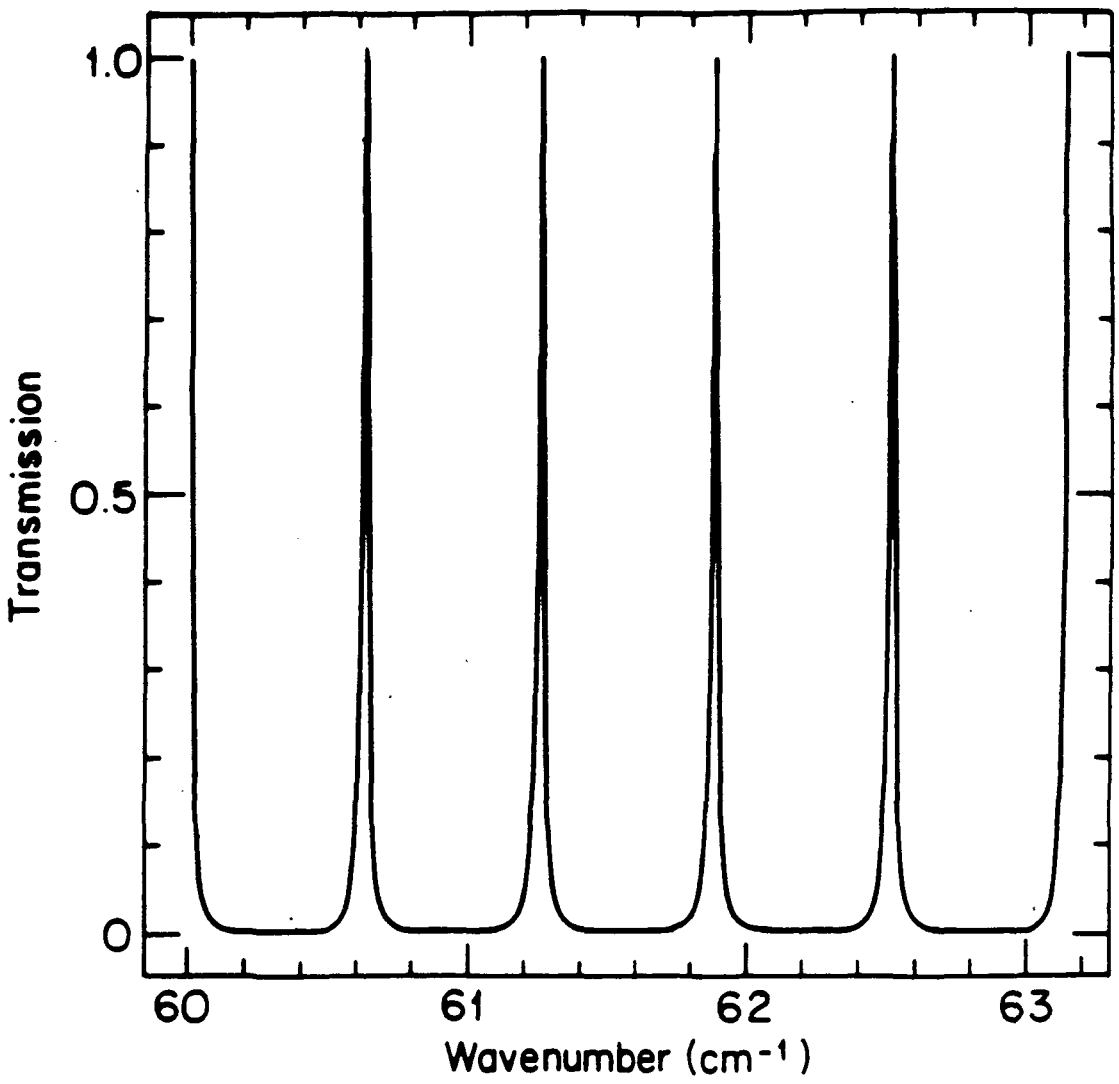

FIGURE 3.2 A transmission profile for a Fabry-Perot etalon.

If continuum emission or closely spaced lines are present, it is important to have a high contrast in order to avoid confusion in line flux measurements. The contrast is a function only of the reflectivity.

3.2.2 Limitations to the Finesse

The above theoretical description of a FPS is for a perfect system. The usual measure of performance for a FP is its finesse. In a perfect system, the finesse is given by N_R. No system is perfect, however, and the limitations of various components will result in a lower resolving power and hence, in a lower value for the instrumental finesse.

There are several factors that limit the finesse of a FPS. The first is the size of the entrance aperture. Since the aperture is extended, radiation incident upon the etalon is not totally collimated. Hence, if β is the angle subtended by the aperture as seen by the etalon, then it follows from (3.7) that the range of wavenumbers that are passed in a given order is

$$\delta\nu_A = \nu_{0m}[1 - \cos(\frac{\beta}{2})] \ , \tag{3.14}$$

where ν_{0m} is the wavenumber of the radiation that is passed through in order m for a perfect system. We assume here that the radiation is incident normal to the first etalon surface. Since the apertures are small, we can replace the cosine function with the first term in the Taylor expansion to obtain the familiar

$$\frac{\delta\nu_A}{\nu_{0m}} = \frac{\beta^2}{8} \ . \tag{3.15}$$

The aperture finesse is then given by

$$N_A = \frac{Q}{\delta\nu_A} = \frac{4}{\sigma\,\beta^2\,\nu_{0m}} = \frac{8Q}{\beta^2\,\nu_{0m}} \ . \tag{3.16}$$

Diffraction effects will also play a role in degrading the resolution. Consider an aperture of size a. Then we know from diffraction theory that the diffraction

pattern as a function of angle θ is

$$I(\theta) = 4I_0 \operatorname{sinc}^2(\pi \nu a \sin\theta) \ . \tag{3.17}$$

At half-maximum intensity, the argument of the sinc function is 2.24. This leads to an angular spread in the beam of

$$\delta\theta_{\text{diff}} = \frac{1.43}{\nu a} \ . \tag{3.18}$$

Again, from (3.7) we find that the diffraction finesse is given by

$$N_{\text{diff}} = \frac{2a^2\nu}{\sigma} \ . \tag{3.19}$$

Another component of a FPS which affects the finesse is the flatness of the plates comprising the etalon. The finesse due to nonflatness can be calculated in the following manner. We divide the etalon into a collection of many microetalons. Each microetalon is characterized by a separation, σ_i. If the σ_i constitute a normal distribution about a mean, σ_0, with an error $\delta\sigma$, then it follows from (3.7) that

$$\frac{\delta\nu}{\nu} = -\frac{\delta\sigma}{\sigma} \ , \tag{3.20}$$

and that the nonflatness finesse is

$$N_{\text{nf}} = \frac{1}{2\nu\,\delta\sigma} \ . \tag{2.21}$$

The shape of the bandpass will be affected by the distribution of the nonflatness errors. Here, we simply assume that it is a normal distribution.

If the plates in the etalon are not parallel to each other, then another degradation of the performance will occur. This tilt finesse can be obtained in the same manner as the nonflatness finesse above. Let one plate be tilted with respect to the second plate by an angle, θ_t. Then it follows that the finesse due to the tilt is

$$N_t = \frac{2}{\nu D \theta_t} \ , \tag{3.22}$$

where D is the diameter of the beam as it enters the etalon.

The FWHM contributions from each of these factors add in quadrature. This implies that the resulting instrumental finesse is given by

$$\frac{1}{N^2} = \frac{1}{N_R^2} + \frac{1}{N_A^2} + \frac{1}{N_{diff}^2} + \frac{1}{N_{nf}^2} + \frac{1}{N_t^2} \,. \tag{3.23}$$

We therefore find that the instrumental finesse can be no better than the worst finesse imposed by one of the above mentioned considerations.

3.2.3 The Effect of Absorption

One certainly will expect some losses from the plates due to absorption. For each plate, we let T be the transmittance and R be the reflectance. If we denote the absorption by A, then it follows that

$$T + R + A = 1 \,. \tag{3.24}$$

Using (3.4) and substituting for A from (3.24), we find that

$$I(\phi) = I_0 \left(1 + \frac{A}{1-R}\right)^2 \left[1 + \frac{4R}{(1-R)^2} \sin^2(\frac{\phi}{2})\right]^{-1} \,. \tag{3.25}$$

It is important to note that the absorption will not change the characteristics of the system such as finesse or resolving power. It will, however, limit the transmission in a non-linear way. When A has the value of $0.3(1-R)$, or $T = 0.7(1-R)$, the transmission of a peak is down to 50%. Even if the absorption is one or two percent, this is an important factor if high resolution, and therefore, high reflectivity, plates are desired.

3.2.4 Isolation of a Spectral Element

As we saw in section 3.2.2, the FP will transmit a series of relatively narrow lines separated by the free spectral range. Changing the spacing of the plates will change the wavelengths of the transmitted lines as dictated by (3.7). In actual

usage, only one of these lines is to be isolated. The suppression of the other lines must be accomplished by some method, and several such methods shall be listed below.

The simplest method to isolate a line is to use a combination of filters. It is difficult to obtain a narrow bandpass with a filter stack, and one should not expect to have a bandpass narrower than a few tens of microns. If one is using a high resolution FPS, then the finesse will have to be several thousand. This is not a practical finesse for the FIR, where finesse values on the order of a few tens to one hundred are more appropriate. The diffraction and aperture finesse values are not very large, and to make them so requires having a large entrance aperture located far from the etalon.

Another problem with using filters to suppress the unwanted orders is that you are very limited in the range of wavelengths that you can observe. This is undesirable since not all FIR lines of astrophysical interest are contained within a narrow band of the spectrum.

The second method of order sorting that is used is a combination of filters and a grating. The filters can cut out most of the radiation below a certain wavelength, and then the grating can be used to select a bandpass in the first order of the grating. Again, if one desires high resolution and the instrumental finesse is a few tens, then the grating resolution must be about one thousand or so. In order to achieve this resolution in the FIR, one will need a grating at least 10 cm in size.

A third method that can be used is to combine filters and another FP that works in a different order in tandem with the primary FP. In this way, it is possible to effectively sort out one order over a rather broad wavelength range with the second etalon and then let the filters suppress any sidelobes further out. This can best be accomplished when the second FP is used in a very low order. Figure 3.3 demonstrates this method. The primary FP in the system is set for a specific wavelength in a certain order and finesse. The second FP is set also for that wavelength, but in first order. The resulting instrumental profile is a convolution of the two profiles from the two FP etalons. This is shown in the bottom box of figure 3.3.

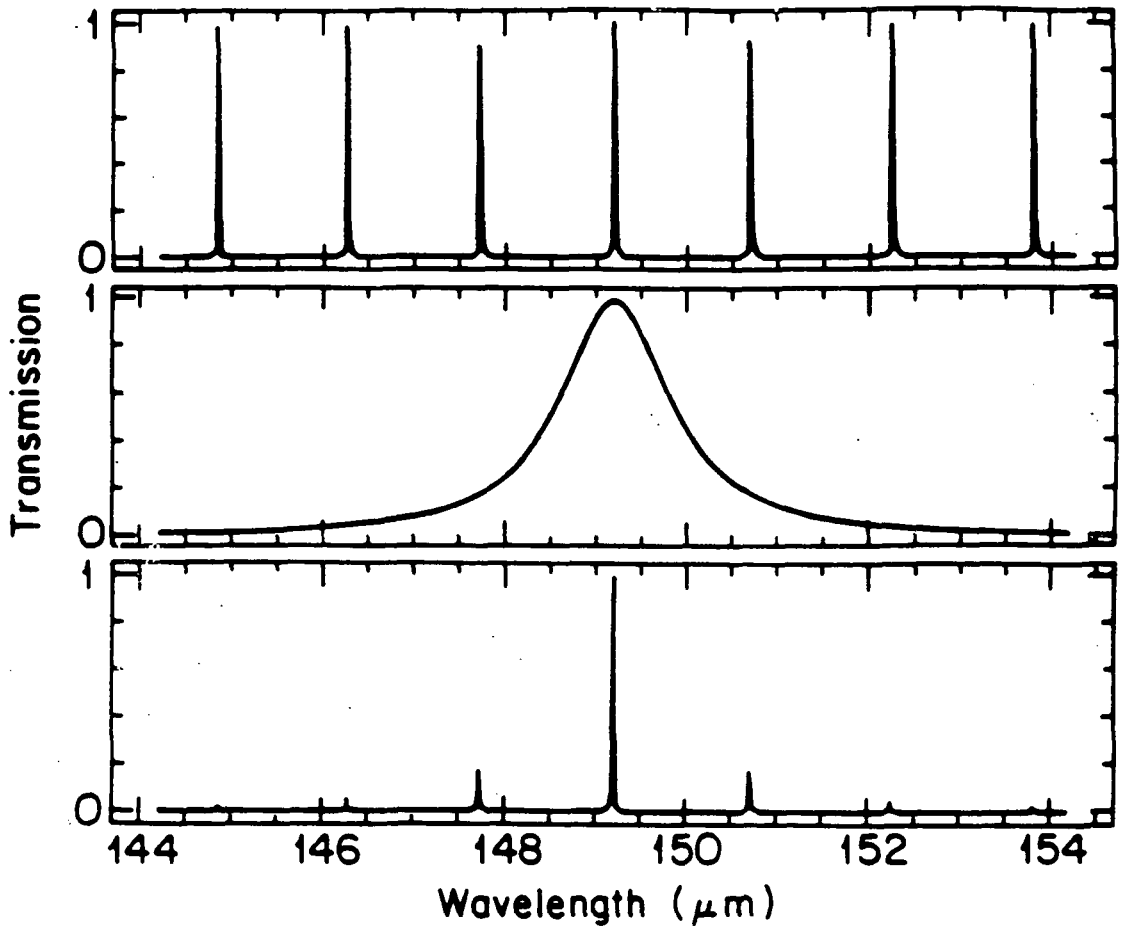

FIGURE 3.3 Transmission profiles for a Fabry-Perot working in a high order (*top*), for one working in first order (*middle*), and for a tandem FP (*bottom*), incorporating both of the above Fabry-Perot systems.

One notices right away that the suppression ability of this setup is very good. The central order is changed very little due to the wide envelope of the second FP. Since we are in first order, the second order wavelength is half of the first and for the FIR, the higher order radiation is well blocked by salt filters.

For more information on Fabry-Perot systems, see Watson (1982), Born and Wolf (1980), Roesler (1974), and James and Sternberg (1969).

3.3 The Hinge—A Qualitative Analysis

3.3.1 Inspiration

In a normal FPS, the spacing between the plates is adjusted using piezoelectric stacks. The spacing is then a function of the voltage applied across these stacks. Owing to the nature of such a design, the electronic circuitry can become very complicated. Maintaining parallelism of the plates ofttimes requires human intervention, a service that is missing if such a device is sent into space aboard a satellite. This is not to say that a FPS cannot be successfully launched and operated, only that such an instrument must be flown with a retinue of complicated circuitry and instrumentation in order to maintain alignment and parallelism, as well as determining the spacing between the plates.

A tandem FP instrument is limited in the range of wavelengths it can cover. Usually, only a few narrow spectral regions can be seen, and the lack of continuous spectral coverage is a severe handicap. Because of this, the FP/grating combination is considered more desirable. However, the complications that are associated with a variable etalon are also found in the FP/grating instrument.

If it were possible to vary the spacing between the plates while keeping the plates stationary, this would be quite helpful. For various reasons, simply tilting the etalon to vary θ is not always an acceptable solution (Roesler 1974). If a reflecting surface could be placed within the etalon cavity, then movement of the surface could tune the cavity. However, there is still the requirement that the reflecting surface must move in some predetermined way. The easiest way to move a surface is to rotate it about an axis. If that surface were the grating, then it might be possible

to tune the FP and the grating at the same time.

Not only can such an instrument be compact, but if there is only one moving part and that part rotates, then it is also extremely sturdy. Another advantage is that it should be tunable over a broad range of wavelengths. Such an instrument would be perfectly suited for high-resolution spectroscopy in FIR space missions.

3.3.2 Principle of Operation

In order to realize such a design, we should first try to understand a diffraction grating. Consider the setup depicted in figure 3.4. A diffraction grating works on the principle of interference. Each ruling in the grating will act as a slit. If a collimated beam of radiation is incident upon the grating at an angle of incidence α and is diffracted at an angle β, then by the grating equation (2.8), we know the wavelengths that will be passed through. The path difference between rulings turns out to be an integral number of wavelengths. In first order, the difference is one wavelength; two wavelengths for second order, and so forth. We can consider a fiducial ruling on the grating and construct from that ruling two planes that intersect the ruling and are perpendicular to either the incident beam or the diffracted beam (see figure 3.4). It follows that radiation perpendicular to both planes will add constructively only for the wavelengths that satisfy the grating equation.

There was nothing special about the angles α and β. Since they can change, we can consider what will happen when we rotate the grating. The only change that occurs is that the wavelength of the radiation that is passed through the system will change. It is still true that radiation perpendicular to both plates will constructively interfere for the wavelengths that satisfy (2.8).

If we place highly reflecting plates where these planes are, then we find that we have a tunable FP cavity. The radiation that enters the etalon will be reflected/ diffracted back and forth between the plates and the grating.

The instrumental finesse of the system is a measure of the number of times that the light bounces inside the cavity. For a finesse of 10, that means that there will be roughly ten bounces. On each bounce, the light will hit the grating twice, and so in effect the beam will appear to have hit 20 times the number of rulings that

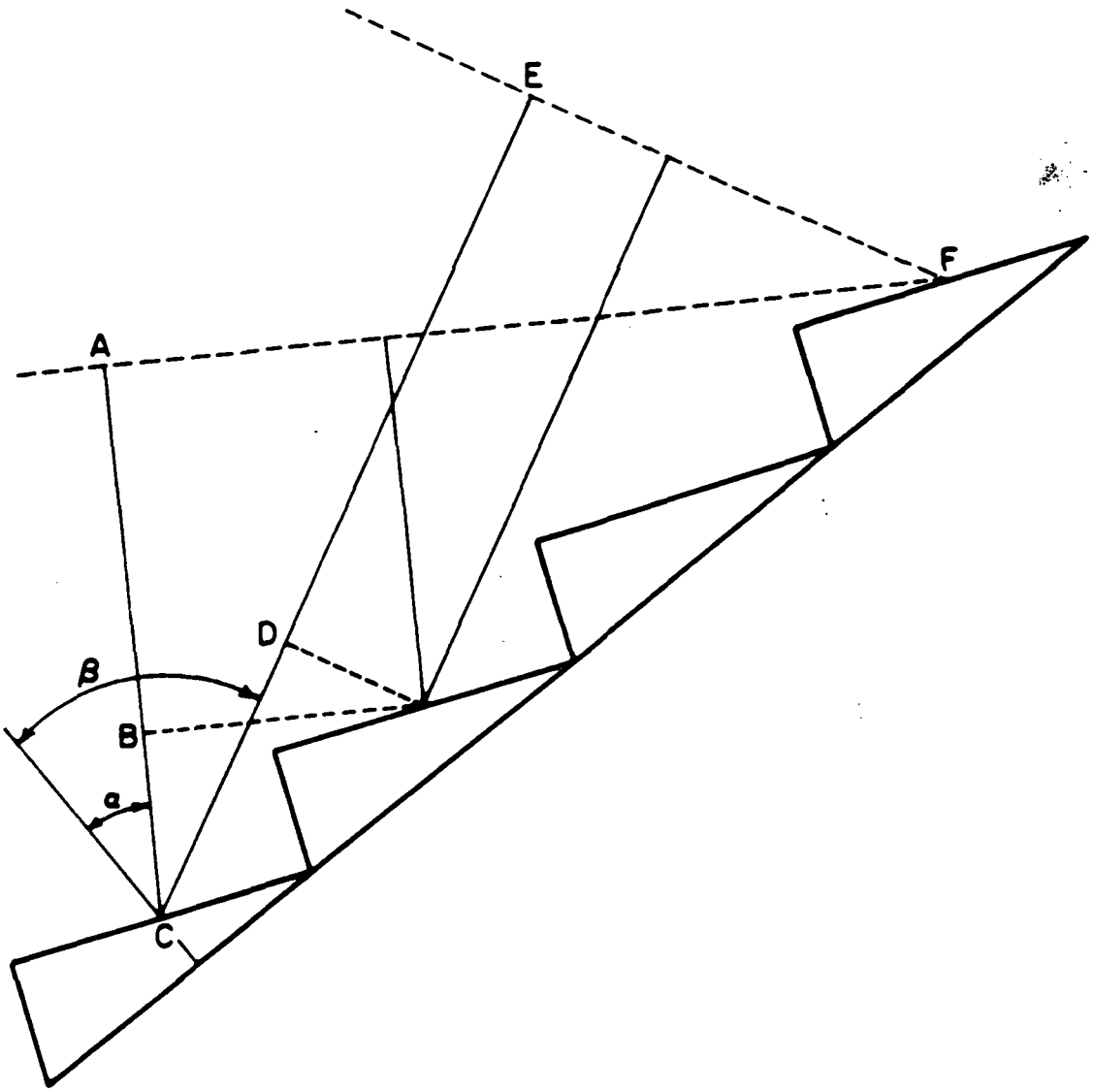

FIGURE 3.4 Principle of operation of the Hinge. Light enters along the direction AC, and is diffracted by the grating along CE. For the two beams presented here (thin solid lines), the phase difference between them is represented by BC + CD, which is equal to one wavelength. The total optical path, AC + CE is equal to an integral number of wavelengths, since F is coincident with a grating step. If highly reflective meshes are placed along the planes represented by AF and EF, then one has a FP system convolved with a grating in the middle.

it illuminates. This means that if the grating has a normal resolution of about 200, then it will appear to have a resolution of roughly 4000. Hence, not only will the grating tune the FP cavity, but it will act as a very good spectral element isolator.

3.4 The Hinge—Theory

Placing a grating inside a FP etalon alters the characteristics of the etalon. Since each successive ruling of the grating produces a relative phase shift of one wavelength, the cavity can be thought of as being composed of a series of microetalons, each microetalon having a spacing one wavelength longer than the previous one. In other words, each microetalon will operate in a different order, no two orders being the same. Because of this, the transmission profile of the hinged grating FPS will differ from that of a regular FP/grating system.

To find out what the transmission of the Hinge should be, we consider the following construction. In figure 3.5, we have the grating and the two plates that make up the FP cavity. Since it is not possible to have the plates actually intersect at the grating axis, the beam illuminates the grating an integral number of rulings down from the fiducial ruling.

We begin by considering each of four phase delays for the different rulings. Every part of the beam will undergo the two phase delays ϕ_1 and ϕ_4. Additional delays due to the grating are ϕ_2 and ϕ_3. If the angle of incidence upon the grating is α, then for radiation of wavelength λ, it follows that

$$\phi_1 = \frac{2\pi}{\lambda} \mathrm{N}_1 \, g \sin\alpha \, , \tag{3.26}$$

where g is the ruling spacing on the grating and N_1 is the number of the first ruling to be illuminated, starting with $\mathrm{N} = 0$ for the ruling coincident with the rotation axis. Likewise, if the diffraction angle is β,

$$\phi_4 = \frac{2\pi}{\lambda} \mathrm{N}_1 \, g \sin\beta \, . \tag{3.27}$$

The grating will also contribute to the phase delay. The radiation that falls on the m^{th} ruling from the first illuminated one will undergo an additional phase

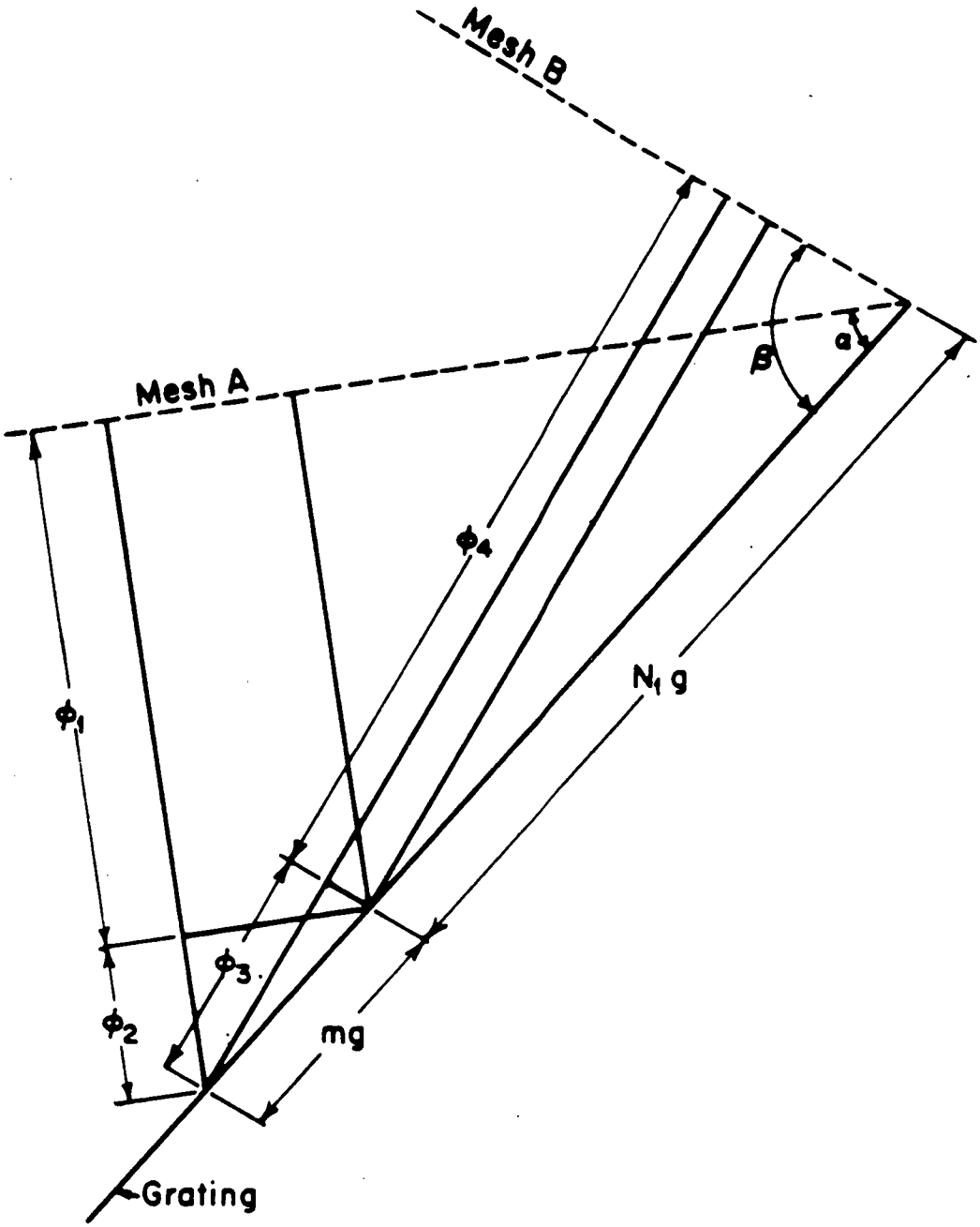

FIGURE 3.5 Theory of the operation of the Hinge. The symbols are explained in the text.

delay of

$$\phi_2 = \frac{2\pi}{\lambda} \mathrm{m}\, g \sin\alpha \,, \tag{3.28}$$

due to the incident path difference and

$$\phi_3 = \frac{2\pi}{\lambda} \mathrm{m}\, g \sin\beta \,, \tag{3.29}$$

due to the diffraction path difference. We see that for radiation to go from plate A to plate B, for each ruling the phase delay will be

$$\phi = \phi_1 + \phi_2 + \phi_3 + \phi_4 \,. \tag{3.30}$$

Using (3.26) to (3.29), we find that

$$\phi = \frac{2\pi}{\lambda} (\mathrm{N}_1 + \mathrm{m})\, g\, (\sin\alpha + \sin\beta) \,. \tag{3.31}$$

In a FP etalon, the phase difference is due to the optical path from one plate to the other and back again. Obviously, if ϕ_m is that phase difference, then $\phi_\mathrm{m} = 2\phi$. We use the subscript m to indicate that the phase difference will depend on which ruling is illuminated, given that the other parameters are fixed.

Since each ruling defines a microetalon, it follows from (3.2) that the total electric field for this microetalon for the m^{th} ruling is

$$\begin{aligned} E_m &= E_0 \sum_{\mathrm{n}=0}^{\infty} t^2\, r^{2\mathrm{n}}\, \mathrm{e}^{-\mathrm{i}(\mathrm{n}+\frac{1}{2})\phi_\mathrm{m}} \\ &= E_0\, T\, \frac{1 - R\,\mathrm{e}^{\mathrm{i}\phi_\mathrm{m}}}{1 + R^2 - 2R\cos\phi_\mathrm{m}}\, \mathrm{e}^{-\mathrm{i}\phi_\mathrm{m}/2} \\ &= E_0\, T\, \frac{\mathrm{e}^{-\mathrm{i}\phi_\mathrm{m}/2}}{1 + R^2 - 2R\cos\phi_m} \left[1 - R\cos\phi_\mathrm{m} - \mathrm{i}\sin\phi_\mathrm{m}\right] . \end{aligned} \tag{3.32}$$

To find the total electric field from all of the microetalons, we sum over the M illuminated rulings to get

$$E_{\mathrm{tot}} = E_0\, T \sum_{\mathrm{m}=0}^{\mathrm{M}-1} \frac{1 - R\,\mathrm{e}^{\mathrm{i}\phi_\mathrm{m}}}{1 + R^2 - 2R\cos\phi_\mathrm{m}}\, \mathrm{e}^{-\mathrm{i}\phi_\mathrm{m}/2} \,. \tag{3.33}$$

The intensity is then given by

$$I = I_0 T^2 \left\{ \left[\sum_{m=0}^{M-1} \left(\frac{(1-R)\cos(\frac{\phi_m}{2})}{1+R^2-2R\cos\phi_m} \right) \right]^2 + \left[\sum_{m=0}^{M-1} \left(\frac{(1+R)\sin(\frac{\phi_m}{2})}{1+R^2-2R\cos\phi_m} \right) \right]^2 \right\} . \quad (3.34)$$

The calculation of I must be done numerically, since it is most likely that (3.34) cannot be written in an analytic form. More will be said about the computations later.

3.5 The Hinge—Construction

3.5.1 Design Considerations

One of the advantages of the Hinge is its compactness. The Hinge was designed to fit within the present dewars that we have been using for the past five years or so. These dewars have a diameter of 6 inches and can house a spectrometer up to 10 inches tall and 5.5 inches in diameter. This size constraint did not prove to be much of a problem.

Figure 3.6 is a schematic of the Hinge assembly. The Hinge was designed as an off-axis spectrometer. Light enters the Hinge and is baffled by two entrance apertures. Black poly, CsBr, and BaF_2 filters are placed between the entrance apertures to block out unwanted optical and near infrared radiation.

The diverging f/17 beam is directed by two planar diagonal mirrors along the perimeter of the spectrometer to a collimating mirror. From the collimating mirror, the radiation is directed to the FP cavity. For the FIR, the etalon plates are usually made of a grid or mesh.

Since we are constrained to place the intersection of the mesh planes coincident with the rotation axis of the grating, the meshes need to be accurately aligned. This can most easily be accomplished by constructing a mesh/grating holder which accurately places the grating pivot point in the mesh planes. The meshes are then allowed to rest upon the holder, which serves to define their planes.

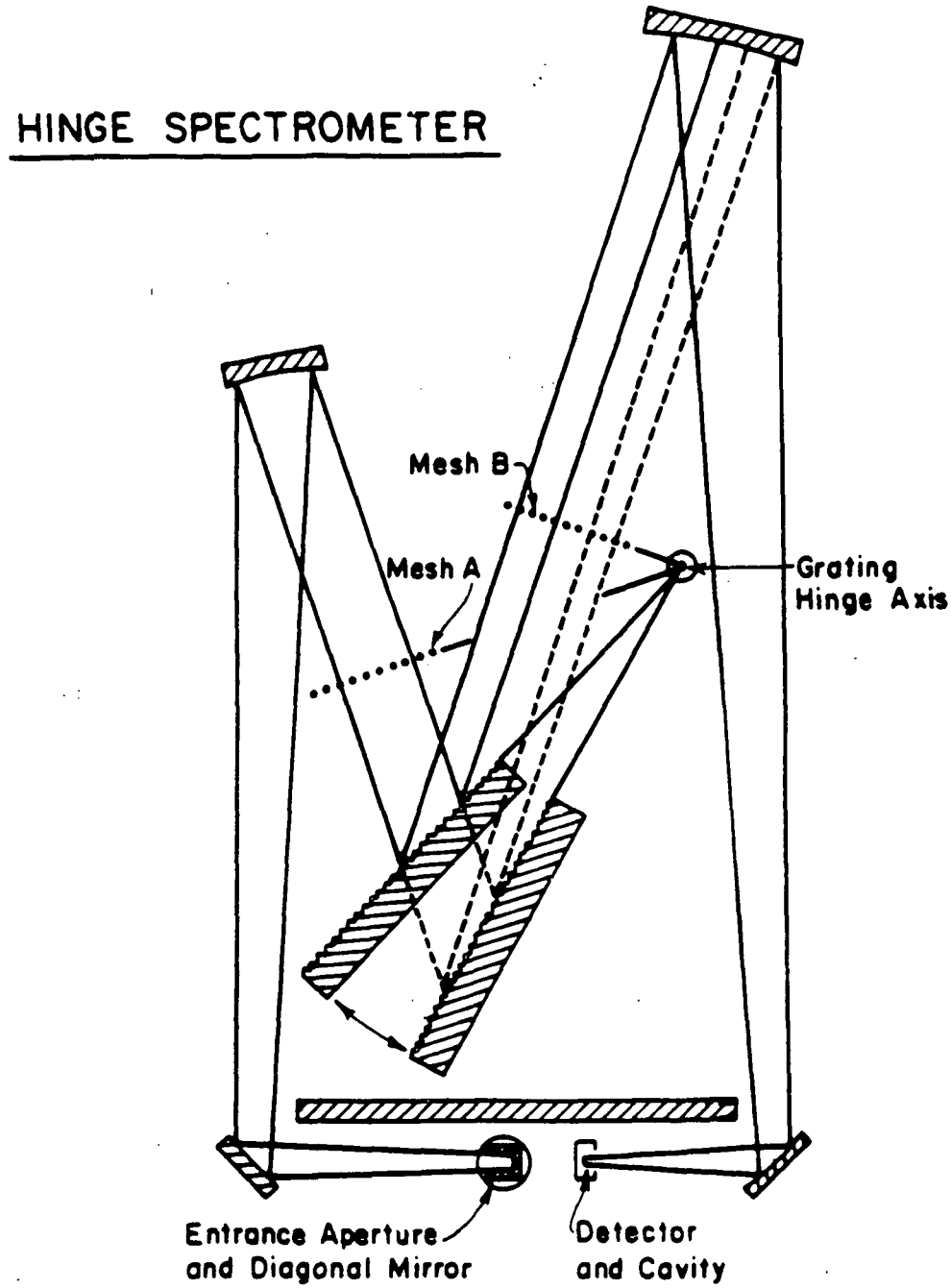

FIGURE 3.6 Schematic diagram of the FIR Fabry-Perot hinged grating spectrometer. An f/17 beam of radiation enters at the bottom, perpendicular to the page, and is then reflected towards the collimating mirror at top left. The collimated beam is then directed into the FP etalon, where it is reflected and diffracted a number of times before exiting to the post-optics, which focus the radiation down onto the detector.

The grating plane must intersect the two mesh planes at the pivot axis. Since the beam will not actually be hitting the grating near this position, but several centimeters away, it is not necessary to rule the entire grating. It is necessary, however, that the rulings are an integral number of spacings away from the pivot point.

With the present size of the FPS, the grating can be rotated through 14°. A somewhat larger spectrometer could easily accomodate a larger rotation. As it is, the angle of incidence on the grating ranges from 26–40°, with the angle of diffraction being 38° larger than the angle of incidence. The corresponding range of wavelengths is from 140 to 170 μm for a ruling spacing of 104 μm.

The grating is made of stress-relieved aluminum, as are the rest of the spectrometer's structural and optical members. This allows the entire structure to contract uniformly upon cool down, alleviating problems with unnecessary stresses and shifting focal planes. The bearing housing and the axle for the grating pivot are stainless steel, but owing to the circular symmetry, the differential contraction upon cooldown will not shift anything. The grating has a thin layer of gold evaporated upon its surface to minimize losses.

Finally, after the FP cavity, there are post optics which take the collimated light beam and converge it upon the detector cavity. A AgCl filter is positioned at the focus just outside of the detector light cone.

The spectrometer itself is only 10 inches high and 5.5 inches in diameter. It is actually somewhat smaller than the grating spectrometer described in chapter II. All of the mirrors and the grating are heat sunk in order to facilitate the cooling down time and to also make sure that all parts of the instrument are cold in order to insure a minimum of background radiation.

As one can tell, the package is quite compact. The entire dewar is less than 30 inches in length with a diameter of 6 inches. The weight is less than 30 pounds. This configuration allows a liquid helium supply which lasts for roughly 20 hours. With the cryogen technology that has been used for IRAS, it is most certainly possible to equip a small telescope with a high-resolution Fabry-Perot of this type and launch it in a space vehicle. Short or long term missions comprised of individually targeted

spectral line observations or even whole sky surveys are possible with such a rugged instrument.

3.5.2 The Meshes

Many groups have constructed infrared FP systems using wire grids for their highly reflective plates. There are several ways in which the grids can be fabricated. Grids that are in the form of free standing screens are the most common. These sheets of mesh may be stretched flat across a ring and be made into an etalon plate.

Other methods of constructing meshes is to deposit a mesh structure onto an optically flat transparent medium such as crystal quartz or silicon. The deposition can be done as either a positive or a negative. In either case, one will have a highly reflecting plate for a certain spectral regime.

For grid deposition, we will only consider the positive deposition. Periodic structures in the form of crossed dipoles or tripoles have also been used. For more information concerning these, see Rhoads, Damon, and Munk (1982); Durschlag and Temple (1981); and Tomaselli et al. (1981).

For the Hinge, free standing metal meshes were first considered for use. Since the mesh plane of the Hinge is defined by the mesh/grating holder (MGH), it is necessary to first mount the mesh on a mesh ring of some sort in order to maintain flatness, and then press that against the MGH. The mesh rings used are like those shown in figure 3.7.

The mesh is made of nickel and is manufactured by Buckbee-Mears Co. in St. Paul, Minnesota. Nickel was chosen over copper due to its better cycling capability. Copper tends to not cycle well cryogenically and in time will become stretched.

The mesh rings must define the flatness of the mesh. In order to accomplish this, the ring (figure 3.7) is constructed with an optically flat surface over which the mesh is stretched. A beveled outer surface gives one room to glue the mesh to the ring. The bonding agent is cyanoacrylate, also known as 'Superglue'. Normal epoxies do not cycle well, but there are epoxies for low temperature work. The advantage to cyanoacrylate is that is can be readily dissolved with acetone to remove a mesh which is torn or improperly made. This is extremely helpful to the neophyte

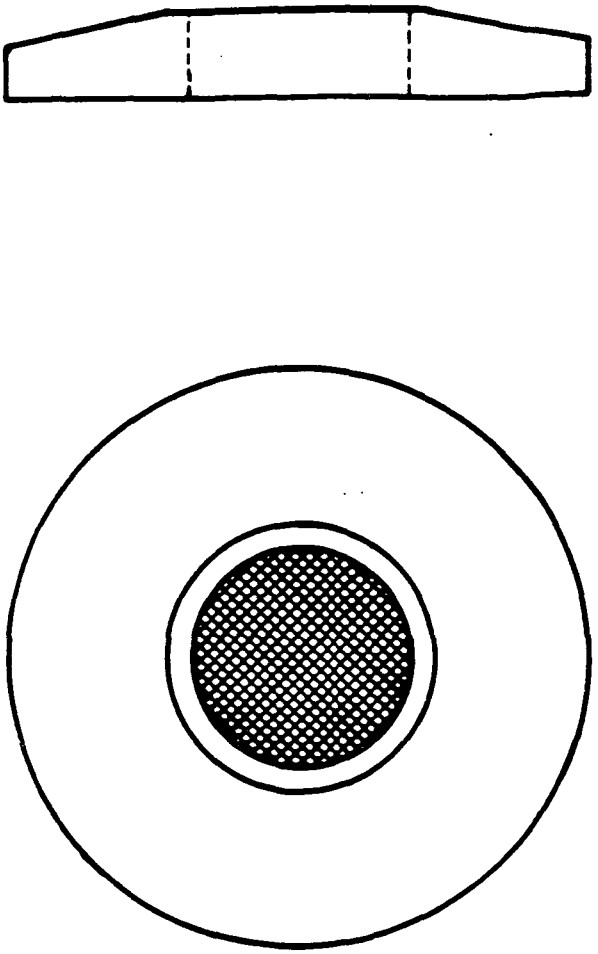

FIGURE 3.7 Drawing of the mesh holders. These holders are constructed of stainless steel, the mesh is nickel. The narrow, flat annulus on the top of the holder is ground and polished to 1/100th of a wave, and then the mesh is stretched over the top and glued down on the wide beveled annulus. These free-standing meshes were later abandoned in favor of aluminum mesh photo-deposited on optically flat crystal quartz.

mesh-maker.

Once the mesh is stretched and glued onto the ring, the ring may then be inverted so that the mesh is sandwiched between the MGH and the ring. The ring must be made of a material that has a lower coefficient of thermal expansion than Ni, else the ring will contract more than the mesh upon cooldown and the surface will no longer be flat. Stainless steel was chosen as the ring material. Since the mesh is sandwiched between dissimilar metals (stainless steel and aluminum), it is possible to tear the mesh upon cooldown. A torn mesh can sag and the FP action can be lost. Care must therefore be taken in order to insure that the MGH surface is smooth and flat, to minimize the chance of snagging.

At first, #400 and #500 meshes were used. (#400 mesh has 400 lines per inch.) The results seemed to suggest that the Hinge had little Fabry-Perot action; i.e., it was acting like a grating instrument with two neutral density filters installed. The resulting instrument profile was almost as wide as that of the grating alone. Sagging of the meshes was suspected.

It was decided that the sagging could be a real problem, and the only clear alternative to using metal mesh was to use mesh deposited on quartz or silicon. The transmission of crystal quartz in the FIR is roughly 75% for a 1 mm thick sample. Fused quartz has a much lower transmission (Kimmitt 1970).

The properties of a mesh are altered when the mesh is placed on a substrate. The most significant change is that the diffraction edge is shifted to longer wavelengths by a factor that is equal to the index of refraction of the subtrate (Durschlag and DeTemple 1981). In other words, the spacing of the mesh is in effect increased by a factor of n, where n is the substrate's index of refraction.

The mesh that we are using was photodeposited on optically flat crystal quartz by Nellie Whetten at the National Research and Resource Facility for Submicron Structures here at Cornell. The grid is made of aluminum, with spacings of 25 μm and line widths of 10 μm. The index of refraction for crystal quartz at 2 K is 2.120 at 150 μm (Loewenstein, Smith, and Morgan 1973). These plates are then equivalent to #480 mesh. The quartz is slightly wedged to prevent unwanted FP effects within the crystal itself.

The radiation that is reflected by the mesh is shifted in phase by an amount that is almost equal to π radians. It is, however, closer to 0.95π, owing to non-zero transmittance. Therefore, this must be taken into account in the placement of the meshes; and the mesh planes are adjusted accordingly.

3.6 Error Analysis

Associated with any instrument are the complementary errors that exist due to imperfections in either design or construction. The Hinge has several sources of errors which could almost totally frustrate the Fabry-Perot action if the errors were large enough. In this section, we shall consider these sources of error and see how significant they are.

One source of error is that the actual mesh plane is displaced from where it should be by an amount δ. We will assume that the displacement is perpendicular to the plane. To understand how much the displacement will affect resolution, we need to consider each illuminated ruling of the grating as a part of a microetalon. There are N such microetalons. Let us first consider the situation when $\delta = 0$. For one edge of the beam, the distance between the plates is spanned by N_1 wavelengths of radiation with wavelength λ_0. At the other edge of the beam, there are N_2 such wavelengths.

When the mesh plane is displaced by a distance δ, then each microetalon will transmit a slightly different wavelength. The range in wavelengths can easily be calculated. For the $N_1{}^{th}$ microetalon, the transmitted wavelength is

$$N_1 \lambda_1 = N_1 \lambda_0 + \delta \ . \tag{3.35}$$

Likewise, for the $N_2{}^{th}$ microetalon,

$$N_2 \lambda_2 = N_2 \lambda_0 + \delta \ . \tag{3.36}$$

We can therefore estimate the bandwidth by finding the difference between λ_1 and λ_2. This is

$$\Delta\lambda = \delta \left(\frac{1}{N_1} - \frac{1}{N_2} \right) . \tag{3.37}$$

At 153 μm, $N_1 = 700$ and $N_2 = 892$ for a beam 1.7 cm in diameter. If we want the resolution to be at least 10000, then δ must be 2.0 mils or less (1 mil equals 0.001 inch).

Another source of error is having the plane of the rulings not intersect the mesh planes along the rotation axis, but displaced by an amount δ. It can be shown that the displacement of the grating will produce a shift in the spacing of the microetalons, $\delta\sigma$. This shift is independent of position on the grating and is given by

$$\delta\sigma = \delta\left(\cos\alpha + \cos\beta - \frac{\sin(\beta-\alpha)}{\cos\alpha}\right), \tag{3.38}$$

where α and β are the angles of incidence and diffraction, respectively. As above, we have the following range of wavelengths that are transmitted:

$$N_1\,\lambda_1 = N_1\,\lambda_0 - \delta\sigma$$

$$N_2\,\lambda_2 = N_2\,\lambda_0 - \delta\sigma\,, \tag{3.39}$$

from which we find

$$\Delta\lambda = \delta\sigma\left(\frac{1}{N_1} - \frac{1}{N_2}\right). \tag{3.40}$$

Again, for $\lambda_0 = 153\,\mu$m and a resolution of 10^4, we find that $\delta\sigma = 2.0$ mils, or the grating may be displaced by as much as 4.2 mils. This is well within ordinary machining capabilities, as is the mesh displacement criterion.

The grating offers two other sources of error. The first is if the rulings are displaced along the grating surface by an amount δ. That is to say, the rulings are not an integral number of spacings from the pivot axis. We measure from the center of each ruling to determine distance. The displacement will cause a range of wavelengths to be transmitted, since the difference in spacing between each succesive microetalon is no longer constant. Again, with similar analysis as above, we find

$$\Delta\lambda = \frac{\delta\,\lambda_0}{g}\left(\frac{1}{N_1} - \frac{1}{N_2}\right), \tag{3.41}$$

where g is the ruling spacing (96 rulings per centimeter). For a resolution of 10000 at 153 μm, we have a machining tolerance of 1.3 mils.

The other source of error from the grating is a side-to-side tilt. This situation will result in the beam walking off of the plates. This walkoff alone will limit the resolution. However, along with the walkoff, each succeeding bounce off the grating will result in a longer cavity spacing. The walkoff will lead to a lower transmission for obvious reasons. If we assume that there are now M traversals in the cavity before the beam walks off, then for each microetalon, we have from (3.2)

$$I = I_0 (1 - R^{\mathrm{M}})^2 \left[\frac{1 + \frac{4R^{\mathrm{M}}}{(1-R^{\mathrm{M}})^2} \sin^2(\frac{\mathrm{M}\phi}{2})}{1 + \frac{4R}{(1-R)^2} \sin^2(\frac{\phi}{2})} \right], \tag{3.42}$$

where ϕ is the phase delay as given in (3.1) and (3.30). The factor on the right will determine the resolution. For the canonical resolution of 10000 at 153 μm, we find that the number of traversals within the cavity is relatively independent of the reflectivity. Six bounces, or twelve reflections off the grating, are necessary. Let ψ be the tilt angle of the grating. With each reflection off the grating, the deviation of the radiation will double. After 12 reflections, we find that the deviation is $\approx 32\psi$ meters. The maximum deviation that can be tolerated is roughly 0.4 inch, allowing for the fact that the mesh is oversized. This implies that ψ must be roughly 3×10^{-4} rad. Over the span of the grating width, 1.5 inches, this tolerance means that the grating axis must be positioned within 0.48 mil. The post optics and the exit aperture will dictate that this tolerance be even more stringent, and we should expect to be able to place the grating axis within 0.25 mil of where it should be.

Each reflection off the tilted grating will produce a somewhat longer path length than the previous reflection. This longer path length will tend to spread the FWHM of the transmitted peak. To keep the spread under one part in 10000, this means that the grating must not be tilted by more than 0.001 rad, or a machining error of no more than 1.5 mils. This constraint is much more relaxed than that for the previous effect, which means that this is the less important of the two effects that a tilted grating will produce.

The final set of errors that can arise from machining imperfections is due to the meshes being tilted. There are two directions of tilt, along the direction of dispersion and perpendicular to it. We shall first consider the latter.

C-2

If the mesh is tilted side-to-side, then we have the same problem that we had before with the grating. However, this time the radiation hits the mesh only once per bounce as opposed to hitting the grating twice per traversal through the cavity. This suggests that the tilt error can be no more than 1.6 mils in order to prevent the beam from walking off the mesh. However, again, the exit aperture will dictate a tolerance which is about a factor of 2 more stringent.

For a tilt along the direction of dispersion, the tolerances are approximately a factor of 10 smaller. This is due to the fact that a small change in angle will result in a large movement along the grating owing to the steep diffraction angles. The angular error grows with each bounce as well. At 153 μm, a tilt of 2×10^{-4} rad in one of the meshes will cause the beam to walk across the radius of the second mesh. Since the mesh diameter is 1.2 inches, this corresponds to a tolerance of better than 0.24 mil.

The machining constraints that are imposed by these errors are not very demanding in general. There are a few exceptions where tolerances of less than a mil are necessary, but these tolerances are still not beyond the skills and techniques of a very good machinist. Because of this, the machining costs of the Hinge were very reasonable. In fact, they were much less than the price for the ruling of the grating, though that price was dictated by the need to have the grating plane accurately pass through the hinge axis.

3.7 Simulations

3.7.1 Programming Considerations

In order to determine the instrument profile, it is necessary to know what (3.34) looks like. There is no straightforward analytical solution to this equation, so numerical computation is required.

There are several ways to calculate (3.34). In practice, it is desirable to have a minimum number of calculations, especially trigonometric functions. Written as is, (3.34) requires 2M trigonometric calculations, where M is the number of rulings illuminated by the beam. This number is ~ 200. We can reduce this by a factor of

at least two or more.

In order to do that, we go back to (3.32) and (3.33). Instead of first summing over the number of reflections, we should sum over the number of rulings illuminated. Equation (3.33) then becomes

$$E_{\rm tot} = E_0 T \sum_{\rm n=0}^{\infty} \sum_{\rm m=0}^{\rm M-1} R^{\rm n} \, {\rm e}^{-{\rm i}({\rm n}+\frac{1}{2})\phi_{\rm m}} \; . \tag{3.43}$$

We can rewrite $\phi_{\rm m}$ as

$$\begin{aligned} \phi_{\rm m} &= \frac{4\pi}{\lambda} \, g \, ({\rm N}_1 + {\rm m}) \, (\sin\alpha + \sin\beta) \\ &= \varsigma + {\rm m}\kappa \; , \end{aligned} \tag{3.44}$$

where

$$\begin{aligned} \varsigma &= \frac{4\pi}{\lambda} \, g \, {\rm N}_1 \, (\sin\alpha + \sin\beta) \\ \kappa &= \frac{4\pi}{\lambda} \, g \, (\sin\alpha + \sin\beta) \; . \end{aligned} \tag{3.45}$$

This gives us the following expression for the total electric field:

$$E_{\rm tot} = E_0 \, T \sum_{\rm n=0}^{\infty} R^{\rm n} \, \frac{\sin[({\rm n}+\frac{1}{2})\frac{{\rm M}\kappa}{2}]}{\sin[({\rm n}+\frac{1}{2})\frac{\kappa}{2}]} \, {\rm e}^{-{\rm i}({\rm n}+\frac{1}{2})[\varsigma+\frac{\kappa}{2}({\rm M}-1)]} \; . \tag{3.46}$$

We calculate the intensity to be

$$\begin{aligned} I = I_0 \, T^2 \left\{ \sum_{\rm n=0}^{\infty} R^{\rm n} \, \frac{\sin[({\rm n}+\frac{1}{2})\frac{{\rm M}\kappa}{2}]}{\sin[({\rm n}+\frac{1}{2})\frac{\kappa}{2}]} \cos\left[\left({\rm n}+\frac{1}{2}\right)\varsigma + \left({\rm n}+\frac{1}{2}\right)\frac{\kappa}{2}({\rm M}-1) \right] \right\}^2 \\ + I_0 \, T^2 \left\{ \sum_{\rm n=0}^{\infty} R^{\rm n} \, \frac{\sin[({\rm n}+\frac{1}{2})\frac{{\rm M}\kappa}{2}]}{\sin[({\rm n}+\frac{1}{2})\frac{\kappa}{2}]} \sin\left[\left({\rm n}+\frac{1}{2}\right)\varsigma + \left({\rm n}+\frac{1}{2}\right)\frac{\kappa}{2}({\rm M}-1) \right] \right\}^2 . \end{aligned} \tag{3.47}$$

In practice, one need only sum over a small and finite number of reflections instead of over an infinity of them. It turns out that the finesse is a good measure of how

many bounces over which one needs to sum. If we consider N bounces, then one sees that we need only calculate 4N trigonometric functions. For a finesse of 30, this method gives the computer almost a factor of two fewer trigonometric functions to calculate.

From the dimensions of the Hinge and its optical configuration, we can calculate N_1 and M. From α and β, we can then figure out ς and κ. It is then a simple matter to perform the sums in (3.47) and to calculate the intensity as a function of wavelength for meshes with reflectivity R.

3.7.2 Results

The transmission profiles of the Hinge have been calculated for various reflectivities. Figure 3.8 shows two profiles, one for $R = 0.7$ and the second for $R = 0.9$. These were calculated for the grating tuned to 154.6179 μm radiation. As one can see, there are several interesting features of these profiles.

The first thing to notice is that there is a narrow central spike which is due to the combined constructive interference from all of the microetalons. The sidelobes are suppressed by the action of the grating. As one can tell, higher mesh reflectivity yields better sidelobe suppression. This is because a higher reflectivity increases the number of bounces within the FP cavity and causes the effective bandpass of the grating to decrease.

The sidelobes are spaced approximately 0.1 μm apart. One can calculate the resolution from the simulation profiles and find an equivalent ordinary FP system. At this wavelength, we find a good fit for a plate spacing of 12.28 cm. The actual pathlength between plates for the central portion of the beam is 12.44 cm, but this pathlength ranges between 10.94 and 13.95 cm across the size of the beam. The equivalent FP system will result in a $Q_{\text{equiv}} \approx 0.10\,\mu$m, which is what we observe in figure 3.8.

Since there is a range of orders going through the etalon cavity, there is also a range of Q values. For the simulations at 154.6179 μm, Q will range from 0.086 to 0.109 μm. This means that the sidelobes should be much broader than the central peak. Since the Q values cover a relatively broad range, this can also explain

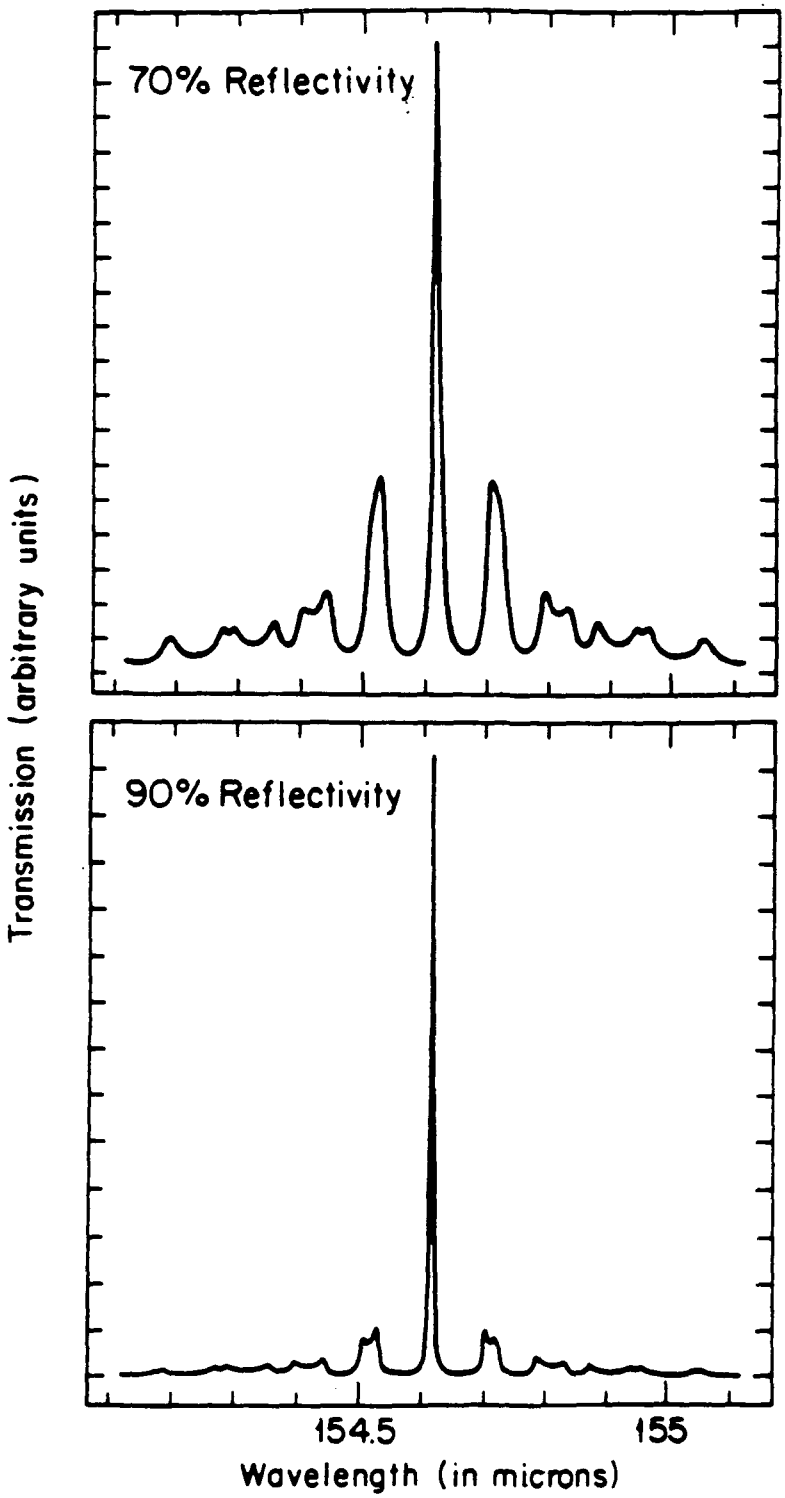

FIGURE 3.8 Theoretical tranmission profiles of the Hinge for mesh reflectivities of 70% (*top*) and 90% (*bottom*).

the apparent bifurcation of some of the sidelobes as different parts of the beam come into or go out of phase with other parts.

The resolution of the system closely follows that for the equivalent FP system. This is shown in figure 3.9 as a function of mesh reflectivity. For reflectivities approaching 95%, the resolution nears 10^5. As the reflectivity goes down below 20%, the resolution of the Hinge drops below that for the equivalent FP system. The grating profile dominates at low reflectivities.

If we have high resolution, it is important that the sidelobes are suppressed in order to avoid confusion. In this system, higher reflectivities not only give higher resolution, but automatically give better sidelobe rejection due to the increasing number of times that the beam hits the grating. For 70% reflectivity, the first sidelobe is 67% of the central peak. At 90% reflectivity, this number is down to less than 20%.

The grating is not 100% efficient, as was assumed in the above simulations. If the grating is 90% efficient in the one polarization, it acts as a neutral density filter and effectively lowers the reflectivity of the meshes by $\sim$ 10%.

3.7.3 Errors

Errors due to machining imperfections have been incorporated into the transmission profile programs. This is done by simply following the beam of each microetalon separately as it encounters tilted meshes or displaced meshes and gratings. We have already discussed the various sources of error in section 3.6.

Figure 3.10 is a transmission profile with one mesh that is tilted along the direction of dispersion by 0.10 mil. It is tilted so that the beam will walk down the grating. What we see is that the total transmission is down by a factor of 4 or more, and the peaks have shifted to somewhat longer wavelengths. The resolution is also degraded, as well as the symmetry of the profile.

It is evident that the transmission profile is very sensitive to tilt errors. These errors can arise in several ways, including a misalignment of the optics. Hence, it is important to carefully align the optics in order to minimize any degradation to the system.

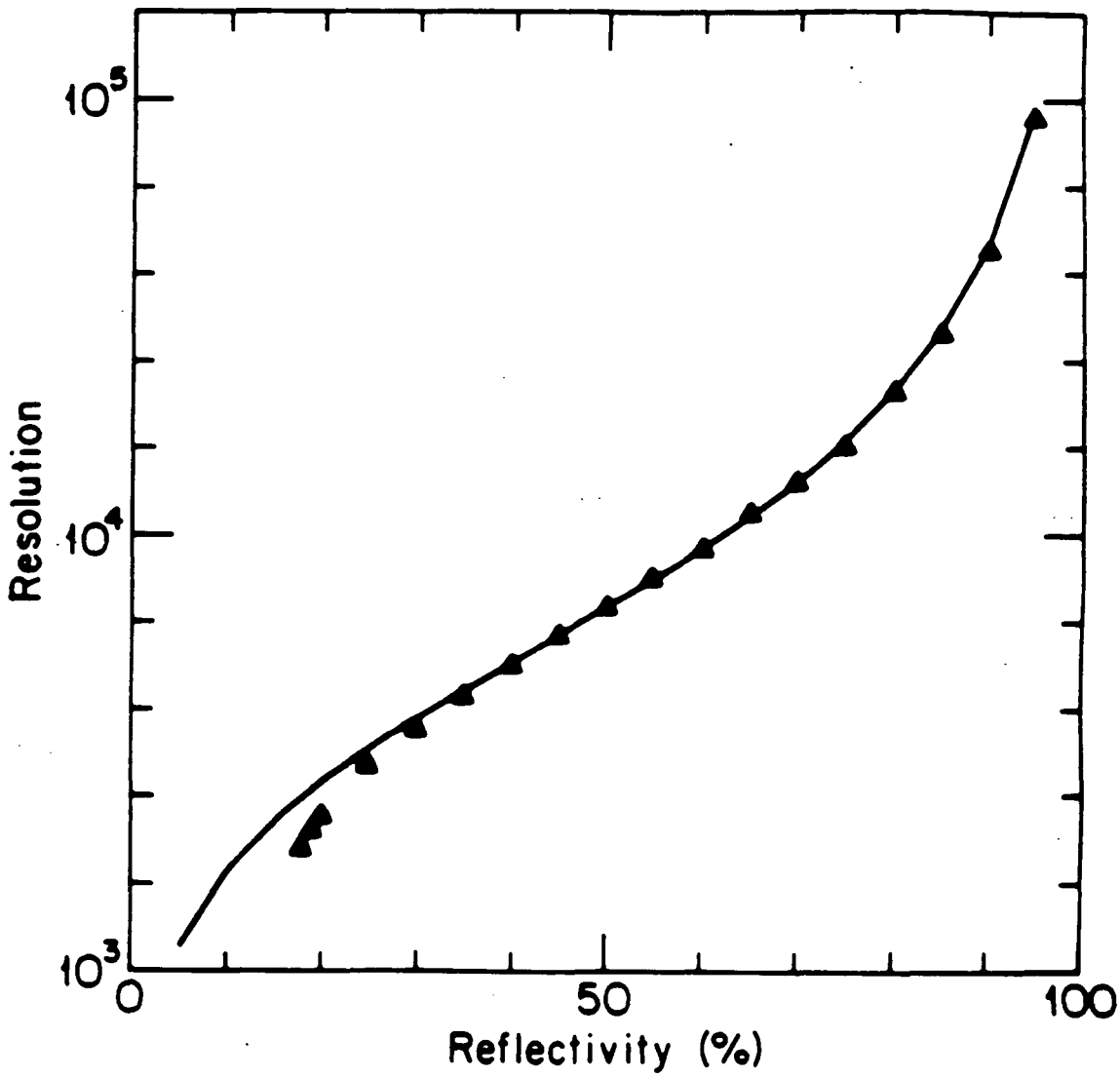

FIGURE 3.9 Theoretical resolution as a function of mesh reflectivity for the Hinge. The solid curve represents the resolution for an equivalent ordinary FP system. At low reflectivities, the grating profile dominates, causing lower resolution for the Hinge as opposed to the equivalent system.

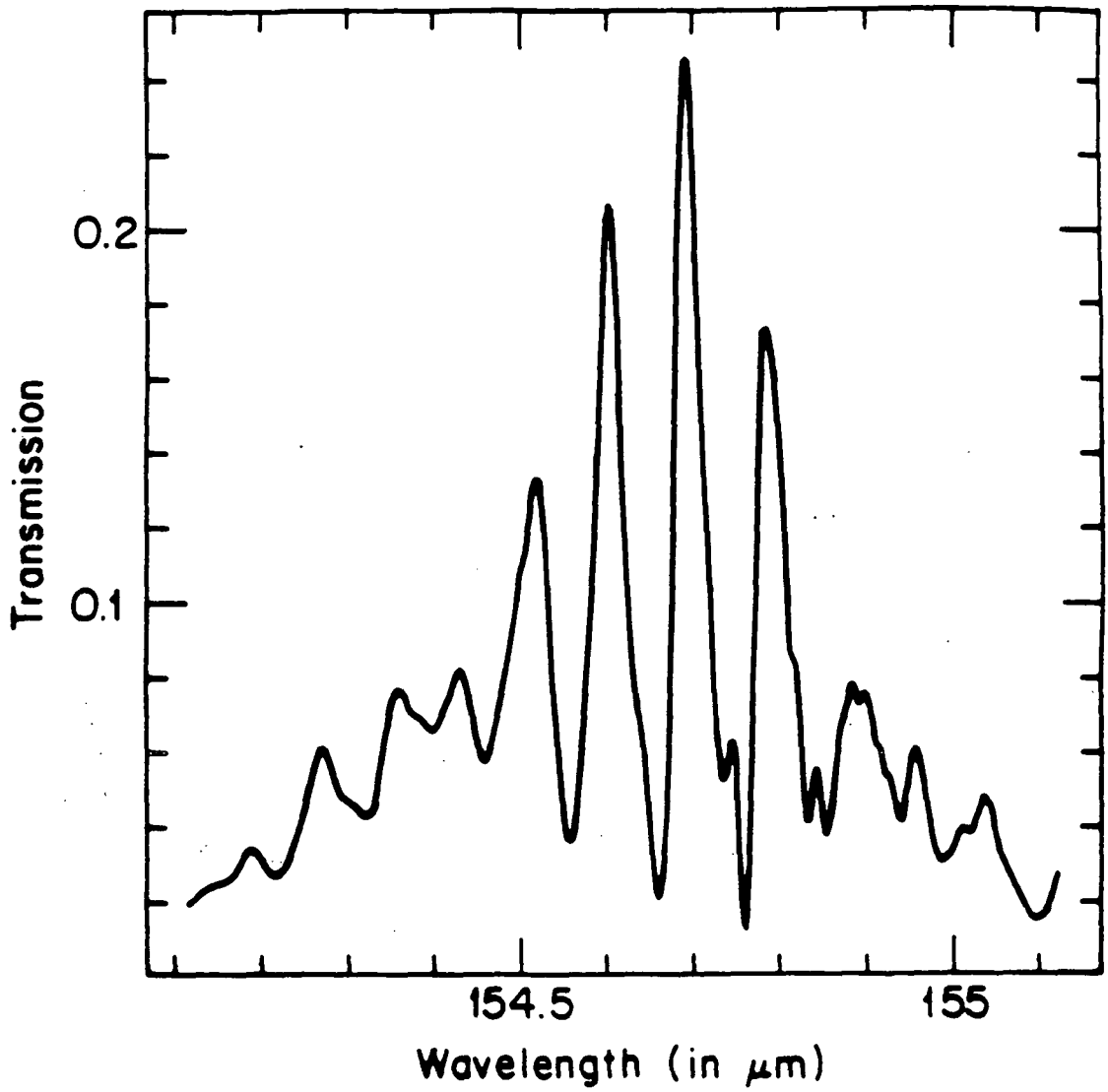

FIGURE 3.10 Transmission profile of the Hinge if one of the meshes is tilted by 0.01 radian. The transmission is decreased due to walkoff problems, the transmitted radiation is shifted towards longer wavelengths (as directed by the tilt), and the profiles are widened and asymmetric.

Displacement shifts of the grating do not affect the profiles very much. Basically, the profile will shift in wavelength depending on whether the cavity is shortened or lengthened by the grating displacement.

3.8 Laboratory Results

3.8.1 Spectra Through the Interferometer

In order to determine the actual instrumental profile, we made two sets of measurements in the laboratory. The first set was made using the interferometer. The second was using a narrow line source.

Meshes deposited on crystal quartz were installed into the instrument. These meshes have reflectivities on the order of 85%. With the interferometer, we were able to determine the Hinge profile with a resolution of over 4000 at 153 μm. Figure 3.11 shows the result. Each bin of the spectrum is 0.038 μm wide. To within a fraction of that, the central peak is centered in one bin and is less than one bin wide. We know from this that the resolution is better than 4000, but we do not know how much better.

Unfortunately, we cannot get more resolution out of the interferometer. The spectrum is noisy out in the wings, primarily due to the fact that the system sensitivity was not very good at this stage. This was primarily caused by the detector losing stress and the quantum efficiency plummetting at these long wavelengths.

During this same time, we concentrated our efforts at obtaining information at 142 μm, where the signal was strongest. This spectrum is shown in figure 3.12. As one can tell, the sidelobes are about 30% of the signal. This is consistent with a reflectivity of 85%. The wings of the spectrum are also close to 0.

3.8.2 Absorption Spectrum of CO

The interferometer allows us to look at the gross characteristics of the Hinge. In the earlier tests that were run, it was noted that there was a short wavelength leak (about 20 μm less than the central peak). In order to combat this, the CsBr salt filter was installed to purge any radiation below 138 μm from entering. The cause

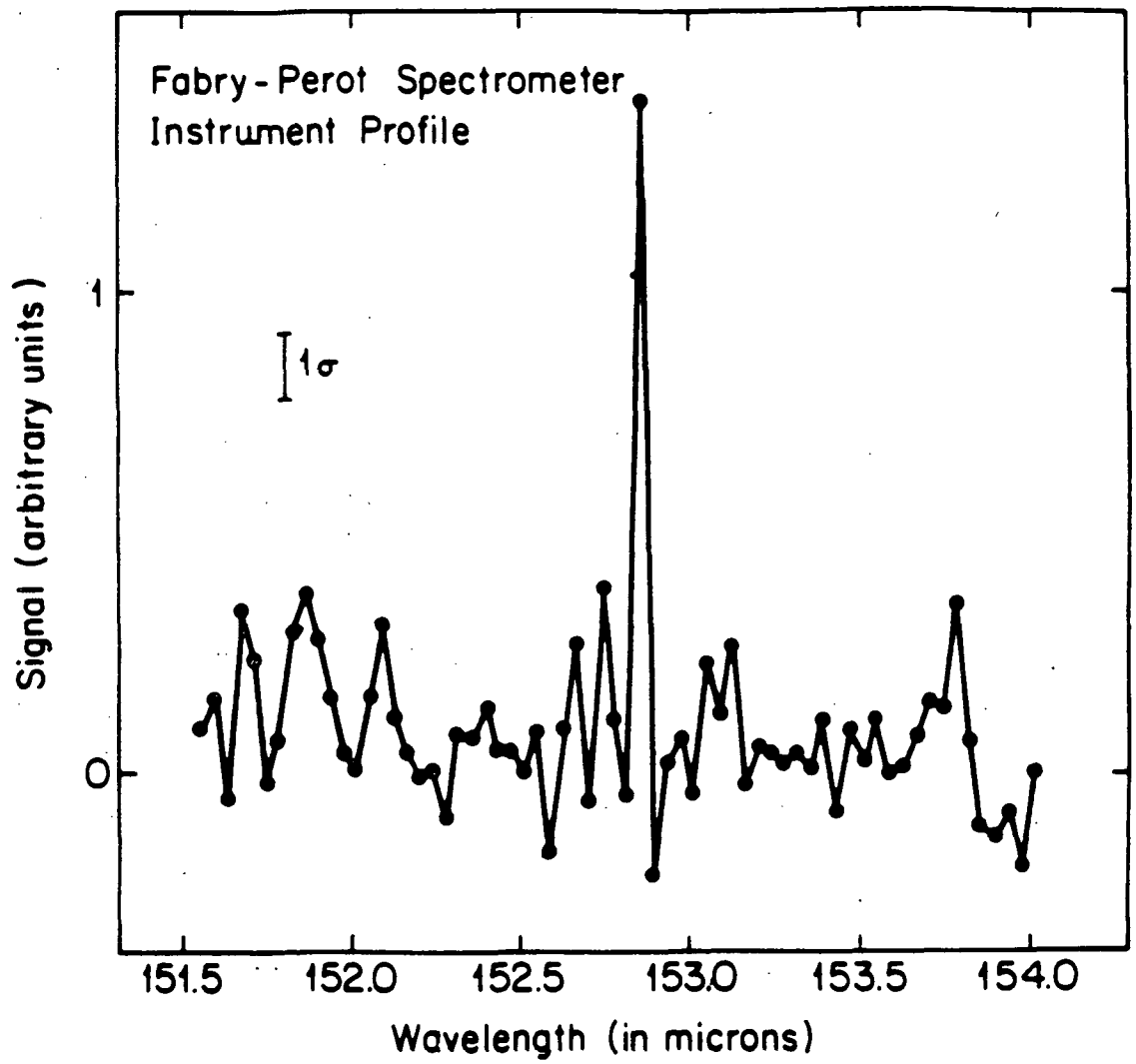

FIGURE 3.11 Laboratory transmission profile of the Hinge at 153 μm. These data were obtained using the interferometer to determine the instrument profile of the Hinge. The instrumental resolution of the interferometer was about 4000. Clearly, the Hinge's bandpass is narrower than what the interferometer can measure.

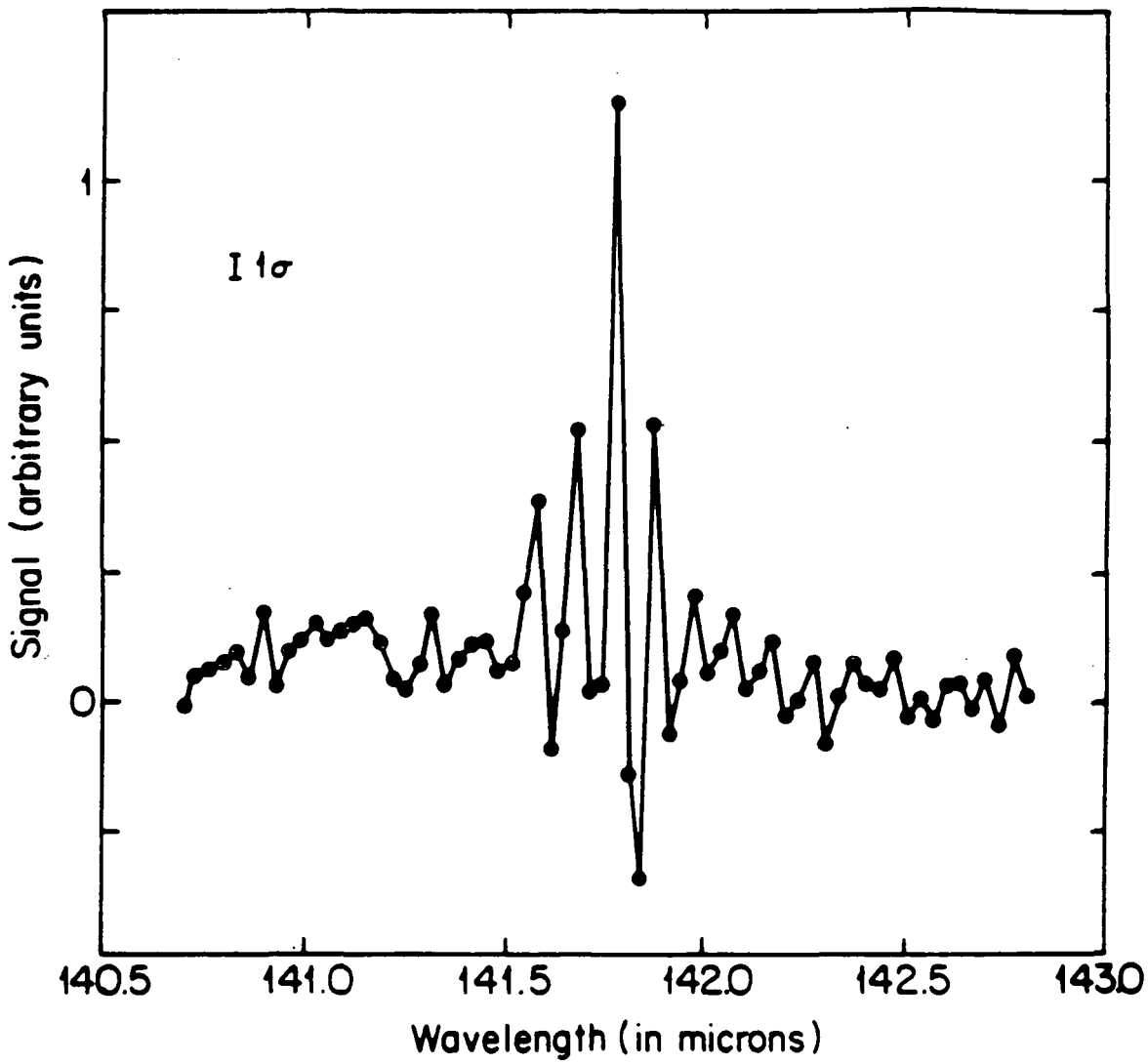

FIGURE 3.12 Laboratory transmission profile of the Hinge at 142 μm. These data were obtained in the same manner as the 153 μm data in figure 3.11. Note the sidelobe structure.

of the leak is most likely radiation that is bouncing off of one of the mesh/grating holder apertures and hitting the grating at a somewhat shallower angle.

In order to determine the actual resolution, it is necessary to have a source of narrow line emission or absorption. This is accomplished by placing a cell of CO gas in the beam. There is a transition from the $J = 16 \rightarrow 17$ rotational levels of CO at 153.2667 μm. This transition would be seen in absorption. By stepping the grating, it is possible to sweep the instrumental profile along this narrow absorption line and determine the transmission profile.

The Hinge can be stepped in bursts of 3.9×10^4 μm. This was determined using the interferometer to calibrate the Hinge from 140 μm to past 153 μm. By determining the halfwidth of the absorption feature, we can determine the resolution.

Figure 3.13 is the result of this endeavor. The data were fitted by a Gaussian (although a Lorentzian should be the true shape). The FWHM is found to be 0.00716 μm, or the resolution is 21400. This is also consistent with a mesh reflectivity of 85%, if the grating efficiency is 93%. This is most likely the case.

Since the pressure in the cell was close to atmospheric at the time, it is quite possible that the actual resolution of the system is better. The cell we were using had a slow leak, and in order to integrate for the length of time we needed for a good signal-to-noise ratio, it was easiest to simply keep the cell at ambient pressure. Due to this, the CO line may be pressure broadened. Owing to a lack of data on the collision rate of N_2–CO for this transition, it is not possible to accurately calculate the pressure broadening. Estimates of the N_2–CO collision rates from tabulated He–CO collision rates yield a pressure broadening width which is over a factor of 10 larger than that observed.

3.9 Summary

We have demonstrated that the Hinge is a viable instrument capable of producing high resolution ($R \approx 21000$) spectral observations in the FIR. The instrument is compact, highly rugged, and reliable. We have cooled it down several times, realigning the optics each time, and have found similar results with every cooldown. The Hinge is also stable in the sense that the grating may be tuned to within 1/3

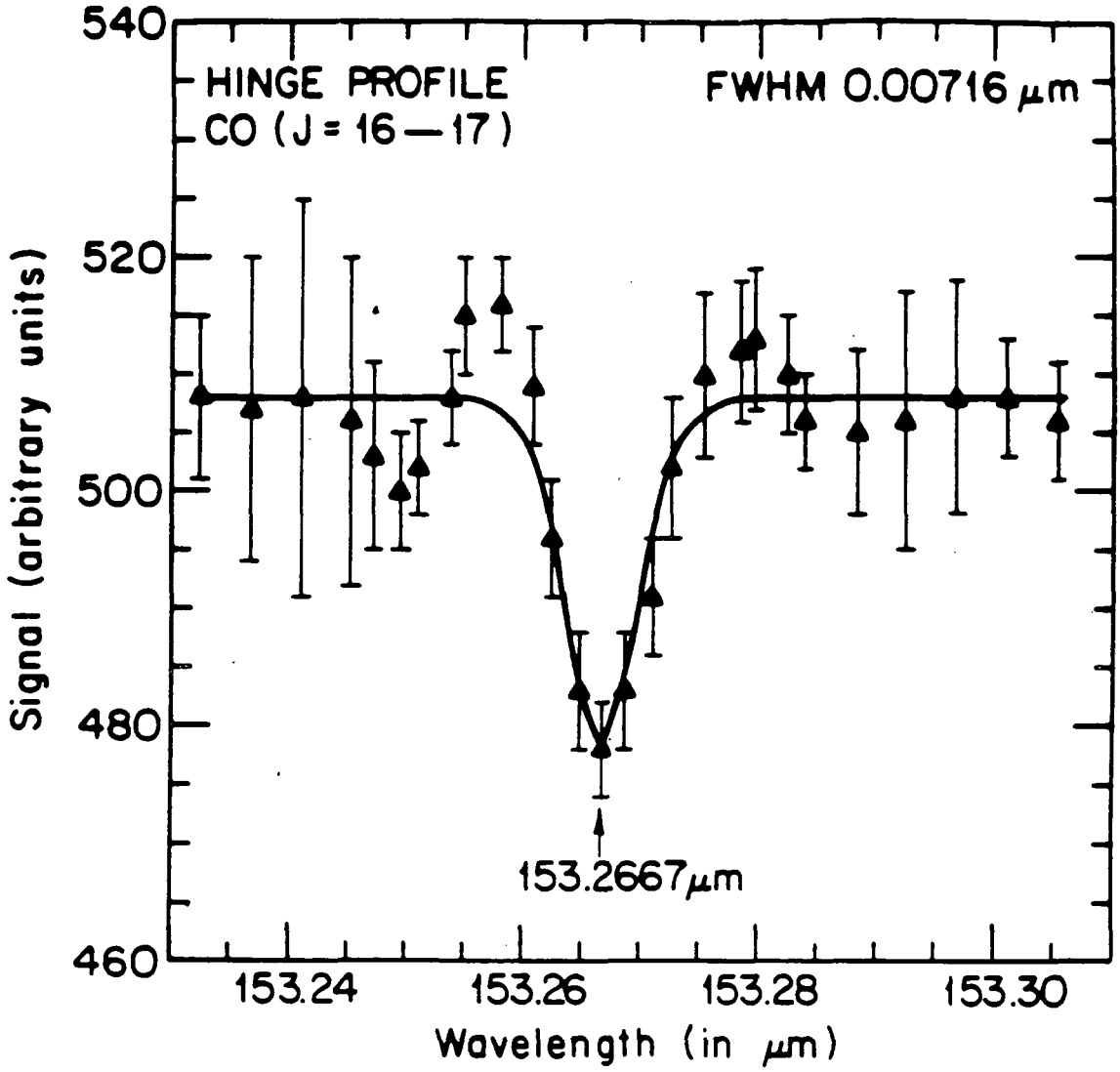

FIGURE 3.13 Laboratory transmission profile of the Hinge at 153 μm. These data were obtained by observing a narrow absorption feature due to CO and sweeping the grating of the Hinge through the feature. Assuming that the absorption line is not significantly pressure broadened, teh resolution of the Hinge is roughly 21500. The solid line is a profile fit to the data.

to 1/2 of a resolution element.

An instrument such as this is very attractive for use in space missions where a Fabry-Perot spectrometer can be used. This instrument is very simple in that it has only one moving part. That part is a grating and the motion is a simple rotation. There are no needless complexities that are associated with regular FPS systems where the movable plate must be kept parallel to the fixed plate.

The sidelobe rejection is adequate in the Hinge, and rivals that found in other FIR FPS systems. With this instrument, FIR emission and absorption lines can be resolved, line profiles can be determined, and a greater understanding of FIR sources can be achieved.

IV. Molecular Rotational Lines and Radiative Transfer

4.1 Introduction

Within many astronomical systems, molecules are present, sometimes in great abundance. They are remarkably durable and exist in environments which are not conducive to either their formation or survival (Dalgarno 1985a). Owing to their complex energy level structure, they serve as excellent probes of the physical conditions that exist within regions in which they are found. Molecular emission or absorption lines have been detected from the interstellar gas in external galaxies and from molecular clouds in our own Galaxy. These observations have helped in the understanding of these sources. Other areas of astronomical study which have benefited from molecular spectroscopy include masers, circumstellar shells, protostars, H II regions, planetary nebulae, Herbig-Haro objects, sun spots, comets, and planetary atmospheres. We are beginning to gain a much fuller overview of star formation regions, stellar mass loss, galactic structure, and planetary atmosphere dynamics from these observations.

The most abundant molecule almost certainly is H_2. Most of this cannot be directly observed, and it is only through other molecular studies (mainly CO) that an estimate of the H_2 abundance is known. From this, one concludes that molecular hydrogen makes up 10–20% of the mass of the inner disk of the Galaxy (Shull and Beckwith 1982) and is probably responsible for 50% of the hydrogen gas content beyond the solar orbit (Li, Riley, and Wolfendale 1983).

Other molecules which have been found in abundance include CO, OH, CN, CS, HCN, HCO, and NH_3, to name a few. As of 1984, 64 molecules and 46 isotopic variants had been observed in a host of sources. These range from the simplest diatomics to cyanodecapentayne ($HC_{11}N$) (Rydbeck and Hjamlarson 1985). The universe is rich in molecular chemistry.

Different transitions, which occur in different parts of the electromagnetic

spectrum (ranging from the ultraviolet to radio), will eminate from different parts of the region in which the molecules are found. The molecules serve an ancillary role as probes. Often, they will control the structures, both thermal and ionization, of the systems in which they are found. Their presence can dramatically alter the dynamical instabilities, and hence the evolution, of these systems.

In this thesis, we will be mainly concerned with the shocked region of the Orion Molecular Cloud (OMC-1) surrounding the Becklin-Neugebauer object and the Kleinmann-Low nebula (BN/KL). The shocked region is most likely a result of a massive stellar wind from very young stars plowing into the surrounding molecular cloud. The gas in the shock is hot ($\sim$ 1000 K) resulting in significant populations for the higher rotational levels of molecules such as CO and OH. Next to H_2, these molecules are some of the most abundant in the region.

The major portion of the radiation from these molecules will result from rotational transitions in the FIR. The millimetric lines are suppressed owing to the small values for the spontaneous transition coefficients, and the mid- and near-infrared lines are suppressed owing to the small level populations. For CO, the peak intensity occurs for J$\sim$15, which is near 160 μm (McKee et al. 1982). Theoretical studies of the shocked region in Orion suggest that CO emission should be significant for a wide range of J values, probing a temperature range of a few degrees Kelvin to a few thousand degrees Kelvin (Draine and Roberge 1984; Chernoff, Hollenbach, and McKee 1982; Draine and Roberge 1982). The FIR observations of CO and other molecules can enhance our understanding of these shocked regions.

By observing many rotational emission lines of CO and OH, it is possible to piece together a fairly constrained model of the emitting region. Since different lines probe different parts of the shocked region, our understanding of the area's overall structure can be greatly enhanced. It is our goal here to undertake this task. A significant part of the groundwork for the understanding of the CO emission lines has been laid down by Draine and Roberge (1984); Chernoff, Hollenbach, and McKee (1982); Draine and Roberge (1982); McKee et al. (1982); and Watson (1982). Not until in the past several years have enough OH lines been measured to facilitate an analysis similar to that tried with the CO line intensities.

4.2 Molecular Physics

4.2.1 Theory and Nomenclature

Since this thesis deals primarily with CO and OH, we shall limit ourselves to the physics of diatomic molecules alone. Interested readers may refer to Herzberg (1945) and Townes and Schawlow (1975) for more information concerning polyatomic molecules. We shall generally follow Herzberg (1950) for the discussion of diatomic molecules.

For a diatomic molecule, we first consider the case of a rigid rotator consisting of two masses, m_1 and m_2, separated by a distance r. Let us assume for the moment that the molecule is spinning about an axis perpendicular to the internuclear (figure) axis. The moment of inertia is given by

$$I_{\rm B} = \mu r^2 \,, \tag{4.1}$$

where μ is the reduced mass of the system. The rotational energy is then written as

$$E = \frac{1}{2} I_{\rm B} \omega^2 \,, \tag{4.2}$$

where ω is the angular velocity of rotation. Eigenstates of the Schrödinger equation exist for

$$E = \frac{h^2 J(J+1)}{8\pi^2 I_{\rm B}} \,, \tag{4.3}$$

where J is a positive integer. The total angular momentum, excluding spin, can be written as

$$|\mathbf{J}| = \sqrt{J(J+1)}\frac{h}{2\pi} \,. \tag{4.4}$$

Equation (4.3) can be rewritten as

$$E = B\, J(J+1)\ {\rm cm}^{-1} \,, \tag{4.5}$$

where

$$B = \frac{h}{8\pi^2 c\, I_{\rm B}} \,. \tag{4.6}$$

B is known as the rotational constant.

In general, the total angular momentum of a rotator is not necessarily perpendicular to the figure axis since the electrons will contribute to a nonzero moment of inertia about the line joining the nuclei. This moment of inertia is known as I_{A}. In most cases, I_{A} is much smaller than I_{B}. However, the corresponding angular momenta are nearly the same because the electrons orbit the nuclei at higher frequency.

The component of **J** that is parallel to the figure axis is called **Λ**. This is a measure of the electronic angular momentum, and as such, we have

$$|\mathbf{\Lambda}| = \Lambda \frac{\mathrm{h}}{2\pi} \ . \tag{4.7}$$

Here, Λ is the angular momentum quantum number of the electrons about the figure axis. If we let **L** be the total electronic orbital angular momentum, then one can show that the component of **L** about the figure axis is a constant of the motion. **L** will precess about this axis with a constant component $M_{\mathrm{L}}(h/2\pi)$, where

$$M_{\mathrm{L}} = L, L-1, \cdots, -L \ . \tag{4.8}$$

Hence, from (4.7) and the above discussion, we have

$$\Lambda = |M_{\mathrm{L}}| \ . \tag{4.9}$$

The values of Λ can range from $0, 1, 2, \cdots, L$. For $\Lambda = 0, 1, 2, 3, \cdots$, the corresponding molecular states are designated as $\Sigma, \Pi, \Delta, \Phi, \cdots$, quite analogous to the atomic spectral nomenclature.

Likewise, the component of **J** that is perpendicular to the figure axis is designated **N**. It represents the rotation of the nuclei. Figure 4.1 shows a vector diagram of the diatomic molecule and the various momentum vectors. As can be seen, the direction of **Λ** can be in one of two senses. For a given **N**, there are two modes of motion of the system corresponding to the two directions of **Λ** for each value of J. This double degeneracy is evident from (4.9), where for a non-zero Λ, M_{L} may have two values, Λ and $-\Lambda$.

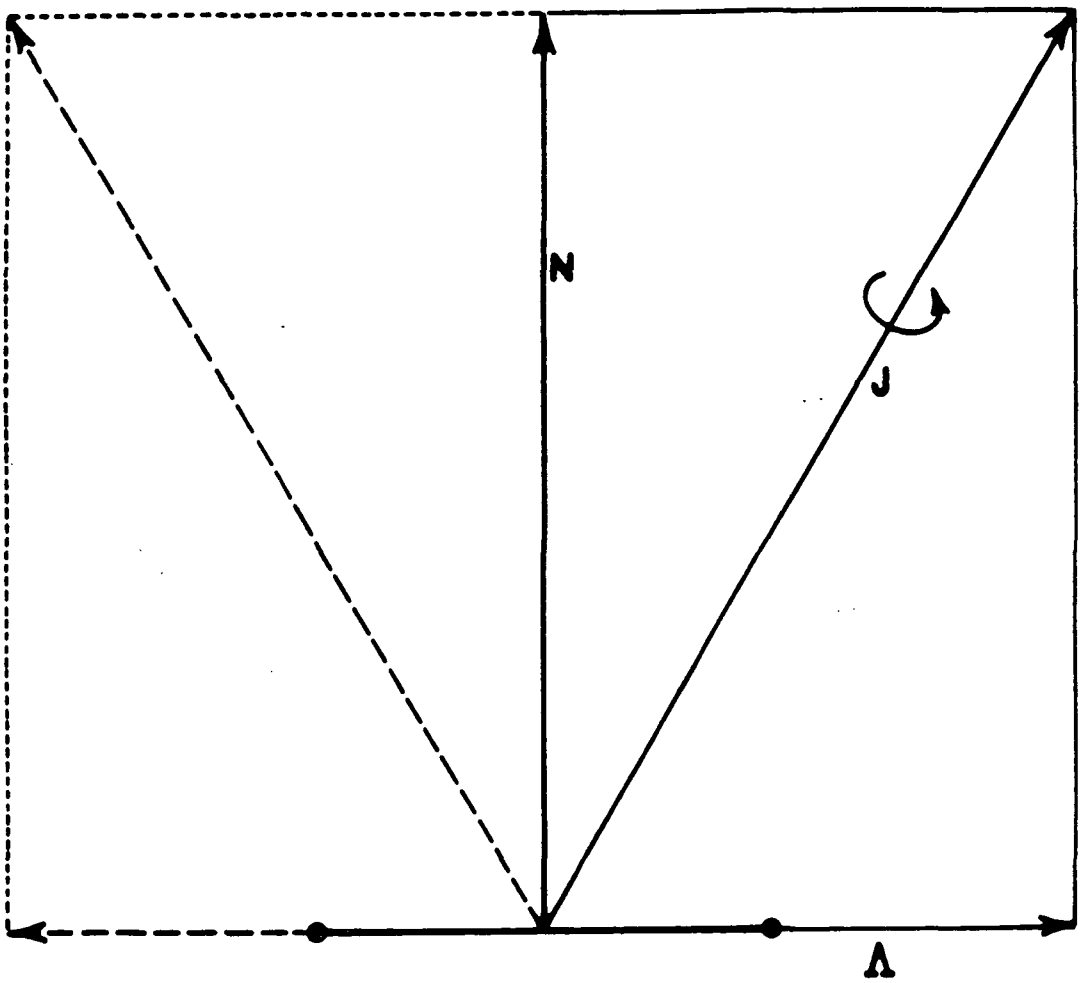

FIGURE 4.1 Vector diagram for the rigid rotor. The actual rotation is around J and is depicted by the curved arrow. N is the component of the rotation about an axis perpendicular to the intermolecular axis while Λ is that component about the intermolecular axis. After Herzberg (1950).

We can treat the electronic spin similarly. The component of the spin in the direction of the internuclear axis is given by Σ. If the resulting total spin is S, then

$$\Sigma = S, S-1, \cdots, -S \ . \tag{4.10}$$

As opposed to Λ, Σ can be either positive or negative.

The total angular momentum along the internuclear axis is obtained by adding Λ and Σ. Since both of these vectors lie along the same axis, we only need to add algebraically. The sum is given by

$$\Omega = |\Lambda + \Sigma| \ . \tag{4.11}$$

The multiplicity of the state is given by $2S+1$. Hence, as in atomic nomenclature, the multiplicity is written as a superscript to the left of the molecular state designation and $(\Lambda + \Sigma)$ is a subscript to the right. For example, if $\Lambda = 2$ and $S = 1$, then the possible states are ${}^3\Delta_3, {}^3\Delta_2, or {}^3\Delta_1$.

The symmetry parity of the rotational states depends on the value of Λ. For $\Lambda = 0$, the even J levels have positive parity, or the eigenfunctions do not change under an inversion. The odd J levels have negative parity. If $\Lambda \neq 0$, then each rotational level is doubly degenerate, one eigenfunction being positive, the other negative. The selection rule for transitions associated with dipole radiation is this: transitions between like parity states are forbidden.

When we include spin in the coupling mechanisms, we find that J becomes a resultant of the molecular rotation and the total electronic angular momentum. Hence, we may write

$$J = \Omega, \Omega+1, \Omega+2, \ldots \ . \tag{4.12}$$

With a rotation of the molecule, the states that are doubly degenerate owing to a non-zero Λ will split in energy. This splitting is known as Λ-doubling.

One can also observe hyperfine structure, produced by nuclear spin, in the rotational spectrum of diatomic molecules. If we let T be the total nuclear spin, then the resulting quantum numbers are

$$F = J+T, J+T-1, \ldots, |J-T| \ . \tag{4.13}$$

The coupling strength between different angular momenta and rotations is dependent upon the molecule in question and how fast it is rotating. For this reason, the above analysis does not always hold. There are five major cases, known as Hund's cases (a) through (e), whereby different couplings hold for each case. We have followed Hund's case (a), which describes fairly well the OH molecule.

4.2.2 Non-rigid Rotors and Rotation Constants

So far, we have been treating diatomic molecules as rigid rotators. This is, however, only an approximation. We know that molecules also display vibrational spectra, which means that the distance between the two atoms can change.

If one considers the diatomic molecule to consist of two masses connected by a stiff spring, one sees that for faster rotation, the two masses will be pulled further apart and the moment of inertia, I_B, will increase, decreasing the rotational energy.

To accurately fit the rotational spectra of diatomic molecules, we write the energy of a level as a sum of the vibrational contribution (which is a function of the vibrational quantum number, v) and the rotational contribution (a function of J). Then we can expand in the appropriate variables to find (Mantz et al. 1975; Herzberg 1950)

$$\begin{aligned} E = {} & \omega_e(v+\frac{1}{2}) - \omega_e x_e(v+\frac{1}{2})^2 + \omega_e y_e(v+\frac{1}{2})^3 - \cdots \\ & + J(J+1)[B_e - \alpha_e(v+\frac{1}{2}) + \gamma_e(v+\frac{1}{2})^2 - \delta_e(v+\frac{1}{2})^3 + \cdots] \\ & + J^2(J+1)^2[D_e - \beta_e(v+\frac{1}{2}) + \pi_e(v+\frac{1}{2})^2 - \cdots] \\ & + J^3(J+1)^3[H_e - \eta_e(v+\frac{1}{2}) + \cdots] + J^4(J+1)^4[L_e - \cdots] , \end{aligned} \quad (4.14)$$

where the subscript 'e' refers to the equilibrium values. The different variables are defined in the standard references on molecular spectra and won't be redefined here. Terms in the top line represent the vibrational contribution. The other terms represent the contributions from the rotation of the molecule. This equation may

also be rewritten as (Townes and Schawlow 1975)

$$E = \sum_{l,j} Y_{l,j} \left(v + \frac{1}{2}\right)^l J^j (J+1)^j \ , \tag{4.15}$$

where the summation is carried out from 1 to infinity over j and l. The coefficients, $Y_{l,j}$, are known as Dunham coefficients. In practice, only the lower Dunham coefficients are necessary. Either set of coefficients may be experimentally determined and used to calculate energy levels and transition frequencies.

For further information on the physics of molecular spectra, see Herzberg (1950) and Townes and Schawlow (1975).

4.2.3 Selection Rules and Einstein A Coefficients

A molecule cannot undergo an arbitrary radiative transition from one level to another. As for atoms, there are allowed and forbidden transitions for dipole radiation. The selection rules for the allowed transitions are given as follows:

$$\Delta J = 0, \pm 1$$

$$\Delta F = 0, \pm 1$$

$$\Delta v = 0, \pm 1$$

$$\Delta \Lambda = 0, \pm 1$$

$$- \rightarrow + \ , \ + \rightarrow - \tag{4.16}$$

The transition probability is represented by the Einstein A coefficient, which gives the lifetime of an atom or molecule in the excited state before it decays to a specific lower energy state. It is well known that the transition probability of spontaneous emission is

$$A_{nm} = \frac{64\pi^4 \nu_{nm}^3}{3h} |R^{nm}|^2 \ , \tag{4.17}$$

where ν_{nm} is the energy difference between levels n and m in wavenumbers, and $\mathbf{R}^{nm}$ is the dipole matrix element. If $\Delta J = -1$, the transition to a lower energy level occurs by changing J by 1; and Townes and Schawlow (1975) show that

$$|\mathbf{R}^{nm}|^2 = \mu^2 \frac{J+1}{2J+3} , \tag{4.18}$$

where μ is the permanent dipole moment of the molecule. This dipole moment depends, to some extent, on the molecular state (Σ, Π, etc.). For the most part, we shall only be concerned with rotational levels within the ground vibrational state of the ground electronic state. The energy differences between rotational states is on the order of a few meV; between vibrational states, ~1 eV; and between different electronic states, several to several tens of electron volts. For the temperatures with which we shall be dealing, the molecules are, in general, in their ground vibrational and electronic states.

4.3 The Molecules

4.3.1 CO

The major thrust of this work is to understand the physical conditions in the shock region of OMC-1 that is the source of CO and OH emission from highly excited rotational states. This is done by collecting data on a number of different transitions and then using radiative transfer to determine temperatures and densities. In order to do this, we shall anticipate the transport theory and present here the sources of the molecular data necessary to determine such quantities as level energies, spontaneous transition probabilities, collisional cross-sections, etc.

The CO molecule has a straightforward rotational spectrum structure. The ground molecular state is a $^1\Sigma$, with $\Lambda = 0$ and $S = 0$. This means that J is identical to the nuclear angular momentum, N. Figure 4.2 shows an energy level diagram for the $^1\Sigma$ ($v = 0$) rotational lines. The values for the energies were derived from the rotational and Dunham coefficient data of Mantz et al. (1975) and Todd et al. (1976).

To find the Einstein A coefficient, we may use the results of (4.5), (4.17),

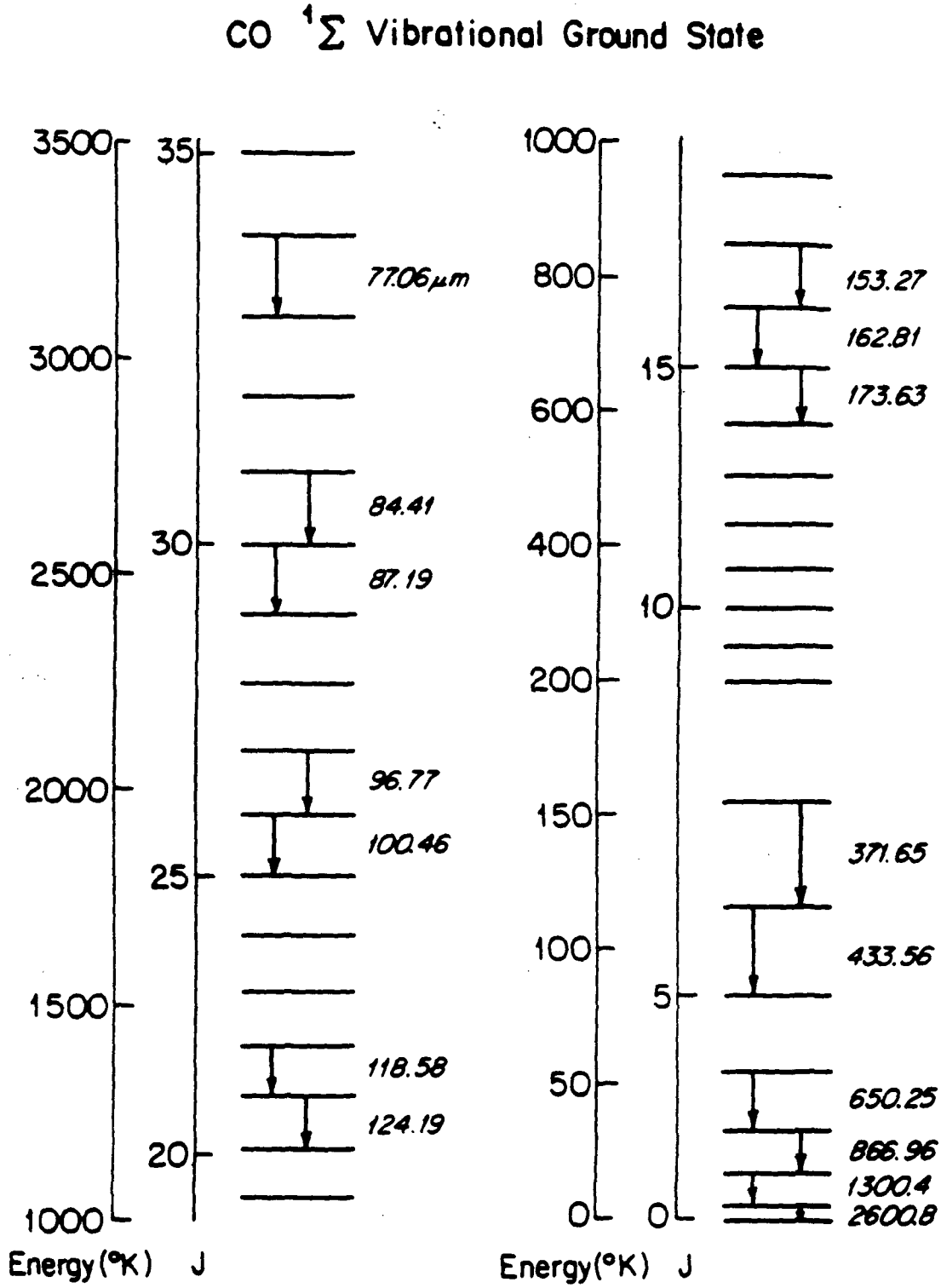

FIGURE 4.2 Rotational energy level diagram for CO in its ground electronic and vibrational states. Transitions which have been observed in OMC-1 are indicated by arrows along with their respective wavelengths in microns.

and (4.18). Equation (4.5) is a good approximation for finding the energy levels. Combining all of these, we find that the spontaneous emission rate is

$$A_{J\rightarrow J-1} = \frac{512\pi^4}{3h^4c^3} B^3 \mu^2 \frac{J^4}{2J+1} \, \mathrm{s}^{-1} \, , \tag{4.19}$$

for B in units of ergs. If J is large, (4.19) may be approximated by

$$A_{J\rightarrow J-1} = A_0 J^3 \, , \tag{4.20}$$

where A_0 is found to be $1.118 \times 10^{-7}\,\mathrm{s}^{-1}$. The dipole moment of CO is 0.112 debye (D) (Muenter 1975).

Transitions among levels can take place not only radiatively, but through collisional processes as well. In the interstellar medium, most collisions are with H_2, the most abundant constituent. Collisional excitation rates for CO by H_2 have been calculated by Green and Chapman (1978) and McKee et al. (1982). Since the potential energy surface (PES) was not known very well at that time, these rates were extrapolated from He–CO collision rates, being multiplied by a factor dependent on the velocity difference between H_2 and He. Green and Thaddeus (1976) argue that scaling by the velocity ratio works for H_2, but only when the potential surface is roughly spherical. This describes para-H_2 (even j values), but it is possible that ortho-H_2 (odd j values) may be abundant as well, and then the scaling arguments lose ground. However, owing to the small dipole moment of CO, the difference between ortho- and para-H_2 may be small. Recently, Flower and Launay (1985) have calculated para-H_2–CO collision rates which tend to agree with those of Green and Thaddeus (1976). Schinke et al. (1985) have recently incorporated a more accurate H_2–CO PES in calculating the collision rates. Their rates differ significantly from those of McKee's group for the large ΔJ transitions. Experimental results at low temperatures would be very useful. It should also be noted that most of the calculations are for temperatures of 300 K or less. This is not always the case, especially in the shocked regions where H_2 vibrational spectra indicate $T \sim 10^3$ K.

4.3.2 OH

The ground electronic state of OH is a $^2\Pi$ state, where $\Lambda = 1$ and $S = 1/2$. Ω can take on two values, 1/2 or 3/2. This leads to a splitting of the levels into two ladders, one for $\Omega = 1/2$ and the other for $\Omega = 3/2$. Figure 4.3 is a schematic of these two ladders, showing the Λ-doubling due to the parity. The hyperfine levels within each parity level are not shown.

The Einstein A coefficients for the various Λ-doubling transitions within a rotational level have been calculated by Destombes et al. (1977). Brown et al. (1982) have published similar data for the various rotational transitions including hyperfine structure. The energy levels of OH found by Brown's group are more reliable since they were measured by laser magnetic resonance. The transition probabilities are consistent between the two groups.

Collisional excitation rates for H_2–OH interactions have not, until recently, been known very well. Dewangan and Flower (1981, 1983) made an improved calculation over that of Bertojo, Cheung, and Townes (1976); however, recent experimental results (Andresen, Häusler, and Lülf 1984) suggest that the theoretically expected cross-sections are significantly in error. Schinke and Andresen (1984) have recently performed another set of calculations for H_2–OH collisional excitation, and their results match the trends in level populations observed experimentally. The actual values of the theoretical cross-sections, however, still do not agree entirely with experimental results. Again, these results assume that the hydrogen is in a para state.

4.4 The Chemistry and Physics of Shocks

In this section, we will discuss some of the physical and chemical properties of shocks. The treatment of shocks includes some very complex and often little-understood areas of study, and it is not within the framework of this thesis to discuss these in depth. We do wish to provide a general overview of shocks in the interstellar medium as they are understood today. This will follow the outline of Dalgarno (1985b).

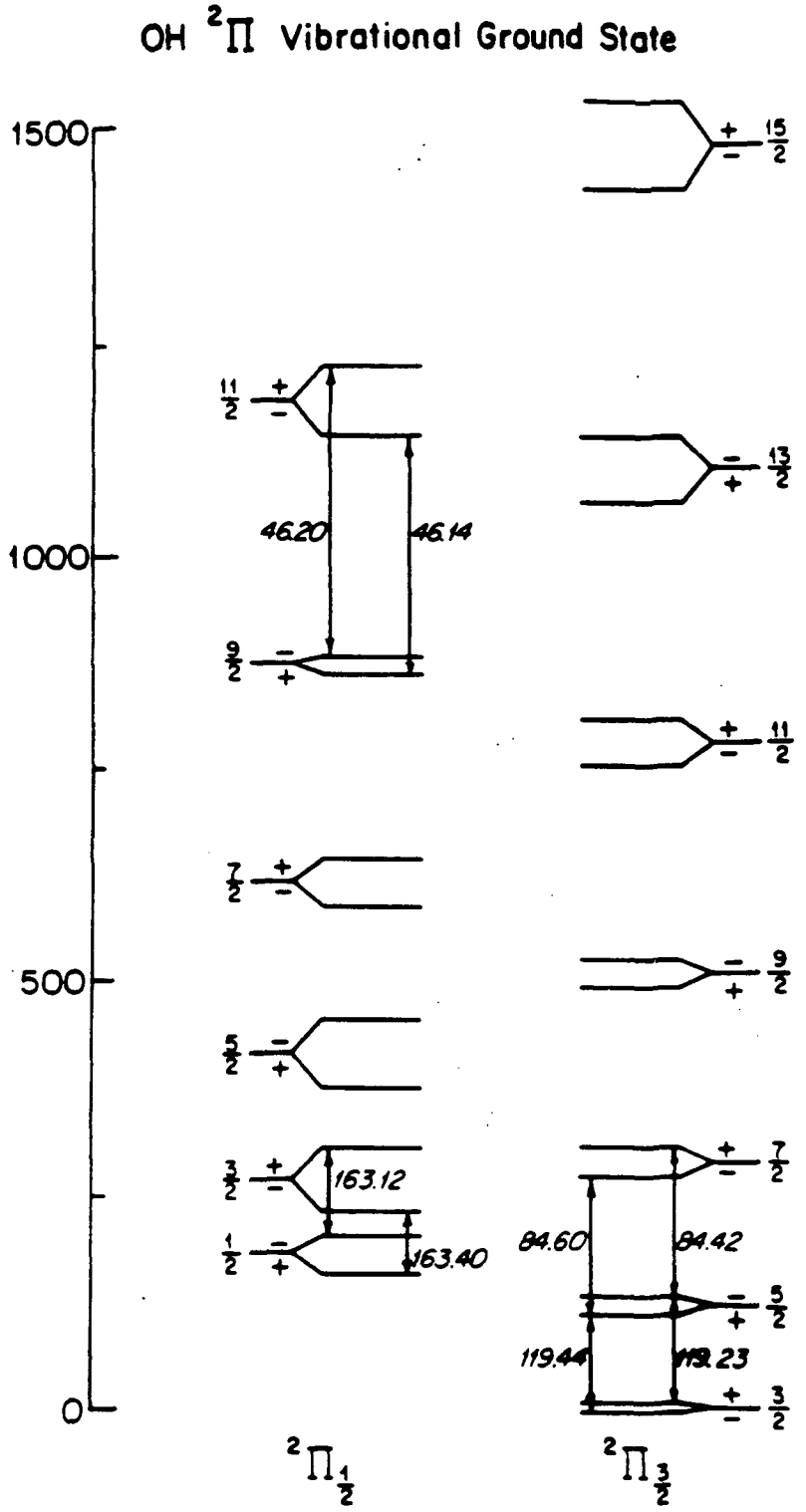

FIGURE 4.3 Rotational energy level diagram of OH in its ground electronic and vibrational states. Transitions which have been observed in OMC-1 are indicated by arrows along with their respective wavelengths in microns.

The first question that must be addressed is the definition of a shock. A shock consists of a supersonic propagation of a disturbance in a fluid medium, usually a gas. Since the information concerning the disturbance cannot propagate upstream faster than the local speed of sound, the medium cannot anticipate and react to the disturbance until the shock actually arrives. Upon the arrival of the shock, the gas is compressed and heated. The boundary layer separating the upstream gas from the hot, compressed, shocked gas is known as the shock front.

Shocked regions are associated with many different astronomical phenomena. They are most commonly linked to stars. In stellar formation processes, strong winds driven by mass loss and radiation pressure, will plow into the ambient parent gas cloud and cause a shock wave to form. Massive stars will continue to feed the shock wave throughout most of their lives via radiation pressure or stellar winds. Cataclysmic stellar deaths (supernovae) will produce enormous mass losses which also result in shock waves. Collisions of interstellar clouds are yet another source for shocks.

Various factors affect the physics of the shock. The shocked material will be compressed and heated. This heating can result in dissociation and ionization, whereupon recombination will produce photons capable of ionizing and dissociating the upstream material. This will change the nature of the shock as it progresses through the cloud medium. Magnetic fields complicate further the shock physics. Magnetohydrodynamic (MHD) considerations suggest that magnetic precursors can preceed the shock and compress the material before the shock arrives.

Much of the kinetic energy in the shock front is transformed into thermal energy. It is very simple to roughly determine the temperature, T_s, of the shocked region for a shock velocity, v_s, by equating the kinetic energy to the random thermal energy. For atomic hydrogen, this results in

$$T_s \approx 40\, v_s^2 \text{ K} , \tag{4.21}$$

where v_s is measured in km s^{-1}. If the shock is slow, the temperature will rise, but not enough to actually cause much dissociation. Instead, the gas will become warm and the chemical composition will evolve. For fast shocks, dissociation and

ionization will result, with new molecular populations being born out of the cooling downstream gas.

The shock regions are sites of complex chemical and physical interactions. Dissociation is collisionally induced, but how fast molecular dissociation progresses depends upon density and radiative transfer. For low density clouds, a shock velocity of about 50 km s^{-1} will result in dissociating 90% of the H_2. Since atomic hydrogen reacts very efficiently with CO to produce C and O, CO dissociates at $v_s \approx 40\,\mathrm{km\ s^{-1}}$. Higher densities decrease the radiative stabilization of molecular hydrogen by increasing the probability of collisionally dissociating a molecule in a vibrationally excited state, resulting in nearly complete dissociation at shock velocities of 25 km s^{-1}. At this velocity, the CO will have a better chance of surviving owing to the lower shock temperature. When magnetic fields are present, the hydrogen may not dissociate until velocities on the order of 45 km s^{-1} are reached (Draine, Roberge, and Dalgarno 1983).

The chemistry of the shocked region is governed mainly by reactions with atomic and molecular hydrogen. Prasad and Huntress (1980) have listed over 1400 reactions among 137 species. Improved reaction rates and overlooked reactions have been listed by Mitchell (1984) and references within for 113 chemical species.

Once the shock has passed, the temperature of the region is raised and chemical reactions begin. These reactions, and the abundances of the resulting products, depend to a large extent on the physical parameters of the region, such as temperature and density. The gas is primarily cooled by fine-structure transitions of O I and the rotational and vibrational lines of H_2, CO, OH, and H_2O. Hence, the thermal and chemical structures are interdependent.

A schematic of the oxygen and carbon chemical reaction families is presented in figure 4.4. In brief, the oxygen will tend to combine with carbon to form CO or else with hydrogen to ultimately form H_2O. Small amounts of O and OH will also be present, with OH enhancement present near the shock front (Draine and Roberge 1982). For more details on the chemistry and physics of shock regions, see Dalgarno (1985b); Draine (1985); Mitchell (1984); Draine, Roberge, and Dalgarno (1983); Chernoff, Hollenbach, and McKee (1982); Draine and Roberge (1982, 1984);

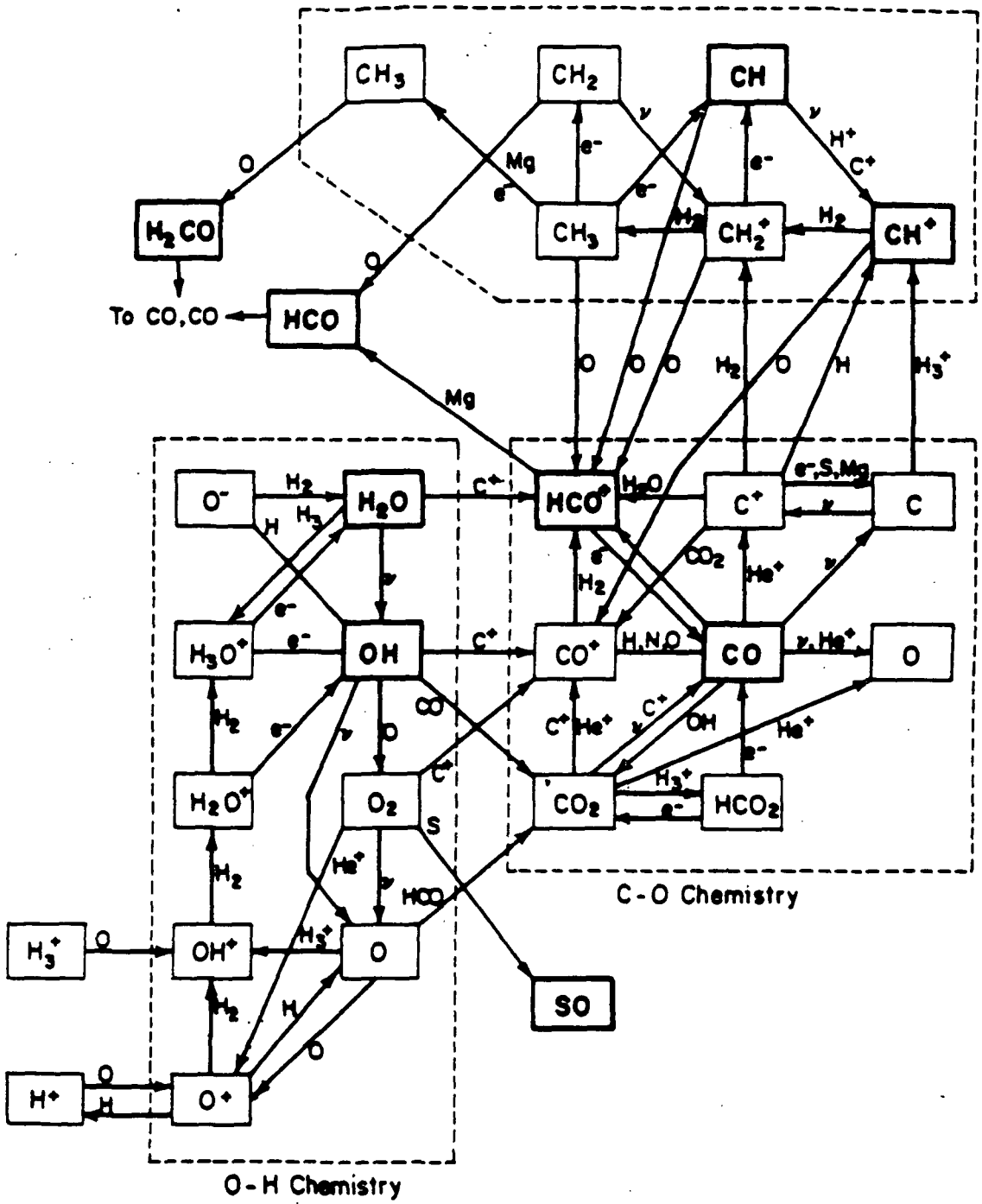

FIGURE 4.4 A schematic diagram of the carbon and oxygen chemistry that is believed to occur in star formation regions and molecular clouds. After Prasad and Huntress (1980).

Prasad and Huntress (1980); and references within.

4.5 Radiative Transfer

4.5.1 Definitions

In just about any area of astrophysics, one is dealing with the transport properties of a medium. For molecular shocks, the interaction of the radiation field with the gas is very important in determining the chemical and thermal structure of the region. This interdependence requires a knowledge of radiative transfer.

It is desirable that the terms for the description of radiation and its measurable quantities be properly defined. We will be using the terminology of Gray (1976) and Rybicki and Lightman (1979).

We begin by considering a radiating surface of area dA. The specific intensity is a measure of the amount of radiant energy, dE_ν, between ν and $d\nu$, emitted at an angle, θ, from the normal to the surface, and contained within a solid angle $d\Omega$ in the time interval dt. This can be written as

$$I_\nu = \frac{dE_\nu}{\cos\theta \, dA \, d\Omega \, dt \, d\nu} \, . \tag{4.22}$$

Averaging over direction, we obtain the mean intensity, J_ν, which may be written as

$$J_\nu = \frac{1}{4\pi} \int I_\nu \, d\Omega \, . \tag{4.23}$$

The integration is performed over the whole unit sphere centered on the area, dA.

The flux is defined as the net energy flow across an area dA, in a time dt, and in a spectral range $d\nu$, or

$$F_\nu = \frac{\int dE_\nu}{dA \, dt \, d\nu} \, , \tag{4.24}$$

where the integration is again performed over the unit sphere. Combining (4.22) and (4.24), we find that

$$F_\nu = \int I_\nu \cos\theta \, d\Omega \, . \tag{4.25}$$

As radiation passes through a medium, emission and absorption processes may add or subtract energy from it. The absorption of energy is characterized by an absorption coefficient, α_ν, in units of cm^{-1}. The change in the specific intensity is given by

$$dI_\nu = -\alpha_\nu I_\nu \, ds \ , \tag{4.26}$$

where ds is the length of the medium through which the radiation has traveled. If n is the number density of absorbers, and σ_ν is the cross-section of each absorber for radiation of frequency ν, then it can be easily shown that

$$\alpha_\nu = n \, \sigma_\nu \ . \tag{4.27}$$

For absorption processes, the change in the specific intensity is proportional to the intensity itself.

The emission coefficient j_ν can be defined in much the same way as the absorption coefficient. In general, j_ν is independent of the specific intensity. We may write the change in intensity as

$$dI_\nu = j_\nu \, ds \ . \tag{4.28}$$

The units of the emission coefficient are energy per unit time per unit solid angle per unit volume per unit frequency interval. There are two processes that can contribute to j_ν, either real emission or scattering.

It is quite simple to incorporate the emission and absorption into the equation of radiative transfer, which is

$$\frac{dI_\nu}{ds} = -\alpha_\nu I_\nu + j_\nu \ . \tag{4.29}$$

The absorption and emission of radiation is governed by quantum mechanical considerations. If we assume that we have a system which has two energy levels, 1 and 2, then there are three processes that were identified by Einstein that can take place. The first is that of spontaneous emission. Here, the system begins in

the higher energy level, 2, makes a transition to level 1, and in so doing, emits a photon corresponding to the energy difference. This transition occurs without outside influence, and the transition probability rate is denoted by A_{21}. The units are s^{-1}.

If the system is in level 1, then there is the chance that it can absorb a photon of the appropriate energy to boost it into level 2. The probability rate for this process must be proportional to the photon density. We can write this probability as

$$\text{probability rate} = B_{12} \int_0^\infty J_\nu \, \phi(\nu) \, d\nu \ , \tag{4.30}$$

where $\phi(\nu)$ is the line profile and B_{12} is the Einstein coefficient for absorption.

The system can interact with an external radiation field in another way, and that is via the process of stimulated emission. In this process, the system is in the excited level and a photon of appropriate energy will interact with the system so as to induce it to emit a photon and jump to the lower energy level. The probability rate is defined much like that for absorption, and the Einstein coefficient for stimulated emission is written as B_{21}.

4.5.2 Relations and Special Cases

In this section, we look in more detail at the equation of radiative transfer and several special cases.

We start by assuming that we have pure emission and no absorption. In this case, $\alpha_\nu = 0$ and the solution to (4.29) is

$$I_\nu(s) = I_\nu(s_0) + \int_{s_0}^{s} j_\nu(s') \, ds' \ , \tag{4.31}$$

where we integrate from some initial s_0 to s.

Next, we consider pure absorption without emission. In this case, $j_\nu = 0$ and the solution for the equation of radiative transfer is

$$I_\nu(s) = I_\nu(s_0) \, e^{-\tau_\nu(s)} \ , \tag{4.32}$$

where

$$\tau_\nu(s) = \int_{s_0}^{s} \alpha_\nu(s')\, ds' \ . \tag{4.33}$$

The variable τ_ν is the optical depth, and it is a measure of the probability of a photon being absorbed within the medium. The greater the optical depth, the greater the chance for absorption. Typically, if the medium has an optical depth less than unity, it is considered to be transparent; whereas for optical depths of unity or greater, the medium is opaque. It should be apparent that

$$\tau_\nu = \alpha_\nu\, ds \ . \tag{4.34}$$

If we divide (4.29) by α_ν, then we have

$$\frac{dI_\nu}{d\tau_\nu} = -I_\nu + \frac{j_\nu}{\alpha_\nu} \ . \tag{4.35}$$

The ratio of the emission coefficient to the absorption coefficient is known as the source function S_ν. This allows us to rewrite (4.35) as

$$\frac{dI_\nu}{d\tau_\nu} = -I_\nu + S_\nu \ . \tag{4.36}$$

The general solution to this equation is

$$I_\nu(\tau_\nu) = I_\nu(0)\, \mathrm{e}^{-\tau_\nu} + \int_0^{\tau_\nu} \mathrm{e}^{-(\tau_\nu - \tau'_\nu)}\, S_\nu(\tau'_\nu)\, d\tau'_\nu \ . \tag{4.37}$$

We can interpret the first term on the right hand side as the initial intensity diminished by the absorption. The second term is then the integrated source diminished by absorption.

For a constant source function, the solution for (4.37) is

$$I_\nu = S_\nu + \mathrm{e}^{-\tau_\nu}\, (I_\nu(0) - S_\nu) \ . \tag{4.38}$$

We see that the intensity approaches the source function as the optical depth increases.

Rybicki and Lightman (1979) have offered a simple physical interpretation of the source function and the transfer equation. If we consider (4.36), then for $I_\nu < S_\nu$, I_ν will increase along the ray. If $I_\nu > S_\nu$, then I_ν will decrease along the ray. In either case, I_ν will tend towards S_ν. The intensity will actually become equal to the source function if the optical depth is sufficiently large.

From Kirchoff's law for thermal emission, the source function is dependent only upon the temperature of the medium, and is given by

$$S_\nu = B_\nu(T) \equiv \frac{2h\nu^3}{c^2}\left[e^{-h\nu/kT} - 1\right]^{-1} , \tag{4.39}$$

where h is Planck's constant, c is the speed of light in vacuum, k is Boltzmann's constant, and T is the temperature of the medium. From (4.38), we see that for sufficiently large optical depths, the intensity will also approach $B_\nu(T)$. This is the condition for blackbody radiation.

It is often more convenient to rewrite the equation of transfer in terms of the Einstein coefficients. Let us first consider a two level system that is in thermodynamic equilibrium at temperature T. If n_1 and n_2 represent the number density of atoms in levels 1 and 2, respectively, then the steady state solution dictates that

$$n_1 B_{12} J = n_2 A_{21} + n_2 B_{21} J . \tag{4.40}$$

Since the line profile is usually very narrow, we may approximate the integral in (4.30) as being equal to J. Solving for J, we find

$$J = \frac{A_{21}}{B_{21}}\left[\left(\frac{n_1}{n_2}\right)\left(\frac{B_{12}}{B_{21}}\right) - 1\right]^{-1} . \tag{4.41}$$

In thermodynamic equilibrium, the level population ratio is given by

$$\frac{n_1}{n_2} = \frac{g_1}{g_2} e^{h\nu_{21}/T} , \tag{4.42}$$

where $h\nu_{21}$ is the energy difference between the two levels and g_i is the degeneracy of the i^{th} level. However, in thermodynamic equilibrium, $J_\nu = B_\nu$, and hence we

see that

$$g_1 B_{12} = g_2 B_{21}$$

$$A_{21} = \frac{2h\nu_{21}^3}{c^2} B_{21} \tag{4.43}$$

From the definition of the emission coefficient, we can see that in terms of the spontaneous emission coefficient,

$$j_\nu = \frac{h\nu_{21}}{4\pi} n_2 A_{21} \phi(\nu) \ . \tag{4.44}$$

Likewise for the absorption coefficient, we may write

$$\alpha_\nu = \frac{h\nu_{21}}{4\pi} \phi(\nu)(n_1 B_{12} - n_2 B_{21}) \ . \tag{4.45}$$

It should be remembered that the stimulated emission is proportional to the intensity and is, in many respects, like negative absorption. For this reason, it is included in the absorption coefficient. Using (4.29), (4.44), and (4.45), we obtain

$$\frac{dI_\nu}{ds} = -\frac{h\nu}{4\pi}(n_1 B_{12} - n_2 B_{21})\, \phi(\nu)\, I_\nu + \frac{h\nu}{4\pi} n_2 A_{21}\, \phi(\nu) \ . \tag{4.46}$$

We can rewrite this using the optical depth and the source function. The absorption coefficient and the source function may then be rewritten as

$$\alpha_\nu = \frac{h\nu}{4\pi} \phi(\nu)\, n_1 B_{12} \left(1 - \frac{g_1 n_2}{g_2 n_1}\right)$$

$$S_\nu = \frac{n_2 A_{21}}{n_1 B_{12} - n_2 B_{21}}$$

$$= \frac{2h\nu^3}{c^2 \left(\frac{g_2 n_1}{g_1 n_2} - 1\right)^{-1}} \ . \tag{4.47}$$

4.5.3 Collisional Excitation and Multi-Level Systems

Most systems do not have just two levels, but usually many levels that must be considered. Collisional excitation and de-excitation processes also add to determine the final equilibrium level population of atomic and molecular systems. Let γ_{jk} be the collision rate coefficient for producing a transition from level j to level k. The units are $cm^3\ s^{-1}$. If n_c is the number density of the colliders, then $n_c\gamma_{jk}$ is the probability rate for a collisional transition. Let us consider the j^{th} level. In a steady state, the rate of change of n_j is zero. That is to say, the processes which contribute to increasing the j^{th} level exactly match those which contribute to decrease it. This may be written as follows:

$$\sum_{k\neq j} n_k(n_c\gamma_{kj} + B_{kj}J_{\nu_{kj}}) + \sum_{k>j} n_k A_{kj} = n_j\left[\sum_{k\neq j}(n_c\gamma_{jk} + B_{jk}J_{\nu_{kj}}) + \sum_{k<j} A_{jk}\right] . \quad (4.48)$$

The right hand side of (4.48) represents the processes which will increase the j^{th} level population. They are collisional excitation and de-excitation into the level, stimulated emission and absorption, and spontaneous emission from higher levels. The left hand side represents the debit half of the ledger, and includes the same processes; only this time depopulating the level.

The collisional rate coefficients γ_{jk} and γ_{kj} are related to each other through detailed balance. This is simply derived, and results in

$$\gamma_{jk} = \gamma_{kj}\frac{g_k}{g_j}e^{-(E_k-E_j)/kT} , \quad (4.49)$$

where E_j is the energy corresponding to the j^{th} level.

It is possible to solve (4.48) for a system that has reached a steady state if all of the collisional and Einstein coefficients are known. The level populations will then be known. Use of (4.46) and (4.47) will then enable one to solve for the intensities and fluxes that one would expect from the medium. In general, this is a non-trivial process if the number of levels is greater than 2.

4.6 Escape Probability Theory

4.6.1 Castor's Method

For regions that contain velocity gradients, the radiative transfer is complicated still further owing to doppler shifts that vary throughout the medium. If the flow velocity is much greater than the thermal width, as in the case of OMC-1, then it seems clear that a photon's chance of being absorbed diminishes quite rapidly the further it moves away from its source. Hence, the radiative transfer becomes a local problem and it is possible to treat the chance of a photon travelling out of the region as an escape probability. Much work has been done on this subject, first introduced by Sobolev (1957). We shall mainly follow the relevant papers of Castor (1970) and Goldreich and Kwan (1974).

Since the escape probability formalism was first established in order to understand spectral line formation and profiles as a result of radial flow in the atmospheres of Wolf-Rayet stars, we shall derive the relevant formalism assuming spherical geometry. The minor revisions for plane-parallel geometry will be discussed later. One should keep in mind that we will be dealing with radiative line transfer and not continuum transfer.

We begin by defining the geometry. We assume that we have an optically thick internal source of radiation which constitutes the core of the region and has a radius r_c. Owing to the spherical geometry, we need only consider radiation moving in one specific direction; viz., the z-axis. This radiation will be a function of the cylindrical coordinate, p. The geometry is shown in figure 4.5. It should be clear that $p^2 + z^2 = r^2$. We can then write the equation of transfer, (4.29), as

$$\frac{\partial I(\nu, p, z)}{\partial z} = \alpha(\nu, p, z)\Big(I(\nu, p, z) - S(r)\Big) \ . \tag{4.50}$$

The sign convention is a little different in (4.50) from that in (4.29), due to the way in which the coordinate systems are set up.

There exist two regimes for solutions. The first one is for $p > r_c$ or $z > 0$. If $p > r_c$, then the core will not contribute directly to the observed intensity if scattering is negligible. The second regime must include the contributions from the

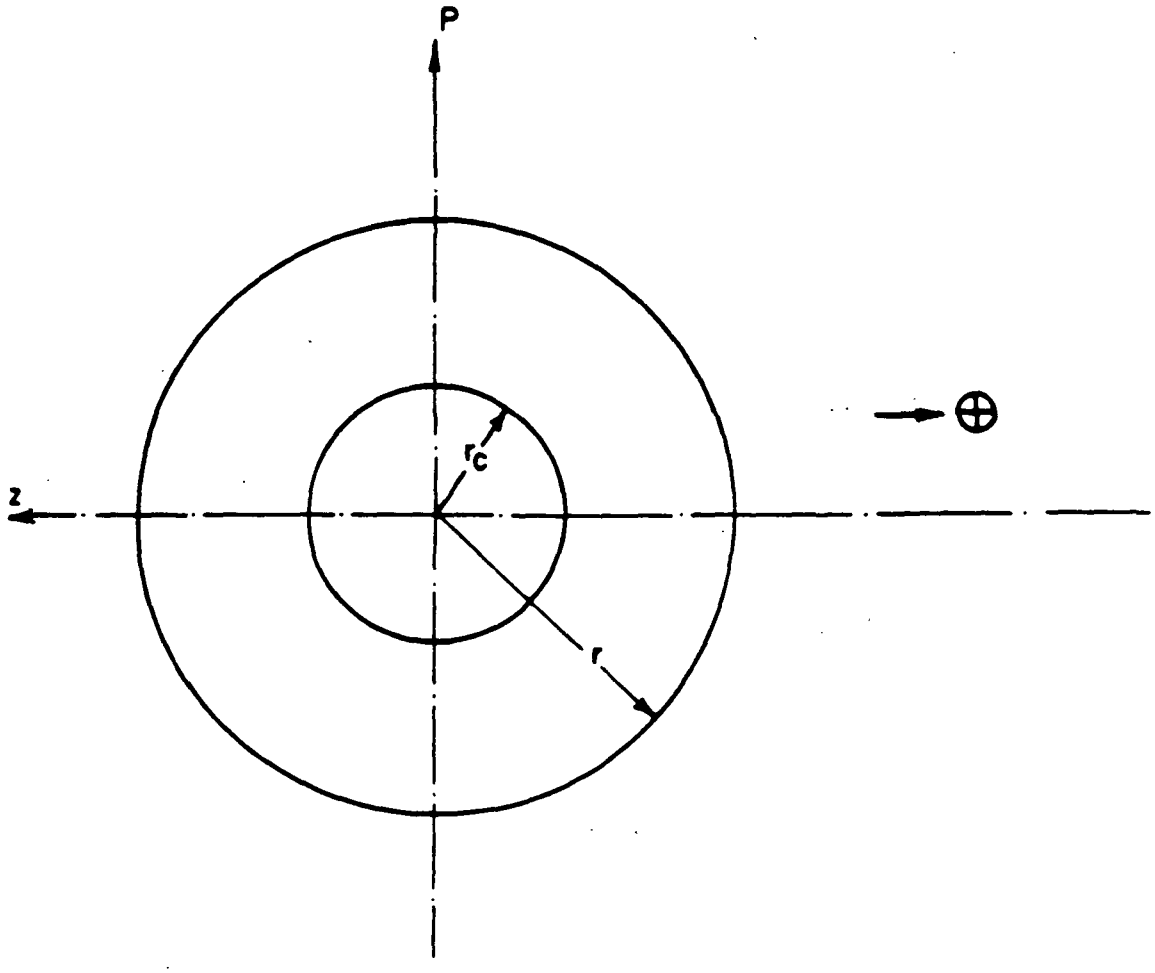

FIGURE 4.5 A schematic of the geometry used for the escape probability formalism. P and z define the coordinates, and r_c delineates the radius of the optically thick continuum core. After Castor (1970).

core. In the first regime, we find using (4.37) that

$$I(\nu,p,z) = \int_z^\infty S\Big((p^2+z'^2)^{\frac{1}{2}}\Big)\exp[\tau(\nu,p,z)-\tau(\nu,p,z')]\,d\tau(\nu,p,z') \ . \qquad (4.51)$$

If $p < r_c$ and $z < 0$, then the solution is

$$I(\nu,p,z) = \int_z^{-(r_c^2-p^2)^{\frac{1}{2}}} S\Big((p^2+z'^2)^{\frac{1}{2}}\Big)\exp[\tau(\nu,p,z)-\tau(\nu,p,z')]\,d\tau(\nu,p,z')$$

$$+ \ I_c \exp\{-[\tau\Big(\nu,p,-(r_c^2-p^2)^{\frac{1}{2}}\Big)-\tau(\nu,p,z)]\} \ , \qquad (4.52)$$

where I_c is the intensity from the optically thick core. The optical depth for a ray traveling at constant p is defined as

$$\tau(\nu,p,z) = \int_{-\infty}^z \alpha(\nu,p,z')\,dz' \ . \qquad (4.53)$$

Since we are assuming spherical symmetry, the velocity of a region is dependent only upon the distance from the center. Hence, for a line profile $\phi(\Delta\nu)$ in the rest frame, and a rest frame absorption coefficient at line center equal to $\alpha_0(r)$, we have

$$\alpha(\nu,p,z) = \alpha_0(r)\,\phi\Big(\nu+\frac{\nu_0}{c}\frac{V(r)}{r}z-\nu_0\Big) \ , \qquad (4.54)$$

where ν_0 is the frequency of the radiation at line center. Since $\phi(\Delta\nu)$ is usually a very narrow function, most of the contributions to $\alpha(\nu,p,z)$ will come from a rather small region where $\Delta\nu \approx 0$. This occurs for $z \approx z_0$, where z_0 satisfies

$$\frac{V\Big((p^2+z_0^2)^{\frac{1}{2}}\Big)}{c\,(p^2+z_0^2)^{\frac{1}{2}}}z_0 = \frac{\nu_0-\nu}{\nu_0} \ . \qquad (4.55)$$

We can then approximate the optical depth equation, (4.53), by

$$\tau(\nu,p,z) \approx \alpha_0\Big((p^2+z_0^2)^{\frac{1}{2}}\Big)\int_{-\infty}^z \phi\Big(\nu+\frac{\nu_0}{c}\frac{V(r')}{r'}z'-\nu_0\Big)\,dz' \ . \qquad (4.56)$$

Substituting x for the argument of ϕ, we can define the function y to be

$$y(x) = \int_{-\infty}^{x} \phi(x')\, dx' \ , \tag{4.57}$$

with the boundary conditions $y(-\infty) = 0$ and $y(\infty) = 1$. Substituting into equation (4.56), we find

$$\tau(\nu, p, z) = \frac{\alpha_0\left((p^2 + z_0^2)^{\frac{1}{2}}\right)}{\left(\frac{\partial}{\partial z}\right)_{p,\nu}\left(\frac{\nu_0}{c}\frac{V(r)}{r}z\right)\Big|_{z_0}} y\left(\nu + \frac{\nu_0}{c}\frac{V(r)}{r}z - \nu_0\right) = \tau(\nu, p, \infty)\, y \ . \tag{4.58}$$

Evaluating the partial derivative in (4.58) and dropping the subscript 0, we obtain for the optical depth at infinity

$$\tau(\nu, p, \infty) = \alpha_0(r)\frac{c}{\nu_0}\frac{r}{V(r)}\frac{1}{1 + \frac{z^2}{r^2}\left(\frac{d\ln V(r)}{d\ln r} - 1\right)} \ . \tag{4.59}$$

Knowing the optical depth, we can now substitute equation (4.58) into (4.51) and (4.52) to find the intensity. Due to the fact that the major contribution to the intensity will have its source in a very small range of z, we may approximate the integration to find

$$I(\nu, p, z) \approx S\left((p^2 + z_0^2)^{\frac{1}{2}}\right)\left[1 - \exp\{\tau(\nu, p, \infty)\,[y(z) - 1]\}\right] \ , \tag{4.60}$$

for $p > r_c$ *or* $z > 0$. For $p < r_c$, $z < 0$, the solution is

$$I(\nu, p, z) \approx S\left((p^2 + z_0^2)^{\frac{1}{2}}\right)\left\{1 - \exp\left\{\tau(\nu, p, \infty)\left[y(z) - y\left(-(r_c^2 - p^2)^{\frac{1}{2}}\right)\right]\right\}\right\}$$

$$+ \ I_c \exp\left\{\tau(\nu, p, \infty)\left[y(z) - y\left(-(r_c^2 - p^2)^{\frac{1}{2}}\right)\right]\right\} \ . \tag{4.61}$$

In order to evaluate (4.48), the detailed balance equation, we need to determine J, the mean intensity. This is evaluated in cylindrical coordinates by

$$J = \frac{1}{2r}\int_{-r}^{r} dz \int_0^{\infty} \phi\left(\nu + \frac{\nu_0}{c}\frac{V(r)}{r}z - \nu_0\right) I\left(\nu, (r^2 - z^2)^{\frac{1}{2}}, z\right) d\nu \ . \tag{4.62}$$

Equations (4.60) and (4.61) can then be substituted into (4.62). Since most of the contributions to the integrals come from values of ν and z that satisfy $z \approx z_0$, we can expand the source function as well as $(p^2 + z_0^2)^{1/2}$ in a power series. The part of (4.62) that involves the source function then reduces to

$$\frac{1}{2r}\int_{-r}^{r} dz\left\{S(r)\int_0^\infty \left\{1-\exp\left[\tau(\nu,p,\infty)\,(y-1)\right]\right\}\phi(\Delta\nu)\,d\nu\right\}. \tag{4.63}$$

We need to digress here for just a moment and consider the form of equation (4.38). This equation can be rewritten as

$$I_\nu = e^{-\tau_\nu} I_\nu(0) + (1 - e^{-\tau_\nu})\, S_\nu\ . \tag{4.64}$$

Looking at the contribution from $I(0)$, we see that the coefficient $e^{-\tau_\nu}$ represents the probability that the background photons incident on the medium will escape the medium.

We may apply a similar understanding for the contribution from $S(r)$ to J in the Wolf-Rayet star model. If we denote the escape probability by β, we may write (4.63) as (Elitzur 1984; Rybicki 1984; Canfield, Puetter, and Ricchiazzi 1981; Castor 1970)

$$J = (1-\beta)S(r)\ . \tag{4.65}$$

From this, we see that

$$\begin{aligned}\beta &= \frac{1}{2}\int_{-1}^{1} d\mu \int_0^1 \exp[-\tau(r,\mu)\,(1-y)]\,dy \\ &= \int_0^1 d\mu \frac{1-e^{-\tau_0(r,\mu)}}{\tau_0(r,\mu)}\ ,\end{aligned} \tag{4.66}$$

where μ is the cosine of the angle between the ray and the radius, or equivalently, z/r; and

$$\tau(r,\mu) = \frac{\tau_0(r)}{1+\mu^2\left(\frac{d\ln V(r)}{d\ln r}-1\right)}\ , \tag{4.67}$$

where

$$\tau_0(r) = \alpha_0(r)\frac{c}{\nu_0}\frac{r}{V(r)} \ . \tag{4.68}$$

Likewise, with the contribution from the core, we can find the escape probability for that radiation and this is (Castor 1970)

$$\beta_c = \frac{1}{2}\int_{(1-r_c^2/r^2)^{1/2}}^{1} d\mu \frac{1-e^{-\tau_0(r,\mu)}}{\tau_0(r,\mu)} \ . \tag{4.69}$$

It is then very easy to find the total J, which is given by

$$J = (1-\beta)S(r) + \beta_c I_c \tag{4.70}$$

For plane-parallel atmospheres, the results are similar to those derived above for spherical geometries. Scoville and Solomon (1974) have calculated the escape probability for such a geometry using the method of Lucy (1971), who used the Eddington approximation (Stacey 1985). The result is that for the two-stream approximation, the emergent flux requires $\mu = 1/\sqrt{3}$. This yields the following expression for the escape probability:

$$\beta = \frac{1-e^{-3\tau_0(z)}}{3\tau_0(z)} \ , \tag{4.71}$$

where

$$\tau_0(z) = \alpha_0(z)\frac{c}{\nu_0}\frac{dz}{dV(z)} \ . \tag{4.72}$$

Equation (4.70) simplifies somewhat to become

$$J = (1-\beta)\, S(z) + \frac{1}{2}\beta\, I_0 + \beta\, I_{BB} \ , \tag{4.73}$$

where $S(z)$ is given by (4.47), I_0 is the background radiation field impinging on only one side of the cloud, and I_{BB} is the 2.7 K microwave background radiation field (Elitzur 1984).

4.6.2 Detailed Balance and the Escape Probability Method

The goal of the escape probability method is for us to be able to determine in a self-consistent fashion the level populations for the atomic or molecular systems under consideration as well as the line intensities or fluxes that we should observe. To this end, we shall construct once again the equation of detailed balance. In keeping with convention, we shall redefine n_j to be the population density of the j^{th} level divided by the degeneracy.

We begin by looking at the j^{th} level and determining the rate of change of the population due to the various processes that occur. For now, let us be concerned only with the levels that lie above j. Spontaneous emission from these upper levels will tend to populate the level. Since the radiative transfer of the line photons is now a local problem, we see that a spontaneous emission will result in an actual increase in the population of level j if the photon can escape. That is to say,

$$\left(\frac{dn_j}{dt}\right)_{spont} = \sum_{k>j}\left(\frac{g_k}{g_j}\right)\beta_{kj}\,A_{kj}\,n_k\ . \tag{4.74}$$

Let the background radiation field be the cosmic blackbody field. Stimulated emission from level k to j will also help to populate level j. Similar arguments concerning the true amount of population due to this process lead us to the result that

$$\left(\frac{dn_j}{dt}\right)_{stim} = \sum_{k>j}\left(\frac{g_k}{g_j}\right)\beta_{kj}\,A_{kj}\,n_k\,F(T_{BB},\nu_{kj})\ , \tag{4.75}$$

where $F(T_{BB},\nu_{kj})$ is the photon occupation number, equal to $[e^{h\nu_{kj}/kT_{BB}}-1]^{-1}$, for a blackbody temperature $T_{BB}=2.7\,K$. For absorption from level j to k, we can write in the same spirit

$$\left(\frac{dn_j}{dt}\right)_{abs} = -\sum_{k>j}\left(\frac{g_k}{g_j}\right)\beta_{kj}\,A_{kj}\,n_j\,F(T_{BB},\nu_{kj})\ . \tag{4.76}$$

Adding (4.74), (4.75), and (4.76) together, we find the radiative processes involving

the higher levels will contribute to a true population rate for level j of

$$\left(\frac{dn_j}{dt}\right)_{rad} = \sum_{k>j}\left(\frac{g_k}{g_j}\right)\beta_{kj}\,A_{kj}\left[n_k + (n_k - n_j)\,F(T_{BB},\nu_{kj})\right] . \qquad (4.77)$$

Collisional processes will also help to either populate or depopulate the levels. For the higher levels, we have either population of level j through de-excitation or depopulation of level j through excitation. Using (4.49), we can write the collisional term as

$$\left(\frac{dn_j}{dt}\right)_{coll} = \sum_{k>j} g_k\,C_{kj}\left[n_k - n_j\,e^{-h\nu_{kj}/kT_{kin}}\right] , \qquad (4.78)$$

where C_{kj} is the collisional transition rate from level k to level j ($= \gamma_{kj}\,n_c$) divided by the degeneracy of level j, and T_{kin} is the kinetic temperature of the region. We can determine the corresponding rates for the lower lying levels, and the final total rate is given by

$$\begin{aligned}\left(\frac{dn_j}{dt}\right) = \sum_{k>j}\Bigg[&\left(\frac{g_k}{g_j}\right)\beta_{kj}\,A_{kj}\left[n_k + (n_k - n_j)\,F(T_{BB},\nu_{kj})\right] \\ &+ g_k\,C_{kj}\left(n_k - n_j\,e^{-h\nu_{kj}/kT_{kin}}\right)\Bigg] \\ - \sum_{k<j}\Bigg[&\beta_{jk}\,A_{jk}\left[n_j + (n_j - n_k)\,F(T_{BB},\nu_{jk})\right] \\ &+ g_k\,C_{jk}\left(n_j - n_k\,e^{-h\nu_{jk}/kT_{kin}}\right)\Bigg] . \end{aligned} \qquad (4.79)$$

Equation (4.79) will give us m equations with m unknowns for an m-level system. We solve for n_j, and from that, we can calculate the emergent intensity. Using (4.38) and (4.47), we find that

$$I_{kj}(r,\mu) = \frac{2h\,\nu_{kj}^3}{c^2}\left[\left(1 - e^{-\tau_{kj}(r,\mu)}\right)\left(\frac{n_k}{n_j - n_k}\right) + e^{-\tau_{kj}(r,\mu)}\,F(T_{BB},\mu)\right] . \qquad (4.80)$$

Finally, it is also possible to include the role of internal sources of radiation, such as dust grains imbedded in the cloud. See Elitzur, Goldreich, and Scoville (1976) for details.

V. Shocked OH and CO Emission Lines From The Orion Molecular Cloud

5.1 Introduction

Regions of recent star formation evince massive bipolar flows, which are apparently a common phenomenon (Bally and Lada 1983). These flows show velocity widths in the low J CO emission line wings of up to 130 km s^{-1}, and should be hypersonic. One then expects shock waves as a result of the flows plowing into the ambient molecular cloud surrounding the star formation region or else adjacent to it, as in the blister models of Balick, Gammon, and Doherty (1974) and Zuckerman (1973) . The presence of vibrationally excited H_2 in almost all of these regions suggests that there is shock heating occuring as well (Kwan 1977).

Rotational and vibrational emission lines of H_2, CO, and OH serve as excellent tracers of different parts of these shocked regions (Chernoff, Hollenbach, and McKee 1982), as do other molecular constituents, such as NH_3, CS, and SO (Keene, Blake, and Phillips 1983; Townes et al. 1983; Genzel et al. 1982; Plambeck et al. 1982; Goldsmith et al. 1980; Ho and Barrett 1978).

For typical preshock densities and flow velocities, the shocks should induce CO emission from a broad range of rotational levels from $J = 1$ to $J \approx 35$ (Draine and Roberge 1984; Chernoff, Hollenbach, and McKee 1982; Draine and Roberge 1982; McKee et al. 1982; and references therein). These levels range from several degrees Kelvin to several thousand degrees Kelvin (see figure 4.2), and therefore sample different regions within the molecular cloud. In fact, the low J transition emission features of CO usually display a very narrow spike from the ambient quiescent gas and a very broad plateau from the shocked gas.

One of the most extensively studied star formation regions is the Orion Molecular Cloud (OMC-1). During the last 20 years, OMC-1 has been the subject of observing programs at a variety of wavelengths from the near infrared to the radio.

Of interest to us is the region of the cloud that contains the Becklin-Neugebauer object as well as the Kleinmann-Low nebula. This region appears to be a site of recent star formation which has triggered a massive outflow of material. This has, in turn, contributed to the production of H_2O, OH, and SiO masers, which can be used to outline the shock front (Plambeck et al. 1982; Genzel et al. 1981).

Since the OMC-1 is relatively nearby, being at a distance of 500–530 parsecs (Mezger and Höglund 1967; Becker and Fenkart 1963), we are given a unique chance to study shock chemistry and physics through the observation of molecular rotational transitions in the FIR. By comparing the intensities of different rotational lines involving the same molecule, it is possible to derive a set of constraints on the actual temperature and density of the emitting region.

The CO lines that have been measured thus far suggest a two-component model for the shocked and post-shock regions. The warm component has a temperature on the order of 750 K and a molecular hydrogen density of about $3 \times 10^6\,\mathrm{cm}^{-3}$. For the hot component, these values are 2000 K and $1 \times 10^6\,\mathrm{cm}^{-3}$, respectively (Watson 1982).

This thesis is concerned mainly with the initial detections of several FIR OH rotational lines in emission from the BN–KL shock region in OMC-1. The hydroxyl radical is much more readily dissociated than CO, and is therefore much more sensitive to the physical conditions in this region. Because of this, we do not expect the OH to be as extensive as the CO, but to be found in significant abundance in a relatively thin sheet within the shock front (Draine and Roberge 1982).

Along these lines, we have also made the first astronomical detection of the $J = 15 \rightarrow 14$ rotational transition of CO at 173 μm. The significance of this line shall also be discussed below.

5.2 A Brief Overview of the Orion Nebula

The Orion Nebula is barely visible to the naked eye under the best conditions as an unresolved patch of light. It is not mentioned in any records, medieval or ancient, and it is interesting to note that Galileo also apparently never pointed his telescope in that direction (Gingerich 1982; Burnham 1977). Nicholas Peiresc is

credited with discovering the nebula in 1611. It wasn't until 1656 that a drawing of the nebula was published by Christiaan Huygens. It is claimed that Orion so stirred Sir William Herschel when he first looked toward the heavens with his new telescope in 1774, that he dedicated the rest of his life to such studies. It was in 1771 that Charles Messier published his first listing of clusters and nebulae, and the designation M42 is probably the most well known catalog name of this object. In 1880, Henry Draper took the first successful photograph of a nebula, the subject being Orion.

Jumping ahead 100 years, we find a consistent picture of the Nebula beginning to emerge from the data collected thus far. Visually, the nebula is illuminated by the Trapezium stars and θ^2 Orionis. These stars are relatively young, and there are stars still in the process of formation within the region. The nebula is composed of the surrounding H II region, ionized by θ^1C Orionis, which forms a blister on a much larger giant molecular cloud (Werner 1982; Pankonin, Walmsley, and Harwit 1979; Balick, Gammon, and Doherty 1974; Zuckerman 1973). This molecular cloud has an estimated mass of 2.5×10^4–$1.0 \times 10^5\,M_\odot$ (Tucker, Kutner, and Thaddeus 1973).

To the north and west of θ^1C Orionis lies the infrared nebula known as the Kleinmann-Low (KL) nebula (Kleinmann and Low 1967). This near-infrared source of radiation is most likely the recent birthplace for several hot O and B stars. This nebula was discovered after a compact $2\,\mu$m source in the vicinity was found by Becklin and Neugebauer (1967). These two objects are about $11''$ apart on the sky, and are collectively known as BN–KL. The coordinates of BN are $\alpha_{1950} = 5^h32^m46.7^s$, $\delta_{1950} = -5°24'17''$.

In the region of BN–KL, there is an infrared source known as IRc2. This source is now believed to be the central engine that is supplying energy to the massive outflow that has been observed. The dynamic processes were first found to be phenomena associated with outflows centered on BN or IRc2 through millimetric CO observations by Solomon, Huguenin, and Scoville (1981). This outflow was determined to be molecular and bipolar by Erickson et al. (1982). Directly surrounding IRc2 is an expanding central disk that is about 70 astronomical units

in size (see figure 5.1). This disk is inferred from interferometric observations of the SiO maser (Wright and Plambeck 1983) as well as from the placement and velocity centroid of the so called H_2O "shell" masers (Genzel et al. 1981).

Surrounding this inner disk is a torus or doughnut of gas that is expanding at low velocity ($\sim$18 km s^{-1}) and is most apparent in thermal emission from SO (Plambeck et al. 1982) and in the low velocity H_2O and OH masers (Downes et al. 1981). This flow is in the NE-SW direction, very much along a ridge of quiescent gas. The torus is somewhat tilted with respect to our line and on the order of 0.02 pc in size.

Perpendicular to the ridge, and nearly centered on IRc2, hot high velocity gas has been found to exist on a scale of roughly 0.1 pc. It was initially discovered by Thaddeus et al. (1972) in an H_2S line. Observations of SO, SO_2, HCN, and SiO also showed evidence for high velocity wings (Dickinson et al. 1976; Snyder et al. 1975; Wannier et al. 1974; Gottlieb and Ball 1973). Earlier CO observations showed the high velocity gas, but it was overlooked due to the intense, low-velocity central peak. This gas is believed to be part of a high velocity outflow in the NW-SE direction centered on IRc2. Looking at the H_2 2 μm emission map of Beckwith et al. (1978), we see that the emission forms a double-lobed structure centered on IRc2 (see figure 5.2). This structure is perpendicular to the quiescent ridge and is on the order of 0.1 pc in extent. The line profiles for H_2, CO, OH, and other molecules show high velocity plateau features with widths ranging from 50 to 130 km s^{-1}. The H_2 data suggest temperatures of 2000 K and densities on the order of 10^5 cm^{-3}. The velocities, temperatures, and densities make sense if we assume an hypersonic outflow into the ambient molecular cloud, forming a shock wave which heats and excites the various molecules.

The BN object was at first considered to be a protostar, but it is now considered to be a young hot star that is losing mass (Downes et al. 1981). This mass loss has enshrouded the star in a cloud of gas and dust. Recent radio observations at the VLA indicates a size of no more than $0''.07$, or 5×10^{14} cm (Moran et al. 1983).

Continuum maps in the FIR show a single maximum centered on the BN–KL region (Keene, Hildebrand, and Whitcomb 1982; Werner et al. 1976). The source

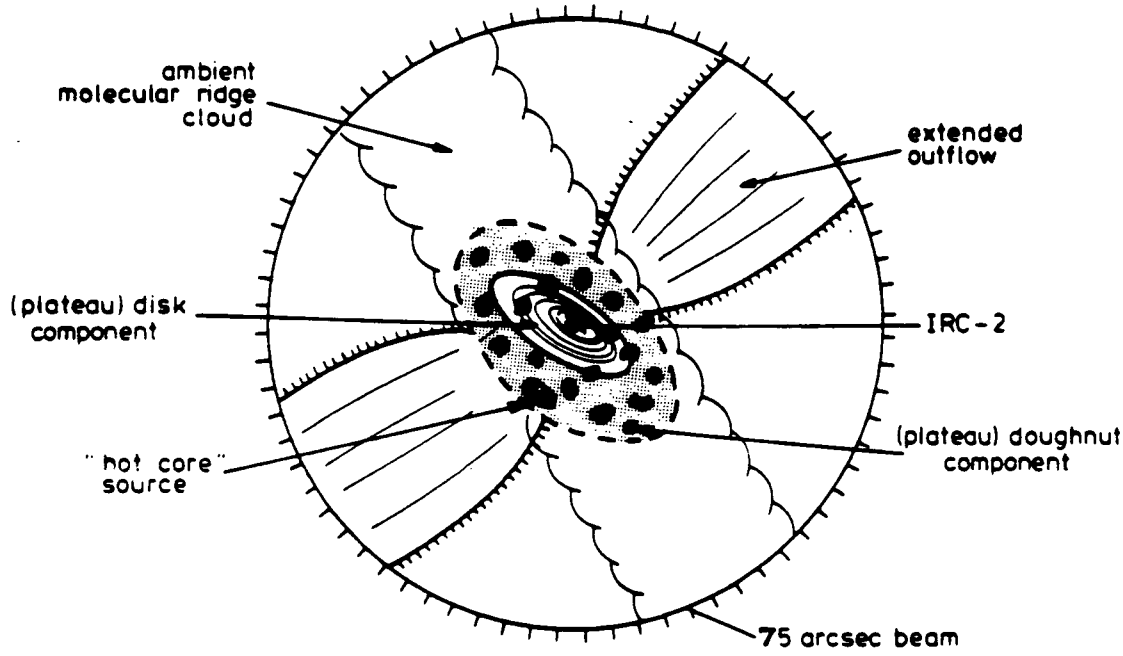

FIGURE 5.1 A schematic of the region of OMC-1 containing IRc2 and BN–KL. One arc-minute corresponds to 4.5×10^{17} cm at the distance of OMC-1. From Watt et al. (1985).

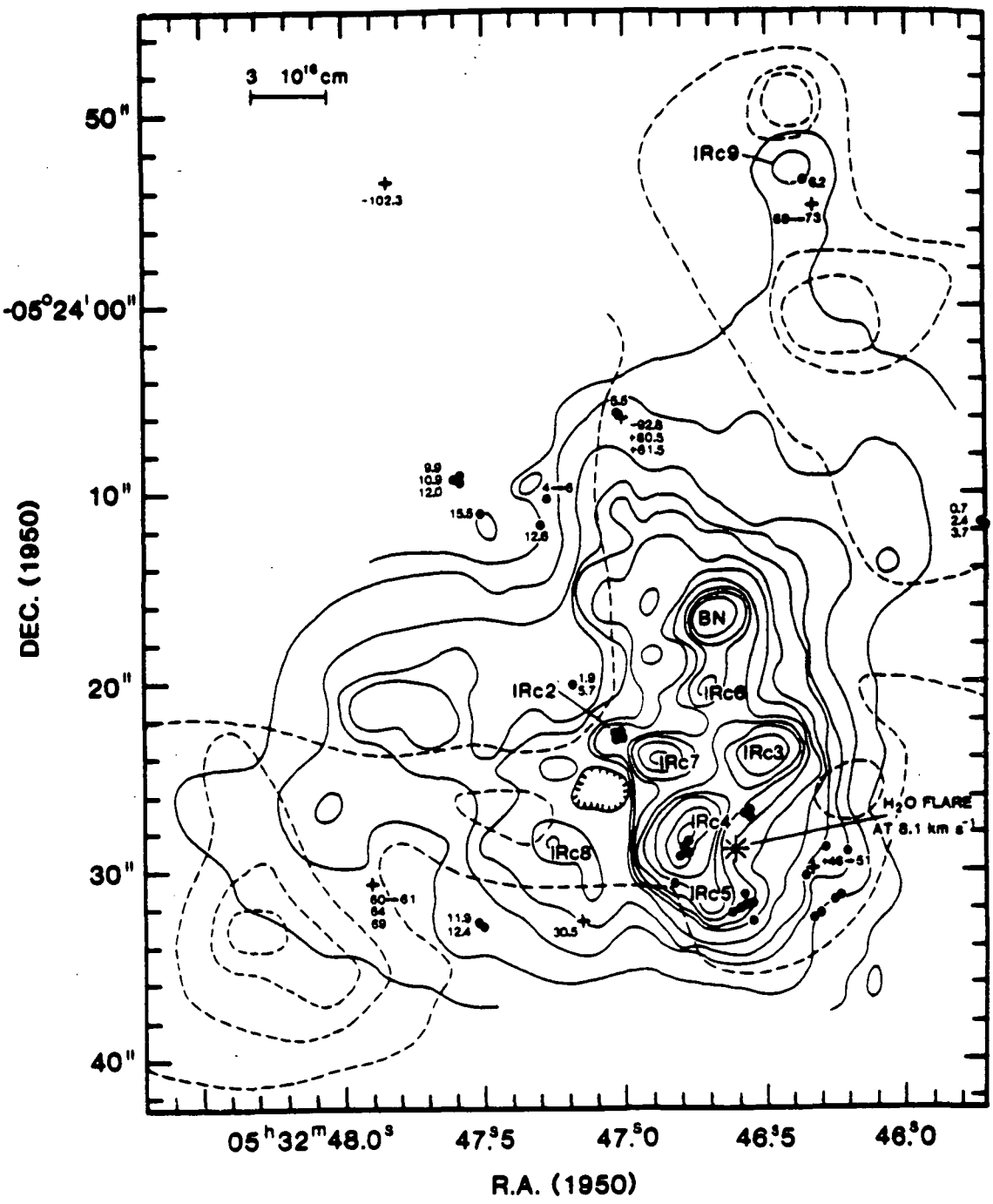

FIGURE 5.2 Locations of H_2O masers in BN-KL. The LSR radial velocities are given next to the maser locations. Solid contours are from the 20 μm continuum data. Dashed contours are those of the $v = 1 \rightarrow 0)$ S(1) transition of H_2 from Beckwith et al. (1978). From Downes et al. (1981).

of this continuum is most likely dust grains that absorb the starlight from IRc2, BN, and KL, and then reradiate it, mostly from the infrared to the submillimeter part of the spectrum. Since the source size (HWFP) is roughly $1'$ for the continuum source and for the shocked gas, and this size corresponds to the diffraction limited beam size in our observations, we look at the BN–KL object to observe the shocked gas.

For other histories and overviews on the Orion Nebula, see Stacey (1985); Glassgold, Huggins, and Schucking (1982), and Watson (1982).

5.3 OH Observations Toward BN–KL

5.3.1 Inspiration

The BN–KL region has been the subject of many recent millimeter and submillimeter observations in the rotational transitions of OH and CO, as well as in a plethora of transitions of diatomic and more complex molecules (Rydbeck and Hjalmarson 1985; Schultz et al. 1985; Johansson et al. 1984; Storey et al. 1981; and references therein, to name a few). The CO and OH measurements suggest that the emitting region resides in the shocked and post-shock gas. Measurements of the various ro-vibrational transitions of H_2 have shown that $n_{H_2} \sim 2 \times 10^5\,\mathrm{cm}^{-3}$ within the shock region and that the temperatures are on the order of 2000 K (Nadeau and Geballe 1979; Beckwith et al. 1978). The Berkeley group found that the CO transitions are consistent with a temperature ~750 K and molecular densities $\sim 3 \times 10^6\,\mathrm{cm}^{-3}$ for the warm component of the emitting region (Watson 1982). This suggests that most of the observed CO lies within the post-shock gas closest to the shock front.

Since OH is chemically more active than CO, we do not expect the OH to coexist extensively with the CO. More likely, the OH will be abundant in a relatively confined sheet in the shocked or post-shock gas, with smaller abundances throughout the rest of the region. The OH may also tend to be more clumpy than the CO.

Recent observations of the $^2\Pi_{3/2}$ $J = \frac{5}{2} \rightarrow \frac{3}{2}$ transition at 119 μm (Watson

1982; Storey, Watson, and Townes 1981), along with several Λ-doubling radio lines, led us to observe four more OH transitions in the FIR. From this set of observations, it should be possible to apply radiative transfer theory to place constraints upon the temperature and density of the OH-emitting region.

The FIR observations of OH are important not only in understanding the physical parameters of the OH-emitting region, but also in attempting to understand the pumping mechanism of the OH masers that are associated with BN–KL and other H II regions. Much has been written about the pump mechanism, and it is still not known if radiative pumping or collisional pumping dominates (see, for example, Genzel 1985; Elitzur 1982; Reid and Moran 1981; and references therein) . By observing the two parity transitions for each FIR transition, we may be able to shed some light on this issue.

5.3.2 The 163 μm Observations

In 1983 March, we made sub-millimeter OH observations toward the BN–KL region. The 91 cm bent-Cassegrain telescope on board the KAO was used as our observing platform. The observing altitude was 13–14 kilometers and the diffraction-limited beam size was 1.′0 square. The instrument used was our interferometer/grating-spectrometer, capable of an instrumental resolution $\lambda/\Delta\lambda \approx 1200$, and described in detail in chapter II. The Orion data from this flight series constituted the first detection of the $^2\Pi_{1/2}$ $J = \frac{3}{2} \rightarrow \frac{1}{2}$ OH rotational transitions and was reported in Viscuso et al. (1985a). The laboratory wavelengths for these transitions are 163.12 and 163.40 μm (Brown et al. 1982). In 1984 January and 1985 January, we reconfirmed the 163 μm flux measurements with an improved instrumental resolution of ≈4000.

As we saw in chapter II, the spectrum one derives from an interferogram is a convolution of the instrumental profile of the spectrometer with the source profile. The instrumental profile, as best as we can tell from laboratory measurements, is approximately Gaussian.

The OH results from the 1983 March flight series are displayed in figure 5.3. The instrumental resolution at the time was roughly 1200 at 163 μm. The

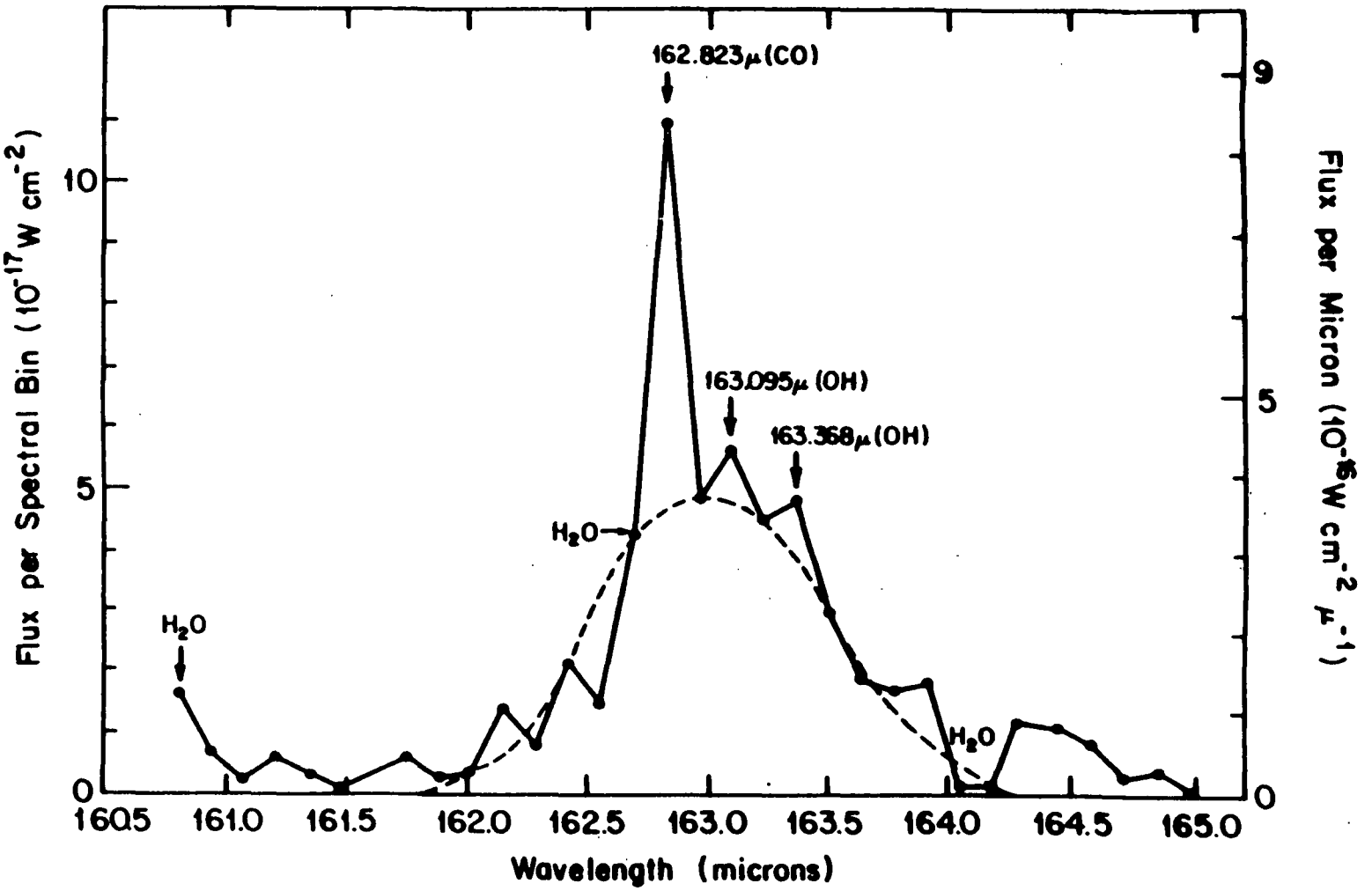

FIGURE 5.3 Spectrum of BN–KL at 163 μm. The smooth dashed curve represents the expected continuum profile. The CO line is due to the $J = 16 \rightarrow 15$ rotational transition. This line is much stronger than the two OH lines from the $^2\Pi_{1/2}$ $J = \frac{3}{2} \rightarrow \frac{1}{2}$ transition. Regions of telluric water vapor contamination are marked. The noise may be estimated from the departure of the continuum data from the expected profile. Data were obtained in 1983 March.

interferometer was not upgraded until the next year. At this resolution, it is possible to separate the two sets of lines arising between the different parity states, but the hyperfine transitions cannot be separated. The hyperfine transitions within one parity transition occur at wavelengths that differ by one part in 10^5, on average. The two parity transitions (see figure 4.3) are separated by 0.275 μm, and are therefore resolvable at this instrumental resolution.

Figure 5.3 displays the 1983 March spectrum which is drawn on top of the instrumental profile (dotted line). Since the continuum level is roughly constant over this small wavelength range, the dotted line represents the instrumental profile times a scaling factor that simply reflects the constant continuum level.

Werner et al. (1976) have found the continuum intensity from the BN–KL region to follow a blackbody distribution for a temperature of 70 K and with an emissivity that is inversely proportional to wavelength and is unity at 20 μm. At 163 μm, for a 1′ beam, we find that the continuum flux level we measure is 5.77×10^{-17} W cm^{-2} in each bin at a resolution of 1200.

Looking at figure 5.3, the first obvious feature is the $J = 16 \rightarrow 15$ rotational transition of CO at 162.8116 μm. This line was first observed by Stacey et al. (1983), and the flux in the line is 7.8×10^{-17} W cm^{-2}. Stacey et al. (1983) give a slightly smaller estimate, but the two agree within the errors, most of which are due to determining where the continuum level actually lies on the spectrum.

The next two bumps to the right of the CO line are the two OH lines. Although the lines are not necessarily significant (i.e., the signal-to-noise is not greater than 5), they are suggestive since they do happen to lie in the correct positions and are both raised the same amount. If we also look at the fit to the continuum, we see that the fit is very good except for those two lines and the two places where telluric water vapor features lie. There is very little signal in the wings, which indicates that the overall system noise is low. Another indication that the OH lines were real came from the removal of the CO line from the original data. Since the wavelength of the CO line is well known, its contribution to the interferogram can be calculated and removed. This removal preserved the OH features, indicating that they were not caused by the dominant CO line.

The interferometer was upgraded in 1983 December, and was successfully flown the next month on the KAO. The 163 μm OH line measurements were confirmed at an instrumental resolution of $\approx$ 3700, albeit not with much improvement in the signal-to-noise ratio. In 1985 January, we again looked at BN–KL and dedicated another 30 minutes of observing time to obtain five 163 μm spectra at moderately high resolution (R$\approx$2800). The result is shown in figure 5.4. The data superimposed upon a Gaussian instrument profile which should define to reasonable accuracy the continuum level from Orion. The flux levels are 1.75×10^{-17} and 2.1×10^{-17} W cm^{-2} for the 163.12 and 163.40 μm lines, respectively. These values are higher than the 1.2×10^{-17} W cm^{-2} derived from the 1983 March data (Viscuso et al. 1985a).

These data show a poor fit to a Gaussian at the lower and upper ends of the wavelength scale. Here, the signal seems to be much higher, especially on the short wavelength side. The reason for this is the fact that the spectrometer is not aliasing properly for such a small free spectral range at this wavelength. This can be seen in figure 5.5, which shows the data superimposed on a laboratory calibration spectrum run near this wavelength. The calibration clearly shows significant asymmetry, with the lower end of the spectrum being effectively raised. The free spectral ranges for the calibration spectrum and the data are slightly different, and that most likely explains why the match is not perfect. However, the calibration spectrum does show the effect of imperfect aliasing, and explains the raised ends of the spectrum.

Subsequent confirmation attesting to the existence of the 163 μm lines has been offered by Melnick (1985), who used the Berkeley group's Fabry-Perot spectrometer to detect the 163 μm OH lines. Their instrumental resolution at the time was 9000 at this wavelength. Flux measurements were only secured for the 163.12 μm line, giving 1.3×10^{-17} W cm^{-2} (Crawford et al. 1986).

5.3.3 The 84 μm Observations

In a cooperative venture with Dr. Edwin Erickson and his group at NASA/Ames Research Center, measurements of the $^2\Pi_{3/2}$ $J = \frac{7}{2} \rightarrow \frac{5}{2}$ transition of OH at 84 μm were acquired on 1983 November 22–23 using the NASA/ARC Cooled Grat-

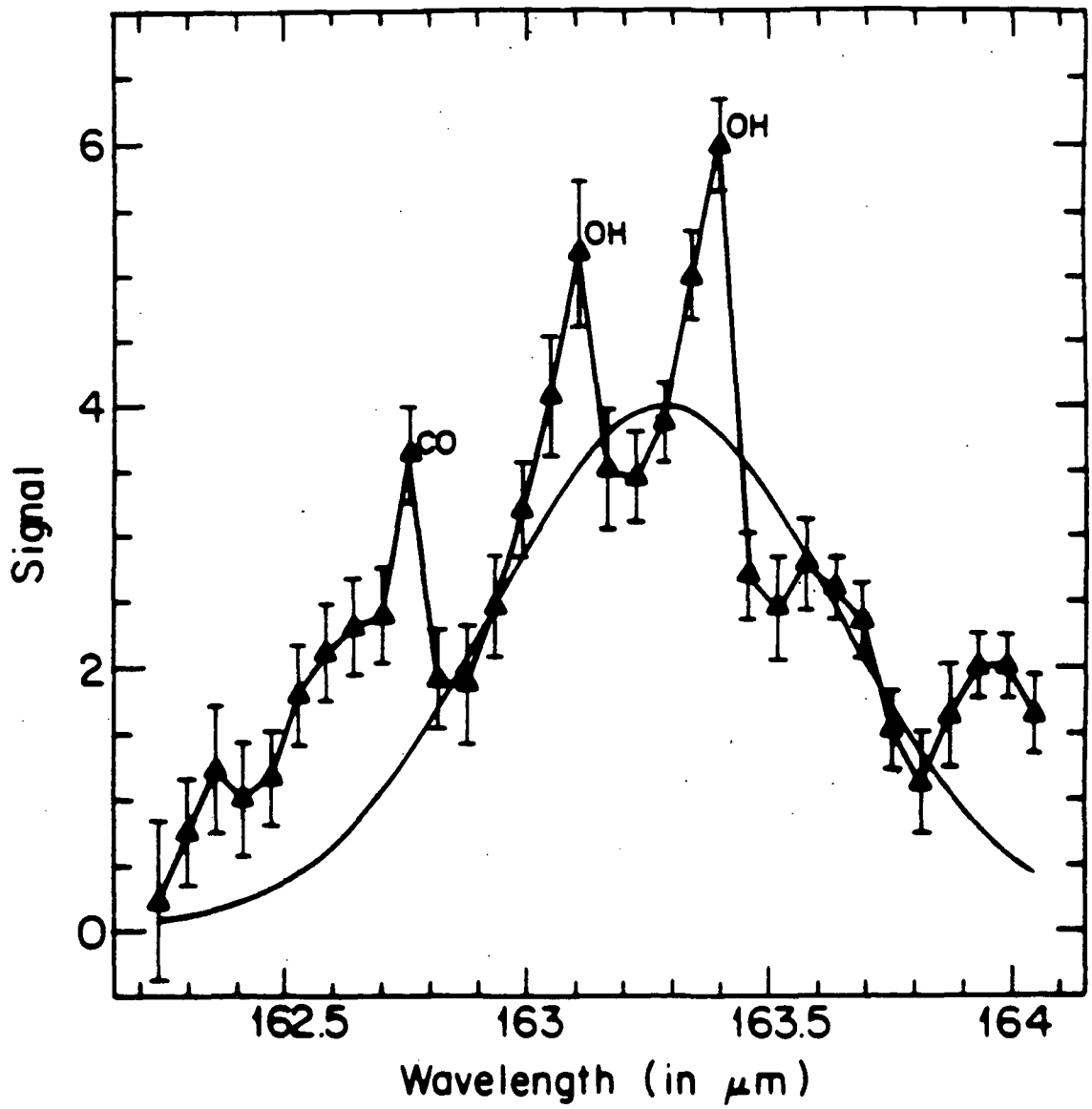

FIGURE 5.4 Spectrum of BN–KL at 163 μm. The smooth solid line represents the expected continuum profile. The interferometer/spectrometer was used to obtain these data in 1985 January with an improvement in the system resolution by a factor greater than 3 over that used to obtain the data in figure 5.3. The integration time was about 50 seconds per point. The signal scale is arbitrary. The rise in the profile on the left is due to an incomplete aliasing of the order by the instrument. The CO line does not appear as strong in these data due to its placement far out on the instrumental wing.

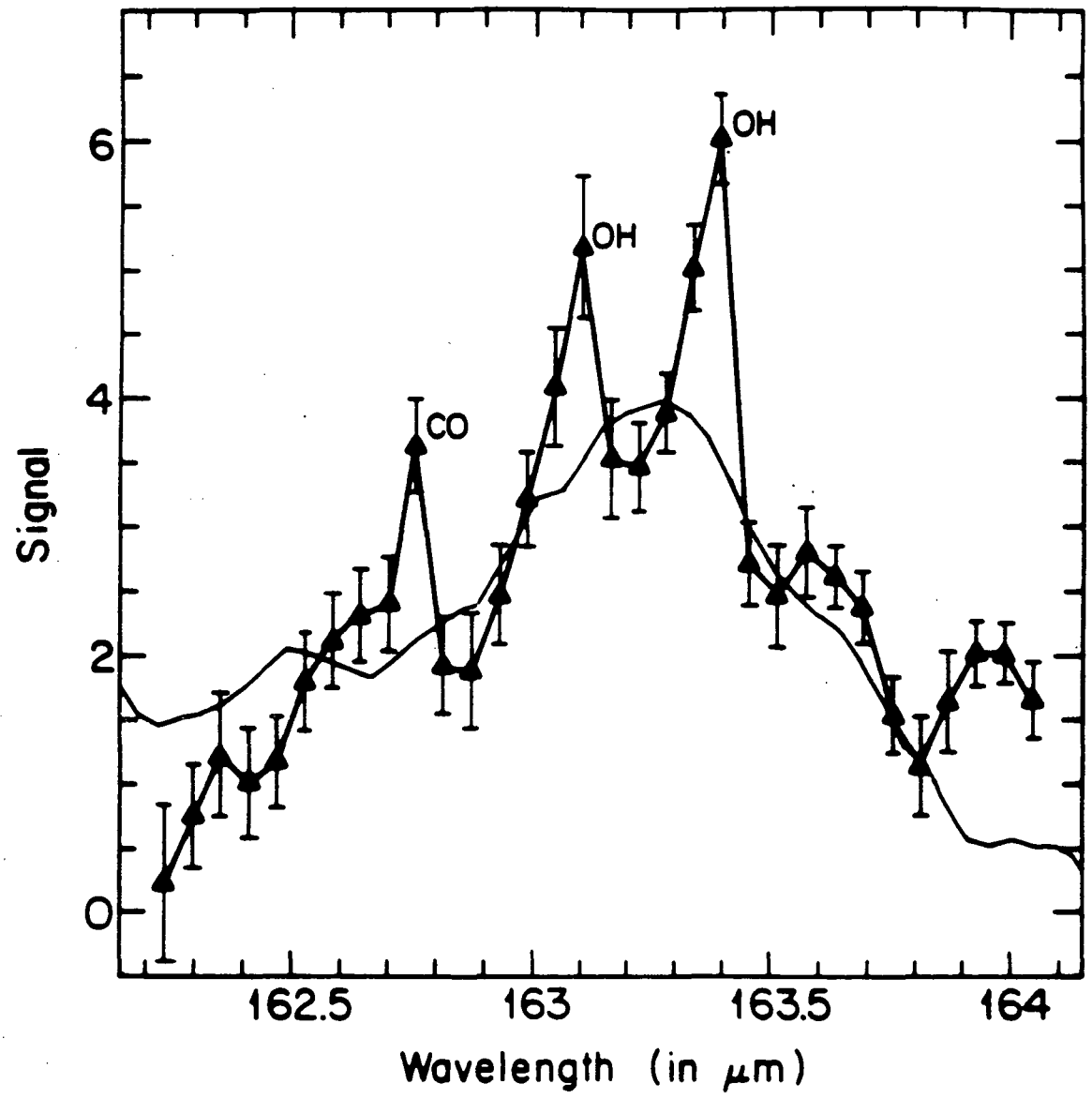

FIGURE 5.5 Spectrum of BN-KL at 163 μm. These data are the same as those in figure 5.4, except that the instrumental profile was replaced with a laboratory blackbody spectrum. Note the better profile matchup on the left. The sampling rates used for both spectra are different, and that accounts for the imperfect match between the two profiles.

ing Spectrometer (CGS) facility instrument (Erickson et al. 1984). This instrument basically consists of a huge grating that is operated in high order (m $\sim$ 75), and has a resolution of from 4000 to 10000, depending on wavelength. The whole assembly fits in a cryogenic barrel that looks like a somewhat scaled down version of a 55-gallon drum. At the time of operation, there was an array of 6 Ge:Ga detectors which were separated by 0.0184 μm. The diffraction overlap caused the resolution to be 26% lower than that found by simply using the detector separation. The resolution was 3400 and the circular beam size was $1'$ in diameter.

Figure 5.6 shows the spectra for the two parity transitions at 84.42 and 84.60 μm (Brown et al. 1982). Since the detectors needed to be calibrated, the raw spectra were divided by a continuum spectrum at a nearby wavelength of 87.08 μm, a region free from any expected telluric or astronomical spectral features. Owing to different instrumental response at the different wavelengths, the baselines are sloped. Detector #5 was inoperable during the flight, which accounts for the missing point in the data. Line flux determination is again made by comparing the line strength against the continuum level. For the 84.42 μm line, the flux is $1.0 \pm 0.3 \times 10^{-17}$ W cm^{-2}, while the 84.60 μm line flux is $1.4 \pm 0.4 \times 10^{-17}$ W cm^{-2}. These results were first reported in Viscuso et al. (1985b). Verification of these lines was published later in Watson et al. (1985). It should be noted, however, that the latter group had actually made their observations earlier. Their beam size is $30''$ compared with $1'$ for ours, and the resulting flux level is down by roughly a factor of 2.

The 84.4202 μm data are controversial at this point because of the nearby CO line at 84.4107 μm ($J = 31 \rightarrow 30$). The two lines are separated by only 33 km s^{-1}, which is not enough for them to be resolved with the Berkeley FPS or the NASA/ ARC CGS. The measured flux from the line is consistent with that expected from the CO, given the data from all of the other CO lines that have been unambiguously measured. However, the flux is also consistent with that expected from OH given the flux from the other OH line at 84.60 μm. More will be said about this later.

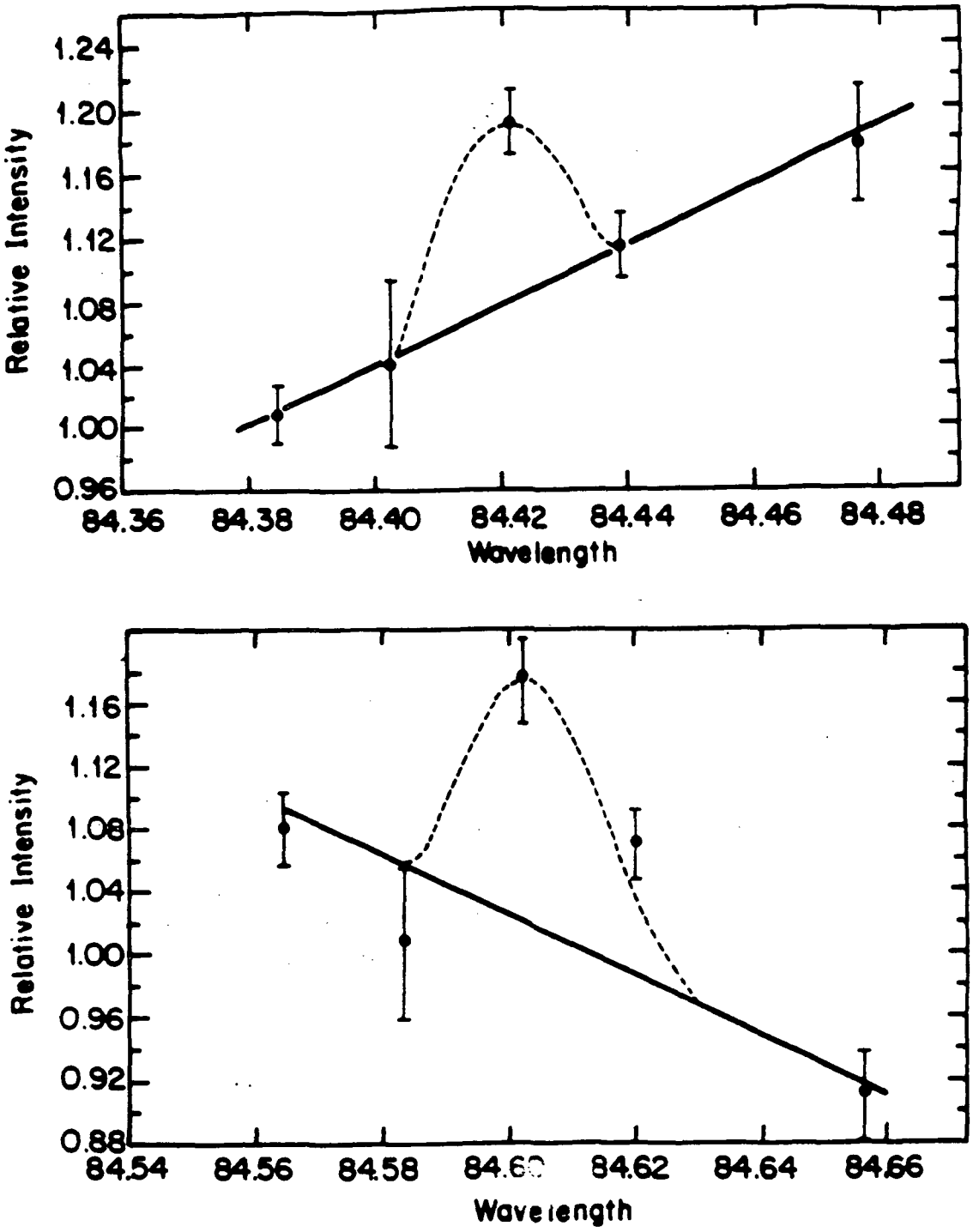

FIGURE 5.6 Spectrum of BN–KL at 84 μm. Data were obtained in 1983 November with the NASA/ARC facility cooled grating spectrometer. Dashed lines represent the expected instrumental profiles for the emission lines. The solid lines represent the continuum baselines. The residual baseline slopes are due to instrumental effects.

5.3.4 Other OH Observations

Other various rotational transitions in OH have been observed toward BN–KL. Table 5.1 gives a list of observations that have been carried out and reported, including intensities and beam sizes where known.

The Λ-doubling lines of the $^2\Pi_{3/2}$ $J = \frac{3}{2}$ level have been well known for many years. Maser action is seen for the 1665 MHz line towards BN–KL (Reid and Moran 1981; and references therein). These masers are associated with the expanding doughnut of gas, and their formation is still not completely understood.

The $^2\Pi_{3/2}$ $J = \frac{7}{2}$ $F = 4^+ \rightarrow 4^-$ Λ-doubling transition (13441 MHz) was detected in emission from BN–KL by Matthews et al. (1984). This feature is about 25 km s^{-1} wide (23 ± 4), with a line antenna temperature of 20 ± 4 mK. The F = $3^+ \rightarrow 3^-$ hyperfine transition at 13435 MHz was marginally detected with a line antenna temperature of 10 ± 5 mK. The 140 foot telescope of the NRAO was used for the observations, with a sensitivity of 4.5 Jy K^{-1}.

The $^2\Pi_{3/2}$ $J = \frac{9}{2}$ $F = 4^- \rightarrow 4^+$ and $F = 5^- \rightarrow 5^+$ Λ-doubling transitions at 23817 and 23826 MHz have not been detected toward Orion (Walmsley 1985). Guilloteau et al. (1984) report a possible detection of the 6035 MHz line due to the $^2\Pi_{3/2}$ $J = \frac{5}{2}$ $F = 3 \rightarrow 3^+$ Λ-doubling transition. Knowles, Caswell, and Goss (1976) have published a detection of this line toward Orion, showing a relatively narrow emission with a flux density of 4 Jy. This may possibly be a weak maser line.

The $^2\Pi_{3/2}$ $J = \frac{5}{2} \rightarrow \frac{3}{2}$ rotational transitions of OH at 119.23 and 119.44 μm have been detected by the Berkeley group (Watson et al. 1985; Watson 1982; Storey, Watson, and Townes 1981). The more recent estimates for the line fluxes are on the order of 7×10^{-18} W cm^{-2}.

Table 5.1 OH Observations of OMC-1

Transition	Wavelength	Flux (10^{-17} W cm^{-2})	Reference
$^2\Pi_{1/2}\, J = \frac{3}{2} \rightarrow \frac{1}{2}$	163.40 μm	1.2±0.6	1
	163.40 μm	2.1±0.7	2
	163.12 μm	1.2±0.6	1
	163.12 μm	1.7±0.7	2
$^2\Pi_{3/2}\, J = \frac{5}{2} \rightarrow \frac{3}{2}$	119.44 μm	0.7±0.3	3
	119.23 μm	0.83±0.3	3
$^2\Pi_{3/2}\, J = \frac{7}{2} \rightarrow \frac{5}{2}$	84.60 μm	1.4±0.4	4
	84.42 μm	1.0±0.3	4
$^2\Pi_{3/2}\, J = \frac{7}{2}\, F = 4^+ \rightarrow 4^-$	2.24 cm	9×10^{-9}	5

A list of the published OH observations to date toward the Orion Molecular Cloud. The errors in the 163 and 84 μm lines are primarily due to uncertainty in the calibration as opposed to variances in the signal strengths. The reference numbers refer to the following articles: 1) Viscuso et al. (1985a); 2) this work; 3) Watson et al. (1985); 4) Viscuso et al. (1985b); 5) Matthews et al. (1984).

5.4 OH in Orion: A Simple Approach to a Complex Problem

5.4.1 The Modus Operandi

We now have a limited, but significant, set of observations involving the lower level transitions of OH found in the shock region of OMC-1. It is the purpose of this chapter to see if these observations are consistent with each other.

For the most part, we will assume that there is only one overall area of the cloud that contains the OH emitting regions, an assumption that is not necessarily true. Another simplifying assumption that is invoked is that of uniformity among the emitting regions. Even though we allow for clumps when we introduce the filling factor, we assume that the clumps may be explained with one temperature and density. Therefore, we will assume that there is an average temperature and density which will represent the OH emitting regions.

We will begin by analyzing the 163 μm data, deriving from them a molecular hydrogen density. Then, we can determine the expected 119 μm flux, using the new collisional cross sections of Andresen, Häusler, and Lülf (1984). The discrepancy between the expected and measured fluxes is resolved when we consider the effects of collisional de-excitation as a means of destroying photons. The 84 μm data will be analyzed along similar lines, and we will attempt to predict the 13.4 GHz flux as well.

The analysis that will be carried out in this chapter does not carry with it any evolution due to shocks and shock chemistry. The latter considerations present a complex exercise that will hopefully be carried out at a later time. The present treatment, however, is still very important, since it can be used as a springboard in the understanding of the OH line fluxes, and also be used to check and provide limits to the MHD shock models that have been run recently by Chernoff and Draine.

We did not have sufficient resolution to determine the line widths for the 84 and 163 μm line data. Since the 119 μm lines show a width of 30 km s^{-1}, we shall assume that the other OH lines are also that wide. Recent results from Melnick (1985) suggest that the 163.12 μm line is about this wide, or a bit wider. The

163.4 μm line in the data is cut off by a telluric water vapor feature, and so a width determination is impossible at this time for that line.

5.4.2 The H_2 Density

The 163 μm data allow us to obtain an estimate of the H_2 density within the emitting region. The total 163 μm line flux is in the range 2.4–3.8 $\times 10^{-17}$ W cm^{-2}. Using 520 parsecs as the distance to the Orion Nebula, we find that the total 163 μm luminosity is 6.4–10.1 $\times 10^{47}$ photons s^{-1}. Since we expect the OH to reside within the shock and post-shock region (from earlier arguments), we can choose as a starting point for the temperature and density of the region those parameters that were found from the CO measurements, namely $T \sim$750 K and $n_{H_2} \sim 3 \times 10^6$ cm^{-3}. The dominant excitation mechanism at these temperatures and densities is collisional excitation by H_2. Recent experimental values for the collisional cross-sections from the $^2\Pi_{3/2}$ $J = \frac{3}{2}$ level to higher levels have been obtained by Andresen, Häusler, and Lülf (1984). These cross-sections are significantly different from those obtained theoretically by Dewangan and Flower (1981,1983) and Schinke and Andresen (1984). The experimental cross-sections are listed in table 5.2.

To find an expression for the molecular hydrogen density, we note that the collisional cross-sections from the ground state to excited states within the $^2\Pi_{1/2}$ ladder is roughly 3.6Å^2. Since the spontaneous emission rates are much higher than the collisional de-excitation rates, we may assume that most of the excited levels in the $^2\Pi_{1/2}$ ladder will result in a 163 μm photon being released. We can then equate the collisional excitation rate directly to the 163 μm luminosity.

The oxygen to hydrogen ratio is given as 4.25 $\times 10^{-4}$ by number (Draine, Roberge, and Dalgarno 1983). According to the shock models of Draine and Roberge (1982,1984), the OH abundance will be most enhanced in a region that has a thickness of roughly 5 $\times 10^{14}$ cm. The OH to O ratio in this region is close to 1%. We will therefore assume that most of the OH emission will come from this thin region. If we let $\epsilon = [OH]/[H_2]$, then $\epsilon \approx 8.5 \times 10^{-6}$.

Table 5.2 H_2–OH Collisional Cross Sections (in $Å^2$)

Final J	$^2\Pi_{3/2}$	$^2\Pi_{1/2}$
$\frac{1}{2}^+$	—	1.1
$\frac{1}{2}^-$	—	1.2
$\frac{3}{2}^+$	—	0.8
$\frac{3}{2}^-$	—	1.1
$\frac{5}{2}^+$	2.5	0.5
$\frac{5}{2}^-$	2.5	0.75
$\frac{7}{2}^+$	0.75	0.15
$\frac{7}{2}^-$	1.05	0.3
$\frac{9}{2}^+$	0.15	0.04
$\frac{9}{2}^-$	0.35	0.08

A list of the H_2–OH collisional cross sections as obtained from experimental measurements for collision energies of 83 meV (Schinke and Andresen 1984; Andresen, Häusler, and Lülf 1984). All of these measurements are for transitions from the $^2\Pi_{3/2}$ $J = \frac{3}{2}$ ground state.

Equating the excitation rate to the 163 μm luminosity, we may write

$$(\sigma\,\bar{v}\,n_{H_2})\,(N_{H_2}\,\epsilon\,f_0) = L_{163}\ , \tag{5.1}$$

where σ is the collisional excitation cross-section, equal to 3.6 Å (see table 5.2); $\bar{v}$ is the average collision velocity; n_{H_2} is the molecular hydrogen density, N_{H_2} is the number of H_2 molecules present in the emitting region; f_0 is the fraction of the OH molecules in the ground state; and L_{163} is the photon luminosity in the 163 μm lines.

The observations were carried out using a 1′ square beam. If we let D be the size of the region represented by a side of the beam, and let d represent the thickness of the emitting region (we will assume this to be 5×10^{14} cm), then we may write the volume of the emitting region to be

$$V = \frac{N_{H_2}}{n_{H_2}} = D^2\,d\,g_f\ , \tag{5.2}$$

where g_f is the filling factor for the beam. We assume that the OH-bearing region is uniform in the direction of d, as is suggested by the MHD models. The above two equations may be combined to yield

$$n_{H_2} = (L_{163})^{\frac{1}{2}}\,(D^2\,d\,g_f\,\sigma\,\bar{v}\,\epsilon\,f_0)^{-\frac{1}{2}}\ . \tag{5.3}$$

For a kinetic temperature of 750 K, we find

$$n_{H_2} \approx 2.6\text{–}4.2 \times 10^6 g_f^{-1/2}\,f_0^{-1/2}\ \mathrm{cm}^{-3}\ . \tag{5.4}$$

Using the OH data of Watson (1982), we calculate for the OH emitting region an expected molecular hydrogen density on the order of $6 \times 10^6\,\mathrm{cm}^{-3}$. We find a minimum expected value for the filling factor to thus be ~ 0.2.

How good is the correspondence between collisional excitation into the $^2\Pi_{1/2}$ ladder and 163 μm emission? If the 163 μm line is optically thick, then you may not actually be measuring the collisional excitations into that ladder. To find the

optical depth, we need to find the cross-section for absorption. If n_{163} is the number density of 163 μm photons, then the absorption rate must be $\sigma\, n_{163}\, c$. But this is equivalent to $B_{ij}\, J_{163}$, where B_{ij} is the Einstein coefficient for absorption, and J_{163} is the mean intensity at 163 μm. The photon number density is related to J by

$$n_\lambda = \frac{4\,\pi\,\lambda}{h\,c^2}\, J_\lambda\, \Delta\lambda\ . \tag{5.5}$$

The cross-section for absorption can then be written as

$$\sigma_{\rm abs} = \frac{g_{\rm j}}{g_{\rm i}}\, \frac{\lambda^3}{8\pi\,\Delta v}\, A_{\rm ji}\ , \tag{5.6}$$

where the various relations among the Einstein coefficients were used. The value of $A_{\rm ji}$ for the 163 μm lines is $0.065\,{\rm s}^{-1}$ per parity transition (Brown et al. 1982). Assuming that Δv is about $30\,{\rm km\ s}^{-1}$ (making use of the various line widths found for other molecules in the shocked region), we find the cross section to be $75\,{\rm \AA}^2$. The column density of OH in the ground state in the $^2\Pi_{1/2}$ ladder cannot be greater than $n_{\rm H_2}\,\epsilon\,d$, the total OH column density, which is approximately $2.6\times10^{16}\,{\rm cm}^{-2}$. Hence, the optical depth for resonant scattering (absorption) at 163 μm is roughly 190.

One must be careful, however, in interpreting this number. Although it is true that the 163 μm photon will be absorbed very quickly, it will also be reemitted via spontaneous and stimulated emission. The only way to destroy the photon is either via collisional de-excitation or emission of a 53 μm photon to the ground state of OH ($^2\Pi_{1/2}\ J=\frac{3}{2} \rightarrow {}^2\Pi_{3/2}\ J=\frac{3}{2}$). The ratio of the collisional de-excitation rate to the overall stimulated emission rate for the upper 163 μm level is on the order of 10^{-3}. This implies that only 1 in 1000 absorptions will result in a destruction of the photon.

The number of absorptions or scatterings that a photon undergoes is proportional to the optical depth. Slater, Salpeter, and Wasserman (1982) have shown that the number of scatterings is nearly equal to twice the optical depth, or

$$N_{\rm ES} \approx 2\tau_{\rm abs}\ . \tag{5.7}$$

The reason why the number of scatterings does not follow a random walk pattern ($N_{ES} \propto r_{abs}^2$) is that not only is there a random walk in space, but also in frequency. An optical depth of 190 will then result in roughly 380 scatterings and the proportion of these that lead to a collisional de-excitation is 0.001. Hence, most of the excited OH molecules will end up undergoing a photon-producing transition which eventually leads to the photon escaping. From this, we can assume that most excitations will lead to the release of a 163 μm photon.

It should also be noted that if there is a strong velocity gradient within the medium, then we must be careful in determining the optical depth. Most of the absorption will be localized, and the effective column density of OH used will be much smaller, leading to a smaller optical depth and to a higher percentage of the photons escaping.

One other component of the molecular cloud that we need to consider is the effect due to the dust component. The photometric observations of Werner et al. (1976) suggests an emissivity inversely proportional to wavelength and equal to unity at 20 μm. Hence, the optical depth of the dust at 163 μm is estimated to be ≈ 0.12, suggesting that the dust is optically thin and most of the 163 μm photons will escape.

5.4.3 The 119 μm Flux: Problems and Solutions

Is the observed 119 μm flux consistent with the 163 μm data? We can obtain an estimate of the expected $^2\Pi_{3/2}$ $J = \frac{5}{2} \rightarrow \frac{3}{2}$ flux in the following way. We stated above that collisional excitation is the dominant mechanism by which the excited states are populated. For the $^2\Pi_{1/2}$ ladder, most of the excited levels ($J > \frac{1}{2}$) will radiatively decay down the ladder; and will ultimately result in the emission of a 163 μm photon. The same argument can be used for the $^2\Pi_{3/2}$ ladder. The total collisional excitation cross-section for the $^2\Pi_{1/2}$ $J > \frac{1}{2}$ ladder is $\approx 3.6\,\text{Å}^2$. For the $^2\Pi_{3/2}$ ladder, $\sigma \approx 7.3\,\text{Å}^2$. Using (5.1), we note that the ratio of the 163 to 119 μm luminosities should be equal to the ratio of the collisional cross sections, since all of the other variables in (5.1) are independent of the transition we are considering.

Hence, if most of the photons escape, the 119 μm luminosity should be

$$L_{119} \approx 1.3\text{–}2.0 \times 10^{48} \text{ photons s}^{-1} . \tag{5.8}$$

From this figure, we find the expected flux at earth to be $6.7\text{–}10.3 \times 10^{-17}$ W cm^{-2}. We measure a total flux that is a factor of 5 to 7 smaller, implying that only about 16% or so of the 119 μm photons actually escape the nebula.

In order to better understand the different processes that can occur, we need to consider what is happening to the 119 μm photons and the OH molecules. The spontaneous emission rate, A_{kj}, for the $^2\Pi_{3/2}$ $J = \frac{5}{2} \rightarrow \frac{3}{2}$ transition is 0.138 s^{-1} per parity state (Brown et al. 1982). This is one path that will lead to a transition from the first excited state to the ground state. A photon is released in the process.

Another photon-producing process is stimulated emission. The emission rate is given by $B_{kj} J_{119}$. Near the surface of the nebula, the mean intensity is simply related to the observed flux. The flux that we observe should be equal to the photon number density times the ratio of the object's solid angle to 4π steradians, and then multiplied by the average component of the speed of light within the solid angle and along the path from the object to the observer, all of this then multiplied by the filling factor. This reduces to

$$n_\lambda = \frac{4\pi \lambda F_\lambda}{h c^2 \delta\Omega g_f} , \tag{5.9}$$

where n_λ is the photon number density, F_λ is the measured flux, and $\delta\Omega$ is the solid angle subtended by the beam. The mean intensity is related to the photon number density via

$$J_\lambda = \frac{h c^2}{4\pi \Delta v} n_\lambda . \tag{5.10}$$

Combining equations, we find

$$J_\lambda = \frac{\lambda F_\lambda}{\delta\Omega \Delta v g_f} . \tag{5.11}$$

There are two sources for J_λ, the OH 119 μm line emission and the emission due to the dust grains. If g_{gr} is the filling factor due to the grains, then we find

that the stimulated emission rate per parity transition is

$$R_{\rm stim} = 5.9 \times 10^{-4}[3.8 g_{\rm f}^{-1} + 8.5 g_{\rm gr}^{-1}]\ {\rm s}^{-1}\ . \tag{5.12}$$

Similarly, we may find the absorption rate , which is

$$R_{\rm abs} = 8.3 \times 10^{-4}[3.8 g_{\rm f}^{-1} + 8.5 g_{\rm gr}^{-1}]\ {\rm s}^{-1}\ . \tag{5.13}$$

We can obtain a very crude estimate for f_0 by assuming that only the first two levels are significantly populated. This assumption leads to 87% of the OH molecules residing in the ground state. We can expect a smaller fraction, and so will assume that roughly 75% of the molecules are in the ground state. The cross-section for absorption is given by (5.6), and is 43.6 Å for the 119 μm photons. The optical depth for absorption is found to be

$$\tau_{\rm abs} \approx 55\, g_{\rm f}^{-1/2}\ , \tag{5.14}$$

where the range is $\pm 23\%$.

Once a 119 μm photon is absorbed, it may be reemitted via spontaneous emission. The photon will travel through the medium in a random fashion, being absorbed and then reemitted many times. As was stated above, the random walk occurs in space and in wavelength. According to Slater, Salpeter, and Wasserman (1982), the actual number of resonant scatters is very nearly twice the optical depth. For this transition, this remains valid until $\tau_{\rm abs}$ approaches values of 10^9 or greater. Hence, the number of scatterings is

$$N_{\rm ES}(119) \approx \tau_{\rm rs} \approx 109\, g_{\rm f}^{-1/2}\ . \tag{5.15}$$

Collisional de-excitations can also lead to a transition to the ground state from the first excited state. The collisional excitation cross-section is roughly 2.5 Å^2 per parity transition (Andresen, Häusler, and Lülf 1984), which means that the de-excitation cross-section is roughly 2.1 Å^2. We have made use of equation (4.49) to

obtain this result. Therefore, the collisional de-excitation rate from the $^2\Pi_{3/2}\ J = \frac{5}{2}$ level to the ground state is given by

$$R_{\rm cd} = \sigma_{\rm cd}\,\bar{v}\,n_{\rm H_2}$$

$$\approx 2.2 \times 10^{-4}\, g_{\rm f}^{-1/2}\ {\rm s}^{-1}\ . \tag{5.16}$$

The optical depth for true absorption is proportional to the number of resonant scatterings, $N_{\rm ES}$. It is, in fact the number of resonant scatterings multiplied by the ratio of the collisional de-excitation (i.e., photon destroying de-excitation) rate to the photon conserving de-excitation rate, or

$$\tau_{\rm true} \approx N_{\rm ES}\,\frac{R_{\rm cd}}{R_{\rm stim} + A} \tag{5.17}$$

For the 119 μm radiation, this reduces to

$$\tau_{\rm true} \approx \frac{10.7}{1 + 2.23\epsilon + 62 g_{\rm f}}\ , \tag{5.18}$$

where ϵ is the ratio of the filling factor for OH to the filling factor for the continuum radiation from grains.

We saw that from the 163 μm data, we expect a factor of ~ 4 times as much 119 μm radiation as we actually observe. This implies that $\tau_{\rm true}$ is on the order of 1.8. We may solve for the OH filling factor, which we find to range from 0.05 to 0.17, depending on the actual 163 μm flux. From this, we find the molecular hydrogen density to be approximately $1.2 \times 10^7\,{\rm cm}^{-3}$, nearly independent of the value that we choose for the 163 μm flux. This implies a column density for hydrogen to be roughly $6 \times 10^{21}\,{\rm cm}^{-2}$ and for OH to be $5 \times 10^{16}\,{\rm cm}^{-2}$. These numbers compare favorably with previous results of Townes et al. (1983) and Watson (1982).

5.4.4 The 84 μm Flux

We must now determine whether the 84 μm data are consistent with the 163 and 119 μm lines and with the parameters which we have determined from the

latter measurements. The Einstein coefficient for spontaneous emission of the 84 μm transition is $A_{kj} = 0.521\,s^{-1}$ (Brown et al. 1982). From (5.6), we can determine the cross-section for resonant absorption of 84 μm photons to be

$$\sigma_{abs}(84) = 53.4\ \text{Å}\ . \tag{5.19}$$

We can then estimate the optical depth for absorption. To do this, we need to know the column density of OH molecules that are in the first excited state ($^2\Pi_{3/2}\ J = \frac{5}{2}$). The fraction of the population in the ground state was estimated to probably be 75%. I will assume that the fraction in the first excited state, f_1, is roughly 20% or less. It then follows that the optical depth for absorption is

$$\tau_{abs}(84) \approx 54\ . \tag{5.20}$$

The collisional excitation cross section from the ground state to the $J = \frac{7}{2}$ state is given as $0.9\,\text{Å}^2$ (Andresen, Häusler, and Lülf 1984). We may estimate the collisional de-excitation rate to be roughly twice that number, or $1.8\,\text{Å}^2$. Then, the collisional de-excitation rate is roughly $7 \times 10^{-4}\,s^{-1}$. The stimulated emission rate can be calculated as in the previous section, and we find that for 84 μm radiation, the stimulated emission rate is

$$R_{stim}(84) \approx 3.1 \times 10^{-3}[g_f^{-1} + 3.8 g_{gr}^{-1}]\ s^{-1}\ . \tag{5.21}$$

The optical depth for true absorption is then found to be

$$\tau_{true} \approx 0.14\ . \tag{5.22}$$

This implies that roughly 86% of the photons will escape the region, while the remainder will be destroyed. The collisional excitation rate from the ground state to the $J = \frac{7}{2}$ state is approximately $3.8 \times 10^{-4}\,s^{-1}$, whereas the spontaneous emission rate is over a factor of 1000 larger. We will assume that collisional excitation is the predominant process which populates this excited upper level. Then, the flux

that we expect to see from each of the 84 μm parity lines is found to be between 1.2 and 3.3×10^{-17} W cm^{-2}. We are nearer to the lower limit in the actual detections, which indicates that the 163 μm flux is probably closer to 1.2×10^{-17} W cm^{-2}.

5.4.5 The 13.4 GHz Data

One final set of OH data which we must consider is that of the $^2\Pi_{3/2}$ $J = \frac{7}{2}$ $F = 4^+ \rightarrow 4^-$ Λ-doubling transition at 13.4 GHz (Matthews et al. 1984). The 13.4 GHz line was found to have a width of 25 km s^{-1}, and the field of view was 2'.1. We may assume that most of the flux was coming from a more confined region comparable to our beam size of ~1'. The flux estimate for this particular transition is 0.09 Jy. This corresponds to a photon flux of 1.0×10^{-2} photon cm^{-2} s^{-1}. From the 3 K background, there is a photon density of 7×10^{-10} cm^{-3}. The spontaneous emission rate is 9.3×10^{-9} s^{-1}, while the stimulated emission rate is 3.4×10^{-8} s^{-1} (Destombes et al. 1977). One can determine the expected flux from this transition by the following method. Assume that all of the $^2\Pi_{3/2}$ $J = \frac{7}{2}$ $F = 4^+ \rightarrow 4^-$ flux is coming from a 1' region centered on BN-KL. We know that for the J= $\frac{5}{2}$ level, the population fraction is about 20%. If we assume that the $J = \frac{7}{2}$ level population is down by another factor of ~5, then we expect the level to contain about 4% of the OH. Knowing the emission rate, we then can deduce that the expected flux is $\sim 1.2 \times 10^{-2}$ cm^{-2} s^{-1}. This takes into account the fact that only one polarization was observed. The measured flux is about 20% less than this value, suggesting that at least to first order we have a consistent picture of the OH emitting region.

5.5 Shocked vs. Post-Shock Gas: A Quandary

5.5.1 Statement of the Problem

The FIR rotational lines of CO have been used to trace out the hot shocked gas (T ~1000 K). These lines have excitation temperatures on the same order. According to Draine and Roberge (1982), an enhancement of OH in the shock front is to be expected, primarily due to accelerated production. Since the line widths of OH (as determined by Watson 1982) are similar to those of the hot, shocked CO,

we may assume that these two molecular species are coexistent.

This is not surprising, but an equally, if not more, important component was not included in the previous analysis. In the post-shock region which extends for roughly 10^{17} cm in radius (Genzel 1985), the gas is warm ($T \sim 100$ K, as determined by numerous observations of molecules such as HCN, SiO, NH_3, etc.) and the OH abundance is roughly 1/40 that in the shock front. However, since the lower lying transitions that have been measured in OH have excitation temperatures of only 250 K or less, these molecules can contribute a great deal to the emission mechanisms. Since the total column density in this region is greater than that from the shock front, this component may actually dominate.

This section will deal with this component of the region, proceeding through the same analysis as before, but for a warm gas in a region of size 1×10^{17} cm.

5.5.2 The Post-Shock Treatment

Once again, we begin with the 163 μm flux. Using the same arguments as before, we find that

$$n_{H_2} \approx 1.87\text{–}2.35 \times 10^6 \, g_f^{-1/2} \, f_0^{-1/2} \; cm^{-3} \; . \tag{5.23}$$

Much of the difference in the numbers lies with the collisional excitation rate, which is proportional to $\bar{v}$, the average relative collision velocity. This is decreased by a factor of about 3, due to the decrease in temperature.

When we redo the analysis for the 119 μm line emission, we find the following to occur. Since the thickness of the region, d, is much larger, the optical depth for resonant scattering is much larger. This will in turn drive the filling factor down, since the optical depth for true absorption remains unchanged. This is, indeed, what we see. The filling factor now varies over a range between 0.041 and 0.074. The molecular hydrogen density, however, is nearly constant over this range, and is given by

$$n_{H_2} \approx 1.0 \times 10^7 \; \mathrm{cm}^{-3} \; . \tag{5.24}$$

This leads to upper limits for the H_2 and OH column densities of

$$N_{H_2} = 1.0 \times 10^{24} \text{ cm}^{-2}$$

$$N_{OH} = 2.1 \times 10^{17} \text{ cm}^{-2} \quad (5.25)$$

Again, the 84 μm line is consistent with this picture, and implies that the 163 μm flux is probably closer to its lower value of 1.2×10^{-17} W cm^{-2}. The 13.4 GHz flux is also predicted by this model.

Although the hydrogen column density is high, this is due to the assumption that the region is uniform in the direction of d, which is now 10^{17} cm long. Most likely, this is not the case. If the region is uniformly clumpy, then we can reduce the column density by a factor of ~ 3. The mass of hydrogen associated with this OH-emitting region is roughly 13 $M_\odot$. This agrees rather well with estimates from CO lines and MHD models. More about this will be discussed in the next chapter.

We see that we can explain the OH observations with two very different models. It is not clear which one is actually correct, or if both regions can be contributing to the observed fluxes. More data are needed in order to understand the OH emitting regions, especially data from the higher level transitions. MHD models of OMC-1 that have been run indicate that it is the post-shock gas that contributes most of the 119 μm photons. This is most likely also true of the 84 μm and 163 μm photons. These transitions may help trace out the OH emitting regions in the warm gas.

5.6 A Measurement of Hot, Shocked CO in Orion: The J = 15 → 14 Observation

5.6.1 Inspiration

Carbon is one of the most abundant elements with Z>2 in the interstellar medium. Although it is not known how much carbon is tied up in grains, CO is one of the end products of carbon chemistry. CO is ubiquitous in the Galaxy, a fact that has enabled several surveys of the galactic plane to be conducted, looking at

the 2.6 mm $J = 1 \rightarrow 0$ transition.

The bond between the carbon and oxygen atoms is strong, requiring about 11 eV to dissociate. Because of this, CO is the dominant carbon-bearing molecule in the ISM. CH, on the other hand, has a bond energy of about 4.2 eV.

There has been a host of CO observations toward OMC-1, covering transitions with excitation temperatures of several degrees Kelvin to over 3000 K. These data tell us much about the molecular cloud and its structure. The high J transitions must arise in the shocked gas and from any post-shock gas that has not cooled considerably.

The millimeter observations of the low J transitions of CO have shown a narrow spike and a broader plateau region in the spectra. The spike has a width of $\approx$5 km s^{-1}, whereas the plateau region has a FWHM from 30 to 150 km s^{-1} (Schultz et al. 1985; Phillips, White, and Watt 1982; Zuckerman, Kuiper, and Rodriguez Kuiper 1976). The spike is ubiquitous in a region covering many arc minutes in angular extent (Zuckerman and Palmer 1975). In contrast, the plateau region which is centered on the BN object is about 36″ in size when measured in the $J = 1 \rightarrow 0$ transition (Solomon, Huguenin, and Scoville 1981). Estimates of the size of the plateau region by interferometric means using CO brings this value down to roughly 17″ (Masson et al. 1984). For higher J transitions, the source size seems to be appreciably larger, $\sim$1′.5 (Storey et al. 1981). The spike feature is not pronounced toward the BN region for $J > 6$. This is indicative of the spike originating in a cool, quiescent region. The fact that high J transitions ($J = 34$) have been seen (Watson et al. 1985) implies that the plateau feature originates in a hot part of the cloud. Since H_2 measurements show regions of peak intensity near the edge of the plateau emitting region (Solomon, Huguenin, and Scoville 1981; Beckwith et al. 1978), this strongly suggests that this hot component is due to shocked or post-shock gas at temperatures up to 2000 K.

McKee et al. (1982) have shown that the higher J transitions for CO should be optically thin. One of the conclusions of their paper is that the CO transitions for $J \sim 15$ are rather insensitive to temperature and density, once the critical values of both parameters are reached. Such is the case in Orion. Hence, it is possible to

obtain from the measurement which we report in this paper the mass of hot shocked CO in the nebula.

The CO observations that were available in 1982 led Watson (1982), Chernoff, Hollenbach, and McKee (1982), and Draine and Roberge (1982) to attempt to fit the data with a model. Watson's model consisted of a two component system (warm and hot, corresponding to post-shock and shock) while the other two models employed MHD shocks with shock chemistry and evolution. The results showed that a fit to the data was possible. Since the low J transitions arise from the whole molecular cloud—hot, warm, and cold gas—and since these lines are optically thick, the fits to the data from these regions are sometimes not very good.

We were inspired to make the 173 μm observation for three reasons. The first is that according to the fit to the data, the shocked region has a temperature of roughly 1000 K. In this temperature region, the intensity of this CO transition is nearly independent of density over the range that is expected for Orion (McKee et al. 1982). We can determine the amount of molecular hydrogen that is associated with the hot CO by finding the amount of CO present, and then extrapolating to hydrogen. This was first done by Stacey et al. (1983), using the $J = 17 \rightarrow 16$ transition at 153.3 μm.

The second reason for observing the 173 μm line was to extend the FIR observations that have taken place to a longer wavelength. Before this observation, no detections of spectral lines longward of 163 μm had been made in the FIR. This detection constitutes the first beyond 163 μm and, as a result, is the first astronomical detection of the 173 μm CO feature.

The third reason that this line was observed was for calibration purposes for our instruments. Since this line was expected to be bright, it was an obvious choice to use in order to help us calibrate the grating spectrometer and interferometer. During the same flight series, we also observed several other objects, some at wavelengths out to 175 μm. Since these lines were expected to be weak, the calibration of the grating spectrometer was essential to have optimum throughput.

5.6.2 The Observations

On the night of 1985 January 23–24, we observed the BN–KL region using the KAO, flying at an altitude of 12.5 km. The beam-size was $1'$ square. During the integration time, some mild turbulence was experienced, causing the beam to wander about the source. This meandering was only occasional, and was no larger than roughly $15''$ at worst. Since the CO source is believed to be slightly larger than $1'$, this should not have affected the results very much. However, turbulence in the atmosphere means changing boresight water vapor, and that can introduce fluctuations in the signal strength.

Figure 5.7 shows the resulting spectrum at this wavelength. Telluric water vapor features occur near 173.34 and 173.72 μm. In addition, a broad feature lies between 174.24 and 175.09 μm. The calibration of the spectrum was obtained by calibrating on the continuum of Orion (Werner et al. 1976). This calibration was confirmed by a calibration of Venus at this wavelength. The total flux in the line is 4.85×10^{-17} W cm^{-2}.

5.6.3 Interpretation

The excitation temperature of the J = 15 rotational level is roughly 10^3 K. We therefore expect the 173 μm emission to arise from the hot, shocked CO in and near the shock front. The size of the CO emitting region is roughly $1'.5$ (Storey et al. 1981). This implies that the total 173 μm flux that we should measure is about 80% higher than our observed value of 4.85×10^{-17} W cm^{-2}. From this, we deduce that the total photon luminosity of OMC-1 at 173 μm is $\sim 7.5 \times 10^{48}$ photons s^{-1}.

For temperatures and densities that are likely to exist in the shock region, McKee et al. (1982) find that the specific intensity of the CO molecules is $\approx 1.78 \times 10^{-20}$ erg s^{-1} str^{-1} molecule^{-1}. From this we can deduce that there must be $\sim 1.2 \times 10^{53}$ CO molecules in the emitting region. If we assume cosmic abundance of carbon and that approximately 25% of the carbon is in the form of CO (the rest being in grains and other carbon molecules), then the total mass of H_2 is found to be $\approx 1.0\,M_\odot$. This compares favorably with the $1.5\,M_\odot$ which was found for the

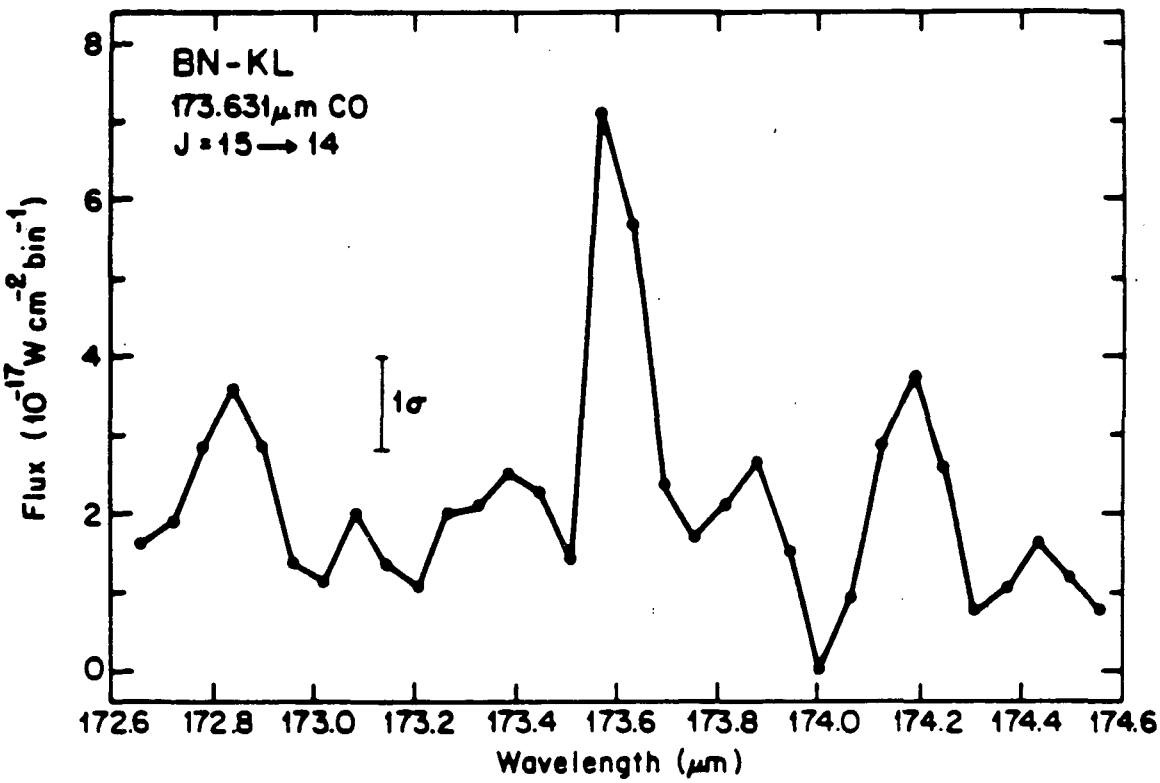

FIGURE 5.7 Spectrum of BN-KL at 173 μm. The $J = 15 \rightarrow 14$ CO emission line at 173.631 μm arises in the hot shocked gas surrounding IRc2. Data were obtained in 1985 January with an integration time of 20 seconds per point. All data were obtained using a 1′ beam.

$J = 17 \rightarrow 16$ transition at 153.3 μm (Stacey et al. 1983), and with the 1.0 $M_\odot$ given by Watson et al. (1985).

5.7 Discussion of Results

5.7.1 The Present Findings

The CO observation fits in well with the rest of the CO data that has been gathered to date on Orion. Table 5.3 lists these data and they are displayed in figure 5.8. We see that the 173 μm line lies on the curve that is a model fit to the data (Watson et al. 1985). Since the region around $J \sim 16$ is nearly independent of density, this line tells us little by itself. It is only when we use it with the rest of the data that we can determine temperatures and densities, and specific intensities from McKee's models. We have been able to determine the mass of hot, shocked gas that is in the Orion nebula. This mass turns out to be roughly 1 $M_\odot$. We may determine the filling factor of CO by using the results of Chernoff, Hollenbach, and McKee (1982). They have found that the shock region contains about 8 $M_\odot$ of gas. This implies that the filling factor is roughly 0.13.

If we assume that the shock front forms a roughly spherical shell around the outflow region, with a size of $\sim 10^{17}$ cm, then we can determine the thickness of this region by using the n_{H_2} densities obtained for the shock region by Watson et al. (1985) and comparing the volume of the shell to that containing 1 $M_\odot$ of hydrogen. This thickness turns out to be $\sim 3 \times 10^{13}\, g_f{}^{-1}$ cm, where g_f is the filling factor for the CO. Plugging in, we get a shell thickness of 2.4×10^{14} cm. That is to say, the hot, shocked CO most likely lies within a shell of minimum thickness 2.4×10^{14} cm. The reason why this is a lower limit is due to the fact that there may be clumping, as suggested by Wynn-Williams et al. (1984) and Geballe et al. (1986). If g_{cl} is the clumping factor (the ratio of the total clump volume to the total volume), then the thickness of the shell will be inversely proportional to g_{cl}. Draine and Roberge (1982) expect a shock front to have a thickness on the order of 2×10^{15} cm. If this is the case, then we can estimate a clumping factor on the order of 0.1.

The OH data do not lend themselves so easily to interpretation as do the

Table 5.3 CO Observations of OMC-1

Transition	Wavelength (in μm)	Beam Size	Intensity (W cm^{-2} str^{-1})	Reference
1–0	2600.76	65″	5.0×10^{-14}	1
		45″	3.3×10^{-14}	2
2–1	1300.40	1′	6.4×10^{-13}	3
		1.′7	1.8×10^{-12}	4
3–2	866.963	55″	3.6×10^{-12}	5
6–5	433.556	35″	2.0×10^{-10}	6
		35″	5.8×10^{-10}	7
7–6	371.650	34″	1.2×10^{-10}	8
15–14	173.631	1′ × 1′	5.7×10^{-10}	9
16–15	162.812	1′ × 1′	7.6×10^{-10}	10
		1′	7.5×10^{-10}	11
17–16	153.267	1′ × 1′	8.3×10^{-10}	12
21–20	124.193	1′	1.3×10^{-9}	13
		60″	1.0×10^{-9}	14
22–21	118.581	1′	2.1×10^{-9}	13
		44″	1.1×10^{-9}	15
26–25	100.461	44″	3.8×10^{-10}	15
27–26	96.7725	60″	6.5×10^{-10}	14
30–29	87.190	60″	2.4×10^{-10}	14
31–30	84.4107	30″	$1.8\text{–}2.6 \times 10^{-10}$	15
34–33	77.0587	44″	8.6×10^{-11}	15

A list of the published CO observations to date toward the BN-KL region of the Orion Molecular Cloud. The reference numbers refer to the following articles: 1) Zuckerman, Kuiper, and Rodriguez Kuiper (1976); 2) Scoville (1981); 3) Wannier and Phillips (1977); 4) Phillips, White, and Watt (1982); 5) Richardson et al. (1985); 6) Goldsmith et al. (1981); 7) Koepf et al. (1982); 8) Schultz et al. (1985); 9) Viscuso (1985); 10) Stacey et al. (1983); 11) Crawford et al. (1986); 12) Stacey et al. (1982); 13) Watson et al. (1980); 14) Storey et al. (1981); 15) Watson et al. (1985).

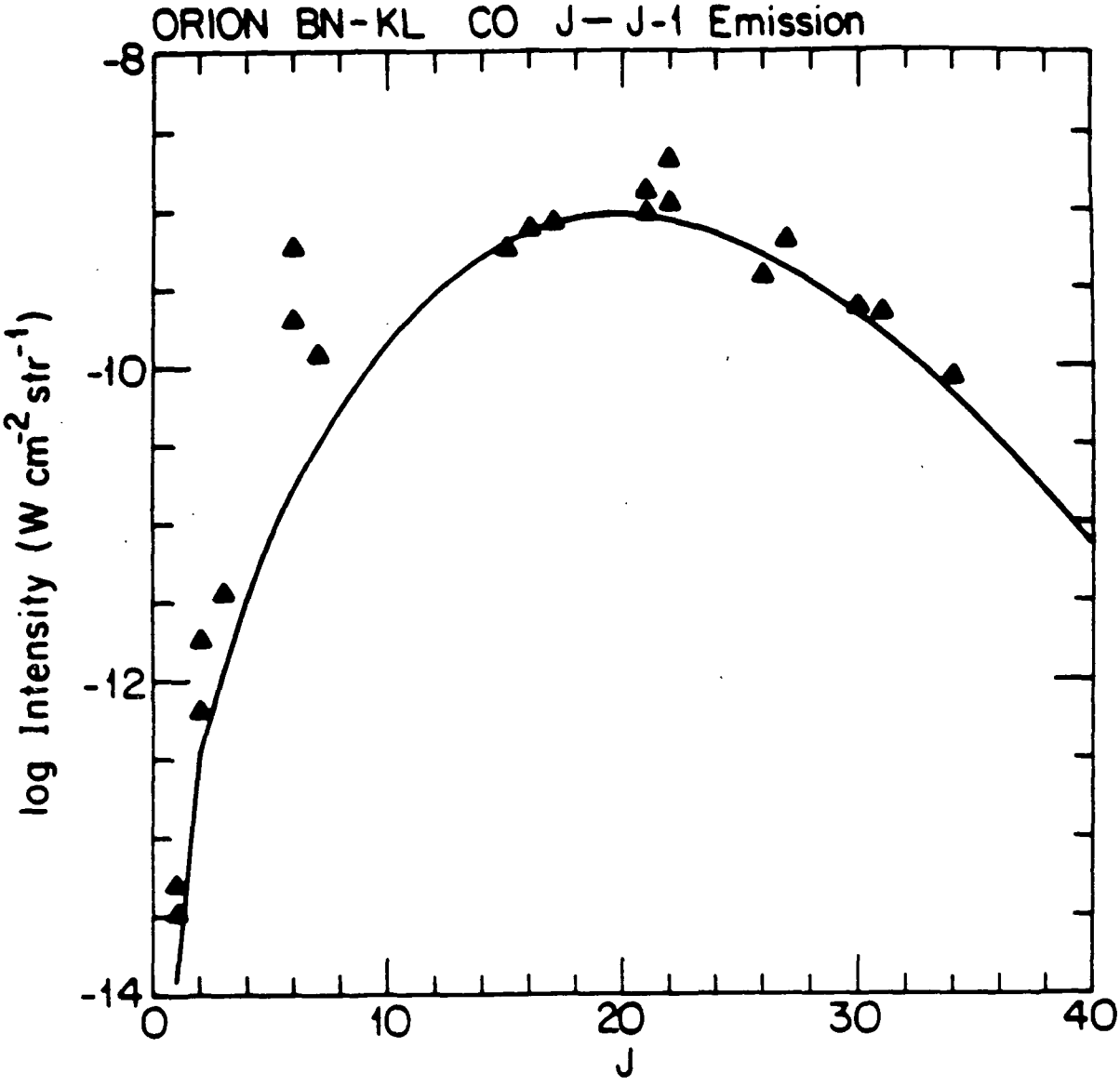

FIGURE 5.8 Plot of the CO intensity towards BN-KL versus the transition ($J \rightarrow J-1$). The solid curve is a theoretical fit to the data from the MHD model of Draine and Roberge (1982). The fit is worse for low J transitions, owing partly to the increasing optical depth with decreasing J. Observational data are listed in table 5.3.

CO data. As we saw above, it is possible to construct two different models of the region that fit the data. Whereas the interpretation that the OH emission arises from the shocked gas was discussed in Viscuso et al. (1985a), Chernoff (1986) favors the post-shock gas as the source of the OH lines. It is unclear which regime makes the more significant contribution, but most likely both are important.

Clearly, the OH lines resulting from highly excited levels will trace out the hot component of the gas. These lines, however, have not been detected with any degree of assurance.

The CO data have helped enormously in directing the way for MHD shock calculations. The model that Watson used in his thesis is based upon a simple escape probability method, which neglects the shock structure and evolution. The fits were not strongly dependent upon temperature, leading to the approximation of an isothermal slab.

Velocity gradients do exist within the flow region, as determined by H_2O masers. Since much of the OH emission may be coming from the post-shock gas, we expect velocity gradients. In fact, it is most likely due to these gradients that the observed line widths ($30\,\mathrm{km\ s^{-1}}$) are a factor of 80 bigger than those expected from random thermal motions alone. The treatment of the region is not necessarily amenable to such a simple radiative transfer model as that above. Following the CO work, it is desirable to perform a numerical radiative transfer study on the OH lines that have already been observed. Such a study can take into account the velocity gradient, as well as incorporate a multi-level molecular structure. The next chapter will deal with just such an endeavor. The goal is to be able to determine whether the OH emission is from the thin shock front or the much more extended post-shock region.

We have demonstrated that it is possible to determine some of the parameters in the OH emitting region. The density of the molecular hydrogen is roughly $1.0 \times 10^7\,\mathrm{cm^{-3}}$, almost independent of temperature. Collisional de-excitation plays a very important role in the destruction of the $119\,\mu$m photons, and a minor role in the frustration of the 84 and $163\,\mu$m flux.

5.7.2 Predictions for the Future

With better signal-to-noise ratios for the 163 and 119 μm lines, we could estimate the relative line fluxes between the two different parity states. From the collisional cross-sections, we should expect the 163.4 μm line to be $\approx$70% as strong as the 163.1 μm transition. For the $^2\Pi_{3/2}$ $J = \frac{5}{2} \rightarrow \frac{3}{2}$ transitions, the 119.2 μm line flux will be $\approx$87% as strong as the 119.4 μm flux. Since the $^2\Pi_{1/2}$ ladder decays slowly to the ground state, we also expect that the lowest levels in this ladder will be populated more than anticipated, and therefore, the 53 μm and the 96 μm fluxes should be higher than the ratios of the Einstein coefficients alone would lead us to expect.

5.8 Other Observations in Orion

During the 1983, 1984, and 1985 winter flight series aboard the KAO, we also undertook a program whereby we searched for FIR emission from several other molecular species, namely CH and CH_2. These two species are important links in the carbon chemistry. The chemistry of shock regions is not very well understood, but the CH and CH_2 fluxes are not expected to be very large owing to small abundances. The carbon chemistry suggests that the CH would readily combine with any atomic oxygen to form CO. This would imply that very little CH would exist. Rydbeck et al. (1976) have found that CH is $\sim$4 times less abundant than OH in extended H II regions; however, with the shocked region in OMC-1, the CH/OH abundance ratio could be wildly different from 1/4. This suggests that the FIR emission lines from these species may be near the limit of detectability.

The observations resulted in no positive detections of any of the lines. We were able to place an upper limit of 1.0×10^{-17} W cm^{-2} on the individual fluxes from the $^2\Pi_{1/2}$ $J = \frac{3}{2} \rightarrow \frac{1}{2}$ CH transitions at 149.09 and 149.39 μm (Brown and Evenson 1983) and the $^3B_1$ $N_{K_aK_c} = 3_{12} \rightarrow 3_{03}$ CH_2 transitions at 148.846, 148.933, and 149.188 μm (Sears et al. 1984).

VI. Escape Probability and OH in OMC-1

6.1 Inspiration

In chapter V, we saw how it was possible to apply radiative transfer to perform back-of-the-envelope calculations on the OH data presently available for OMC-1. The molecular hydrogen density could be determined quite well, but the temperature of the OH-emitting region remains uncertain to within factors of 10 or more. The filling factor is also not very well determined, albeit its fractional range is smaller than that for the temperature.

This state of affairs is not surprising, especially in light of the simplified treatment used in chapter V. In order to more accurately determine the physical parameters of the OH-bearing region, it is necessary to incorporate interactions among all of the populated energy levels in the analysis. This is best done by numerical methods. We expect that the results of the numerical treatment should be close to those of the back-of-the-envelope treatment if the assumptions that were made in the previous chapter are valid.

It is our goal to accurately fit the OH data from OMC-1 by using a one- or two-component model. This model will give us average molecular hydrogen densities and average temperatures for the OH-emitting region. The most straight-forward method used in solving the radiative transfer equations for multi-level, non-LTE (Local Thermodynamic Equilibrium) systems is the escape probability formalism outlined in chapter IV.

6.2 The Radiative Transfer Code

6.2.1 Modus Operandi

The computer code that was written for this task began as an effort by Sean Colgan here at Cornell for analyzing OH maser and H_2CO (formaldahyde)

data. This program was used as a template for our code. We have completely rewritten the code, implementing some streamlining changes and improving the overall rate of convergence to a solution. The program outline follows below.

The equations to be solved are those of (4.79) and (4.80). We need to determine the level populations for a given kinetic temperature and molecular hydrogen density. Other parameters that must also be specified are the total OH-column density, the OH line widths, and any dust or background sources of radiation and their associated parameters, and the charged particle density. The latter sources are known, and we include the dust parameters of Tielens and Hollenbach (1985) and Pipher, Duthie, and Savedoff (1978) in our calculations.

The solution for which we search is the steady-state solution, in which the populations of each energy level approaches a constant value. If we assume that we have k levels, then the rate of change in the population of each level must be zero in the steady-state solution, or

$$\frac{dn_i}{dt} = 0 \ , \quad i = 1, \ldots, k \ . \tag{6.1}$$

If we replace n_i by $f_i(n_1, \ldots, n_k)$, then the set of equations in (6.1) can be rewritten as

$$\begin{aligned} f_1(n_1, \ldots, n_k) &= 0 \\ f_2(n_1, \ldots, n_k) &= 0 \\ &\vdots \qquad\qquad \vdots \\ f_k(n_1, \ldots, n_k) &= 0 \ . \end{aligned} \tag{6.2}$$

To solve this non-linear coupled set of equations for the level populations, we expand the functions in a Taylor series. We shall retain only terms of first order to facilitate the computation of the populations. If we begin with an initial point in solution space, $\{a_i\}$, then we have

$$
\begin{aligned}
0 &= f_1(a_1,\ldots,a_k) + \frac{\partial f_1}{\partial n_1}\delta_1 + \frac{\partial f_1}{\partial n_2}\delta_2 + \cdots + \frac{\partial f_1}{\partial n_k}\delta_k \\
0 &= f_2(a_1,\ldots,a_k) + \frac{\partial f_2}{\partial n_1}\delta_1 + \frac{\partial f_2}{\partial n_2}\delta_2 + \cdots + \frac{\partial f_2}{\partial n_k}\delta_k \\
&\vdots \qquad\qquad\qquad\qquad\qquad\qquad\qquad\qquad \vdots \\
0 &= f_k(a_1,\ldots,a_k) + \frac{\partial f_k}{\partial n_1}\delta_1 + \frac{\partial f_k}{\partial n_2}\delta_2 + \cdots + \frac{\partial f_k}{\partial n_k}\delta_k \,, \qquad (6.3)
\end{aligned}
$$

where the δ_i represent the deviations from a_i. We can now compute the new approximation to our solution from

$$n_i = a_i + \delta_i \qquad i = 1,\ldots,k \,. \qquad (6.4)$$

Using this new solution, we can then go back and repeat the process until the appropriate degree of convergence is achieved. One should note that this process does not guarantee convergence to a solution.

The usual starting point is to assume that we have LTE. From here, we then calculate the partial derivatives and solve the resulting linear set of equations for the δ_i. This solution is accomplished by using a decomposition and backsubstitution scheme. This scheme was borrowed from Press et al. (1986). We then find the new $\{n_i\}$, and repeat the process. For more information concerning the solution of coupled-equations, see Acton (1970) and Press et al. (1986).

Once we have found the solution to the level populations, we use equation (4.80) to derive the expected line intensities for all of the allowed transitions.

6.2.2 Molecular Parameters

The code as it now stands is capable of obtaining solutions for one of three molecular species, OH, CO, or H_2CO. In this thesis, we are concerned only with the first two molecules. Some of the molecular parameters for OH and CO have already

been discussed in chapters IV and V. We briefly mention here other processes that are also necessary to consider.

These involve collisional excitation and de-excitation rates, primarily for collisions with charged particles. For OH, charged-particle collisional excitation rates for transitions in the Λ-doublets have been calculated by Bouloy and Omont (1977, 1979). Charged-particle collisional rates for the transitions between arbitrary levels have also been calculated by Goss and Field (1968). These are used in determining the effects of charged particles in the molecular cloud.

For CO, new and improved collisional excitation rates by molecular hydrogen have recently been published by Schinke et al. (1985). They include rates from $J = 0$ to L. From these rates, we have been able to use the infinite-order sudden approximation (IOS) of Goldflam, Green, and Kouri (1977) to calculate the inter-level rates from J to J'. The IOS approximation is valid for changes in rotational energy much less than the collisional kinetic energy. This means that for large ΔJ, the method breaks down. However, DePristo et al. (1979) showed that it is possible to use the simple IOS formalism with a scaling factor to take the energy difference between levels into account and arrive at collision rates that match those found for more exact calculations. We plan to use these new rates in the near future to redo the fits of McKee et al. (1982) and Watson (1982) to the Orion CO data.

6.3 Preliminary Analysis

It is useful in the interpretation of the results from the code to first determine what we may expect to find under certain conditions. For now, we shall be concerned with the 163, 119, and 84 μm data, in particular, the 163:119 μm and 84:119 μm flux ratios. In this chapter, we shall continue to use the convention that n_i refers to the i^{th} level population divided by the degeneracy.

It is useful to first determine the flux ratios in the case of LTE. The OH will reach LTE if it is strongly coupled to the gas through collisions, i.e., collisional excitation and de-excitation dominate over radiative processes in the final solution for the level populations. Clearly, for a given temperature, if the density is low, then collisions will be few and spontaneous emission will depopulate levels. If the

density is very high, the collisions will occur frequently enough that the population of the levels is little affected by radiative processes. There is a critical density where the collisional excitation rate of a level equals the spontaneous emission rate. For level i, we may write this condition as

$$\sum_{j<i} g_j \, n_j \, n_{crit} \, \gamma_{ji} = \sum_{j<i} g_i \, n_i \, A_{ij} \ , \tag{6.5}$$

where n_{crit} is the critical density of the colliders, which in our situation are hydrogen molecules. The H_2–OH collisional cross-sections are on the order of $1 Å^2$ (Schinke and Andresen 1984), meaning that the collisional excitation rates are on the order of $10^{-12} T^{1/2} \, cm^3 \, s^{-1}$, where T is the kinetic temperature. The Einstein A coefficients for the infrared transitions are on the order of $0.1\text{–}1 \, s^{-1}$ (Brown et al. 1982), leaving us with an estimate of the critical density of

$$n_{crit} \sim 10^{12} \, T^{-1/2} \, cm^{-3} \ . \tag{6.6}$$

For temperatures between 100 and 1000 K, we expect to approach LTE for densities greater than $3 \times 10^{10} \, cm^{-3}$. From our previous analysis of the OH data and the CO results discussed in chapter V, we don't expect densities much greater than $10^7 \, cm^{-3}$. Hence, the OH level populations most likely will not approach LTE.

We would also like to know when the collisional rates become unimportant altogether. We can estimate this lower limit to the critical density by looking at the transitions betweeen the significantly populated levels that have small spontaneous emission rates. These are, for the most part, the Λ-doubling radio transitions. For the lower levels, these A coefficients are on the order of 10^{-9} or 10^{-10}. Hence, the density when collisions begin to contribute to the level populations is roughly

$$n_{min} \sim 10^3 \, T^{-1/2} \, cm^{-3} \ . \tag{6.7}$$

For the expected range of temperatures in OMC-1, n_{min} is on the order of 50 to $100 \, cm^{-3}$. This is at least three orders of magnitude below the inferred density in the region.

It is instructive to find the LTE ratios among the 163, 119, and 84 μm lines. This is accomplished in the following manner. Figure 6.1 shows the energy level diagram that we need to consider. This is a simpler version of figure 4.3, for we are not considering hyperfine splitting or parity splitting of the rotational levels. Using equation (4.80) and neglecting the contribution from the microwave background, we find that

$$\frac{I_{163}}{I_{119}} = \left(\frac{119}{163}\right)^3 \left(\frac{1-e^{-\tau_{163}}}{1-e^{-\tau_{119}}}\right)\left(\frac{n_4}{n_3-n_4}\right)\left(\frac{n_1-n_2}{n_2}\right),$$

$$\frac{I_{84}}{I_{119}} = \left(\frac{119}{84}\right)^3 \left(\frac{1-e^{-\tau_{84}}}{1-e^{-\tau_{119}}}\right)\left(\frac{n_5}{n_2-n_5}\right)\left(\frac{n_1-n_2}{n_2}\right), \tag{6.8}$$

where τ_{119} is the optical depth in the 119 μm line, and so on. Since we are assuming LTE, we may simplify these equations by noting that in LTE,

$$n_{\rm i} \propto {\rm e}^{-E_{\rm i}/kT}, \tag{6.9}$$

where T is the kinetic temperature and $E_{\rm i}$ is the energy of the $i^{\rm th}$ level. Using (6.9), (6.8) becomes

$$\frac{I_{163}}{I_{119}} = \left(\frac{119}{163}\right)^3 \left(\frac{1-{\rm e}^{-\tau_{163}}}{1-{\rm e}^{-\tau_{119}}}\right)\left(\frac{{\rm e}^{(E_2-E_1)/kT}-1}{{\rm e}^{(E_4-E_3)/kT}-1}\right),$$

$$\frac{I_{84}}{I_{119}} = \left(\frac{119}{84}\right)^3 \left(\frac{1-{\rm e}^{-\tau_{84}}}{1-{\rm e}^{-\tau_{119}}}\right)\left(\frac{{\rm e}^{(E_2-E_1)/kT}-1}{{\rm e}^{(E_5-E_2)/kT}-1}\right). \tag{6.10}$$

In the case where all three lines are optically thick, the second term in the right-hand side of (6.10) becomes unity as the source function approaches the blackbody function (Kirchoff's law), and can be written as

$$\frac{I_{163}}{I_{119}} = \left(\frac{119}{163}\right)^3 \frac{{\rm e}^{120/T}-1}{{\rm e}^{88/T}-1},$$

$$\frac{I_{84}}{I_{119}} = \left(\frac{119}{84}\right)^3 \frac{{\rm e}^{120/T}-1}{{\rm e}^{170/T}-1}, \tag{6.11}$$

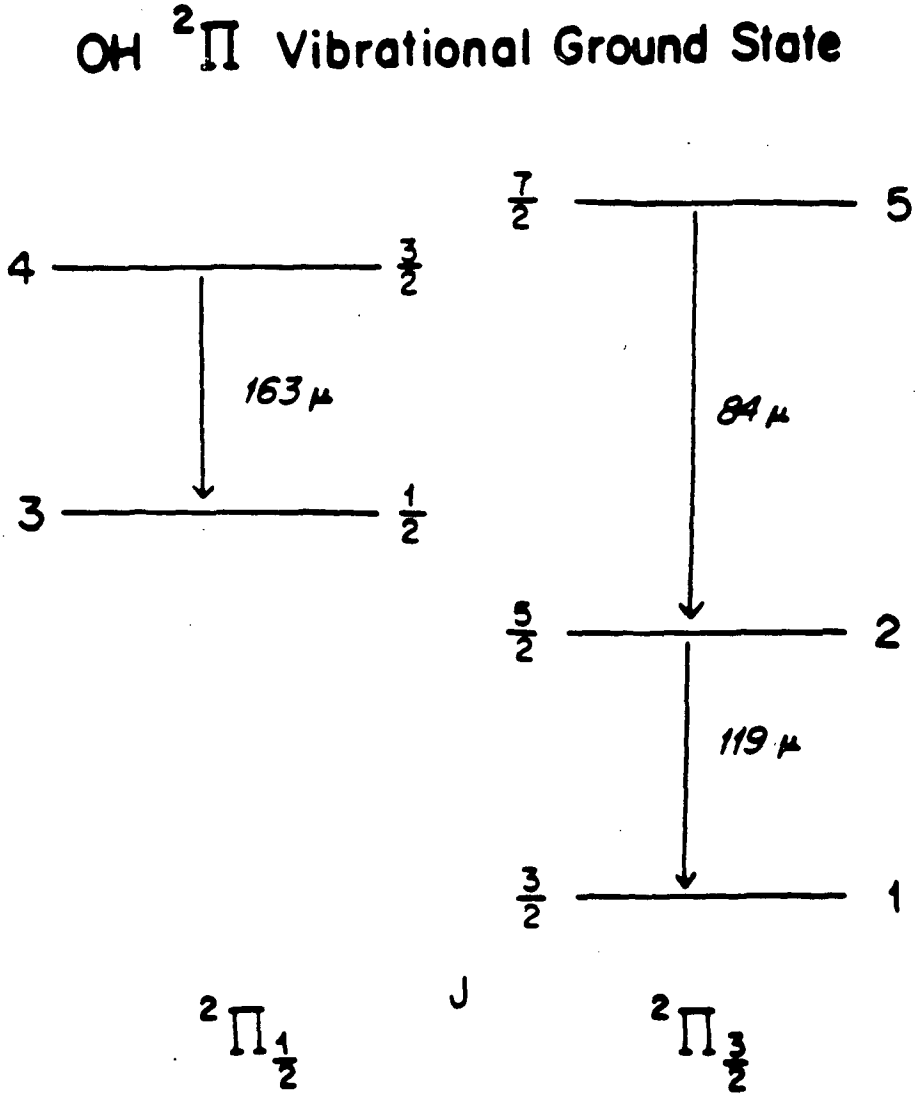

FIGURE 6.1 Simplified OH level diagram used in the determination of LTE level populations. The Λ-doubling of the rotational levels has been ignored. The numbers next to the levels on the outside indicate the level number. (Ground state is level 1, first excited state is level 2, etc.)

where the numerical values in the exponentials represent the energy difference between the appropriate levels in degrees Kelvin. Figure 6.2 shows a diagram of the LTE flux ratios as a function of temperature in the optically thick regime. (The flux ratio differs from the intensity ratio by a factor of (119/163) or (119/84), owing to the inclusion of the line width in determining the flux. We assume a line width that is constant in velocity units.) Above 500 K, the remaining exponentials may be approximated with a MacClaurin series in first order, yielding

$$\frac{I_{163}}{I_{119}} \approx \left(\frac{119}{163}\right)^2 \qquad \frac{I_{84}}{I_{119}} \approx \left(\frac{119}{84}\right)^2 , \tag{6.12}$$

for a hot, optically thick column of OH in LTE. This asymptotic behavior is shown in figure 6.2.

For the flux ratios to be on the order of unity, we note that the temperature must be on the order of 30 K. If the kinetic temperature is warmer, then the 163 μm flux is suppressed relative to the 119 μm emission and the 84 μm flux is enhanced. Conversely, for lower temperatures, the opposite effect is observed.

This analysis suggests that the OH radiation may be coming from the cool post-shock gas at a temperature of about 30 K. I must emphasize that this is merely a suggestion and not a conclusion. The above analysis assumes that the OH is in LTE and that all of the FIR lines are optically thick. The former premise is most likely false, because we must have densities at least 3 orders of magnitude higher than have been deduced from measurements to gain LTE. Most likely, the 119 and 84 μm lines are optically thick, but the 163 μm lines may have optical depths of order unity or less.

At this point in the analysis, we must invoke the aid of numerical methods. There are many different contributors which determine the final populations of the OH energy levels, including the microwave background, the interstellar radiation field (ISRF) impinging upon the molecular cloud from IRc2, BN, KL, all of the other star formation pockets within the region, the Trapezium, and the overall ISRF from the rest of the Galaxy, the radiation field from the warm dust grains within OMC-1, and charged particle collisional excitation, in addition to the spontaneous emission and H_2 collisional processes.

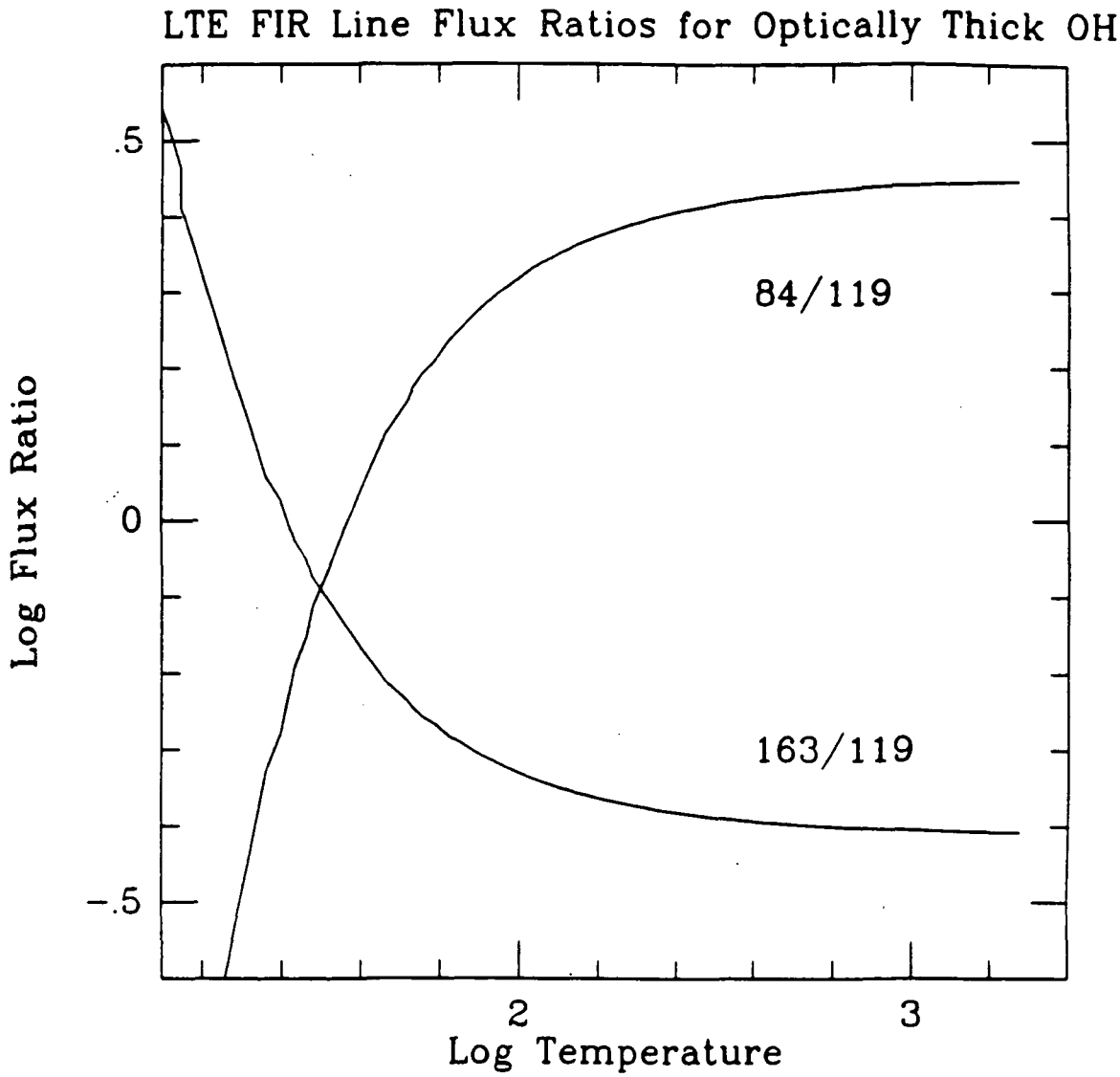

FIGURE 6.2 Flux ratios for optically thick OH in LTE. The ratios are for the 163 to 119 μm and 84 to 119 μm emission lines. We assume line widths of 50 km s^{-1}.

6.4 Numerical Results

6.4.1 Limits to the Physical Parameters

We need to determine some physical limits to the parameters that we can adjust. These parameters are fivefold: the kinetic temperature, the molecular hydrogen density, the electron density, the radiation field from the imbedded stars, and the OH column density divided by the OH linewidth. We assume that the 3 FIR lines originate from the same OH, and so their linewidths in km s^{-1} should be roughly comparable to each other.

The upper limit to the kinetic temperature comes from the H_2 and CO observations of Beckwith et al. (1978) and Watson (1982). This limit is between 1000 and 2000 K, the temperature of the gas in and near the shock front. The OH will exist only in the molecular cloud, so we can discount the high temperatures ($> 10^4$ K) associated with H II regions. We do not expect the gas to be coupled directly to the dust, which is heated by the radiation from the nascent stars, and so a lower limit to the gas temperature can be below 70 K. A lower limit that we will use for the cool post-shock gas is 15 K.

Previous estimates of the hydrogen density are roughly $10^5\,cm^{-3}$ in the pre-shock gas (Chernoff, Hollenbach, and McKee 1982; Draine and Roberge 1982) and $\sim 10^6\,cm^{-3}$ in the hot, post-shock gas (Watson 1982). If we assume pressure equilibrium for the cool post-shock gas, the density could be as high as $10^8\,cm^{-3}$. In order to observe the effects of the collisional processes, we shall include densities from 10^3 to $10^{11}\,cm^{-3}$. At the lower end, the collisions should be negligible in the determination of the population levels. At the upper end, collisions are beginning to totally dominate the radiative processes, and we should begin to approach LTE.

The electron density in the molecular gas is relatively small. However, it can still contribute significantly to the final level populations if the gas is cold. Tielens and Hollenbach (1985) estimate the electron population to be between 10^{-4} and 10^{-6} of the hydrogen density within the molecular cloud. We will assume that this range is correct. Most of the electrons deep within a molecular cloud are generated through the ionization of He and H_2 by cosmic rays, as well as photoionization of

heavy metals such as Mg and Fe. Charge exchange reactions result in the He and H_2 regaining their neutrality while the metals become charged.

The radiation field has several components. The first component is that due to the dust grains. This continuum component has been measured photometrically by Werner et al. (1976); Pipher, Duthie, and Savedoff (1978); and Erickson et al. (1981). The dust is heated by the radiation from nearby stars and converts that radiation to infrared radiation. It is this converted light that gets through to the inner regions of the molecular cloud. This inner region only 'sees' the young O and B stars by the grain radiation. To estimate the contribution from the general interstellar radiation field, we use the results of Mathis, Mezger, and Panagia (1983).

Another parameter which needs upper and lower limits is the OH column density divided by the line width in km s^{-1}. These two variables cannot be separated. However, there are measured values of the line width, yielding somewhere between 30 and 50 km s^{-1} (Crawford et al. 1986; Watson et al. 1985). If the OH emission originates in the post-shock gas, then we do not expect the OH-emitting region to be more than 0.2 parsec long (Genzel 1985; Werner et al. 1976). The post-shock OH abundance is on the order of 2.1×10^{-7} that of molecular hydrogen (see Chapter V). If the hydrogen density is on the order of 10^7, then the resulting OH column density should be less than or about $10^{18}\,cm^{-2}$. We shall use values in the range of 5×10^{14} to $5 \times 10^{18}\,cm^{-2}$. The lower values will help to demonstrate the importance of optical depth in the final solution for the level populations and flux ratios.

Another limit that we can place on the OH column density and abundance ratio is derived from the mass of H_2 that is present in the shocked and post-shock region. If we assume that the OH emission arises from an area roughly $1'$ in size, then we can show that the mass of molecular hydrogen present is given by

$$M_{H_2} = 3 \times 10^{-22}\, g_f \left(\frac{N_{OH}}{\epsilon}\right) M_\odot \,, \tag{6.13}$$

where g_f is the beam filling factor and ϵ is the $[OH]/[H_2]$ ratio.

We can estimate the mass of hydrogen from CO measurements. In the hot, post-shock gas, we know from the analysis in chapter V of this thesis that there is

roughly $1\,M_\odot$ of H_2. This is derived from the high J rotational transitions. The low J transitions will measure not only the hot gas, but also the cooler gas as well. Looking at the optically thin $J = 6 \rightarrow 5$ transition at $433.556\,\mu m$, we can relate the measured line intensity to the column density of CO by

$$I_{65} = \frac{N_{CO}\, f(6)\, A_{65}\, h\, \nu_{65}}{4\pi}\,, \tag{6.14}$$

where $f(6)$ is the fraction of the CO in the $J = 6$ rotational level. From (4.19), we know that A_{65} is about $2.2 \times 10^{-5}\,s^{-1}$. For temperatures ranging from 35 to 300 K, the fraction of the population in the sixth rotational level remains very close to 10% (assuming LTE). Koepf et al. (1982) found the corrected antenna temperature of this line to be about 180 K. The line width was $38\,km\ s^{-1}$, yielding an intensity of $2.3 \times 10^{-10}\,W\ cm^{-2}\ str^{-1}$. The deduced CO column density is $2.9 \times 10^{18}\,cm^{-2}$. If the total size of the region is roughly 0.2 parsec, then the total molecular hydrogen associated with the CO is on the order of $8\,M_\odot$. This assumes that the [CO]/[H] ratio is on the order of 10^{-4}. Since this ratio may be much smaller if more carbon is tied up in grains than we expect, this represents a lower limit to the mass of hydrogen. For the moment, we shall assume that $10\,M_\odot$ of molecular hydrogen is present in the warm, CO-bearing post-shock gas. This mass compares favorably with that deduced from $J = 1 \rightarrow 0$ CO observations (Kwan and Scoville 1976). The mass of hot, shocked and post-shock gas is seen to be negligible.

Assuming that the observed OH is confined to a region roughly $1'$ in size as the data suggest (Watson et al. 1985), we should expect to find the mass of hydrogen associated with the OH to be comparable to that for the CO. We find a lower limit for the hydrogen mass when we assume that most of the OH FIR radiation originates in the thin sheet within the shock front in which the OH abundance is enhanced. If this sheet is 5×10^{14} cm thick, and extends for $1'$ in two dimensions, then by using the density and filling factor that we found in chapter V, we obtain a minimum hydrogen mass of roughly $0.17\,M_\odot$. Remembering that the OH is enhanced in the shock front as opposed to the post-shock gas, we find that this enhancement nearly cancels out the hydrogen mass difference when one is searching for constraints on

the column density of OH. We find that

$$N_{\rm OH} \sim 10^{16}\, g_{\rm f}^{-1}\ {\rm cm}^{-2}\ . \tag{6.15}$$

6.4.2 Analysis of Results

Various runs of the code were made covering the range of parameters listed in the preceding section. These runs were made for a 14 level system, which is quite adequate for temperatures up to about 1000 K. If the kinetic temperature is higher than 10^3 K, then there will be significant population of the higher levels. For these high temperatures, we used a 20 level system.

The Newton method used to find the solution does not guarantee convergence. Although variations on the theme were tried in order to maximize the percentage of converging solutions, this maximum did not exceed 90% for more than 1000 runs. A limit of 50 iterations was placed in the code in order to minimize computational time. This makes it possible that some of these non-converging solutions would have converged if given enough time. Various self-checks in the code guaranteed a non-diverging solution, but these could not guarantee proper convergence. There are several instances where the solution was found for one set of parameters, and a small change of only one input parameter led to a non-converging solution. In these cases, it is sometimes obvious what the final result should be.

Two of the parameters were found to have an insignificant influence in the determination of the level populations. These are the electron abundance and the ISRF. Electron abundances of 10^{-4} or greater will affect the population significantly, but such high abundances are not expected in the region. The general ISRF (not to be confused with the radiation field due to the heated dust grains) also contributes little to the solution. We may therefore ignore these two mechanisms in the ensuing discussion.

This leaves us with 3 parameters to vary, the kinetic temperature, the molecular hydrogen density, and the OH column density divided by the line width in units of velocity. The most straightforward method of approach to the problem is to solve

for the ratio of the line strengths. The ratios of 163 μm to 119 μm and 84 μm to 119 μm line radiation are what we shall consider.

Figures 6.3 to 6.7 show the results of the runs. Displayed is the line flux ratio as a function of H_2 density at several selected temperatures. Each graph is for a different column density of OH. In figures 6.8 to 6.10, the plots are of the ratios as a function of density at several selected column densities. Each of these graphs is for a different temperature.

One should note several trends in these data. For low column densities, one would expect the optical depths to be small. The resulting fluxes are then proportional to the ratio of the optical depths (see equation 6.8). For the 163:119 μm ratio, we observe the following behavior. For low hydrogen densities, we will have few collisions, and the radiative processes shall dominate. The flux ratio will then depend solely on the column density, since the kinetic temperature does not affect radiative processes. We will assume throughout the rest of this chapter that the OH line width is 50 km s^{-1} (Crawford et al. 1986). It should be remembered that the column density parameter for the radiative transfer code is the actual column density divided by the line width.

For low hydrogen densities, as the column density increases, we note that the 163:119 μm flux ratio increases as well, until it reaches a stable value of $\approx$0.48. While it is increasing, the optical depth of the 163 μm line is also increasing. The 119 μm line becomes optically thick rather quickly, unlike the 163 μm line.

When the number density is very high, then we expect the collisions to dominate in determining the steady-state level populations. The final 163:119 μm flux ratio should then be determined by the temperature and the column density of OH. The column density comes into play in determining the line optical depth, and hence the line flux as in (6.8). As all of the lines become optically thick, then the ratio becomes fixed for a given temperature.

As the temperature increases, we see that the trends suggested by our optically thick, LTE model in figure 6.2 are actually obtained. The 163:119 μm ratio decreases as the temperature increases while the 84:119 μm line ratio increases. The actual ratios are quite close to those in our optically thick, LTE model, which is

expected.

In between the two density extremes, we have a region of complicated behavior. For example, if we examine figure 6.5, where the OH column density is $5\times10^{16}\,\mathrm{cm}^{-2}$, we see a trend with the increase in temperature. The peak 163:119 μm flux ratio moves down as the gas becomes hotter. This peak also begins to occur at lower densities, although the density at the peak is weakly coupled to the temperature. The reason for the behavior entails looking at the different populating and de-populating processes in detail. At low temperatures, the collisional processes still dominate in the 119 μm transition. However, radiative processes play the major role for the 163 μm line. As the gas warms up, collisional excitation and de-excitation become important to the 163 μm line, and the collisional processes bring this line flux down. The collisional processes tend to suppress the 119 μm line. Since for low temperatures, only radiative processes contribute to the 163 μm flux while collisions dominate in the 119 μm flux, we get this enhancement in the 163:119 μm ratio.

We do not find this behavior for the low OH column density results (figures 6.3 and 6.4). That is to say, for a particular temperature, the ratio will either monotonically increase or decrease, but it will not have the characteristic bumps shown in figure 6.5. This monotonic behavior is the result of the 119 and 163 μm lines being dominated by the collisional processes at the same densities.

All of the above arguments also hold for the corresponding trends in the 84:119 μm ratio.

6.5 Discussion

We are now in a position to fit the data with a model based upon the results presented above. From the OH data, we know that the 163:119 μm flux ratio is on the order of 1.6 to 2.5, depending on the strength of the 163 μm lines. Most likely, the ratio is nearer to the lower limit. The 84:119 μm flux ratio is roughly equal to 1.6.

We see immediately from the results of our numerical runs that we need to suppress the collisional contributions to the 163 μm transition in order to have such a high flux ratio. In fact, it is only for temperatures less than 50 K that we can

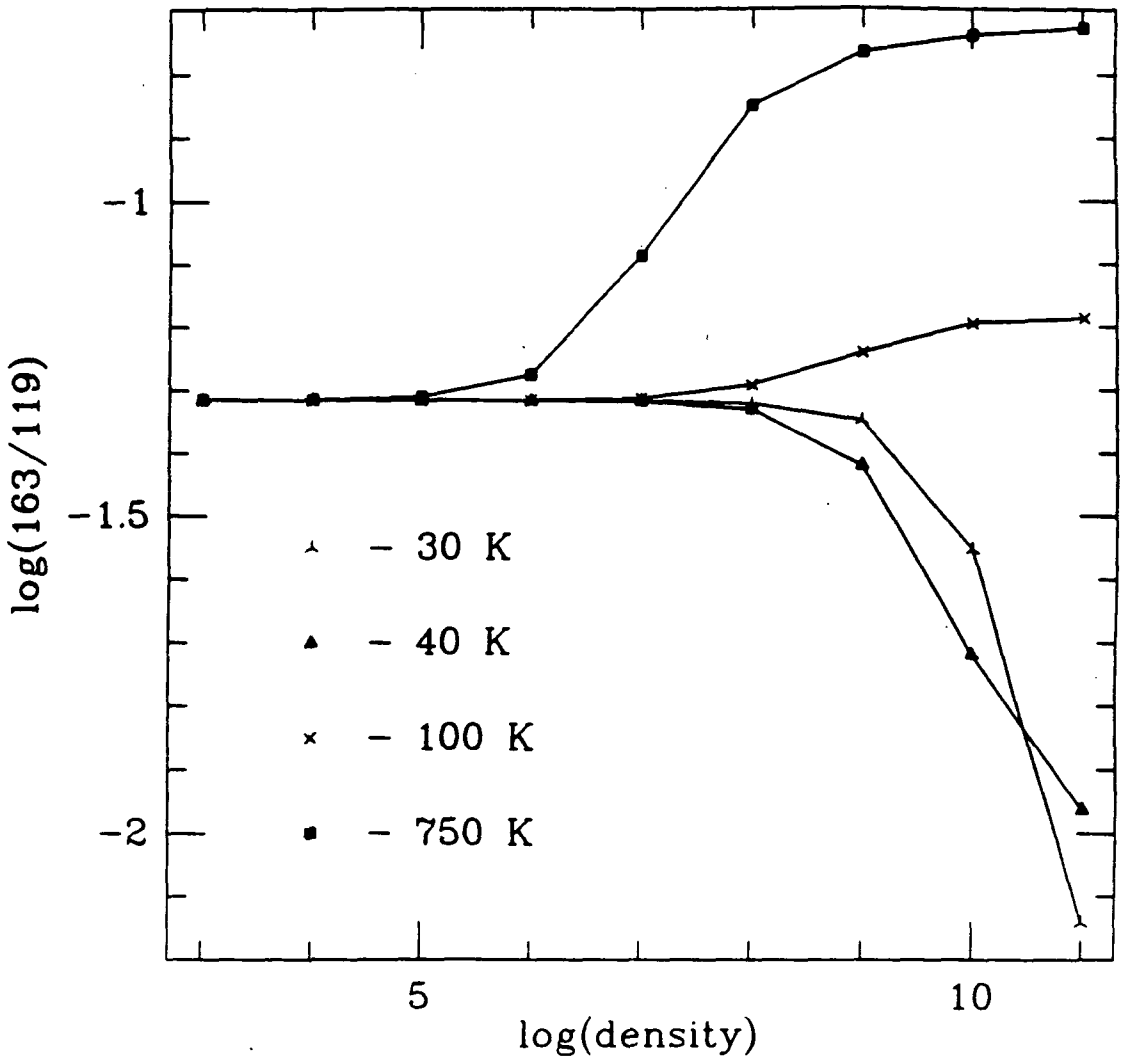

FIGURE 6.3a Flux ratio of 163 to 119 μm OH line radiation as a function of density for several temperatures. The OH column density is $5 \times 10^{14}\,cm^{-2}$. We assume the $[e^-]/[H]$ abundance ratio to be 5×10^{-6}, and use the dust continuum radiation field as found by Pipher, Duthie, and Savedoff (1978).

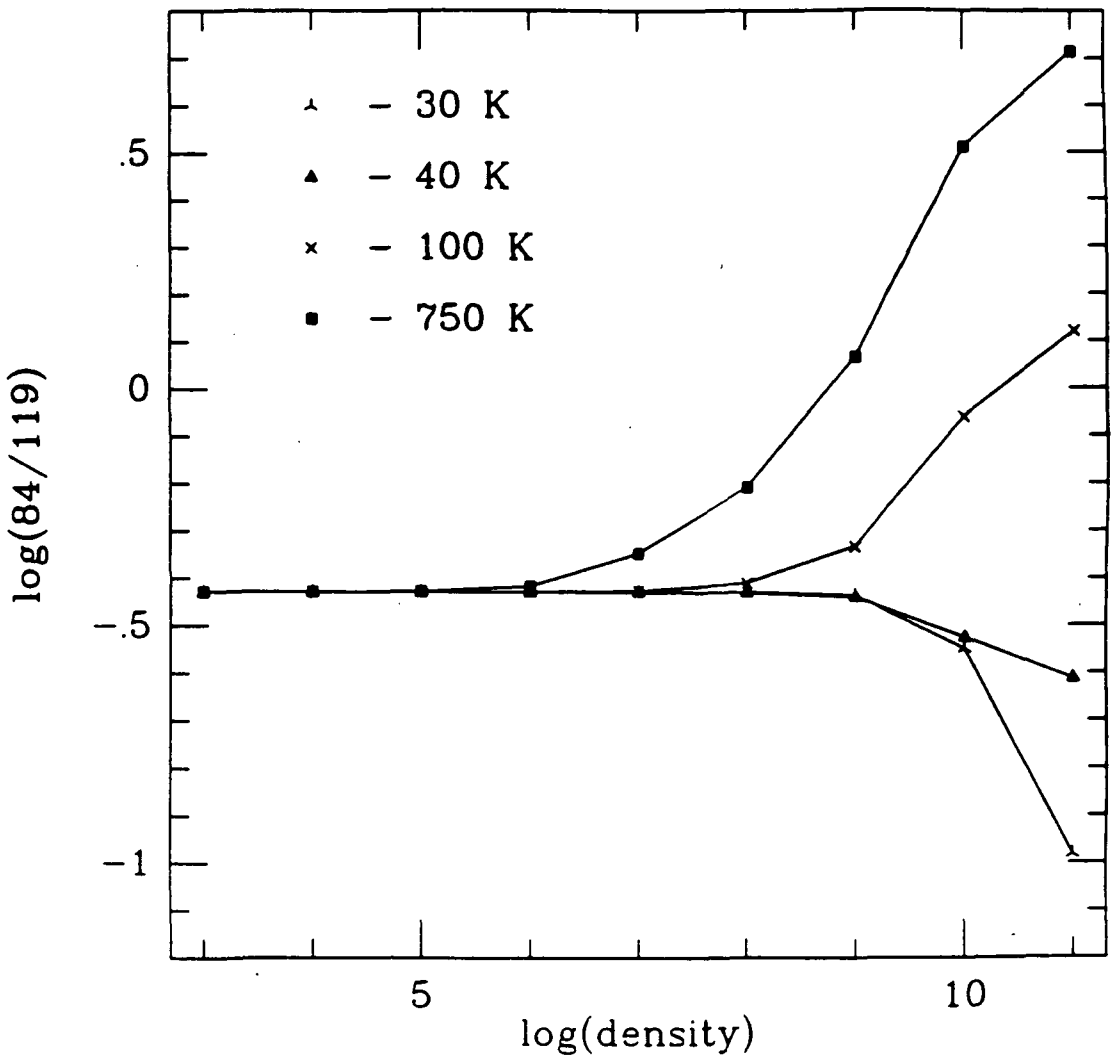

FIGURE 6.3b Same as figure 6.3a, except the line ratio is for the 84 to 119 μm line radiation.

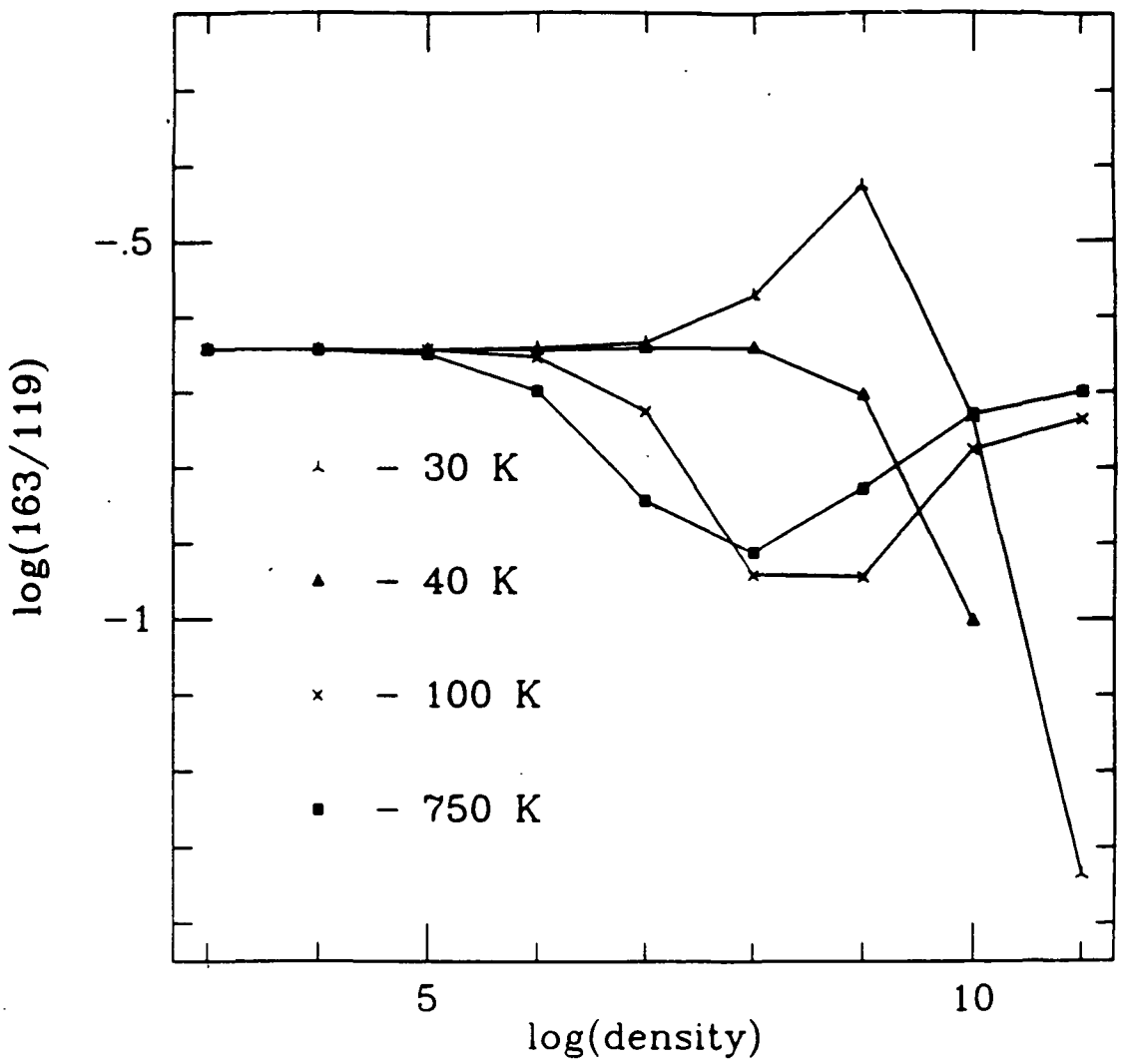

FIGURE 6.4a Same as figure 6.3a, with an OH column density of $5 \times 10^{15}\,\mathrm{cm}^{-2}$.

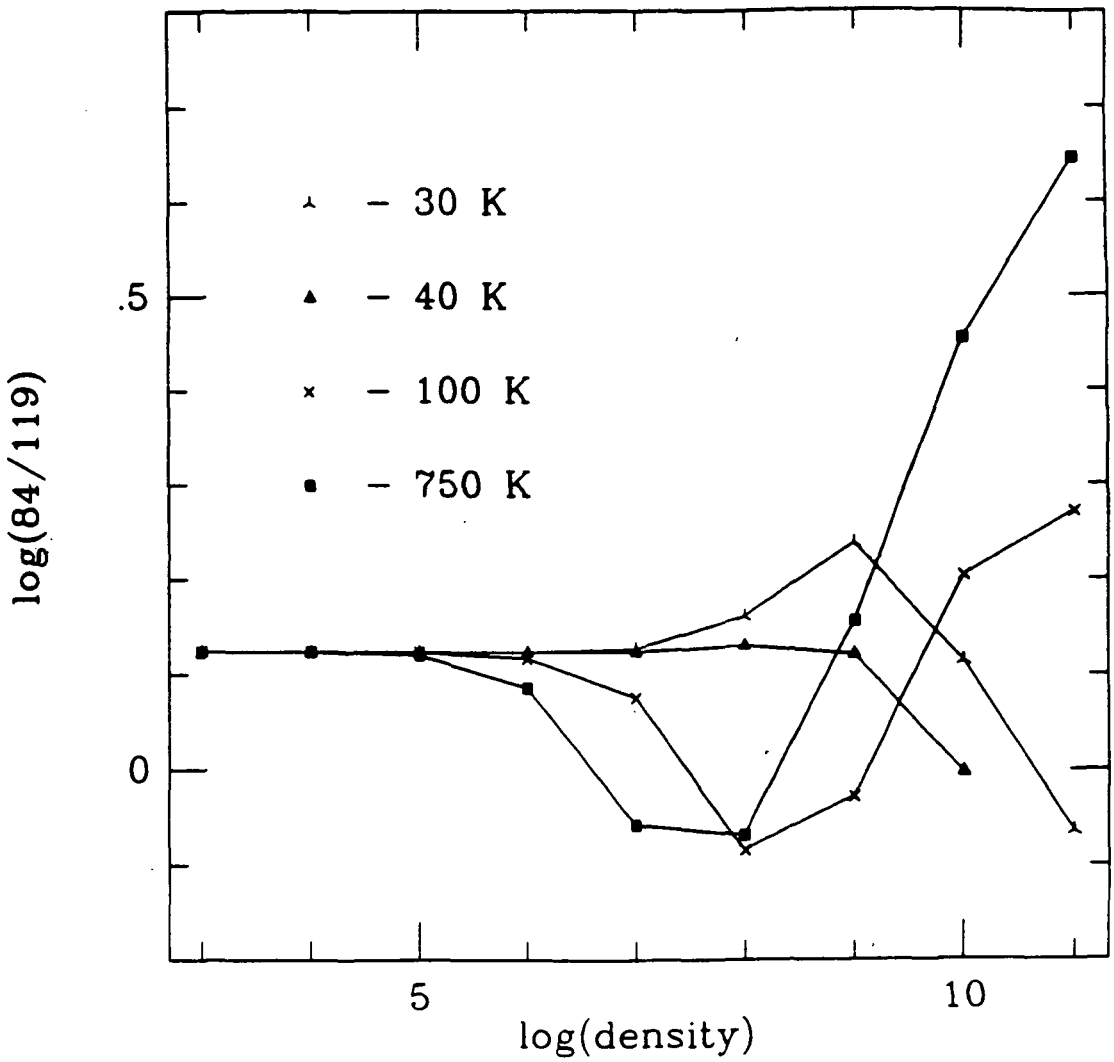

FIGURE 6.4b Same as figure 6.3b, with an OH column density of $5 \times 10^{15}\,\mathrm{cm}^{-2}$.

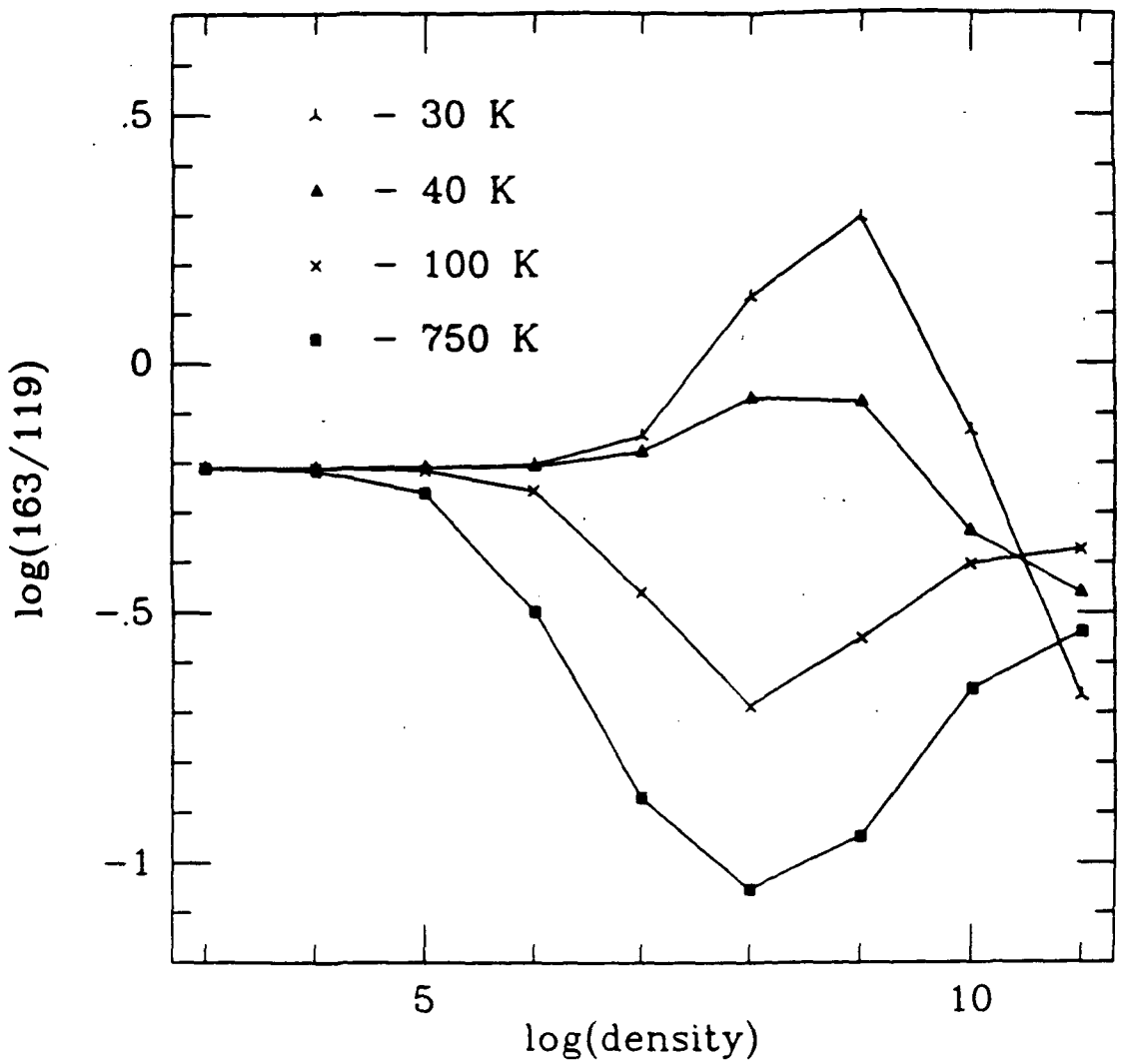

FIGURE 6.5a Same as figure 6.3a, with an OH column density of $5 \times 10^{16}\,cm^{-2}$.

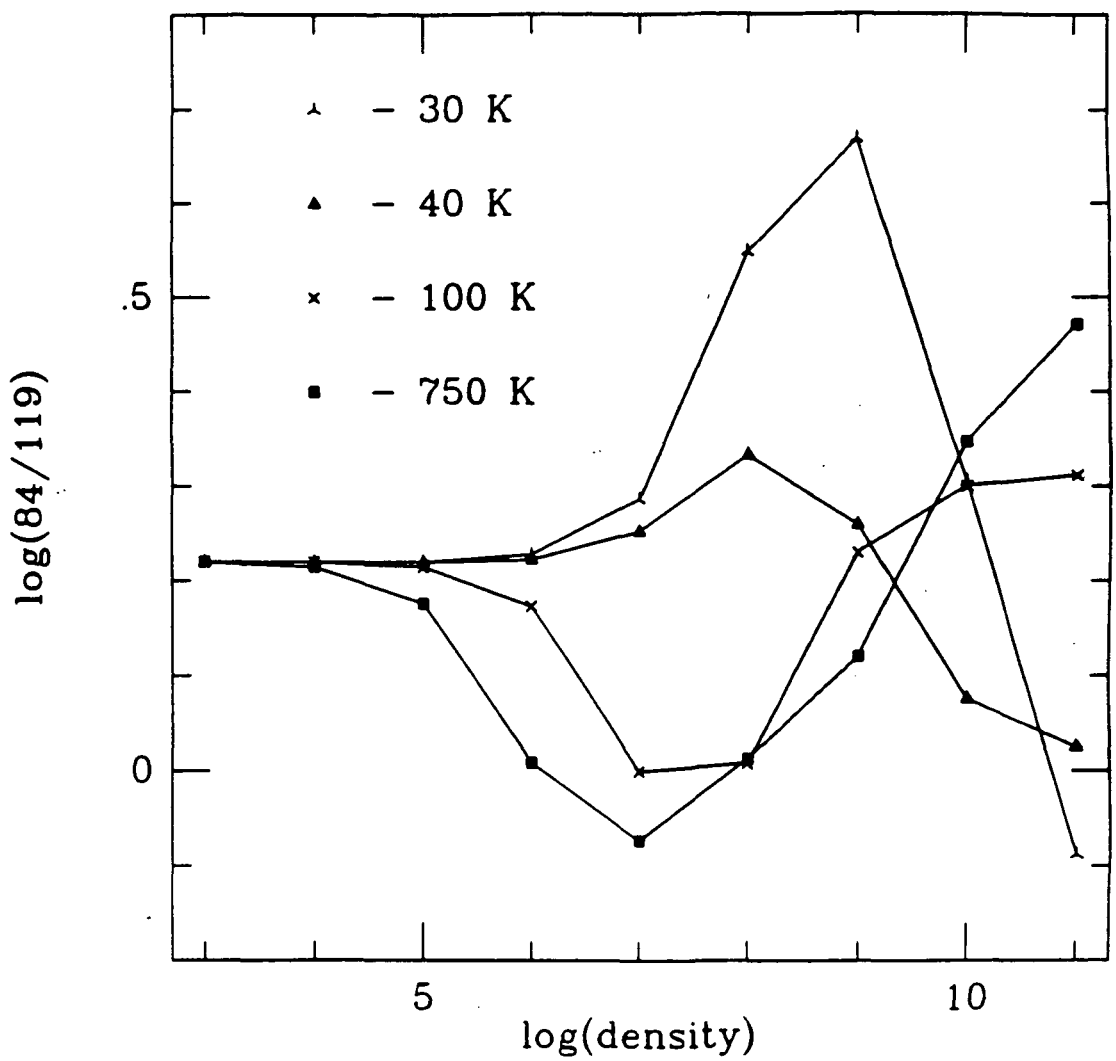

FIGURE 6.5b Same as figure 6.3b, with an OH column density of $5 \times 10^{16}\,cm^{-2}$.

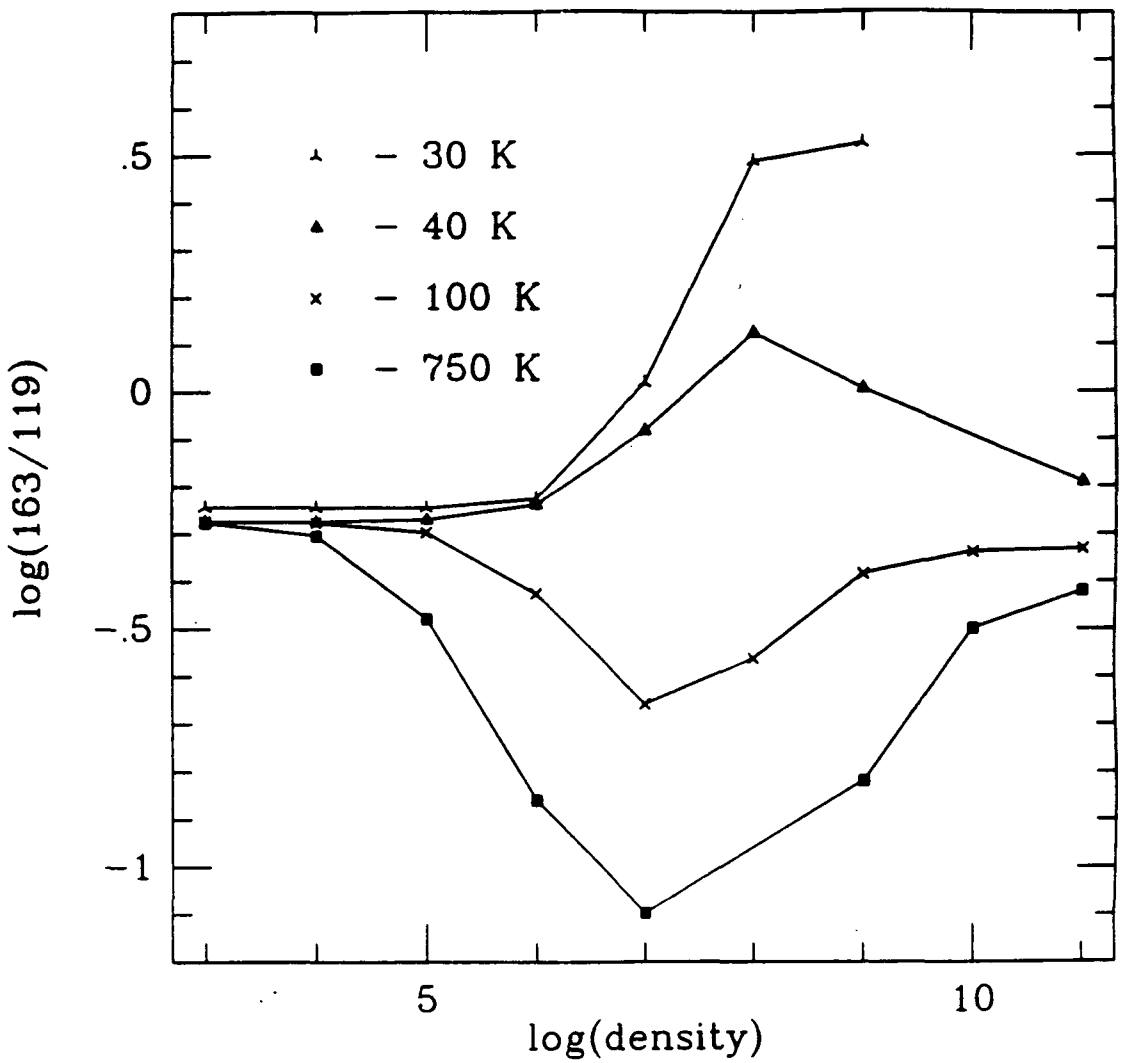

FIGURE 6.6a Same as figure 6.3a, with an OH column density of $5 \times 10^{17}\,\mathrm{cm}^{-2}$.

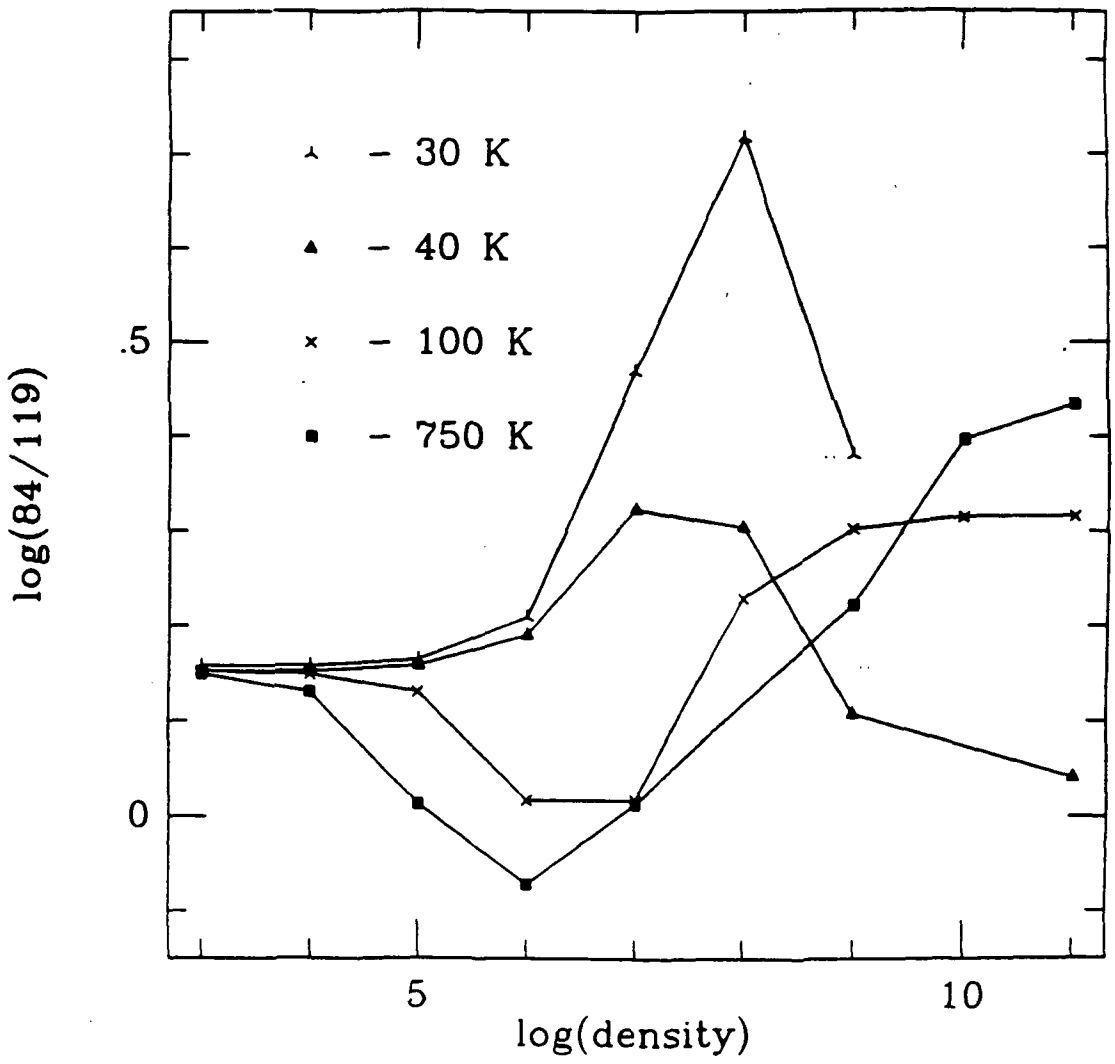

FIGURE 6.6b Same as figure 6.3b, with an OH column density of 5×10^{17} cm^{-2}.

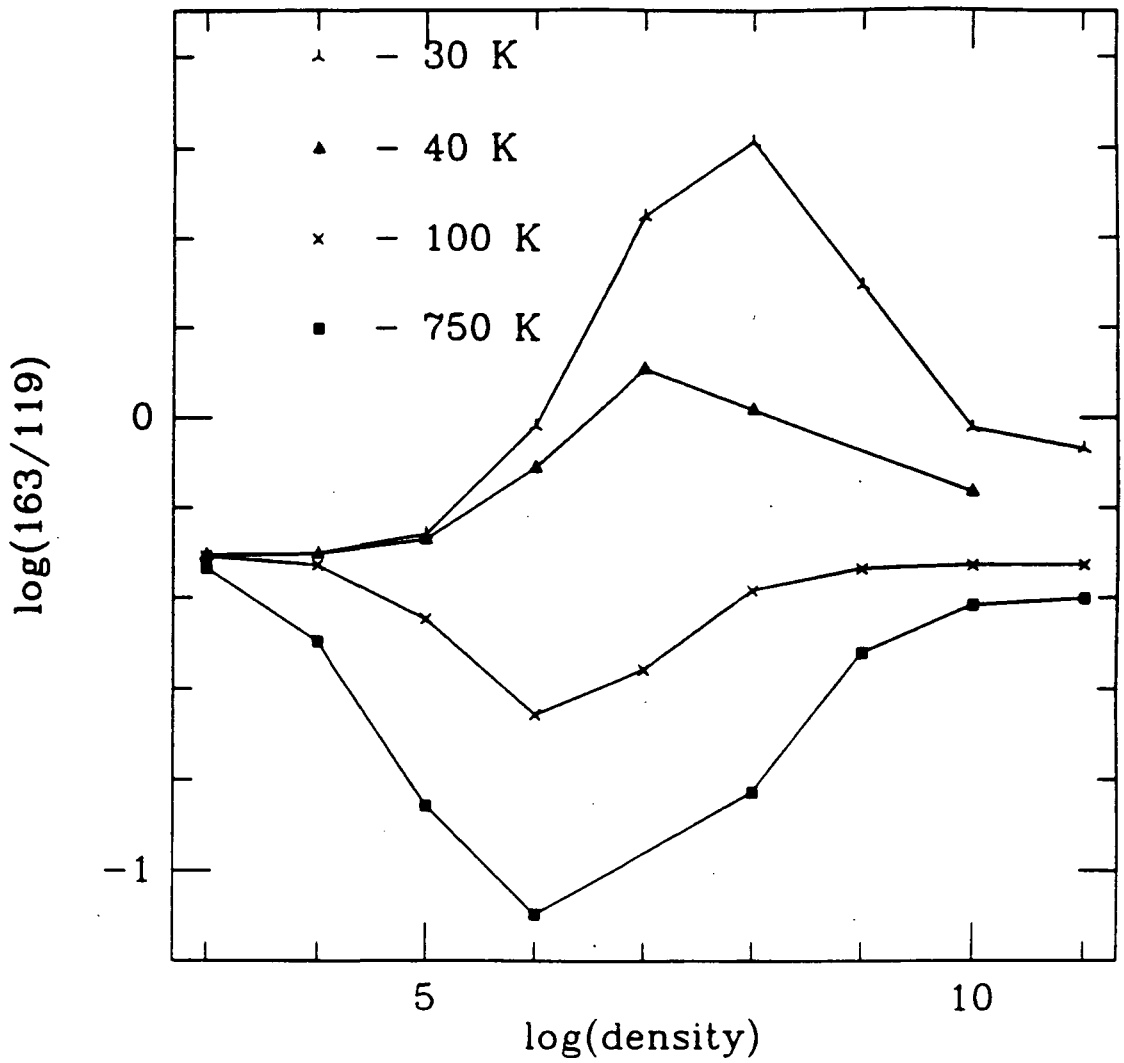

FIGURE 6.7a Same as figure 6.3a, with an OH column density of $5 \times 10^{18}\,\mathrm{cm}^{-2}$.

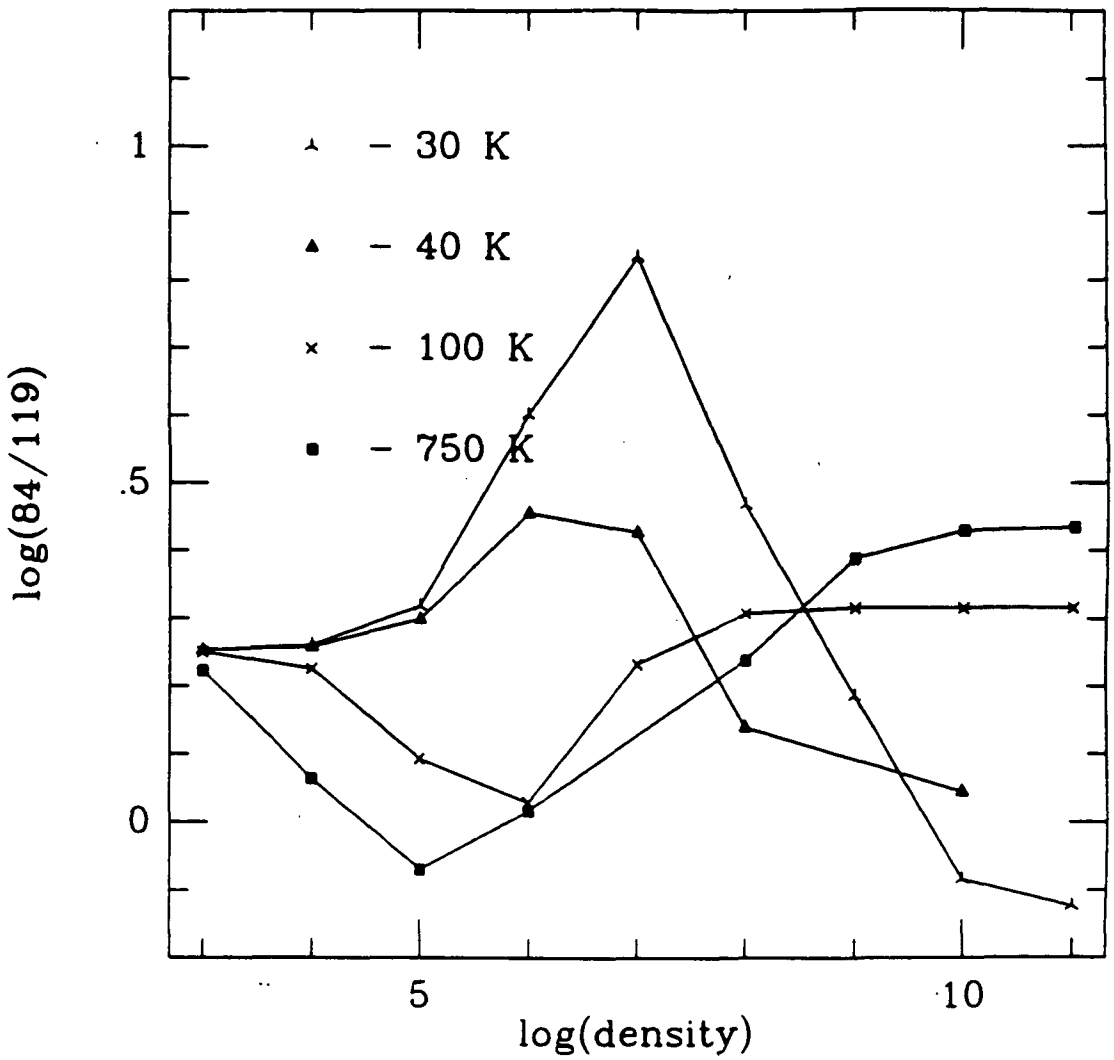

FIGURE 6.7b Same as figure 6.3b, with an OH column density of $5 \times 10^{18}\,cm^{-2}$.

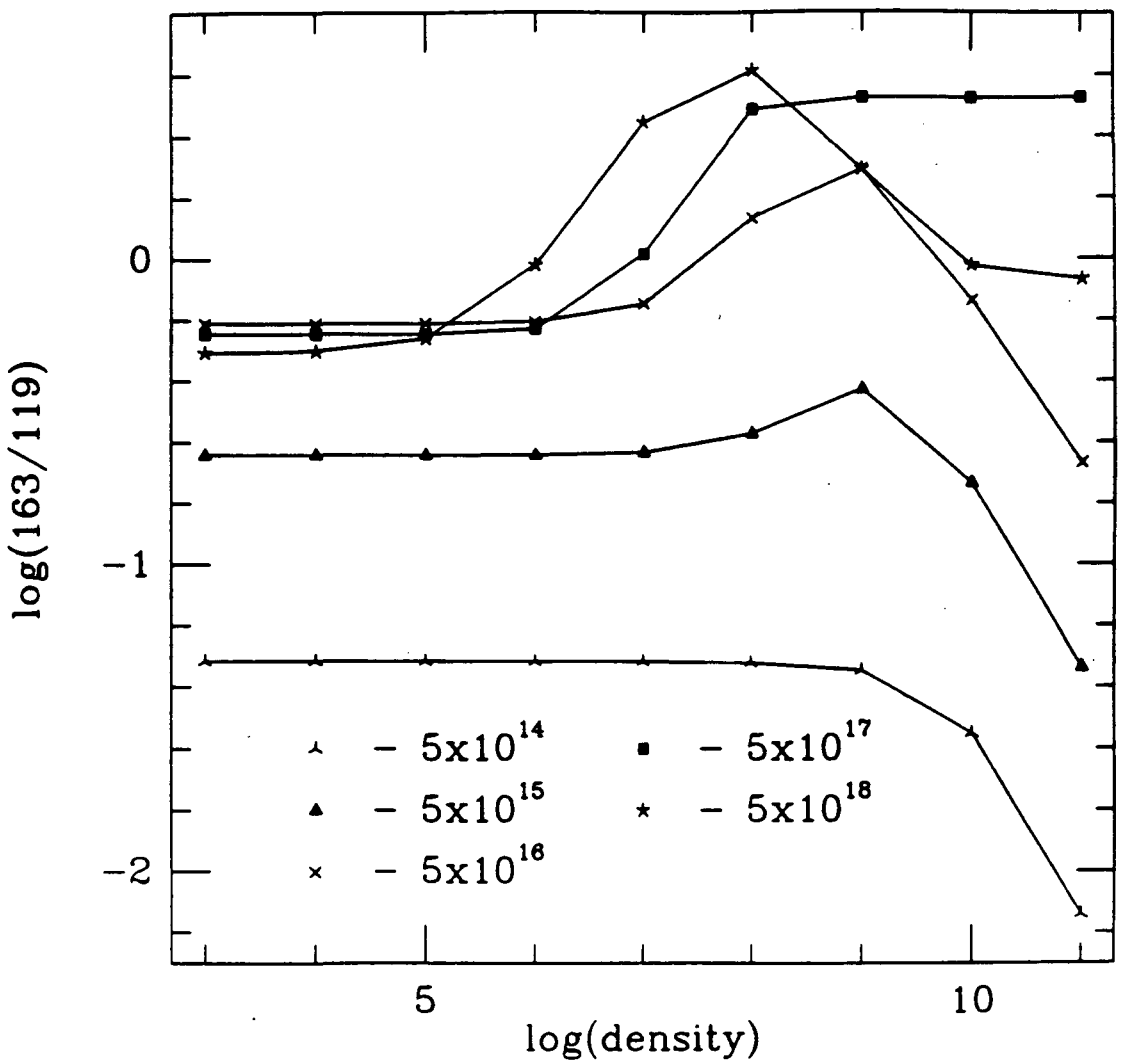

FIGURE 6.8a Flux ratios for 163 to 119 μm line radiation as a function of density for various OH column densities. These data assume a gas temperature of 30 K.

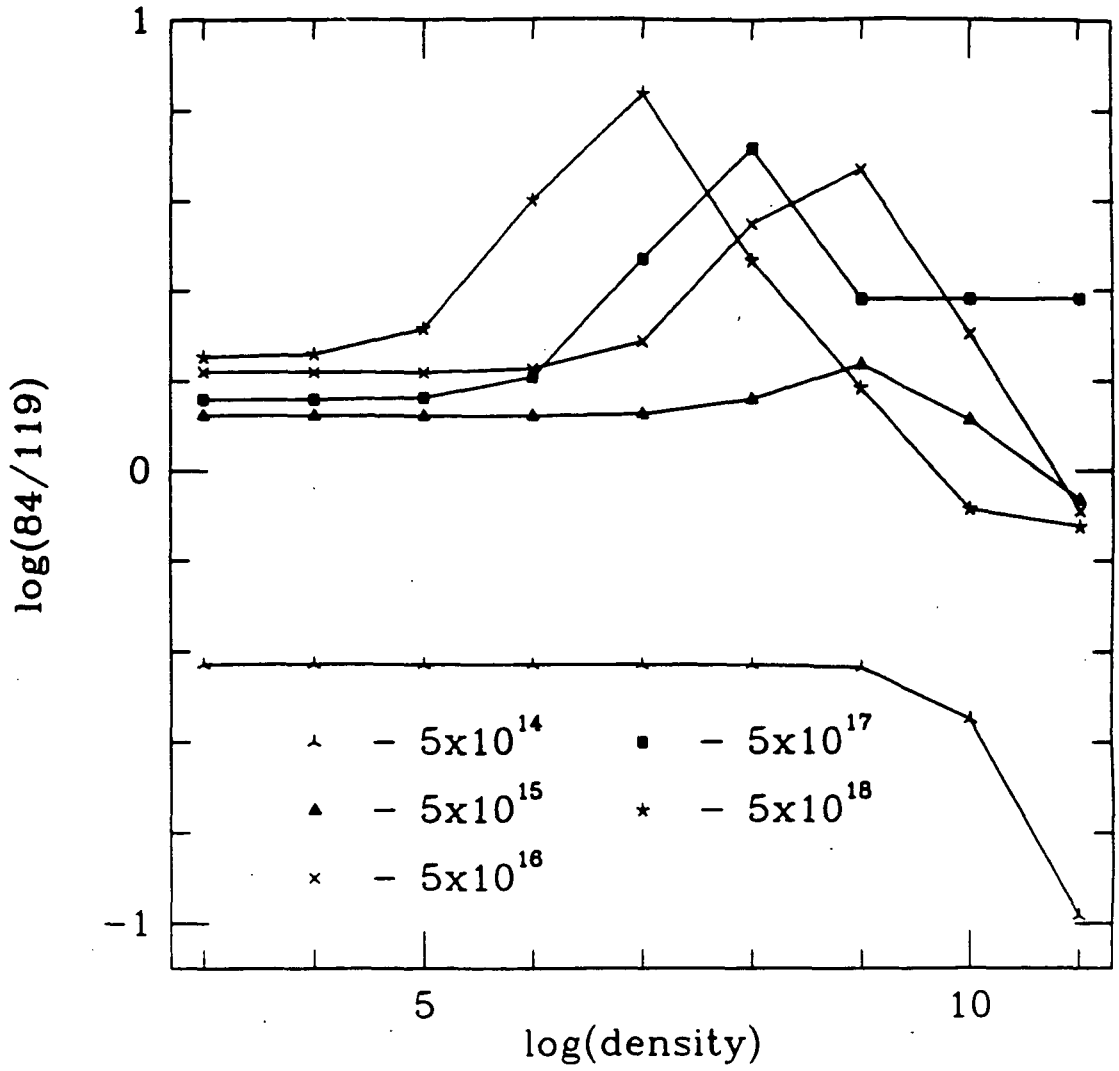

FIGURE 6.8b Same as figure 6.8a, except the line ratio is for the 84 to 119 μm line radiation.

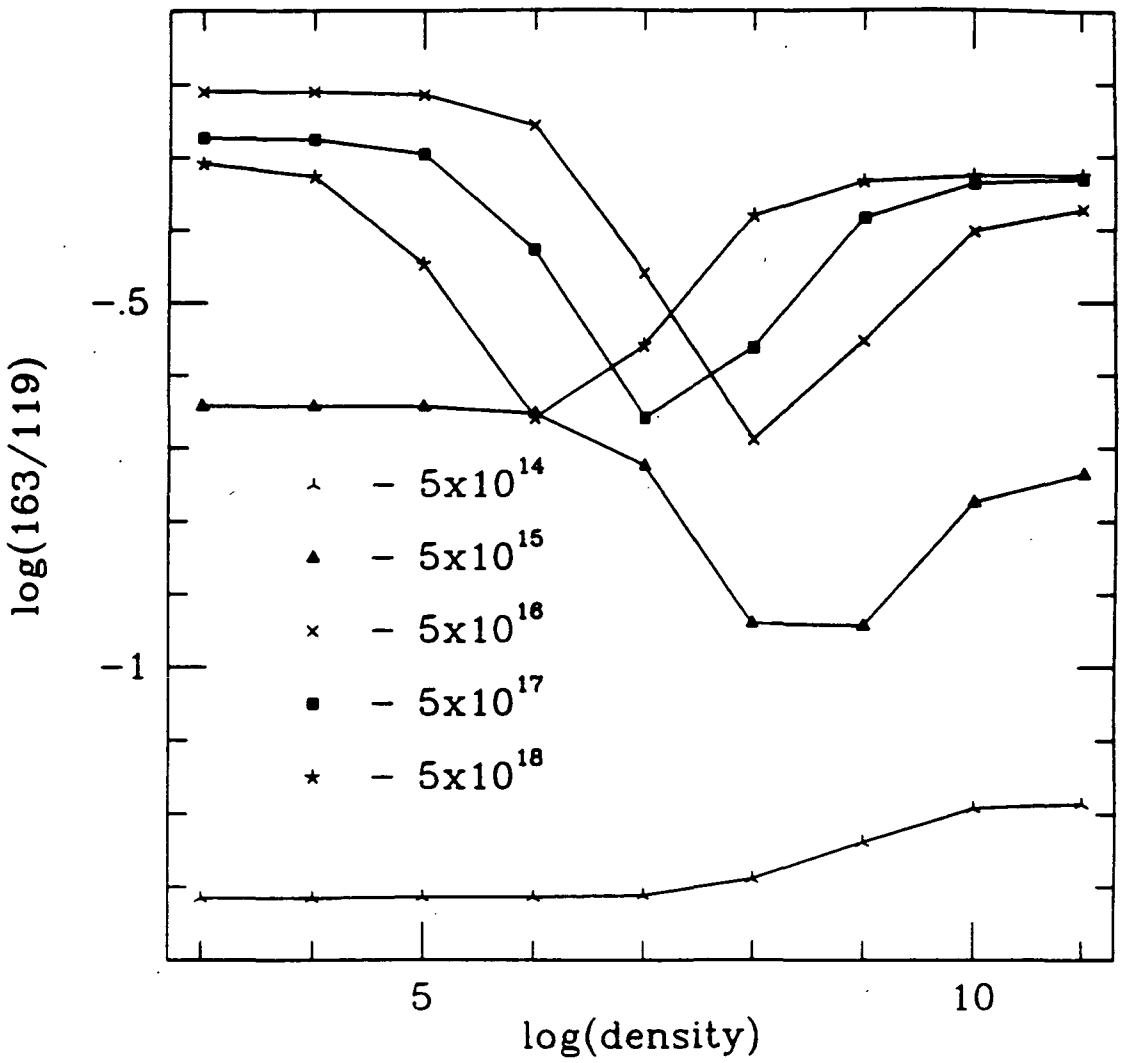

FIGURE 6.9a Same as figure 6.8a, except the gas temperature is 100 K.

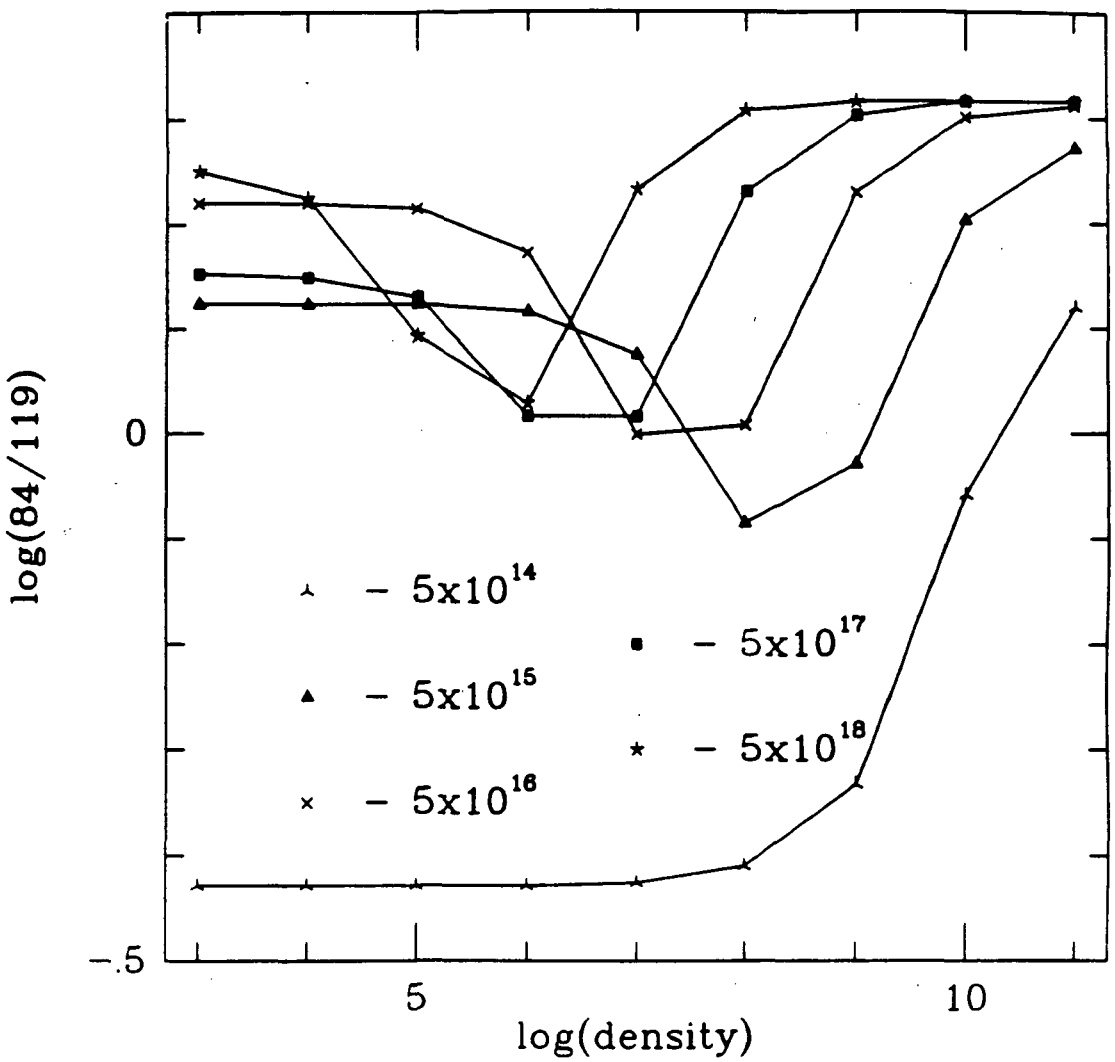

FIGURE 6.9b Same as figure 6.8b, except the gas temperature is 100 K.

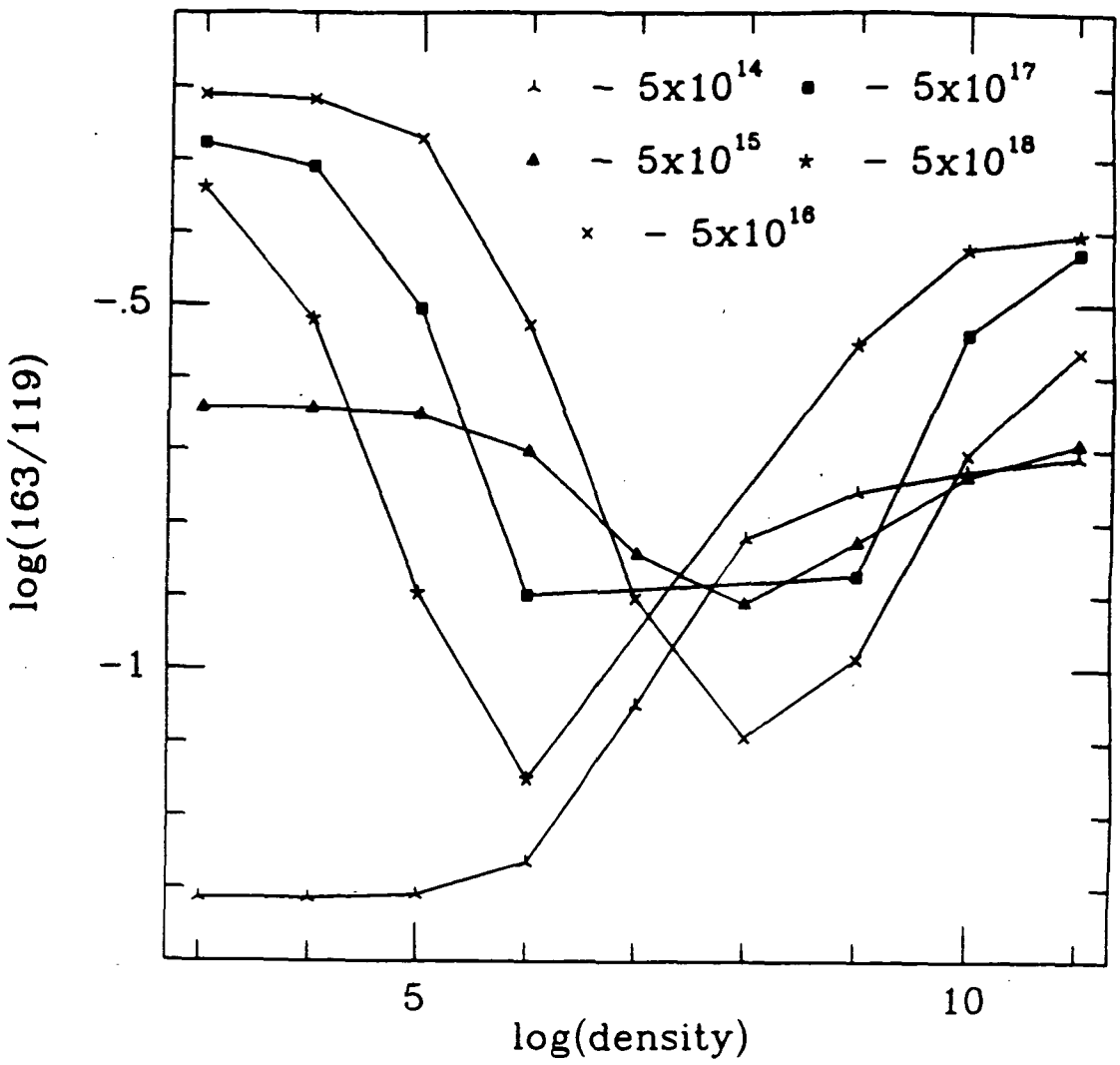

FIGURE 6.10a Same as figure 6.8a, except the gas temperature is 1000 K.

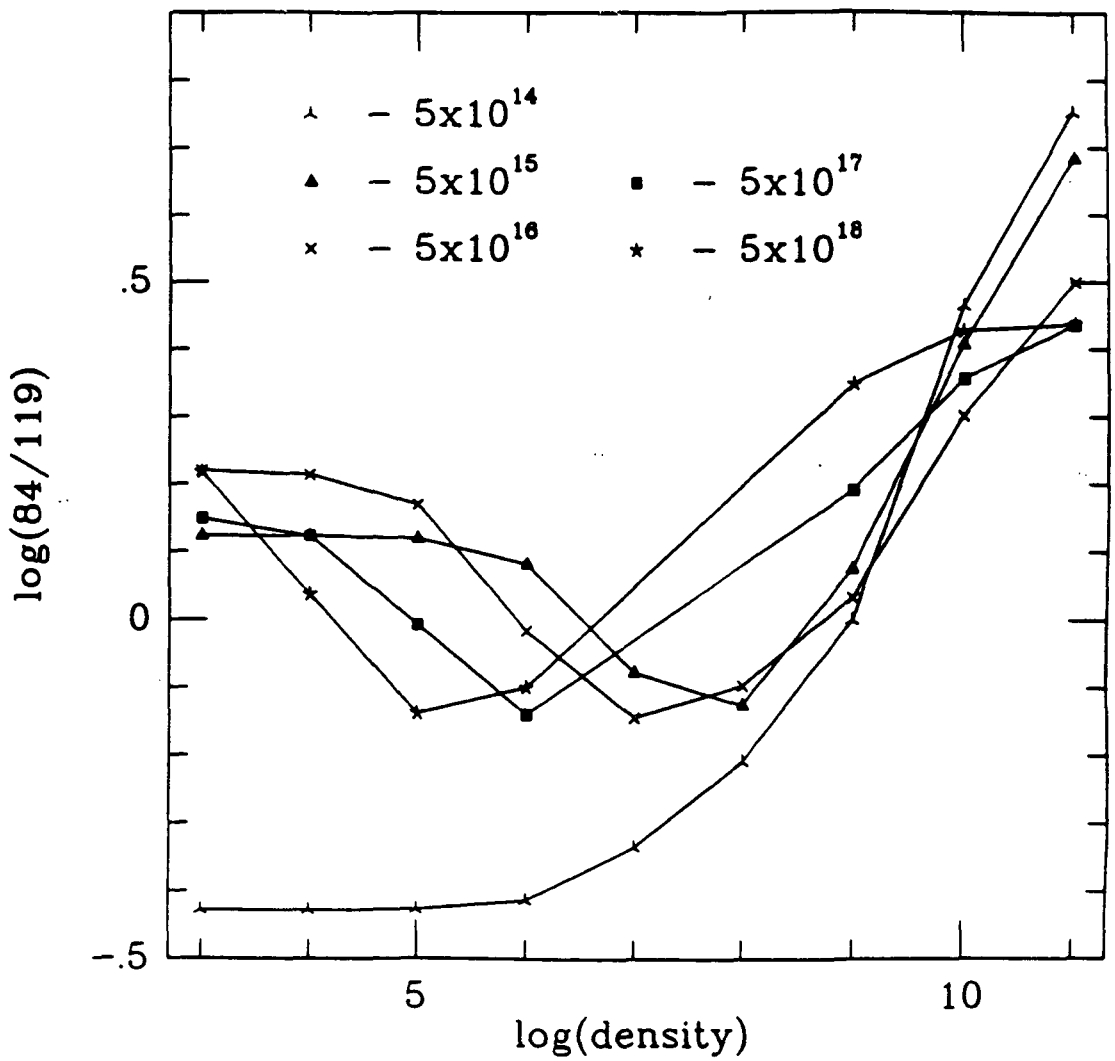

FIGURE 6.10b Same as figure 6.8b, except the gas temperature is 1000 K.

have such a high 163 μm flux.

By using the two ratios, we can determine the temperature of the OH-emitting region to be between 35 and 40 K. No other temperatures give a reasonable fit. At these temperatures, the best fit is obtained for an OH column density of $1.0 \times 10^{17}\,\mathrm{cm}^{-2}$ and a molecular hydrogen density of $4 \times 10^{7}\,\mathrm{cm}^{-3}$. These values are highly indicative of cool, post-shock gas. If the gas were pre-shock, then the density would have to be lower by a factor of 100. That the OH FIR emission originates in this cool gas confirms the suspicion of Melnick (1985).

It is possible for shocked gas at a temperature of 2000 K to cool rapidly to temperatures of 40 K or less. This cooling is done primarily by the CO emission lines. From McKee et al. (1982), we can estimate the cooling rate of the gas as a function of temperature. A rough analytic fit shows that the cooling is proportional to $T^{1.5}$. If a region is heated to 2000 K, then in a matter of 100 years or less, the temperature of the gas (hydrogen plus CO) will be cooled to 40 K by the CO alone. The shock has been moving across the BN–KL complex for several thousand years, leaving behind post-shock gas, most of which has cooled down to 40 K or less. Therefore, the temperature that we have deduced for the OH-emitting region is quite consistent with the picture of the post-shock region.

The expected flux at 119 μm from this range of values is about 3.2 times that actually observed, implying that the beam filling factor is about 31%. If we assume an $[OH]/[H_2]$ ratio of 2.1×10^{-7} (Draine and Roberge 1982), then from the density determination, we find that the OH region is roughly 10^{16} cm deep.

The CO data suggest that the pre-shock gas has a density of $\sim 10^{5}\,\mathrm{cm}^{-3}$, which rules out the pre-shock gas being the source of the OH radiation. The expected temperature of the OH suggests that we are in a cool part of the post-shock gas. The infrared CO transitions imply that the post-shock gas just downstream from the shock front is roughly 750 K with $n_{H_2} \approx 2 \times 10^{6}\,\mathrm{cm}^{-3}$. Simple pressure equilibrium dictates that a 40 K gas will have a density of roughly $4 \times 10^{7}\,\mathrm{cm}^{-3}$. It is unlikely that the density in the OH region is much greater than this estimate. No observations to date suggest higher densities in or near BN–KL, except on very small scales (Genzel et al. 1982).

The above arguments, coupled with the model fit to the data, suggest the following values for the physical parameters of the OH emitting region.

$$T_{gas} \approx 37 \pm 3\,\mathrm{K}$$

$$n_{H_2} \approx 4 \pm 2 \times 10^{7}\ \mathrm{cm}^{-3}$$

$$N_{OH} \approx 1.0 \pm .4 \times 10^{17}\ \mathrm{cm}^{-2}$$

$$g_f \approx 0.36 \pm 0.04$$

$$D_{OH} \approx 1.1 \pm 0.6 \times 10^{16}\ \mathrm{cm}\ ,$$

where g_f is the filling factor and D_{OH} is the length of the OH-emitting region. This assumes that the OH lines are $50\,\mathrm{km\ s^{-1}}$ wide.

From this fit to the data, we can estimate the expected line fluxes for all of the infrared transitions among the 14 lowest energy levels of OH. These are listed in table 6.1. Most of the infrared fluxes are close to $10^{17}\,\mathrm{W\ cm^{-2}}$, well within the detectability of present day instruments. The 13.4 GHz line flux that is estimated from this set of parameters is within a factor of 2 of that actually observed.

We also note that in the Orion Nebula, OH masers are known to be present. These level inversions are found to occur for temperatures substantially greater than the 40 K region that we apparently are observing with the FIR OH emission lines. According to conventional thinking, H II /OH masers are thought to arise in very compact dense areas of the molecular cloud surrounding the associated H II region (Genzel 1985; and references within). Since these areas are small, their filling factor should be small, and we don't expect them to significantly add to the FIR OH emission. OMC-1 is thought to be clumpy (Wynn-Williams et al. 1984; Geballe et al. 1986), and most likely the OH masers are in these clumps.

We can calculate the amount of hydrogen that is associated with the OH, and we find it to be about $50\,M_\odot$. The OH abundance ratio could very well be in error by a factor of 2 or 3, since the abundance is dependent on the initial [O]/[H] ratio in the pre-shock gas and on the temperature and density history of the gas

Table 6.1 Predicted Infrared OH Line Fluxes for OMC-1

Transition	Wavelength	Flux (10^{-17} W cm^{-2})
$^2\Pi_{3/2}\, J = \frac{5}{2} \rightarrow \frac{3}{2}$	119.44 μm	0.81
	119.23 μm	0.83
$^2\Pi_{3/2}\, J = \frac{7}{2} \rightarrow \frac{5}{2}$	84.60 μm	1.2
	84.42 μm	1.2
$^2\Pi_{3/2}\, J = \frac{9}{2} \rightarrow \frac{7}{2}$	65.28 μm	1.1
	65.13 μm	1.1
$^2\Pi_{1/2}\, J = \frac{3}{2} \rightarrow \frac{1}{2}$	163.40 μm	0.87
	163.12 μm	0.90
$^2\Pi_{1/2}\, J = \frac{5}{2} \rightarrow \frac{3}{2}$	98.74 μm	1.9
	98.72 μm	1.9
$^2\Pi_{1/2}\, J = \frac{1}{2} \rightarrow {}^2\Pi_{3/2}\, J = \frac{3}{2}$	79.18 μm	2.2
	79.12 μm	2.2
$^2\Pi_{1/2}\, J = \frac{3}{2} \rightarrow {}^2\Pi_{3/2}\, J = \frac{3}{2}$	53.35 μm	1.8
	53.26 μm	1.8
$^2\Pi_{1/2}\, J = \frac{5}{2} \rightarrow {}^2\Pi_{3/2}\, J = \frac{3}{2}$	34.63 μm	0.39
	34.60 μm	0.39
$^2\Pi_{1/2}\, J = \frac{3}{2} \rightarrow {}^2\Pi_{3/2}\, J = \frac{5}{2}$	96.37 μm	0.90
	96.31 μm	0.89
$^2\Pi_{1/2}\, J = \frac{5}{2} \rightarrow {}^2\Pi_{3/2}\, J = \frac{5}{2}$	48.82 μm	1.2
	48.70 μm	1.1
$^2\Pi_{1/2}\, J = \frac{5}{2} \rightarrow {}^2\Pi_{3/2}\, J = \frac{7}{2}$	115.39 μm	0.030
	115.15 μm	0.031

in relation to the chemistry. Because of this, it is quite likely that the abundance may be greater than what we assume it to be (2.2×10^{-7}), and this will help drive down the amount of hydrogen associated with the OH.

We should note that the mass of hydrogen in the shock region is roughly $20\,M_\odot$ if the average density is $10^5\,cm^{-3}$. The average density is most likely more, since the CO data suggest densities an order of magnitude greater than that. This leads us to believe that a mass of $50\,M_\odot$ is consistent with the overall picture of the BN–KL region.

We propose a one-component model for the FIR OH emission lines from OMC-1. This model suggests that the bulk of the FIR line emission comes from the cool post-shock gas that has a kinetic temperature of 37 K. The molecular hydrogen density is roughly $4 \times 10^7\,cm^{-3}$ and the OH column density is on the order of $1 \times 10^{17}\,cm^{-2}$. This implies that this cool post-shock gas is roughly 10^{16} cm deep, if the $[OH]/[H_2]$ ratio is 2×10^{-7}. The beam filling factor for a one arc-minute beam is about 0.36.

These parameters fit within the current framework of thinking concerning the region of OMC-1 containing BN–KL and IRc2. However, one should view the above values of the physical parameters as merely suggested by the data. Better absolute values of the fluxes are desired, as well as the acquisition of other infrared transition lines of OH. More accurate collisional cross-sections are also needed, as well as measured values of cross-sections between different excited levels. The experimental values for the H_2–OH cross-sections as reported by Andresen, Häusler, and Lülf (1984) differ significantly from those reported by Schinke and Andresen (1984), although both are based upon the same data set.

The radiative transfer code that was used has its own limitations, as well. With it, we may determine the average effective temperature and densities in a uniform cloud. As of yet, no structure of the region is incorporated into the program. We do not take into account any temperature gradients that may exist, or density gradients or chemical or shock evolution. We hope to incorporate these at a later time.

One final note on the OH data. The measured values of the 84.4 and 84.6 μm

lines are comparable. However, the former line is nearly coincident with a CO rotational line ($J = 31 \rightarrow 30$), from which we expect to measure a flux roughly comparable with what has been measured in that spectral region. Current instrumental resolution cannot differentiate between the two lines. The crucial question concerns which molecule we actually saw at 84.4 μm: CO or OH? If the OH is optically thick, then there is a good chance that it will absorb the CO-emitted photons, and suppress the contribution from the CO. For the present set of parameters, the optical depth at line center of the OH is ≈ 12. In the OH wing where the CO will be, the OH optical depth will still be much greater than unity. Most likely, the CO emission is simply being absorbed by the OH, and thus the measured 84.4 μm line flux is a measure of the OH line flux, as originally proposed by Viscuso et al. (1985b), and argued against by Watson et al. (1985).

The results of the numerical method need to be reconciled with those found in chapter V. This reconciliation is based upon the failure of the back-of-the-envelope calculation to adequately treat the OH data from OMC-1. This failure has several sources. The first source comes from the assumption that the collisional excitation rates dominate. This may be true for the 119 and 84 μm lines, but the 163 μm line is radiatively pumped by the radiation field from the dust. This was not properly taken into account in the analysis in chapter V. Not all of the radiative de-excitation processes were taken into account, as well. Because of these competing mechanisms, we were unable to accurately calculate the level populations in chapter V. One of the most important reasons for the failure of the back-of-the-envelope analysis is that the radiative processes occur on a local scale. That is to say that due to the velocity gradient, a photon can be absorbed and/or reemitted only in a localized region, and not throughout the length of the cloud. For these reasons, it is only by using numerical radiative transfer techniques that we can begin to correctly analyze the Orion data.

That is not to say that the analysis presented in the previous chapter is not useful or cannot be accurate. That analysis is certainly powerful in its simplicity and ease of physical understanding. It is possible to gain insight into the workings of the different and competing excitation and de-excitation mechanisms working

on the molecule of interest. If the region to be studied has low temperatures (to keep the number of populated levels small) and a simple structure (no imbedded sources of radiation, for example), then the back-of-the-envelope calculations should be fairly accurate.

6.6 Summary

We have used the escape probability formalism to develop a radiative transfer code with which we have been able to fit the FIR OH emission line data from OMC-1. This fit confirms the suspicions of Melnick (1985) that the OH-emitting region is not associated with the hot, post-shock gas as previously believed (Viscuso 1985a), but is instead part of the cool ($T \approx 40\,\mathrm{K}$), post-shock gas further downstream from the shock front. This is suggested by the fact that the $163\,\mu\mathrm{m}$ flux is enhanced relative to the $119\,\mu\mathrm{m}$ line emission. Radiative transfer models fail to predict the anomolous $163\,\mu\mathrm{m}$ flux for gas temperatures greater than 45 K.

The mass of cool, post-shocked gas is on the order of $50\,\mathrm{M}_\odot$. This much cool, processed gas can exist because the CO is a very efficient coolant in the ISM. The gas should be able to experience a rapid cooling from 2000 K to 40 K in 100 years or less.

The molecular hydrogen density is found to be about $4 \times 10^7\,\mathrm{cm}^{-3}$, and the OH column density is roughly $1 \times 10^{17}\,\mathrm{cm}^{-2}$. The beam filling factor is 36%. These findings are not in complete agreement with the analysis presented in chapter V. The densities are comparable, but the similarities stop there.

Much more work will have to be done in order to better understand the OH emission from OMC-1. Better absolute calibration of the line fluxes is necessary and we also need to expand the present data set to include higher spectral and spatial resolution. More observations of other rotational transitions of OH in the infrared will also help us to further constrain the physical parameters of the OH-bearing region.

Analysis similar to the above, using numerical methods, proves to be extremely helpful in determining the section of parameter space where the model is consistent with the data. Analysis such as presented in chapter V, is important in

obtaining a basic understanding of the data, and for determining, as a first guess, the physical parameters of the region. It is only with mathematically more powerful approaches such as numerical radiative transfer codes that we can begin to bring the whole picture together. Methods such as these should prove invaluable in the analysis of spectral data from ground-based, airborne, and space-based observatories.

VII. Future Efforts

7.1 OH in OMC-1

The OH data available for OMC-1 thus far suffer several serious weaknesses. The uncertainty in the absolute fluxes makes determining the 163:119 μm and 84:119 μm flux ratios difficult. There are problems with beam sizes as well. Since the diffraction-limited beam size is on the order of 1′, which corresponds to a linear size of 5×10^{17} cm at the distance of Orion, we are unable to determine the true size of the region. The data indicate that the beam filling factor is on the order of 0.35, suggesting that either the OH-emitting region is clumpy or, also likely, that it extends as far as the shock front, which has a size of roughly 2×10^{17} cm (Genzel 1985).

Another problem with the OH data is the lack of high spectral resolution. The data collected by our group were taken with instrumental resolutions of 4000 or so. This is not enough to provide us with adequate spectral line profiles, since higher resolution results on the 163.12 μm, 119.23 μm, and 119.44 μm profiles by the Berkeley group suggest linewidths of $\approx$50 km s^{-1} wide (Crawford et al. 1986; Watson et al. 1986).

The last problem with the OH data set is the lack of observations in other transitions. Those that cross the ladders at 53 μm ($^2\Pi_{1/2}\, J = \frac{3}{2} \rightarrow {}^2\Pi_{3/2}\, J = \frac{3}{2}$), 79 μm ($^2\Pi_{1/2}\, J = \frac{3}{2} \rightarrow {}^2\Pi_{3/2}\, J = \frac{3}{2}$), and 96 μm ($^2\Pi_{1/2}\, J = \frac{3}{2} \rightarrow {}^2\Pi_{3/2}\, J = \frac{3}{2}$) are essential in order to understand the population structure of these lower levels (see figure 4.3). The lack of reliable H_2–OH collision cross-sections also cause problems with the understanding of the OH data.

Future plans should include higher spectral and spatial resolution in the observations. The high spectral resolution can be obtained with Fabry-Perot instruments such as the Hinge discussed in chapter III and the Berkeley group's FPS (Watson 1982). High spatial resolution awaits the completion of the 3-meter

class Stratospheric Observatory for Infrared Astronomy (SOFIA), which is likely to become operational in the early 1990's if NASA approves funding. The European Space Agency's Infrared Space Observatory (ISO) and NASA's Space Infrared Telescope Facility (SIRTF) will also be launched in the next decade. These facilities will be able to provide high spectral and spatial resolution.

It is important to be able to map the spatial extent of the OH. We suggested in chapter VI that the OH masers are found in compact, high-density regions with temperatures of 100 K or more. These regions are not expected to contribute much to the lower level rotational transitions which are dominated by the warm (40 K) OH, but they will contribute most of the flux for transitions between highly excited levels. It should be possible to separate these warm and hot components by looking at their spatial extent (the hot component should be confined to or near the shock front while the warm component should be more extended) as well as by the flux ratios between the high J rotational transitions and the lower J transitions.

We hope to be able to obtain high-resolution data on the cross-ladder transitions mentioned above within the next year or two. The higher spatial resolution must await the next generation of infrared observatories, namely SOFIA or a 3-meter balloon-borne system.

7.2 CO in OMC-1

The CO data are in somewhat better shape than the OH data for OMC-1. The CO data, as can be seen in figure 5.8, cover transitions from levels ranging in excitation temperature from 5 K to 3000 K. The recent fits to the CO data have, until now, been based upon the H_2–CO collisional cross-sections of McKee et al. (1982). These cross-sections were calculated by using the He–CO potential energy surface (PES), and then multiplying the resulting de-excitation rates by a factor reflecting the difference in relative velocity reflecting the reduced mass difference between He and H_2.

This procedure neglected the fact that for large ΔJ transitions, the difference in the reduced mass results in an overestimation of the cross-sections by factors of 10 or more (Green 1986, private communication; Schinke et al. 1985). Schinke's group

has used a more accurate H_2–CO PES to calculate the collisional excitation rates. We hope to employ these new rates to analyze the CO data for OMC-1 in order to determine the temperature and density of the CO-emitting region. Since the earlier rates were overestimated for the high J levels, we predict that the temperature and/or density of this region will increase.

7.3 Future Objectives for the Hinge

7.3.1 Airplane-Based Observations

It is now possible to obtain the high spectral resolution needed for the OH observations as mentioned above. Since the Hinge has a resolution of 15 km s^{-1}, this will be more than adequate to determine useful line profiles, which will help greatly in the interpretation of the dynamics of the region. This is also true for the CO lines in the FIR.

There is also interest in observing other molecular species which are predicted to be somewhat abundant by chemical models. These include CN and CS, which are products of the complicated carbon, nitrogen, and sulfur chemistry cycles (Prasad and Huntress 1980; Mitchell 1984).

The needed molecular data for these two species are found in the following literature. For CN, the energy levels can be calculated by using the Dunham coefficients obtained experimentally by Skatrud et al. (1983) and Cerny et al. (1978). The dipole moment of CN is reported by Thomson and Dalby (1966) to be 1.47 D, and is supported by the theoretical results of Lavendy, Gandara, and Robbe (1984). For CS, the Dunham coefficients and rotational constants are found to be in excellent agreement among four different groups (Bogey, Demuynck, and Destombes, 1982; Bergeman and Cossart, 1981; Bustreel et al. 1979; and Todd and Olson, 1979). The dipole moment for CS is reported by Winnewisser and Cook (1968) to be 1.958 D.

To find the expected flux from OMC-1, we need to calculate the specific intensities for CN vs. those for CO. One finds that the CN intensities are a factor of almost 165 times higher than those for CO. This is, in large part, due to the higher dipole moment of the former (1.47 vs. 0.112). The population levels for

the two molecules are almost identical, so the intensities basically differ by their A coefficients. Assuming that the collisional cross-sections for CN and for CO are similar, then we should also expect that the CN transitions for $J \sim 16$ are density independent, as they are for CO. It is therefore only necessary to find the column density of CN and calculate the expected fluxes in the lines.

For CS, the excitation temperatures for $J \sim 38$ (the FIR transitions) are $\sim$ 1700 K. We therefore don't expect a significant population in these levels. However, due to the large degeneracy and the large value of μ, the specific intensities are still factors of 40 higher than CO transitions at these wavelengths. In fact, if CS is in LTE at 750 K, the maximum intensities occur at these far-infrared (FIR) wavelengths. This is also true for CO and for CN, making the FIR lines the best lines for detecting these molecules in dense regions where the level populations can approach LTE.

The CO observations that have been made toward the Orion Molecular Cloud may far outnumber the stars within this vast complex. Towards BN–KL, the column density for CO is $4.1 \times 10^{17}\,\mathrm{cm}^{-2}$ (Viscuso 1985) which agrees with the values determined by Koepf et al. (1982) and Watson et al. (1985). These values for N_{CO} yield fluxes for the FIR transitions of CO on the order of several $\times 10^{-17}\,\mathrm{W\ cm}^{-2}$, which are easily detected.

For CN, the observations suggest that the column density toward OMC-1 is $\sim 1 \times 10^{15}\ \mathrm{cm}^{-2}$ (Wooten et al. 1982; Churchwell 1980; Turner and Gammon 1975; and Jefferts, Penzias, and Wilson 1970). This yields fluxes on the order of $3.4 \times 10^{-17}\,\mathrm{W\ cm}^{-2}$ for the FIR lines ($N \sim 18$). It should be noted that the CN abundance in Orion and other regions is about 6 orders of magnitude higher than chemical equilibrium models predict (Wooten et al. 1982). The CN abundance may also vary among sources due to time-dependent chemical processes as discussed by Allen and Knapp (1978). If this is the case, then CN observations are important in determining chemical processes that are occuring in molecular clouds. This could also help in explaining the apparently non-equilibrium values of CN.

The CS observations indicate a column density on the order of $1.7 \times 10^{14}\,\mathrm{cm}^{-2}$ (Goldsmith et al. 1980; Liszt et al. 1974; Penzias et al. 1971). From these densities,

the CS FIR flux will be $\sim 3 \times 10^{-18}$ W cm^{-2}. This will be detectable for NEP's better than 2×10^{-14} W Hz$^{-1/2}$ with several seconds of integration. Padman et al. (1985) find a CS column density of 7×10^{13} cm^{-2}, but as they point out, the CS emitting regions may be clumpy and this would tend to enhance the density.

We should note that it is not clear that these molecules will approach LTE in their level populations. At the temperature and density of the shocked gas in OMC-1, the CO is not in LTE, although it is close to it for the low J values. It should be noted that the charged particle collision excitation mechanism is proportional to $\mu^{1.5}$ (Goss and Field 1968), so that charged particles will begin to play a major role. Collisions with C II and electrons will help bring the CN and CS closer to LTE since these molecules have a much larger dipole moment than CO. The critical electron density, the ratio of the spontaneous emission rate out of a particular level to the collisional excitation rate into that level, is $\sim 10^3$ cm^{-3} for CO, while for CN, this value is down by a factor of 100, to about ~ 10 cm^{-3}. For CS, the A coefficient is larger due to the higher J number (CN and CO are nearly identical in energy strucutre), and so there isn't as much of an advantage in the higher dipole moment reducing the electron critical density.

The CN and CS FIR emission lines will be able to tell us much about the chemistry of the shock region in Orion. Both species exhibit high velocity wings in their profiles of 30 km s^{-1} or more. They should be relatively bright and their detection would constitute the first FIR astronomical detection of these lines.

7.3.2 Space Missions for the Hinge

As was mentioned in chapter III, the Hinge is well-suited for space missions. Not only can one obtain high spectral resolution, but the package is very small and lightweight and has only one moving part. This makes the Hinge ideal for the SPARTAN and EUREKA payloads. The ruggedness of the system, relying as it does on a rotation of a grating about one axis without the plates moving, also assures better survival through the rigors of launch.

The Hinge should be amenable to redesign for operations at other wavelengths, either shorter or longer. We are looking into the possibility of constructing

an etalon for use at shorter wavelengths around 63 and 88 μm, where neutral and ionized oxygen fine-structure lines contribute significantly to the cooling of the interstellar medium (Stacey 1985).

With the Hinge or a similar instrument in space, it would be possible to do spectral line surveys of selected areas of the sky, or possibly even of the entire sky, depending on how large a cryogen supply can be provided. The recent success of IRAS points to the possibility of making significant advances with high-resolution infrared spectroscopy from space.

REFERENCES

Acton, F. S. (1970), *Numerical Methods That Work*, (New York: Harper & Row).

Allen, M., and Knapp, G. R. (1978), *Astrophys. J.* **225**, 843.

Andresen, P., Häusler, D., and Lülf, H. W. (1984), *J. Chem. Phys.* **81**, 571.

Armstrong, K. R., and Low, F. J. (1973), *Applied Optics* **12**, 2007.

Balick, B., Gammon, R. H., and Doherty, L. H. (1974), *Astrophys. J.* **188**, 45.

Bally, J., and Lada, C. J. (1983), *Astrophys. J.* **265**, 824.

Becker, W., and Fenkart, R. (1963) *Zeit. f. Astrophysik* **56**, 253.

Becklin, E. E., and Neugebauer, G. (1967), *Astrophys. J.* **147**, 799.

Beckwith, S., Persson, S. E., Neugebauer, G., and Becklin, E. E. (1978), *Astrophys. J.* **223**, 464.

Bell, R. J. (1972), *Introductory Fourier Transform Spectroscopy*, (New York: Academic Press).

Bergeman, T., and Cossart, D. (1981), *J. Molec. Spectrosc.* **87**, 119.

Bertojo, M., Cheung, A. C., and Townes, C. H. (1976), *Astrophys. J.* **208**, 914.

Bogey, M., Demuynck, C., and Destombes, J. L. (1982), *J. Molec. Spectrosc.* **95**, 35.

Born, M., and Wolf, E. (1980) *Principles of Optics*, (Oxford: Pergamon), chapter vii.

Bouloy, D., and Omont, A. (1977), *Astron. Astrophys.* **61**, 405.

Bouloy, D., and Omont, A. (1979), *Astron. Astrophys. Suppl.* **38**, 101.

Boyd, R. W. (1982), *Infrared Phys.* **22**, 157.

Bratt, P. R. (1977), *Semiconductors and Semimetals*, ed. R. K. Willardson and A. C. Beer, (New York: Academic Press), **12**, 39.

Brown, J. M., and Evenson, K. M. (1983), *Astrophys. J. Letters* **268**, L51.

Brown, J. M., Schubert, J. E., Evenson, K. M., and Radford, H. E. (1982), *Astrophys. J.* **258**, 899.

Burnham, Jr., R. (1977) *Burnham's Celestial Handbook*, (New York: Dover), pp. 1317–37.

Bustreel, R., Demuynck-Marliere, C., Destombes, J. L., and Journel, G. (1979) *Chem. Phys. Letts.* **67**, 178.

Canfield, R. C., Puetter, R. C., and Ricchiazzi, P. J. (1981), *Astrophys. J.* **248**, 82.

Carli, B. (1972), *Infrared Phys.* **12**, 251.

Castor, J. I. (1970), *Monthly Notices Roy. Astron. Soc.* **149**, 111.

Cerny, D., Bacis, R., Guelachvili, G., and Roux, F. (1978), *J. Molec. Spectrosc.* **73**, 154.

Chernoff, D. F. (1986) private communication.

Chernoff, D. F., Hollenbach, D. J., and McKee, C. F. (1982), *Astrophys. J. Letters* **259**, L97.

Churchwell, E. (1980), *Astrophys. J.* **240**, 811.

Cooley, J. W., and Tukey, J. W. (1965) *Math. Computat.* **19**, 297.

Crawford, M. K., Genzel, R., Townes, C. H., and Watson, D. M. (1985), *Astrophys. J.* **291**, 755.

Crawford, M. K., Lugten, J. B., Fitelson, W., Genzel, R., and Melnick, G. (1986), *Astrophys. J. Letters* **303**, L57.

Dalgarno, A. (1985a), in *Molecular Astrophysics*, eds. G. H. F. Diercksen, W. F. Huebner, and P. W. Langhoff, (Dordrecht: Reidel), p. 3.

Dalgarno, A. (1985b), in *Molecular Astrophysics*, eds. G. H. F. Diercksen, W. F. Huebner, and P. W. Langhoff, (Dordrecht: Reidel), p. 281.

DePristo, A. E., Augustin, S. D., Ramaswamy, R., and Rabitz, H. (1979), *J. Chem. Phys.* **71**, 850.

Destombes, J. L., Marliere, C., Baudry, A., and Brillet, J. (1977), *Astron. Astrophys.* **60**, 55.

Dewangan, D. P., and Flower, D. R. (1981), *J. Phys. B* **14**, 2179.

Dewangan, D. P., and Flower, D. R. (1983), *J. Phys. B* **16**, 2157.

Dickinson, D. F., Gottlieb, C. A., Gottlieb, E. W., and Litvak, M. M. (1976), *Astrophys. J.* **206**, 79.

Downes, D., Genzel, R., Becklin, E. E., and Wynn-Williams, C. G. (1981), *Astrophys. J.* **244**, 869.

Draine, B. T. (1985), in *Molecular Astrophysics*, eds. G. H. F. Diercksen, W. F. Huebner, and P. W. Langhoff, (Dordrecht: Reidel), p. 295.

Draine, B. T., and Roberge, W. G. (1982), *Astrophys. J. Letters* **259**, L91.

Draine, B. T., and Roberge, W. G. (1984), *Astrophys. J.* **282**, 491.

Draine, B. T., Roberge, W. G., and Dalgarno, A. (1983), *Astrophys. J.* **264**, 485.

Durschlag, M. S., and DeTemple, T. A. (1981), *Applied Optics* **20**, 1245.

Elitzur, M. (1982), *Rev. Mod. Phys.* **54**,1225.

Elitzur, M. (1984), *Astrophys. J.* **280**, 653.

Elitzur, M., Goldreich, P., and Scoville, N. (1976), *Astrophys. J.* **205**, 384.

Erickson, E. F., Houck, J. R., Harwit, M. O., Rank, D. M., Haas, M. R., Hollenbach, D. J., Simpson, J. P., and Augason, G. C. (1984), in *Third International Conference on Infrared Physics*, eds. W. Rüegsegger and F. K. Kneubühl, p. 287.

Erickson, E. F., Houck, J. R., Harwit, M. O., Rank, D. M., Haas, M. R., Hollenbach, D. J., Simpson, J. P., and Augason, G. C. (1985), *Infrared Phys.* **25**, 513.

Erickson, E. F., Knacke, R. F., Tokunaga, A. T., and Haas, M. R. (1981), *Astrophys. J.* **245**, 148.

Erickson, N. R., Goldsmith, P. F., Snell, R. L., Berson, R. L., Huguenin, G. R., Ulich, B. L., and Lada, C. J. (1982), *Astrophys. J. Letters* **261**, L103.

Flower, D. R., and Launay, J. M. (1985), *Monthly Notices Roy. Astron. Soc.* **214**, 271.

Gaskill, J. D. (1978), *Linear Systems, Fourier Transforms, and Optics*, (New York: Wiley).

Geballe, T. R., Persson, S. E., Simon, T., Lonsdale, C. J., and McGregor, P. J. (1986), *Astrophys. J.* **302**, 693.

Genzel, R. (1985), in *Masers, Molecules, and Mass Outflows in Star Forming Regions*, ed. A. Haschick, p. 233.

Genzel, R., Downes, D., Ho, P. T. P., and Bieging, J. (1982), *Astrophys. J. Letters* **259**, L103.

Genzel, R., Reid, M. J., Moran, J. M., and Downes, D. (1981), *Astrophys. J.* **244**, 884.

Gillett, F. C., Dereniak, E. L., and Joyce, R. R. (1977), *Opt. Engin.* **16**, 544.

Gingerich, O. (1982), in *Symposium on the Orion Nebula*, eds. A. E. Glassgold, P. J., Huggins, and E. L. Shucking, Annals of the New York Academy of Sciences, **395**, p. 310.

Glassgold, A. E., Huggins, P. J., and Shucking, E. L., eds. (1982) *Symposium on the Orion Nebulae*, Annals of the New York Academy of Sciences, **395**.

Goldflam, R., Green, S., and Kouri, D. J. (1977), *J. Chem. Phys.* **67**, 4149.

Goldreich, P., and Kwan, J. (1974), *Astrophys. J.* **189**, 441.

Goldsmith, P. F., Erickson, N. R., Fetterman, H. R., Clifton, B. J., Peck, D. D., Tannenwald, P. E., Koepf, G. A., Buhl, D., and McAvoy, N. (1981), *Astrophys. J. Letters* **243**, L79.

Goldsmith, P. F., Langer, W. D., Schloerb, F. P., and Scoville, N. Z. (1980), *Astrophys. J.* **240**, 524.

Goss, W. M., and Field, G. B. (1968), *Astrophys. J.* **151**, 177.

Gottlieb, C. A., and Ball, J. (1973), *Astrophys. J. Letters* **184**, L59.

Gray, D. F. (1976) *The Observation and Analysis of Stellar Photospheres*, (New York: Wiley), chapters v–vii.

Green, S., and Chapman, S. (1983), *Chem. Phys. Letters* **98**, 467.

Green, S., and Thaddeus, P. (1976), *Astrophys. J.* **205**, 766.

Guilloteau, S., Baudry, A., Walmsley, C. M., Wilson, T. L., and Winnberg, A. (1984), *Astron. Astrophys.* **131**, 45.

Haas, M. R., Erickson, E. F., Goorvitch, D., McKibbin, D. D., and Rank, D. M. (1985), *Icarus* **64**, 549.

Hadni, A., Claudel, J., Gerbaux, X., Morlot, G., and Munier, J. M. (1965), *Applied Optics* **4**, 487.

Hall, J. J. (1962), *Phys. Rev.* **128**, 68.

Haller, E. E., Hueschen, M. R., and Richards, P. L. (1979), *Appl. Phys. Letters* **34**, 495.

Harwit, M., Kurtz, N. T., Russell, R. W., and Smyers, S. (1981), *Applied Optics* **20**, 3792.

Harwit, M., and Sloane, N. J. A. (1979), *Hadamard Transform Optics*, (New York: Academic Press).

Herter, T., Helfer, H. L., and Pipher, J. L. (1983), *Astron. Astrophys. Suppl.* **51**, 195.

Herzberg, G. (1945) *Infrared and Raman Spectroscopy of Polyatomic Molecules*, (New York: Van Nostrand).

Herzberg, G. (1950) *Spectra of Diatomic Molecules*, (New York: Van Nostrand).

Ho, P. T. P., and Barrett, A. H. (1978), *Astrophys. J. Letters* **224**, L23.

Houck, J. R., and Briotta, D. A. (1982), *Infrared Phys.* **22**, 215.

Houck, J. R., and Ward, D. B. (1979), *Publ. Astron. Soc. Pacific* **91**, 140.

James, J. F., and Sternberg, R. S. (1969), *The Design of Optical Spectrometers*, (London: Chapman and Hall Ltd.).

Jefferts, K. B., Penzias, A. A., and Wilson, R. W. (1970), *Astrophys. J. Letters* **161**, L87.

Jenkins, G. M., and Watts, D. G. (1968), *Spectral Analysis and its Applications*, (San Francisco: Holden-Day).

Johansson, L. E. B., Andersson, C., Elldér, J., Friberg, P., Hjalmarson, Å., Höglund, B., Irvine, W. M., Olofsson, H., and Rydbeck, G. (1984), *Astron. Astrophys.* **130**, 227.

Kazanskii, A. G., Richards, P. L., and Haller, E. E. (1977), *Appl. Phys. Letters* **31**, 496.

Keene, J., Blake, G. A., and Phillips, T. G. (1983), *Astrophys. J. Letters* **271**, L27.

Keene, J., Hildebrand, R. H., and Whitcomb, S. E. (1982), *Astrophys. J. Letters* **252**, L11.

Keyes, R. J., and Quist, T. M. (1970), *Semiconductors and Semimetals*, ed. R. K. Willardson and A. C. Beer, (New York: Academic Press), **5**, 321.

Kimmitt, F. R. (1970) *Far-Infrared Techniques*, (London: Pion Limited), pp. 21-39.

Kleinmann, D. W., and Low, F. J. (1967), *Astrophys. J. Letters* **149**, L1.

Knowles, S. H., Caswell, J. L., and Goss, W. M. (1976), *Monthly Notices Roy. Astron. Soc.* **175**, 537.

Koepf, G. A., Buhl, D., Chin, G., Peck, D. D., Fetterman, H. R., Clifton, B. J., and Tannenwald, P. E. (1982), *Astrophys. J.* **260**, 584.

Kwan, J. (1977), *Astrophys. J.* **216**, 713.

Kwan, J., and Scoville, N. (1976), *Astrophys. J. Letters* **210**, L39.

Lavendy, H., Gandara, G., and Robbe, J. M. (1984), *J. Molec. Spectrosc.* **106**, 395.

Lena, P. (1978) in *Infrared Astronomy*, eds. G. Setti and G. G. Fazio, (Dordrecht: Reidel), p. 231.

Lengeler, B. (1974) *Cryogenics*, (August, 1974), 439.

Li, T-p., Riley, P. A., and Wolfendale, A. W. (1983), *Monthly Notices Roy. Astron. Soc.* **203**, 87.

Liszt, H. S., Wilson, R. W., Penzias, A. A., Jefferts, K. B., Wannier, P. G., and Solomon, P. M. (1974), *Astrophys. J.* **190**, 557.

Loewen, E. G. (1977) *Electro-Optical Systems Design*, (August, 1977), 26.

Loewenstein, E. V., Smith, D. R., and Morgan, R. L. (1973), *Applied Optics* **12**, 398.

Low, F. J. (1961), *J. Optical Soc. Amer.* **51**, 1300.

Lucy, L. B. (1971), *Astrophys. J.* **163**, 95.

Mantz, A. W., Maillard, J.-P., Roh, W. B., and Narahari Rao, K. (1975), *J. Molec. Spectrosc.* **57**, 155.

Masson, C. R., Berge, G. L., Claussen, M. J., Heiligman, G. M., Leighton, R. B., Lo, K. Y., Moffet, A. T., Phillips, T. G., Sargent, A. I., Scott, S. L., Wannier, P. G., and Woody, D. P. (1984), *Astrophys. J. Letters* **283**, L37.

Mathis, J. S., Mezger, P. G., and Panagia, N. (1983), *Astron. Astrophys.* **128**, 212.

Matthews, H. E., Baudry, A., Guilloteau, S., and Winnberg, A. (1984), *Astron. Astrophys.* , preprint.

McKee, C. F., Storey, J. W. V., Watson, D. M., and Green, S. (1982), *Astrophys. J.* **259**, 647.

Melnick, G. J. (1981) Ph.D. Dissertation, Cornell Univ., Ithaca, NY.

Melnick, G. J. (1985), in *Masers, Molecules, and Mass Outflows in Star Forming Regions*, ed. A. Haschick, p. 33.

Mezger, P. G., and Höglund, B. (1967), *Astrophys. J.* **147**, 490.

Mitchell, G. F. (1984), *Astrophys. J. Suppl.* **54**, 81.

Moran, J. M., Garay, G., Reid, M. J., Genzel, R., Wright, M. C. H., and Plambeck, R. L. (1983), *Astrophys. J. Letters* **271**, L31.

Muenter, J. S. (1975), *J. Molec. Spectrosc.* **55**, 490.

Nadeau, D., and Geballe, T. R. (1979), *Astrophys. J. Letters* **230**, L169.

Nyquist, H. (1928), *Phys. Rev.* **32**, 110.

Padman, R., Scott, P. F., Vizard, D. R., and Webster, A. S. (1985), *Monthly Notices Roy. Astron. Soc.* **214**, 251.

Pankonin, V., Walmsley, C. M., and Harwit, M. (1979), *Astron. Astrophys.* **75**, 34.

Penzias, A. A., Solomon, P. M., Wilson, R. W., and Jefferts, K. B. (1971), *Astrophys. J. Letters* **168**, L53.

Phillips, J. P., White, G. J., and Watt, G. D. (1982), *Monthly Notices Roy. Astron. Soc.* **199**, 1033.

Pipher, J. L., Duthie, J. G., and Savedoff, M. P. (1978), *Astrophys. J.* **219**, 494.

Plambeck, R. L., Wright, M. C. H., Welch, W. J., Bieging, J. H., Baud, B., Ho, P. T. P., and Vogel, S. N. (1982), *Astrophys. J.* **259**, 617.

Prasad, S. S., and Huntress Jr., W. T. (1980), *Astrophys. J. Suppl.* **43**, 1.

Press, W. H., Flannery, B. P., Teukolsky, S. A., and Vetterling, W. T. (1986), *Numerical Recipes*, (Cambridge: Cambridge University Press).

Price, P. J. (1961), *Phys. Rev.* **124**, 713.

Reid, M. J., and Moran, J. M. (1981), *Ann. Rev. Astron. Astrophys.* **19**, 231.

Rhoads, C. M., Damon, E. K., and Munk, B. A. (1982), *Applied Optics* **21**, 2814.

Richardson, K. J., White, G. J., Avery, L. W., Lesurf, J. C. G., and Harten, R. H. (1985), *Astrophys. J.* **290**, 637.

Reid, M. J., and Moran, J. M. (1981), *Ann. Rev. Astron. Astrophys.* **19**, 231.

Roesler, F. L. (1974), in *Methods of Experimental Physics*, ed. N. Carleton, **12**, 531 (New York: Academic Press).

Russell, R. W., Melnick, G., Gull, G. E., and Harwit, M. (1980), *Astrophys. J. Letters* **240**, L99.

Rybicki, G. B. (1984), in *Methods in Radiative Transfer*, ed. W. Kalkofen, (Cambridge: Cambridge University Press), p.21.

Rybicki, G. B., and Lightman, A. P. (1979) *Radiative Processes in Astrophysics*, (New York: Wiley), chapter i.

Rydbeck, O. E. H., and Hjalmarson, Å. (1985), in *Molecular Astrophysics*, eds. G. H. F. Diercksen, W. F. Huebner, and P. W. Langhoff, (Dordrecht: Reidel), p. 45.

Rydbeck, O. E. H., Koffberg, E., Hjalmarson, Å., Sume, A., Elldér, J., and Irvine, W. M. (1976), *Astrophys. J. Suppl.* **31**, 333.

Schinke, R., and Andresen, P. (1984), *J. Chem. Phys.* **81**, 5644.

Schinke, R., Engel, V., Buck, U., Meyer, H., and Diercksen, G. H. F. (1985), *Astrophys. J.* **299**, 939.

Schultz, G. V., Durwen, E. J., Rõser, H. P., Sherwood, W. A., and Wattenbach, R. (1985), *Astrophys. J. Letters* **291**, L59.

Scoville, N. Z. (1981), in *Infrared Astronomy*, eds. C. G. Wynn-Williams and D. P. Cruikshank, Reidel, Dordrecht, p. 187.

Scoville, N. Z., and Solomon, P. M. (1974), *Astrophys. J. Letters* **187**, L67.

Sears, T. J., McKellar, A. R. W., Bunker, P. R., Evenson, K. M., and Brown, J. M. (1984), *Astrophys. J.* **276**, 399.

Serabyn, E., and Lacy, J. H. (1985), *Astrophys. J.* **293**, 445.

Shull, J. M., and Beckwith, S. (1982), *Ann. Rev. Astron. Astrophys.* **20**, 163.

Shure, M. A. (1985) Ph.D. Dissertation, Cornell Univ., Ithaca, NY.

Skatrud, D. D., DeLucia, F. C., Blake, G. A., and Sastry, K. V. L. N. (1983), *J. Molec. Spectrosc.* **99**, 35.

Slater, G., Salpeter, E. E., and Wasserman, I. 1982, *Astrophys. J.* **255**, 293.

Snyder, L. E., Hollis, J. M., Ulich, B. L., Lovas, F. J., Johnson, D. R., and Buhl, D. (1975), *Astrophys. J. Letters* **198**, L81.

Sobolev, V. V. (1957) *Soviet Astr. - AJ*, **1**, 678.

Solomon, P. M., Huguenin, G. R., and Scoville, N. Z. (1981), *Astrophys. J. Letters* **245**, L19.

Stacey, G. J. (1985) Ph.D. Dissertation, Cornell Univ., Ithaca, NY.

Stacey, G. J., Kurtz, N. T., Smyers, S. D., and Harwit, M. (1983), *Monthly Notices Roy. Astron. Soc.* **202**, 25P.

Stacey, G. J., Kurtz, N. T., Smyers, S. D., Harwit, M., Russell, R. W., and Melnick, G. (1982), *Astrophys. J. Letters* **257**, L37.

Stewart, J. E. (1970) *Infrared Spectroscopy*, (New York: Marcel Dekker).

Storey, J. W. V., Watson, D. M., and Townes, C. H. (1981), *Astrophys. J. Letters* **244**, L27.

Storey, J. W. V., Watson, D. M., Townes, C. H., Haller, E. E., and Hansen, W. L. (1981), *Astrophys. J.* **247**, 136.

Thaddeus, P., Kutner, M. L., Penzias, A. A., Wilson, R. W., and Jefferts, K. B. (1972), *Astrophys. J. Letters* **176**, L73.

Thomson, R., and Dalby, F. W. (1966), *Can. J. Phys.* **46**, 2815.

Tielens, A. G. G. M., and Hollenbach, D. (1985), *Astrophys. J.* **291**, 747.

Todd, T. R., Clayton, C. M., Telfair, W. B., McCubbin, Jr., T. K., and Plíva, J. (1976), *J. Molec. Spectrosc.* **62**, 201.

Todd, T. R., and Olson, W. B. (1979), *J. Molec. Spectrosc.* **74**, 190.

Tokunaga, A. T., Dinerstein, H. L., Lester, D. F., and Rank, D. M. (1980), *Icarus* **42**, 79.

Tomaselli, V. P., Edewaard, D. C., Gillan, P., and Möller, K. D. (1981), *Applied Optics* **20**, 1361.

Townes, C. H., and Schawlow, A. L. (1975) *Microwave Spectroscopy*, (New York: Dover).

Townes, C. H., Genzel, R., Watson, D. M., and Storey, J. W. V. (1983), *Astrophys. J. Letters* **269**, L11.

Traub, W. A., and Stier, M. T. (1976), *Applied Optics* **15**, 364.

Tucker, K. D., Kutner, M. L., and Thaddeus, P. (1973), *Astrophys. J. Letters* **186**, L13.

Turner, B. E., and Gammon, R. H. (1975), *Astrophys. J.* **198**, 71.

Vaughan, Jr., A. H. (1967), *Ann. Rev. Astron. Astrophys.* **5**, 139.

Viscuso, P. J. (1985), in *ESO-IRAM-Onsala Workshop on (Sub)Millimeter Astronomy Proceedings*, eds. P. A. Shaver and K. Kjär (ESO Conference and Workshop Proceedings No. 22), p. 371.

Viscuso, P. J., Stacey, G. J., Fuller, C. E., Kurtz, N. T., and Harwit, M. (1985a), *Astrophys. J.* **296**, 142.

Viscuso, P. J., Stacey, G. J., Harwit, M., Haas, M. R., Erickson, E. F., and Duffy, P. B. (1985b), *Astrophys. J.* **296**, 149.

Walmsley, C. M. (1985) preprint.

Wannier, P. G., Encrenaz, P. J., Wilson, R. W., and Penzias, A. A. (1974), *Astrophys. J. Letters* **190**, L77.

Wannier, P. G., and Phillips, T. G. (1977), *Astrophys. J.* **215**, 796.

Watson, D. M. (1982) Ph.D. Dissertation, Univ. of California, Berkeley, CA.

Watson, D. M., Genzel, R., Townes, C. H., and Storey, J. W. V. (1985), *Astrophys. J.* **298**, 316.

Watson, D. M., Storey, J. W. V., Townes, C. H., Haller, E. E., and Hansen, W. L. (1980), *Astrophys. J. Letters* **239**, L129.

Watt, G. D., Millar, T. J., White, G. J., and Harten, R. H. (1985), in *ESO-IRAM-Onsala Workshop on (Sub)Millimeter Astronomy Proceedings*, eds. P. A. Shaver and K. Kjär (ESO Conference and Workshop Proceedings No. 22), p. 384.

Werner, M. W. (1982), in *Symposium on the Orion Nebula*, eds. A. E. Glassgold, P. J. Huggins, and E. L. Shucking, Annals of the New York Academy of Sciences, **395**, p. 310.

Werner, M. W., Gatley, I., Harper, D. A., Becklin, E. E., Loewenstein, R. F., Telesco, C. M., and Thronson, H. A. (1976), *Astrophys. J.* **204**, 420.

Winnewisser, G., and Cook, R. L. (1968), *J. Molec. Spectrosc.* **28**, 266.

Wooten, A., Lichten, S. M., Sahai, R., and Wannier, P. G. (1982), *Astrophys. J.* **257**, 151.

Wright, M. C. H., and Plambeck, R. L. (1983), *Astrophys. J. Letters* **267**, L115.

Wynn-Williams, C. G., Genzel, R., Becklin, E. E., and Downes, D. (1984), *Astrophys. J.* **281**, 172.

Zuckerman, B. (1973), *Astrophys. J.* **183**, 863.

Zuckerman, B., Kuiper, T. B. H., and Rodriguez Kuiper, E. N. (1976), *Astrophys. J. Letters* **209**, L137.

Zuckerman, B., and Palmer, P. (1975), *Astrophys. J. Letters* **199**, L35.